Discharging Two-Phase Flow Through Single and Multiple Branches: Experiments and CFD Modelling

By

Meghan K. Guyot

A Thesis Submitted to the Faculty of Graduate Studies

in Partial Fulfilment of the Requirements for the Degree of

Doctor of Philosophy

Department of Mechanical Engineering

University of Manitoba

Winnipeg

Abstract

The main objectives of this study were to obtain new experimental data for conditions not previously tested for discharging two-phase flow through two 6.35 mm diameter branches with centrelines falling in an inclined plane and to assess the applicability of ANSYS CFX in modelling discharging two-phase flow through various single and multiple branch geometries. The present results are relevant to many industrial applications including headers and manifolds, multichannel heat exchangers and small breaks in horizontal pipes.

In the experimental investigation, onsets of liquid and gas entrainment data were obtained, analyzed and correlated for two different branch spacings and two different angles between the branches. For each combination of branch spacing and angle between the branches, a wide range of Froude numbers was used. Two-phase mass flow rate and quality results were also obtained and analyzed for a range of interface heights for 16 different combinations of branch spacing, inclination angle, test section pressure and pressure drop across each branch. New correlations were developed to predict the dimensionless mass flow rate and the quality. The new correlations show good agreement with the present data and with previous correlations.

Using ANSYS CFX, the inhomogeneous, free surface model was used to model discharging two-phase flow through horizontal branches with the following configurations: a single short branch of square cross-section (G1), a single long branch of square cross-section (G2), a single long branch of round cross section (G3), two round branches located one on top of the other (G4), and two round branches with their centreplane angled 30° from the horizontal. For these five geometries, results were compared with previous and present results and showed good agreement for Geometries G1, G2, G3 and G5. For Geometry G4, CFX was unable to predict results when the interface was located such that the two phases flowed through both branches simultaneously. Under these conditions, the flow phenomena were too complicated and further investigations are necessary.

Acknowledgements

Firstly, I would like to express my sincere gratitude to my advisors, Dr. Scott Ormiston and Dr. Hassan Soliman for their continuous guidance and support throughout my Ph.D studies. I would also like to thank Mr. Zeev Kapitanker for his help with constructing and maintaining the experimental apparatus and the internal and external committee members: Dr. Stefan Cenkowski, Dr.Vijay Chatoorgoon and Dr. Yuri Muzychka for their insightful comments and questions.

I would also like to greatly acknowledge the Natural Sciences and Engineering Research Council of Canada and the University of Manitoba for their financial support.

Last but not least, I would like to thank my family: my parents for taking such good care of my children while I studied, my husband Brendan for his endless love and support, and my children Caelan and Damon for their continuous patience.

Table of Contents

Abstract iii

Acknowledgements iv

List of Figures xi

List of Tables xix

Nomenclature xxv

Chapter 1 Introduction 1

1.1 Background 1

1.2 Objectives 4

1.3 Scope 5

Chapter 2 Literature Review 6

2.1 Introduction 6

2.2 Two-Phase Flow in a Simulated CANDU Header 6

2.3 Discharging Two-Phase Flow Through a Single Branch 9

2.3.1 Flow Through a Single Horizontal, Vertically Upward or Vertically Downward Branch 9

2.3.2 Flow Through a Single Branch on an Inclined Wall 17

2.3.3 Summary of Discharging Flow Through a Single Branch 20

2.4 Discharging Two-Phase Flow Through Multiple Branches 21

2.4.1 Flow Through Two Horizontal Branches Located One-On-Top of the Other 21

2.4.2 Flow Through Two Horizontal Branches Located Side-by-Side 25

2.4.3 Flow Through Two Horizontal Branches Separated by a Distance L and an Angle θ 27

2.4.4 Flow Through Three Branches 28

2.4.5 Summary of Discharging Two-Phase Flow Through Multiple Branches 30

2.5 Conclusion 31

Chapter 3 Experimental Investigation 32

3.1 Experimental Parameters 32

3.2 Experimental Apparatus 34

3.2.1 Flow Loop 34

3.2.2 Test Section 38

3.2.3 Separation Tanks 40

3.2.4 Flowrate Measurements 41

3.2.5 Liquid Level Measurements 43

3.2.6 Angle of Inclination Measurements 46

3.3 Experimental Procedure 46

3.3.1 Procedure for Onset of Liquid Entrainment, OLE 46

3.3.2 Procedure for Onset of Gas Entrainment, OGE 48

3.3.3 Procedure for Two-Phase Flow Measurements 49

3.4 Data Reduction 49

3.5 Experimental Uncertainty 52

Chapter 4 Experimental Results and Discussion 53

4.1 Onset of Liquid Entrainment 53

4.1.1 Data Range for OLE 53

4.1.2 Comparison of OLE Results with Previous Experimental Data 53

4.1.3 Flow Phenomena for OLE 54

4.1.4 OLE Results and Correlations 57

4.2 Onset of Gas Entrainment 63

4.2.1 Data Range for OGE 63

4.2.2 Comparison of OGE Results with Previous Experimental Data 64

4.2.3 Flow Phenomena for OGE 66

4.2.4 OGE Results and Correlations 68

4.3 Two-Phase Flow 73

4.3.1 Data Range for Two-Phase Flow 73

4.3.2 Comparison of Two-Phase Flow Results with Previous Experimental Data 74

4.3.3 Two-Phase Flow Results and Correlations 76

4.3.3.1 Two-Phase Flow Results for Case 1 76

4.3.3.2 Effect of ΔP and P_0 on Two-Phase Flow Results 78

4.3.3.3 Effect of L/d on Two-Phase Flow Results 86

4.3.3.4 Effect of θ on Two-Phase Flow Results 92

4.3.3.5 M and x Correlations 104

4.4 Experimental Repeatability 110

4.5 Closure 112

Chapter 5 Numerical Model Description 114

5.1 Model Geometries 114

5.2 Multiphase Flow Models in ANSYS CFX 119

5.3 Governing Equations for the Inhomogeneous Model 121

5.4 Boundary and Initial Conditions 125

5.4.1 Boundary Condition at the Top of the Tank 126

5.4.2 Boundary Condition at the Bottom of the Tank 126

5.4.3 Boundary Condition at a Branch Outlet 127

5.4.4 Initial Conditions 127

5.5 Properties 127

5.6 Mesh and Discretization Schemes 128

5.6.1 Mesh 128

5.6.2 Discretization Schemes 132

5.7 Timestep and Convergence Criteria 133

Chapter 6 Numerical Results and Discussion 134

6.1 Introduction 134

6.2 Results for Geometry with Single Circular Branch (G3) 135

6.2.1 OLE Results for Geometry G3 135

6.2.2 OGE Results for Geometry G3 139

6.2.3 Two-Phase Flow Results for Geometry G3 145

6.2.4 Summary of Results for Geometry G3 147

6.3 The Effect of Branch Cross Section on Single Branch Results 147

6.4 The Effect of Branch Length on Single Branch Results 151

6.5 Results for Geometry with Two Branches with $L/d = 1.5$ and $\theta = 30°$ (G5) 155

6.5.1 OLE Results for Geometry G5 155

6.5.2 OGE Results for Geometry G5 160

6.5.3 Two-Phase Flow Results for Geometry G5 165

6.5.4 Summary of Results for Geometry G5 172

6.6 Results for Geometry with Two Branches Located One on Top of the Other (G4) 172

Chapter 7 Conclusion 177

References 181

Appendix A Instrument Calibration 186

A.1 Thermocouple Calibration 187

A.2 Pressure Gauge Calibration 187

A.3 Water Rotameter Calibration 188

A.4 Air Rotameter Calibration 191

A.5 Pressure Transducer Calibration 194

Appendix B Estimates of Experimental Uncertainty 196

B.1 General Uncertainty Equation 197

B.2 Uncertainty in Mass Flow Rates 197

B.3 Uncertainty in Froude Numbers 198

B.4 Uncertainty in Interface Heights 200

B.5 Uncertainty in Dimensionless Mass Flow Rates and Interface Heights 201

Appendix C Experimental Data 230

C.1 Experimental Data for $\theta = 0°$ and $L/d = 1.5$ 231

C.2 Experimental Data for $\theta = 90°$ and $L/d = 1.5$ 232

C.3 Experimental Data for $\theta = 90°$ and $L/d = 3$ 234

C.4 Experimental Data for $\theta = 30°$ and $L/d = 1.5$ 234

C.5 Experimental Data for $\theta = 30°$ and $L/d = 3$ 239

C.6 Experimental Data for $\theta = 60°$ and $L/d = 1.5$ 244

C.7 Experimental Data for $\theta = 60°$ and $L/d = 3$ 249

Appendix D Numerical Data 254

D.1 Numerical Data for Geometry G1 255

D.2 Numerical Data for Geometry G2 256

D.3 Numerical Data for Geometry G3 258

D.4 Numerical Data for Geometry G4 259

D.5 Numerical Data for Geometry G5 260

List of Figures

Figure		Page
1.1	Cross section of typical CANDU header	2
1.2	h_{OLE} for a horizontal branch	3
1.3	h_{OGE} for a horizontal branch	3
2.1	Typical simulated CANDU header (Shaban and Tavoularis, 2012)	6
2.2	Bartley et al.'s (2008) geometry for OLE experiments	19
2.3	Bartley et al.'s (2008) geometry for OGE experiments	19
2.4	Geometry for dual branches separated by a vertical distance L	21
2.5	Geometry for dual branches separated by a horizontal distance L	26
2.6	Geometry for dual branches separated by a distance L and an angle θ	28
2.7	Geometry for test section with three branches	29
3.1	Geometrical and flow parameters	33
3.2	Variation of $\dot{m}_{TP,A}$ and $\dot{m}_{TP,B}$ with h_A	34
3.3	Schematic of experimental apparatus	35
3.4	Air supply piping and test section	36
3.5	Branches, separators and air headers	37
3.6	Acrylic tube	38
3.7	Front and side views of the brass insert	39
3.8	Brass insert for test section	40
3.9	Separators	41
3.10	Air and water rotameters	42
3.11	Schematic of liquid level measurement	44
3.12	Schematic of needle test set-up	45
4.1	Comparison of OLE data at Branch A with Hassan's (1995) correlation for $L/d = 1.5$	54
4.2	Comparison of OLE data at Branch B with Hassan's (1995) correlation for $L/d = 1.5$	55

4.3 Photographs of OLEs at Branch B for P_0 = 316 kPa and ΔP = 123 kPa 55

4.4 Photographs of OLEs at Branch A for P_0 = 316 kPa and ΔP = 123 kPa 56

4.5 OLE data and Hassan's (1995) correlations at Branch B for L/d = 1.5 57

4.6 OLE data and Hassan's (1995) correlations at Branch B for L/d = 3 58

4.7 Comparison of OLE data at Branch B with Maier et al. (2001) for θ = 30° 59

4.8 Comparison of OLE data at Branch B with Maier et al. (2001) for θ = 60° 59

4.9 OLE data and Hassan's (1995) correlations at Branch A for L/d = 1.5 60

4.10 OLE Data and Hassan's (1995) Correlations at Branch A for L/d = 3 61

4.11 Correlated versus measured values of $\left|h_{OLE,A}\right|/d$ 62

4.12 Correlated versus measured values of $\left|h_{OLE,B}\right|/d$ 63

4.13 Comparison of OGE data at Branch A with Hassan's (1995) correlation for L/d = 1.5 65

4.14 Comparison of OGE data at Branch B with Hassan's (1995) correlation for L/d = 1.5 65

4.15 Photographs of OGEs at Branch A for P_0 = 316 kPa and ΔP = 123 kPa 66

4.16 Photographs of OGEs at Branch B for P_0 = 316 kPa and ΔP = 123 kPa 68

4.17 OGE data and Hassan's (1995) correlation at Branch A for L/d = 1.5 69

4.18 OGE data and Hassan's (1995) correlation at Branch A for L/d = 3 69

4.19 OGE data and Hassan's (1995) correlation at Branch B for L/d = 1.5 70

4.20 OGE data and Hassan's (1995) correlation at Branch B for L/d = 3 71

4.21 Correlated versus measured values of $h_{OGE,A}/d$ 72

4.22 Correlated versus measured values of $h_{OGE,B}/d$ 73

4.23 Comparison of results for M versus H with Hassan (1995) for θ = 0° 75

4.24 Comparison of results for x versus H with Hassan (1995) for θ = 0° 76

4.25 $\dot{m}_{TP}$ versus h_A for Case 1 77

4.26 x versus h_A for Case 1 78

4.27 Experimental results for $\dot{m}_{TP,A}$ versus h_A for Cases 1 and 2 79

4.28 Experimental results for $\dot{m}_{TP,B}$ versus h_B for Cases 1 and 2 79

4.29 Experimental results for x_A versus h_A for Cases 1 and 2 80

4.30 Experimental results for x_B versus h_B for Cases 1 and 2 81

4.31 Schematic of crossing x versus h curves for Cases 1 and 2 81

4.32 Experimental results for M_A versus H_A for Cases 1 and 2 82

4.33 Experimental results for x_A versus H_A for Cases 1 and 2 82

4.34 Experimental results for M_B versus H_B for Cases 1 and 2 83

4.35 Experimental results for x_B versus H_B for Cases 1 and 2 83

4.36 Experimental results for M_A versus H_A for Cases 1 to 4 84

4.37 Experimental results for x_A versus H_A for Cases 1 to 4 85

4.38 Experimental results for M_B versus H_B for Cases 1 to 4 85

4.39 Experimental results for x_B versus H_B for Cases 1 to 4 86

4.40 $\dot{m}_{TP}$ versus h at Branches A and B for Case 12 87

4.41 x versus h at Branches A and B for Case 12 88

4.42 $\dot{m}_{TP}$ versus h at Branches A and B for Case 1 88

4.43 x versus h at Branches A and B for Case 1 89

4.44 $\dot{m}_{TP}$ versus h at Branches A and B for Case 16 90

4.45 x versus h at Branches A and B for Case 16 90

4.46 $\dot{m}_{TP}$ versus h at Branches A and B for Case 5 91

4.47 x versus h at Branches A and B for Case 5 91

4.48 $\dot{m}_{TP}$ versus h at Branches A and B for Case 3 93

4.49 x versus h at Branches A and B for Case 3 93

4.50 $\dot{m}_{TP}$ versus h at Branches A and B for Case 11 94

4.51 x versus h at Branches A and B for Case 11 95

4.52 $\dot{m}_{TP,A}$ versus h_A for θ = 30°, 60° and 90° 96

4.53 x_B versus h_B for θ = 30°, 60° and 90° 96

4.54 Schematic of $\dot{m}_{TP}$ versus h for θ = 30°, 60° and 90° 97

4.55 Schematic of x versus h for θ = 30°, 60° and 90° 97

4.56 $\dot{m}_{TP,B}$ versus h_B for θ = 30°, 60° and 90° 98

4.57 x_B versus h_B for θ = 30°, 60° and 90° 99

4.58 Experimental results for M_A versus H_A for Cases 3 and 11 100

4.59 Experimental results for x_A versus H_A for Cases 3 and 11 100

4.60 Experimental results for M_B versus H_B for Cases 3 and 11 101

4.61 Experimental results for x_B versus H_B for Cases 3 and 11 102

4.62 Experimental results for M_A versus H_A for Cases 7 and 15 102

4.63 Experimental results for x_A versus H_A for Cases 7 and 15 103

4.64 Experimental results for M_B versus H_B for Cases 7 and 15 103

4.65 Experimental results for x_B versus H_B for Cases 7 and 15 104

4.66 Measurement schematic for θ used in correlations 105

4.67 Predicted versus measured values of M_A 106

4.68 Predicted versus measured values of M_B 107

4.69 Predicted versus measured values of x_A 109

4.70 Predicted versus measured values of x_B 110

5.1 Geometry of single branch models (G1 to G3) – side view 115

5.2 Geometry of single branch models (G1 to G3) – front views 115

5.3 Geometry of dual branch models (G4 and G5) – side view 116

5.4 Geometry of dual branch models (G4 and G5) – front views 117

5.5 Locations where $\alpha_{GA,BBI}$ and $\alpha_{GB,BBI}$ were measured during OLE Analysis for Geometry G5 118

5.6 Locations where $\alpha_{GA,BTI}$ and $\alpha_{GB,BTI}$ were measured during OLE Analysis for Geometry G5 119

5.7 Comparison of air volume fraction contours from homogeneous and inhomogeneous models for $\mathrm{Fr}_{G,OLE}$ = 7.74 and h = -10.8 mm 121

5.8 Cropped views of a sample medium mesh for Geometry G1 129

5.9 Cropped views of a sample medium mesh for Geometry G3 129

5.10 Cropped views of a sample medium mesh for Geometry G4 130

5.11 Cropped views of a sample medium mesh for Geometry G5 130

5.12 Typical two-dimensional control volume in CFX 132

6.1 Air volume fraction contours for Geometry G3 for $\mathrm{Fr}_{G,OLE}$ = 22.55 near the OLE 136

6.2 Schematic of interface near OLE 137

6.3 Pressure difference, hydrostatic pressure and air volume fraction for $\mathrm{Fr}_{G,OLE}$ = 22.55 near the OLE 138

6.4 Interface height at the onset of liquid entrainment for Geometry G3 140

6.5 Air volume fraction contours for Geometry G3 for $\mathrm{Fr}_{L,OGE}$ = 26.51 near the OGE 141

6.6 Transient results of $\alpha_{G,BT}$ and $\dot{m}_G$ versus timestep near the OGE for Geometry G3 142

6.7 Pressure contours for Geometry G3 for $\mathrm{Fr}_{L,OGE}$ = 26.51 144

6.8 Interface height at the onset of gas entrainment for Geometry G3 145

6.9 $\dot{m}_{TP}$ versus h for P_0 = 35 and 120 kPa for Geometry G3 146

6.10 M versus H for P_0 = 35 and 120 kPa for Geometry G3 146

6.11 x vs. H for P_0 = 35 and 120 kPa for Geometry G3 147

6.12 Effect of branch cross section on $|h_{OLE}|/d$ versus $\mathrm{Fr}_{G,OLE}$ 148

6.13 Effect of branch cross section on h_{OGE}/d versus $\mathrm{Fr}_{L,OGE}$ 149

6.14 Effect of branch cross section on $\dot{m}_{TP}$ versus h for $P_0 = 120$ kPa 150

6.15 Effect of branch cross section on M versus H for $P_0 = 120$ kPa 150

6.16 Effect of branch cross section on x versus H for $P_0 = 120$ kPa 151

6.17 Effect of branch length on $|h_{OLE}|/d$ versus $\mathrm{Fr}_{G,OLE}$ 152

6.18 Effect of branch length on h_{OGE}/d versus $\mathrm{Fr}_{L,OGE}$ 152

6.19 Effect of branch length on $\dot{m}_{TP}$ versus h for $P_0 = 120$ kPa 153

6.20 Effect of branch length on M versus H for $P_0 = 120$ kPa 154

6.21 Effect of branch length on x versus H for $P_0 = 120$ kPa 154

6.22 Air volume fraction contours for $\mathrm{Fr}_{G,OLE,B} = 21.87$ near the OLE at Branch B for geometry with dual inclined branches (G5) 156

6.23 Numerical data and experimental correlation for $|h_{OLE,B}|/d$ versus $\mathrm{Fr}_{G,OLE,B}$ for Geometry G5 157

6.24 Air volume fraction contours for $\mathrm{Fr}_{G,OLE,A} = 21.87$ near the OLE at Branch A for geometry with dual inclined branches (G5) 158

6.25 Numerical data and experimental correlation for $|h_{OLE,A}|/d$ versus $\mathrm{Fr}_{G,OLE,A}$ for Geometry G5 159

6.26 Air volume fraction contours for $\mathrm{Fr}_{L,OGE,A} = 25.85$ near the OGE at Branch A for geometry with dual inclined branches (G5) 161

6.27 Numerical data and experimental correlation for $h_{OGE,A}/d$ versus $\mathrm{Fr}_{L,OGE,A}$ for Geometry G5 162

6.28 Air volume fraction contours for $\mathrm{Fr}_{L,OGE,B}$ = 25.84 near the OGE at Branch B for geometry with dual inclined branches (G5) 163

6.29 Numerical data and experimental correlation for $h_{OGE,B}/d$ versus $\mathrm{Fr}_{L,OGE,B}$ for Geometry G5 164

6.30 $\dot{m}_{TP}$ versus h_A for Geometry G5 with P_0 = 60 kPa 166

6.31 x versus h_A for Geometry G5 with P_0 = 60 kPa 166

6.32 $\dot{m}_{TP,A}$ versus h_A for Geometry G5 167

6.33 x_A versus h_A for Geometry G5 167

6.34 $\dot{m}_{TP,B}$ versus h_B for Geometry G5 168

6.35 x_B versus h_B for Geometry G5 169

6.36 M_A versus H_A for Geometry G5 170

6.37 x_A versus H_A for Geometry G5 170

6.38 M_B versus H_B for Geometry G5 171

6.39 x_B versus H_B for Geometry G5 171

6.40 $\dot{m}_{TP}$ versus h_A for Geometry G4 with P_0 = 120 kPa 173

6.41 $\dot{m}_{TP}$ versus h_A for Geometry G4 with P_0 = 400 kPa 173

6.42 Sketch of interface shape for $h_{OLE,A} < h < h_{OGE,B}$ as observed in experiments for Geometry G4 174

6.43 Air volume fraction contours for Geometry G4 with P_0 = 120 kPa and h_A = -5.7 mm 174

6.44 Air volume fraction contours for Geometry G4 for P_0 = 120 kPa and h_A = -5.7 mm using the mixture model 176

A.1 Diagram for calibration of pressure transducers 194

A.2 Calibration results for test section pressure transducer 195

List of Tables

Table		Page
2.1	A representative sample of the experimental studies on discharging two-phase flow through a single branch	10
2.2	Coefficients C_1 and C_2 in Equation (2.1) for calculating critical heights at the OLE for horizontal and vertically upward branches	12
2.3	Coefficients C_3 and C_4 in Equation (2.3) for calculating critical heights at the OGE for horizontal and vertically downward branches	13
2.4	A representative sample of the experimental studies on discharging two-phase flow through two or three branches	22
4.1	Experimental matrix for two-phase flow	74
4.2	Repeatability of h_{OLE}/d for $P_0 = 316$ kPa, $\Delta P = 40$ kPa, and $\theta = 60°$	111
4.3	Repeatability of h_{OGE}/d for $P_0 = 316$ kPa, $\Delta P = 40$ kPa, and $\theta = 60°$	111
4.4	Repeatability of two-phase data for $P_0 = 316$ kPa, $\Delta P = 40$ kPa, $L/d = 1.5$ and $\theta = 30°$	111
5.1	Geometries modelled	114
5.2	Grid independence results for Geometry G1 for h = -14.98 mm and P_0 = 120 kPa	131
5.3	Grid independence results for Geometry G3 for h = -6.89 mm and P_0 = 120 kPa	131
5.4	Grid independence results for Geometry G5 for h_A = -6.53 mm and P_0 = 120 kPa	131
A.1	Thermocouple calibration data	187
A.2	Calibrated data for pressure gauges PG1 – PG4	188
A.3	Calibration data for water rotameters Wa1 and Wb1	189
A.4	Calibration data for water rotameters Wa2 and Wb2	189
A.5	Calibration data for water rotameters Wa3 and Wb3	190

A.6 Calibration data for water rotameters Wa4 and Wb4 190
A.7 Calibration data for air rotameters Aa1 and Ab1 192
A.8 Calibration data for air rotameters Aa2 and Ab2 192
A.9 Calibration data for air rotameters Aa3 and Ab3 193
A.10 Calibration data for air rotameters Aa4 and Ab4 193
B.1 Uncertainty in $\dot{m}_L$ 197
B.2 Uncertainty in $\dot{m}_G$ 197
B.3 Uncertainty in Froude numbers for $L/d = 1.5$ and $\theta = 30°$ 199
B.4 Uncertainty in Froude numbers for $L/d = 3$ and $\theta = 30°$ 199
B.5 Uncertainty in Froude numbers for $L/d = 1.5$ and $\theta = 60°$ 199
B.6 Uncertainty in Froude numbers for $L/d = 3$ and $\theta = 60°$ 200
B.7 Uncertainties in Branch A mass flow rates, interface heights and qualities for Case 1 - $P_0 = 316$ kPa, $\Delta P = 40$ kPa, $L/d = 1.5$ and $\theta = 30°$ 202
B.8 Uncertainties in Branch B mass flow rates, interface heights and qualities for Case 1 - $P_0 = 316$ kPa, $\Delta P = 40$ kPa, $L/d = 1.5$ and $\theta = 30°$ 203
B.9 Uncertainties in Branch A mass flow rates, interface heights and qualities for Case 2 - $P_0 = 316$ kPa, $\Delta P = 123$ kPa, $L/d = 1.5$ and $\theta = 30°$ 204
B.10 Uncertainties in Branch B mass flow rates, interface heights and qualities for Case 2 - $P_0 = 316$ kPa, $\Delta P = 123$ kPa, $L/d = 1.5$ and $\theta = 30°$ 205
B.11 Uncertainties in Branch A mass flow rates, interface heights and qualities for Case 3 - $P_0 = 517$ kPa, $\Delta P = 97$ kPa, $L/d = 1.5$ and $\theta = 30°$ 206
B.12 Uncertainties in Branch B mass flow rates, interface heights and qualities for Case 3 - $P_0 = 517$ kPa, $\Delta P = 97$ kPa, $L/d = 1.5$ and $\theta = 30°$ 207
B.13 Uncertainties in Branch A mass flow rates, interface heights and qualities for Case 4 - $P_0 = 517$ kPa, $\Delta P = 235$ kPa, $L/d = 1.5$ and $\theta = 30°$ 208
B.14 Uncertainties in Branch B mass flow rates, interface heights and qualities for Case 4 - $P_0 = 517$ kPa, $\Delta P = 235$ kPa, $L/d = 1.5$ and $\theta = 30°$ 209
B.15 Uncertainties in Branch A mass flow rates, interface heights and qualities for Case 5 - $P_0 = 316$ kPa, $\Delta P = 40$ kPa, $L/d = 3$ and $\theta = 30°$ 210

B.16 Uncertainties in Branch B mass flow rates, interface heights and qualities for Case 5 - $P_0 = 316\,\text{kPa}$, $\Delta P = 40\,\text{kPa}$, $L/d = 3$ and $\theta = 30°$ 211

B.17 Uncertainties in Branch A mass flow rates, interface heights and qualities for Case 6 - $P_0 = 316$ kPa, $\Delta P = 123$ kPa, $L/d = 3$ and $\theta = 30°$ 212

B.18 Uncertainties in Branch B mass flow rates, interface heights and qualities for Case 6 - $P_0 = 316\,\text{kPa}$, $\Delta P = 123$ kPa, $L/d = 3$ and $\theta = 30°$ 213

B.19 Uncertainties in Branch A mass flow rates, interface heights and qualities for Case 7 - $P_0 = 517$ kPa, $\Delta P = 97$ kPa, $L/d = 3$ and $\theta = 30°$ 214

B.20 Uncertainties in Branch B mass flow rates, interface heights and qualities for Case 7 - $P_0 = 517$ kPa, $\Delta P = 97$ kPa, $L/d = 3$ and $\theta = 30°$ 215

B.21 Uncertainties in Branch A mass flow rates, interface heights and qualities for Case 8 - $P_0 = 517$ kPa, $\Delta P = 235$ kPa, $L/d = 3$ and $\theta = 30°$ 216

B.22 Uncertainties in Branch B mass flow rates, interface heights and qualities for Case 8 - $P_0 = 517$ kPa, $\Delta P = 235$ kPa, $L/d = 3$ and $\theta = 30°$ 217

B.23 Uncertainties in Branch A mass flow rates, interface heights and qualities for Case 9 - $P_0 = 316$ kPa, $\Delta P = 40$ kPa, $L/d = 1.5$ and $\theta = 60°$ 218

B.24 Uncertainties in Branch B mass flow rates, interface heights and qualities for Case 9 - $P_0 = 316\,\text{kPa}$, $\Delta P = 40\,\text{kPa}$, $L/d = 1.5$ and $\theta = 60°$ 219

B.25 Uncertainties in Branch A mass flow rates, interface heights and qualities for Case 10 - $P_0 = 316$ kPa, $\Delta P = 123$ kPa, $L/d = 1.5$ and $\theta = 60°$ 220

B.26 Uncertainties in Branch B mass flow rates, interface heights and qualities for Case 10 - $P_0 = 316\,\text{kPa}$, $\Delta P = 123$ kPa, $L/d = 1.5$ and $\theta = 60°$ 221

B.27 Uncertainties in Branch A mass flow rates, interface heights and qualities for Case 11 - $P_0 = 517$ kPa, $\Delta P = 97$ kPa, $L/d = 1.5$ and $\theta = 60°$ 222

B.28 Uncertainties in Branch B mass flow rates, interface heights and qualities for Case 11 - $P_0 = 517$ kPa, $\Delta P = 97$ kPa, $L/d = 1.5$ and $\theta = 60°$ 223

B.29 Uncertainties in Branch A mass flow rates, interface heights and qualities for Case 12 - $P_0 = 517$ kPa, $\Delta P = 235$ kPa, $L/d = 1.5$ and $\theta = 60°$ 224

B.30 Uncertainties in Branch B mass flow rates, interface heights and qualities for Case 12 - P_0 = 517 kPa, ΔP = 235 kPa, L/d = 1.5 and θ = 60° 225

B.31 Uncertainties in Branch A mass flow rates, interface heights and qualities for Case 13 - P_0 = 316 kPa, ΔP = 40 kPa, L/d = 3 and θ = 60° 225

B.32 Uncertainties in Branch B mass flow rates, interface heights and qualities for Case 13 - P_0 = 316 kPa, ΔP = 40 kPa, L/d = 3 and θ = 60° 226

B.33 Uncertainties in Branch A mass flow rates, interface heights and qualities for Case 14 - P_0 = 316 kPa, ΔP = 123 kPa, L/d = 3 and θ = 60° 226

B.34 Uncertainties in Branch B mass flow rates, interface heights and qualities for Case 14 - P_0 = 316 kPa, ΔP = 123 kPa, L/d = 3 and θ = 60° 227

B.35 Uncertainties in Branch A mass flow rates, interface heights and qualities for Case 15 - P_0 = 517 kPa, ΔP = 97 kPa, L/d = 3 and θ = 60° 227

B.36 Uncertainties in Branch B mass flow rates, interface heights and qualities for Case 15 - P_0 = 517 kPa, ΔP = 97 kPa, L/d = 3 and θ = 60° 228

B.37 Uncertainties in Branch A mass flow rates, interface heights and qualities for Case 16 - P_0 = 517 kPa, ΔP = 235 kPa, L/d = 3 and θ = 60° 228

B.38 Uncertainties in Branch B mass flow rates, interface heights and qualities for Case 16 - P_0 = 517 kPa, ΔP = 235 kPa, L/d = 3 and θ = 60° 229

C.1 Experimental OLE and OGE data for $\theta = 0°$ *and* $L/d = 1.5$ 231

C.2 Experimental two-phase flow data for P_0 = 316 kPa, ΔP = 40 kPa, $\theta = 0°$ and $L/d = 1.5$ 231

C.3 Experimental two-phase flow data for P_0 = 517 kPa, ΔP = 235 kPa, $\theta = 0°$ and $L/d = 1.5$ 232

C.4 Experimental OLE and OGE data for $\theta = 90°$ and $L/d = 1.5$ 232

C.5 Experimental two-phase flow data for P_0 = 517 kPa, ΔP = 235 kPa, $\theta = 90°$ and $L/d = 1.5$ 233

C.6 Experimental OLE and OGE data for $\theta = 90°$ and $L/d = 3$ 234

C.7 Experimental OLE and OGE data for $\theta = 30°$ and $L/d = 1.5$ 234

C.8 Experimental two-phase flow data for Case 1 with P_0 = 316 kPa, ΔP = 40 kPa, θ = 30° and L/d = 1.5 235

C.9 Experimental two-phase flow data for Case 2 with P_0 = 316 kPa, ΔP = 123 kPa, θ = 30° and L/d = 1.5 236

C.10 Experimental two-phase flow data for Case 3 with P_0 = 517 kPa, ΔP = 97 kPa, θ = 30° and L/d = 1.5 237

C.11 Experimental two-phase flow data for Case 4 with P_0 = 517 kPa, ΔP = 235 kPa, θ = 30° and L/d = 1.5 238

C.12 Experimental OLE and OGE data for θ = 30° and L/d = 3 239

C.13 Experimental two-phase flow data for Case 5 with P_0 = 316 kPa, ΔP = 40 kPa, θ = 30° and L/d = 3 240

C.14 Experimental two-phase flow data for Case 6 with P_0 = 316 kPa, ΔP = 123 kPa, θ = 30° and L/d = 3 241

C.15 Experimental two-phase flow data for Case 7 with P_0 = 517 kPa, ΔP = 97 kPa, θ = 30° and L/d = 3 242

C.16 Experimental two-phase flow data for Case 8 with P_0 = 517 kPa, ΔP = 235 kPa, θ = 30° and L/d = 3 243

C.17 Experimental OLE and OGE data for θ = 60° and L/d = 1.5 244

C.18 Experimental two-phase flow data for Case 9 with P_0 = 316 kPa, ΔP = 40 kPa, θ = 60° and L/d = 1.5 245

C.19 Experimental two-phase flow data for Case 10 with P_0 = 316 kPa, ΔP = 123 kPa, θ = 60° and L/d = 1.5 246

C.20 Experimental two-phase flow data for Case 11 with P_0 = 517 kPa, ΔP = 97 kPa, θ = 60° and L/d = 1.5 247

C.21 Experimental two-phase flow data for Case 12 with P_0 = 517 kPa, ΔP = 235 kPa, θ = 60° and L/d = 1.5 248

C.22 Experimental OLE and OGE data for θ = 60° and L/d = 3 249

C.23 Experimental two-phase flow data for Case 13 with P_0 = 316 kPa, ΔP = 40 kPa, θ = 60° and L/d = 3 250
C.24 Experimental two-phase flow data for Case 14 with P_0 = 316 kPa, ΔP = 123 kPa, θ = 60° and L/d = 3 251
C.25 Experimental two-phase flow data for Case 15 with P_0 = 517 kPa, ΔP = 97 kPa, θ = 60° and L/d = 3 252
C.26 Experimental two-phase flow data for Case 16 with P_0 = 517 kPa, ΔP = 235 kPa, θ = 60° and L/d = 3 253
D.1 Numerical OLE data for Geometry G1 255
D.2 Numerical OGE data for Geometry G1 255
D.3 Numerical two-phase flow data for Geometry G1, P_0 = 35 kPa 255
D.4 Numerical two-phase flow data for Geometry G1, P_0 = 120 kPa 256
D.5 Numerical OLE data for Geometry G2 256
D.6 Numerical OGE data for Geometry G2 256
D.7 Numerical two-phase flow data for Geometry G2, P_0 = 35 kPa 257
D.8 Numerical two-phase flow data for Geometry G2, P_0 = 120 kPa 257
D.9 Numerical OLE data for Geometry G3 258
D.10 Numerical OGE data for Geometry G3 258
D.11 Numerical two-phase flow data for Geometry G3, P_0 = 35 kPa 258
D.12 Numerical two-phase flow data for Geometry G3, P_0 = 120 kPa 259
D.13 Numerical two-phase flow data for Geometry G4, P_0 = 120 kPa 259
D.14 Numerical two-phase flow data for Geometry G4, P_0 = 400 kPa 260
D.15 Numerical two-phase flow data for Geometry G5, P_0 = 60 kPa 260
D.16 Numerical two-phase flow data for Geometry G5, P_0 = 120 kPa 261

Nomenclature

A_{LG}	interfacial area density
A_1 to A_8	constants in Equations (4.1), (4.5), (4.10), (4.13) and (4.16)
B_1 to B_6	constants in Equations (4.2), (4.6), (4.13) and (4.21)
C_1 to C_4	constants in Equations (2.1) and (2.3)
C_D	drag coefficient
d	branch diameter, m
D	test section diameter, m
D_1 to D_3	constants in Equations (2.9) and (2.11)
E_L	voltage reading from pressure transducer, PT1, Volt
E_1 to E_3	constants in Equations (2.10) and (2.12)
F	surface tension force in momentum equation, N/m^3
Fr	Froude number
g	gravitational acceleration, m/s^2
h	interface height measured from branch centreline, m
H	dimensionless interface height
k	turbulent kinetic energy, m^2/s^2
L	distance between branches, m
L_B	length of branch, m

L_{zero}	height of liquid between pressure transducer and zero location in test section, m
$\dot{m}$	mass flow rate, kg/s
M	dimensionless two-phase mass flow rate
M^D	interphase drag force in momentum equation, N/m^3
n	ratio of specific heats
n_{LG}	interface normal vector
P	pressure, Pa
P_0	test section pressure, Pa
P_S	separator pressure, Pa
P_t	turbulence production, m^2/s^3
ΔP	pressure difference between test section and separator pressures, Pa
R	branch resistance, $(kg \cdot m)^{-1/2}$
S_b	buoyancy source term in momentum equation, N/m^3
T	temperature, K
u	velocity in the x-direction, m/s
v	velocity in the y-direction, m/s
V	average velocity, m/s
w	velocity in the z-direction, m/s
x	quality
y^+	dimensionless wall distance

α	volume fraction
χ	density ratio in Equation (3.2)
δ_{LG}	interface delta function, m^{-1}
∇_S	gradient operator on the interface, m^{-1}
ε	dissipation rate, m^2/s^3
ϕ	branch angle of inclination
γ_1 to γ_3	coefficients in Equation (3.1)
μ	dynamic viscosity, kg/m·s
θ	angle of inclination between two branch centrelines
ρ	density, kg/m^3
σ	surface tension coefficient, N/m
ω	uncertainty error

Subscripts

atm	atmospheric
A	branch A
B	branch B
BB	branch bottom
BBI	branch bottom inclined
BT	branch top
BTI	branch top inclined

CL	centreline
eff	effective
G	gas
IL	interface lower
IU	interface upper
L	liquid
OGE	onset of gas entrainment
OLE	onset of liquid entrainment
out	outlet
rot	rotameter
STD	standard
T	turbulent
th	throat
TP	two phase
α	primary phase
β	secondary phase

Chapter 1
Introduction

1.1 Background

Two-phase (gas-liquid) discharge from a stratified region is important due to its relevance to many industrial applications. Examples of these applications include the flow through small breaks in horizontal pipes during postulated loss-of-coolant accidents in nuclear reactors, the flow distribution in multichannel heat exchangers, and the flow distribution in two-phase headers and manifolds such as the CANDU (Canadian Deuterium and Uranium reactors) header-feeder system during accident scenarios. In applications such as these, with two-phase flow entering a header and discharging through one or multiple branches, it is important to know the mass flow rate and quality exiting through each branch because the performance of components downstream of the header depends on these parameters. For example, the thermal performance of a multichannel heat exchanger is significantly reduced when the two-phase flow is not distributed evenly among the channels.

The CANDU header typically consists of a large diameter horizontal pipe (0.3 - 0.4 m diameter) approximately 10 to 12 m in length that is closed at both ends with single phase liquid at 10 MPa entering through inlet turrets at the top of the pipe and exiting through multiple banks of five branches called feeders located around the bottom half of the pipe and spaced at various axial locations, as shown in Figure 1.1. The flow exiting the header is then directed through the feeders to the fuel channels to provide cooling. If a break happens upstream from the header, the system depressurizes significantly and two-phase water-steam enters the header through the turrets. Under these conditions it is very important to know the mass flow rate and quality of the flow exiting through each branch to ensure adequate heat removal from the reactor's core. The experimental studies that simulated the full CANDU header (e.g., Kowalski and Krishnan, 1987;

Kowalski and Hanna, 1989) found many issues affecting the flow including inlet jetting, swirling in the header and possible hydraulic jumps. These effects make the predictions very hard and, therefore, studies with more simplified geometries were undertaken to gain some understanding of the phenomena involved. To date, there are no predictive models available for the CANDU header.

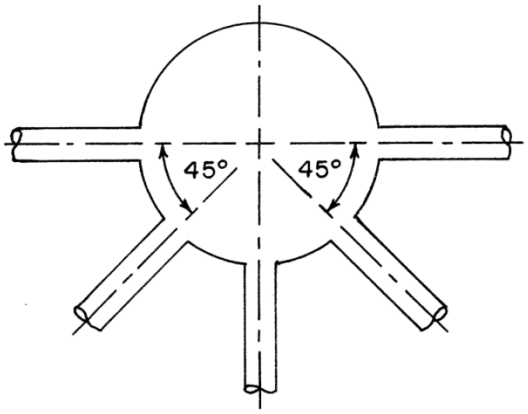

Figure 1.1 – Cross section of typical CANDU header

More simplified geometries such as two-phase flow discharging from a stratified region through a single branch have been studied both experimentally and theoretically to provide better insight to the application of small breaks in horizontal pipes. The focus of single-branch studies was to solve for the following parameters:

- ***The onset of liquid entrainment (OLE)interface height, h_{OLE} :***

  With the gas-liquid interface located well beneath a single-branch inlet, only gas flows through the branch. For the case of a horizontal branch, slowly raising the interface height towards the branch inlet causes the gas-liquid interface to deform at the wall underneath the branch. A critical height is reached when a small stream of water suddenly forms between the deformed interface and the branch inlet. This critical height is the OLE height, h_{OLE}, and is shown in Figure 1.2 for the case of a horizontal branch on the side of a large pipe. The datum for measuring h_{OLE} is the centreline of the branch.

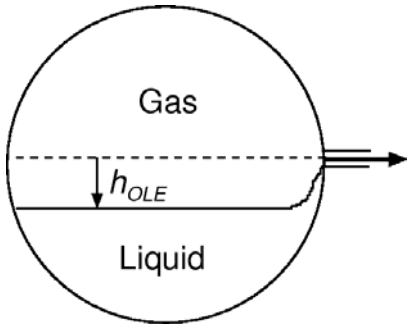

Figure 1.2 – h_{OLE} for a horizontal branch

- ***The onset of gas entrainment (OGE) interface height, h_{OGE} :***

With the interface located well above a single-branch inlet, pure liquid flows through the branch. By slowly lowering the interface height, a critical height is reached at which point a gas cone forms extending from the surface of the interface to the entrance of the branch. The height of the interface at this point is h_{OGE}, as shown in Figure 1.3. Lowering the interface further causes the cone to thicken and flow along the side of the wall above the branch towards the branch opening.

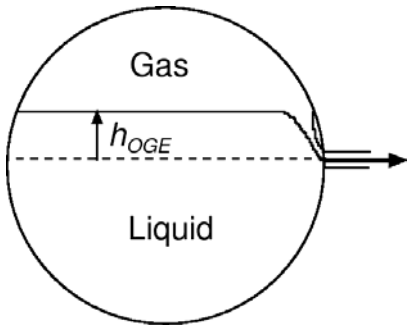

Figure 1.3 – h_{OGE} for a horizontal branch

- ***Two-phase mass flow rate, $\dot{m}_{TP}$, and quality, x :***

With the interface located between h_{OLE} and h_{OGE}, both liquid and gas flow through the opening with $\dot{m}_{TP}$ and x in the branch varying with the interface height location h.

The above parameters were studied theoretically and experimentally over a wide range of conditions for the case of a single branch. The theoretical studies resulted in models that

successfully predicted the interface heights at the onsets of liquid (Craya, 1949) and gas entrainment (Lubin and Springer, 1967); however, there is no complete model yet for predicting the two-phase mass flow rate and quality.

More recently, experiments have been done on two-phase flow discharging from a stratified region through multiple (two or three) branches in an attempt to approach the multichannel header problem. In these studies, the interface heights were measured at the onsets of liquid and gas entrainment and the two-phase mass flow rate and quality were measured for two horizontal branches with centrelines falling in a horizontal or a vertical plane (e.g., Hassan, 1995). Maier (1998) performed experiments on discharging flow through two horizontal branches with centrelines falling in an inclined plane and measured the critical heights at the onsets of liquid and gas entrainment but did not measure $\dot{m}_{TP}$ and x for interface heights located between the two onset heights. In terms of theoretical work for the case of multiple branches, models have been developed to predict h_{OLE} and h_{OGE} but no complete model exists for predicting $\dot{m}_{TP}$ and x.

There exists many computational fluid dynamics (CFD) software packages for solving single or multiphase flow problems; however, none of the available software has yet been proven to predict accurate results for discharging two-phase flow. Understanding the capabilities of commercial CFD software in predicting discharging two-phase flow will benefit not only the nuclear industry but also any industrial applications involving two-phase flow through branching pipes.

1.2 Objectives

To improve our understanding on the topic of two-phase discharging flow and to test the capabilities of CFD software in modelling this type of problem, the objectives of the current research project were as follows:

1. Perform experiments on discharging two-phase flow through two horizontal branches with centrelines falling in an inclined plane and determine h_{OLE} and h_{OGE} at each branch over a range of Froude numbers, and $\dot{m}_{TP}$ and x at each branch over a range of interface heights, h. Experiments were conducted at various test section pressures, P_0, pressure differences

between the test section and the branch outlet, ΔP, branch spacings, L, and angles between the branches, θ.

2. Study the effects of L/d, θ, and ΔP on the experimental data and develop empirical correlations.
3. Develop numerical models using ANSYS CFX for discharging two-phase flow from a large reservoir containing stratified layers of water and air through single and dual horizontal branches.
4. Assess the applicability of using ANSYS CFX in modelling two-phase discharging flow problems by comparing results for h_{OLE}, h_{OGE}, $\dot{m}_{TP}$ and x from the numerical model with present and previous experimental results, correlations, and theoretical models.

1.3 Scope

Chapter 2 of this thesis discusses the previous experimental and theoretical research done on the topic of discharging flow through single or multiple branches. Following this, a description of the experimental apparatus and procedure for the present work is included in Chapter 3 and the experimental results are presented and discussed in Chapter 4. Chapters 5 and 6 focus on the numerical models including a description of the numerical models (geometries, boundary conditions, governing equations, mesh, etc.) in Chapter 5 and a discussion of the numerical results including comparisons with the experimental results in Chapter 6. Chapter 7 contains a conclusion and recommendations for future work.

Chapter 2

Literature Review

2.1 Introduction

This literature review is divided into three main sections. The first section (2.2) focuses on reviewing the previous work on two-phase flow in a simulated CANDU header, the second section (2.3) focuses on the literature concerned with understanding two-phase flow through small breaks in pipes and thus looks at two-phase discharge through single branches and the third section (2.4) focuses on reviewing the literature on two-phase discharging flow through two or three branches.

2.2 Two-Phase Flow in a Simulated CANDU Header

Several experimental and few numerical studies (discussed later) have been conducted to simulate the CANDU header during a loss-of-coolant accident (LOCA) scenario. In general, the test sections consisted of a large header with one or two inlet turrets and multiple banks of five feeders located around the bottom half of the header as shown in Figure 2.1.

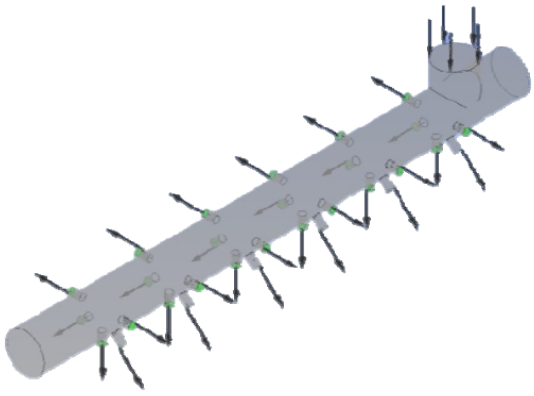

Figure 2.1 – Typical simulated CANDU header (Shaban and Tavoularis, 2012)

Kowalski and Krishnan (1987) and Kowalski and Hanna (1989) performed experiments at the Full-Scale Header test facility at Stern Laboratories Incorporated in Hamilton, Ontario. In these experiments, a steam-water mixture flowed through one or two turrets into an inlet manifold where the flow was divided into six banks of five branches leading to the outlet header. The inlet and outlet headers were 0.325 m in diameter with a length of 4.2 m, equivalent to approximately a half-length of a typical CANDU header. For inlet header pressures of 1, 2 and 5 MPa, experiments were conducted at various water and steam inlet flow rates. For all conditions tested, they reported that the flow remained stratified in the inlet header and that the water level inside the inlet header increased with a decrease in the quality of the injected flow. For the single turret injections, they noted that the water level was lowest beneath the inlet turret and increased rapidly downstream of the turret leading to a possible hydraulic jump. With two inlet turrets, the water level was lowest at both ends of the header underneath the inlet turrets and rose towards the center of the header. They also detected liquid entrainment into the feeders when the interface was located beneath the feeders and gas pull through when the interface was located above the feeders. Kowalski and Krishnan developed correlations for the onset of liquid and gas entrainment heights.

Using this same facility, Kowalski and Hanna (1988) examined how the pressure and flow rates changed with time in the inlet and outlet headers during depressurization due to a break in the inlet turret and studied the effects of initial header temperature and break size and location on the header refill time.

To provide more insight into the two-phase flow distribution in a CANDU header, Teclemariam et al. (2003) performed experiments on an acrylic, scaled-down version of the CANDU header. The header in these experiments was 38.1 mm in diameter and 484.8 mm long with two inlet turrets and six banks of five 6.4 mm diameter outlet feeders. The objective of this study was to observe the flow patterns in the header and obtain mass flow rate measurements in each of the feeders. The results showed a large variation in the mass flow rates and qualities between the feeders and this flow distribution was heavily influenced by the inlet flow rates, inlet qualities and number of inlet turrets.

More recently, Shaban and Tavoularis (2015) performed experiments at the Modular Header Facility at the University of Ottawa. The apparatus consisted of a 203 mm diameter aluminum header with one inlet turret and four banks of five 32.5 mm diameter outlet feeders. In

order to visually observe the flow patterns in the header and near the feeder inlets, clear acrylic observation windows were installed at each end of the header and one on the top of the header. In their experiments, the horizontal and inclined feeders were plugged and tests were conducted using one to four vertically downward outlet feeders to study the effects of feeder axial location and the inlet gas and liquid flow rates on the two-phase flow distribution. The flow patterns in the header and the flow distribution in the feeders were found to depend on the gas and liquid flow rates into the header and the number and location of feeders used. Comparisons of their results with those from Kowalski and Hanna (1989) and Teclemariam et al. (2003) showed that the flow patterns in the header were qualitatively the same. In addition, the flow rate measurements in the feeders showed the same trends as the measurements taken for the downward feeders in Teclemariam et al.'s experiments, despite Teclemariam et al.'s experiments also including horizontal and inclined feeders.

In terms of numerical models**,** Kowalski and Hanna (1988) attempted to model the CANDU header using the Canadian Algorithm for Thermal Hydraulic Network Analysis (CATHENA) code. This one-dimensional, two-fluid model was developed by Atomic Energy of Canada Limited (AECL) to analyze postulated accidents in CANDU reactors. Using this code, a simplified header was modelled where the five feeders at each bank were approximated as a single average feeder and the pressure in the inlet header was compared with the experimental measurements. The results from the model agreed qualitatively but not quantitatively with the experimental results. The CATHENA code was again used by Kowalski and Hanna (1989) in an attempt to predict the water level inside the inlet header for single and double turret injection. The numerical results over-predicted the experimental results at one end of the header and under-predicted the experimental results at the other end.

Shaban and Tavoularis (2012) attempted to generate numerical results for the header/feeder geometry with one inlet turret and six banks of five outlets, simulating the geometry used in Teclemariam et al. (2003). The objective of their work was to compare two computational fluid dynamic codes: ANSYS CFX and OpenFOAM using the homogeneous model, which solves a single set of momentum equations for both phases. The two codes were evaluated by comparing their results with the experimental results by Teclemariam et al. for this same geometry. They observed that the agreement between the numerical and experimental results of the mass flow rates

was poor and the simulations failed to predict the sharp variations in flow rates from feeder to feeder, probably due to the complex geometry and flow phenomena involved.

The complicated flow phenomena involved in modelling the CANDU header has led researchers to study more simplified geometries such as two-phase flow discharging from a stratified region through single, dual or triple branches.

2.3 Discharging Two-Phase Flow Through a Single Branch

Two-phase discharging flow from a stratified region through a single branch is useful as both a first step in understanding the flow phenomena involved in headers and is also applicable to small breaks in horizontal pipes. This section discusses the experimental and theoretical studies performed to measure or predict the critical heights h_{OLE} and h_{OGE}, and the mass flow rate $\dot{m}_{TP}$ and quality x. Table 2.1 provides a representative sample of the experimental studies including the geometry of the test sections, the range of independent variables and the measured quantities for each study. In this table, the parameters $v_{L,main}$ and $v_{G,main}$ refer to superimposed main pipe velocities of liquid and gas, respectively, which were included in some of the investigations and the parameter R refers to the branch resistance.

2.3.1 Flow Through a Single Horizontal, Vertically Upward or Vertically Downward Branch

The first theoretical model to predict the OLE height for discharging flow through side orifices was developed by Craya (1949). In Craya's analysis, the orifice was treated as a point sink and h_{OLE} was shown to depend on the gas Froude number $\mathrm{Fr}_{G,OLE}$ with the following relationship:

$$\left|h_{OLE}\right| / d = C_1 \mathrm{Fr}_{G,OLE}{}^{C_2} \tag{2.1}$$

Where $C_1 = 0.625$, $C_2 = 0.4$ and $\mathrm{Fr}_{G,OLE}$ is defined by the following equation:

Table 2.1 – A representative sample of the experimental studies on discharging two-phase flow through a single branch

Author(s)	Wall Geometry (Flat or Pipe)	Branch d (mm)	Branch Orientation	Fluids	Range of Parameters	Measured Quantities
Schrock et al. (1986)	pipe (D = 102 mm)	4, 6 and 10	vertically up, vertically down and horizontal	air-water, steam-water	0.1MPa < P_0 < 1.07MPa	h_{OGE}, h_{OLE}, $\dot{m}_{TP}$, x
Smoglie and Reimann (1986)	pipe (D = 206 mm)	6, 8, 12 and 20	vertically up, vertically down and horizontal	air-water	P_0 = 0.5 MPa; $10 \leq \Delta P \leq 400$ kPa; $0 \leq v_{L,main} \leq 0.5$ m/s; $0 \leq v_{G,main} \leq 2$ m/s	h_{OGE}, h_{OLE}, $\dot{m}_{TP}$, x
Yonomoto and Tasaka (1988)	flat	10 and 20	vertically up, vertically down and horizontal	air-water	$0.5 \leq P_0 \leq 0.7$ MPa; $2.6 \leq \Delta P \leq 600$ kPa; $0.063 \leq v_{L,main} \leq 0.62$ m/s; $0.16 \leq v_{G,main} \leq 3.5$ m/s	h_{OGE}, h_{OLE}, $\dot{m}_{TP}$, x
Micaelli and Memponteil (1989)	pipe (D = 80 or 135 mm)	12 and 20	vertically up, vertically down and horizontal	steam-water	$2 \leq P_0 \leq 7$ MPa	h_{OGE}, h_{OLE}, $\dot{m}_{TP}$, x
Hassan et al. (1998)	flat	6.35	horizontal	air-water	316 kPa $\leq P_0 \leq$ 517 kPa; 40 kPa $\leq \Delta P \leq$ 235 kPa; $1000 \leq R \leq 3000$ (kg m)$^{-1/2}$	h_{OGE}, h_{OLE}, $\dot{m}_{TP}$, x
Lee et al. (2007)	pipe (D = 184 mm)	16 and 24.8	0°, ±30°, ±40°, ±60°, ±90° from horizontal	air-water	$P_0 \leq 0.95$ MPa; $\dot{m}_{G,main} \leq 94.5 \times 10^{-3}$ kg/s; $\dot{m}_{L,main} \leq 3.5$ kg/s;	h_{OGE}, h_{OLE}
Bartley et al. (2008)	flat	6.35	branch perpendicular to wall located from -90° to 90° from horizontal	air-water	P_0 = 317 and 520 kPa; $3.8 \leq \Delta P \leq 271$ kPa; φ = 0°, ±30°, ±60° and ±90°	h_{OGE}, h_{OLE}
Bartley et al. (2010)	flat	6.35	branch perpendicular to wall located from -90° to 90° from horizontal	air-water	P_0 = 316 kPa; $11 \leq \Delta P \leq 210$ kPa; φ = 0°, ±30°, ±60° and ±90°	$\dot{m}_{TP}$, x

$$\mathrm{Fr}_{G,OLE} = \frac{V_G}{\sqrt{gd\,\dfrac{(\rho_L - \rho_G)}{\rho_G}}} \tag{2.2}$$

Due to the point sink assumption, h_{OLE} in Equation (2.1) approaches zero as $\mathrm{Fr}_{G,OLE}$ approaches zero. This limit is physically unrealistic since even under stagnant conditions, the liquid will enter the branch when the interface rises above the bottom of the branch inlet, i.e., h_{OLE}/d approaches 0.5 as $\mathrm{Fr}_{G,OLE}$ approaches zero. Craya's equation is therefore not valid at low values of $\mathrm{Fr}_{G,OLE}$. Soliman and Sims (1991 and 1992) later developed new analyses for discharging flow through side slots and side orifices taking into account the finite size of the slot and improving the results at low values of $\mathrm{Fr}_{G,OLE}$. Their analyses resulted in two algebraic equations for calculating h_{OLE}/d a function of $\mathrm{Fr}_{G,OLE}$ for both the finite slot and the finite orifice. For both the slot and the orifice, Soliman and Sims' results closely resembled Craya's results for $\mathrm{Fr}_{G,OLE} > 10$ but deviated for $\mathrm{Fr}_{G,OLE} < 10$.

Equation (2.1) was compared by various authors (e.g., Shrock et al., 1986; Smoglie and Reimann, 1986; Yonomoto and Tasaka, 1988) with their experimental data for horizontal and vertical branches. Table 2.2 shows the resulting coefficients in Equation (2.1) that gave the best fit with the data of various authors. For a horizontal branch, the resulting $|h_{OLE}|/d$ from the empirical correlations of Schrock et al. (1986), Smoglie and Reimann (1986) and Micaelli and Memponteil (1989) are all within 0.16% of Craya's (1949) while the deviation between Yonomoto and Tasaka (1988) and Craya's is 10.7% and the deviation between Hassan et al. (1998) and Craya's is less than 9% for the range tested. For an upward branch there is significant deviation between the coefficients; possible reasons for these deviations will be discussed shortly.

Lubin and Springer (1967) published some of the first results for the onset of gas entrainment height, h_{OGE}. In their experiments, two fluids were contained in a cylindrical tank. The bottom fluid (water) was drained from the cylindrical tank through an orifice located at the centre of the bottom of the tank. As the water drained out of the tank, the interface level dropped

Table 2.2 – Coefficients C_1 and C_2 in Equation (2.1) for calculating critical heights at the OLE for horizontal and vertically upward branches

Author	Horizontal Branch		Vertical Upward Branch	
	C_1	C_2	C_1	C_2
Schrock et al. (1986)	0.624	0.4	1.45	0.4
Smoglie and Reimann (1986)	0.626	0.4	1.52	0.4
Yonomoto and Tasaka (1988)	0.558	0.4	0.626	0.4
Micaelli and Memponteil (1989)	0.626	0.4	-	-
Hassan et al. (1998)	0.87	0.31	-	-

until the critical height was reached at which point the top fluid (air, turpentine, silicone-oil, corn oil or kerosene) started flowing through the drain. An analytical model was developed to predict this critical height (h_{OGE}) as a function of $\mathrm{Fr}_{L,OGE}$ by neglecting viscosity and surface tension and applying the Bernouilli equation at two points along a streamline located just below the interface. The resulting equation is of the same form as that of Craya (1949) with constants C_3 and C_4 as follows:

$$h_{OGE} / d = C_3 \mathrm{Fr}_{L,OGE}^{\ C_4} \tag{2.3}$$

Where $C_3 = 0.626$, $C_4 = 0.4$ and $\mathrm{Fr}_{L,OGE}$ is defined by the following equation:

$$\mathrm{Fr}_{L,OGE} = \frac{V_L}{\sqrt{gd\dfrac{(\rho_L - \rho_G)}{\rho_L}}} \tag{2.4}$$

Several empirical correlations have since been developed for h_{OGE} of the same form as Equation (2.3) with constants C_3 and C_4 adjusted to match the corresponding experimental data. The coefficients obtained from these correlations are given in Table 2.3. For both horizontal and vertically downward branches, the coefficients C_4 in Table 2.3 are all equal to Lubin and Springer's (1967) theoretical value of 0.4. For horizontal branches, the coefficients C_3 are all within 9% of Lubin and Springer's value. The slight discrepancy in the results could be due to differences in geometries, flow conditions or measuring techniques for the onset height. Larger

discrepancies exist in the values of C_3 for the downward branch; the source of these discrepancies will be discussed in the following paragraphs.

Table 2.3 – Coefficients C_3 and C_4 in Equation (2.3) for calculating critical heights at the OGE for horizontal and vertically downward branches

Author	**Horizontal Branch**		**Vertical Downward Branch**	
	C3	***C4***	***C3***	***C4***
Smoglie and Reimann (1986)	0.681	0.4	1.816	0.4
Yonomoto and Tasaka (1988)	0.681	0.4	0.909	0.4
Micaelli and Memponteil (1989)	0.626	0.4	1.025	0.4
Hassan et al. (1998)	0.57	0.4	-	-

The experiments performed by the authors listed in Tables 2.2 and 2.3 are summarized in Table 2.1. Schrock et al. (1986), Smoglie and Reimann (1986) and Micaelli and Memponteil (1989) all performed experiments on two-phase flow discharging from a large diameter pipe through a small diameter pipe located either horizontally, vertically up or vertically down. Schrock et al. considered the effects of surface tension and viscosity in their experiments and concluded that for discharge through a single branch located horizontally or vertically up, h_{OLE} is independent of surface tension and viscosity. However, for the onset of gas entrainment, they found that including a Bond number and a viscosity number to account for the effects of surface tension and viscosity in their correlation resulted in a better fit with their data and Smoglie and Reimann's data. For a horizontal pipe, Schrock et al.'s coefficients C_1 and C_2 in Equation (2.1) are nearly identical to Craya's (1949) coefficients. For interface heights between h_{OLE} and h_{OGE}, Schrock et al. measured x and developed empirical correlations for x as a function of h/h_{OLE} for horizontal and vertically upward branches and for x as a function of h/h_{OGE} for horizontal and vertically downward branches. Smoglie and Reimann and Micaelli and Memponteil developed similar correlations to predict x as a function of h/h_{OLE} and ρ_L/ρ_G for horizontal and vertically upward branches and to predict x as a function of h/h_{OGE} and ρ_L/ρ_G for horizontal and vertically downward branches.

Yonomoto and Tasaka's (1988) test section consisted of a large square duct discharging flow through a small diameter pipe. In terms of the critical heights for the OLE and OGE, Equation (2.1) was correlated using their results to obtain the coefficients C_1 and C_2. As shown in Table 2.2, the coefficient C_1 from their correlation deviated slightly from the others for the case of a horizontal branch and there is a significant deviation between their results and Schrock et al.'s (1986) and Smoglie and Riemann's (1986) for the case of an upward branch. The disagreements were thought to be a result of either the different main pipe geometries or the error in the visual determination of the OLE. The value of C_1 is highly dependent on how the onset condition is defined for an upward branch. Yonomoto and Tasaka defined the onset condition to be the interface height at which time most of the generated liquid droplets are entrained into the branch. However, in Schrock et al.'s and Smoglie and Reimann's experiments, the condition when the first water droplets are entrained into the branch defined the onset condition; therefore, their correlations resulted in significantly lower values for C_1. Yonomoto and Tasaka attempted to provide an explanation for the relationship between x and h/h_{OGE} or h/h_{OLE} by developing a theoretical model to express x as a function of density and the single phase gas and liquid flow rates. Comparisons showed good agreement for the quality between the predictions and the experimental results.

The experimental investigations of Smoglie and Reimann (1986), Micaelli and Memponteil (1989) and Yonomoto and Tasaka (1988) included axial flows of liquid and gas in their test sections with velocities of $v_{L,main}$ and $v_{G,main}$, respectively. These studies considered the effects of these superimposed gas and liquid velocities on the flow phenomena and the critical heights at the onsets of gas and liquid entrainment for the various branch geometries. Smoglie and Reimann observed that, for horizontal and vertically upward branches, the effect of a superimposed velocity was insignificant whereas, for a downward branch, a superimposed velocity caused the onset of gas entrainment to transition from vortex to vortex-free flow and the onset of gas entrainment height was significantly reduced. For downward branches, the deviations in the coefficients C_3 in Table 2.3 are therefore likely a result of the different main pipe velocities used in the experiments. Micaelli and Memponteil's and Yonomoto and Tasaka's coefficients were obtained with superimposed velocities and thus under vortex-free flow conditions, while Smoglie

and Reimann's value for C_3 of 1.816 was attained without superimposed velocities and thus under vortex flow conditions.

In Hassan et al.'s (1998) experiments, two-phase flow was discharged from a large reservoir through a small diameter pipe located horizontally on the flat wall of a reservoir. Hassan et al. measured and correlated results for the onset of liquid and gas entrainment, the quality, and the two-phase mass flow rate of discharging two-phase flow through a single horizontal branch. They obtained experimental data for a range of tank pressures P_0, branch resistances R, and pressure drops across the branch ΔP, and plotted their results for $\dot{m}_{TP}$ and x versus h. A parametric study showed that increasing R or decreasing ΔP resulted in a decrease in $\dot{m}_{TP}$ at the same h. Increasing P_0 had negligible effects on the mass flow rate when $h > 0$ but the effect was more significant for $h < 0$. In addition, Hassan et al. showed that the influences of the parameters R and ΔP were absorbed by plotting x and a normalized two-phase mass flow rate M versus a normalized interface height H with M and H defined as follows:

$$M = \left(\dot{m}_{TP} - \dot{m}_{G,OLE}\right)/\left(\dot{m}_{L,OGE} - \dot{m}_{G,OLE}\right) \tag{2.5}$$

$$H = \left(h - h_{OLE}\right)/\left(h_{OGE} - h_{OLE}\right) \tag{2.6}$$

New correlations were obtained for M as a function of H and x as a function of H and ρ_L / ρ_G. Excellent agreement was obtained between the following correlations and the experimental data.

$$M = H^2 \exp\left[-1.84H^2\left(1 - H^2\right)^{1.318}\right] \tag{2.7}$$

$$\begin{aligned} x = {} & 0.2\exp\left[6H\left(1 - 11.67H\right)/\left(1 - H\right)\right] \\ & + 0.8\left(1 - H^2\right)^{1.3}\left[-0.0122 + 0.42/\left(1 + \sqrt{\rho_L / \rho_G}\right)\right]^H \end{aligned} \tag{2.8}$$

Parrott et al. (1991) obtained results for $h_{m,OGE}$ and $h_{f,OGE}$ for the case of a single horizontal discharge branch, where $h_{m,OGE}$ measures the height of the interface from the centreline of the branch to the tip of the meniscus (where the interface intersects the wall above the branch) and $h_{f,OGE}$ measures the height of the interface from the centreline of the branch to the flat part of the interface farther away from the wall. Significant deviation was seen when comparing the

results for $h_{m,OGE}$ and $h_{f,OGE}$. Parrott et al. developed correlations for both onset heights based on their experimental results for the case of a single discharge. The correlations for $h_{m,OGE}/d$ showed better agreement with previous experimental results from Smoglie and Reimann (1986), while Craya's (1949) correlation fell between the correlations for $h_{m,OGE}/d$ and $h_{f,OGE}/d$.

It should be noted that in some of the above single-branch studies the branch was located on a flat wall (e.g., Yonomoto and Tasaka, 1988; Hassan et al., 1998) while in other studies, the branch was located on a round pipe wall (e.g., Schrock et al., 1986; Smoglie and Reimann, 1986). This difference does not appear to have much effect on the results. A summary report by Zuber (1980) stated that the effect of pipe curvature on the velocity field near the branch inlet is not very large. More recent work by Bowden and Hassan (2008) looked at the effects of surface curvature by comparing their results for a curved wall with previous analytical models for a flat wall. These comparisons showed that for $\mathrm{Fr}_{G,OLE} > 10$ there was very little deviation between their h_{OLE} results and the results from the analytical models. Hassan et al. (1997) also studied the effect of surface curvature on two-phase flow results and showed that surface curvature had very little effect on the results of $\dot{m}_{TP}$ and x.

Previous experimental investigations by Bowden and Hassan (2008) and Parrott et al. (1991) considered the effects of surface wetness on h_{OLE} by performing their experiments with an increasing liquid level (ILL), where the wall beneath the branch inlet was dry, and a decreasing liquid level (DLL), where the wall beneath the inlet was wet, and comparing h_{OLE} for both cases. Bowden and Hassan's results showed that for $\mathrm{Fr}_{G,OLE} < 10$, the DLL method consistently resulted in a higher h_{OLE} compared to the ILL method. This was said to be due to an increase in flow resistance on the dry wall between the interface and the branch inlet for the ILL method. For $\mathrm{Fr}_{G,OLE} > 10$, the differences between the ILL and DLL results were insignificant. Parrot et al. concluded that there was an obvious difference in the h_{OLE} results from the two methods but visually detecting the OLE was nearly impossible when the surface was wet and therefore the ILL method gave the most consistent results.

More recent theoretical models have been developed for the onset of gas entrainment through a single horizontal branch by Ahmed et al. (2003) and through a single downward branch by Saleh et al. (2009). Ahmed et al. applied the Bernouilli equation at two points along the interface in both the lighter and heavier fluids and used both a simplified point sink analysis and a three dimensional finite branch analysis to solve for h_{OGE}. In both these models they neglected the effects of surface tension and assumed the liquid flow was inviscid, irrotational, incompressible and quasi-steady. The two models gave almost identical results for $\mathrm{Fr}_{L,OGE} > 10$, while significant deviation in the results occurred for $\mathrm{Fr}_{L,OGE} < 1$. The two models were compared with previous experimental results by Hassan et al. (1998), Parrott et al. (1991) and Smoglie and Reimann (1986) and good agreement was obtained for both models.

Saleh et al. (2009) performed a similar analysis using both the point sink and finite branch methods for a downward branch and introduced the Young (Kelvin)-Laplace equation to consider the effects of surface tension. The results for h_{OGE} from the point sink analysis with surface tension were compared with results from the point sink analysis without surface tension. These comparisons showed that when surface tension is neglected, h_{OGE} was significantly over predicted at low $\mathrm{Fr}_{L,OGE}$ ($\mathrm{Fr}_{L,OGE} < 10$) and slightly over predicted at high $\mathrm{Fr}_{L,OGE}$.

For interface heights between h_{OLE} and h_{OGE}, the only theoretical model developed (to the best of the author's knowledge) was by Gardner (1988) who developed a theoretical model to predict h for a given $\dot{m}_{TP}$ and x. The predicted values of h agreed well with experimental data for a range of Froude numbers. However, this analysis is not useful in practice because normally the designer needs $\dot{m}_{TP}$ and x at a given h, not the other way around.

2.3.2 Flow Through a Single Branch on an Inclined Wall

Experimental measurements for the onsets of liquid and gas entrainment for flow through a single inclined branch were performed by Lee et al. (2007) where the branch inlet was attached normal to the curved wall of a pipe and by Bartley et al. (2008) where the branch was attached normal to a flat plane. In Lee's experiments, h_{OLE} was measured for branch upward inclination angles of 0°, 30°, 45°, 60° and 90° measured from the horizontal. From these measurements it

was found that as the branch angle increased from 0° (horizontal branch) to 90° (vertically upward branch), $|h_{OLE}|$ decreased for the same value of $\mathrm{Fr}_{G,OLE}$. Lee et al. also measured h_{OGE} for branch downward inclination angles of 0°, 30°, 45°, 60° and 90° measured from the horizontal and found that as the downward angle increased from 0° (horizontal) to 90° (vertically down), h_{OGE} increased for the same $\mathrm{Fr}_{L,OGE}$. Semi theoretical models were developed to predict h_{OLE} as a function of $\mathrm{Fr}_{G,OLE}$ and h_{OGE} as a function of $\mathrm{Fr}_{L,OGE}$. Experimental results were used to obtain coefficients for the model.

In the experiments of Bartley et al. (2008), a single outlet branch was located at the centre of a plane orientated at various angles ϕ relative to the vertical plane. Figures 2.2(a) and (b) show how the angle of inclination was measured for the onset of liquid entrainment experiments and Figures 2.3(a) and (b) show how the angle of inclination was measured for the onset of gas entrainment experiments. Measurements of h_{OLE} were taken for ϕ= -90° to 60° in 30° increments and h_{OGE} was measured from ϕ = -60° to 90° in 30° increments.

From the OLE experiments, Bartley et al. (2008) observed that for positive ϕ, the liquid stream travels along the wall towards the branch inlet at the onset of liquid entrainment. Under these conditions, as ϕ increased from 0° to 60°, $|h_{OLE}|/d$ decreased. A correlation was obtained for $|h_{OLE}|/d$ as a function of $Fr_{G,OLE}$ and ϕ for $0° \leq \phi \leq 90°$ and $Fr_{G,OLE} < 45$. The correlation reduces to Equation (2.1) at ϕ = 0° and approaches zero at ϕ = 90°. For the case of negative ϕ, the experiments showed that it was possible for a liquid spout to rise directly from the interface to the branch inlet, without contacting the wall. For these cases, the inclination angle had very little effect on h_{OLE} due to the formation of the liquid spout.

In the OGE experiments, Bartley et al. (2008) observed that for positive ϕ, a gas cone formed that stretched from the interface to the branch inlet and did not touch the wall; for this case, the values for h_{OGE} were therefore nearly independent of ϕ. However, for negative ϕ, the

(a) Negative ϕ (b) Positive ϕ

Figure 2.2 – Bartley et al.'s (2008) geometry for OLE experiments

(a) Negative ϕ (b) Positive ϕ

Figure 2.3 – Bartley et al.'s (2008) geometry for OGE experiments

gas traveled along the wall towards the branch inlet at the onset of gas entrainment and h_{OGE} increased with decreasing $|\phi|$. For negative ϕ, a correlation was developed for h_{OGE}/d as a function of $\mathrm{Fr}_{L,OGE}$ and ϕ for -90° ≤ ϕ ≤ 0°. This correlation reduces to Equation (2.1) with C_1 = 0.475 and C_2 = 0.444 for ϕ = 0° (horizontal branch) and reduces to h_{OGE}/d = 0 for ϕ = -90° (vertically upward branch).

The two-phase mass flow rate and quality were also measured and correlated by Bartley et al. (2010) for the geometries shown in Figures 2.2 and 2.3. They looked at the effects of the inclination angle ϕ on $\dot{m}_{TP}$. For positive ϕ, as shown in Figures 2.2 (b) and 2.3 (b), $\dot{m}_{TP}$ was not significantly influenced by ϕ when the interface height was near h_{OGE} since the gas entered through a cone that did not touch the wall. At lower interface levels, the entrained gas contacted the wall and there was a strong influence of ϕ on $\dot{m}_{TP}$ that caused $\dot{m}_{TP}$ to decrease with an increase

in ϕ. For negative ϕ as shown in Figures 2.2 (a) and 2.3 (a), the opposite trend occurred. When the interface was close to h_{OLE}, ϕ did not have much effect on $\dot{m}_{TP}$ since the liquid was entering the branch through a spout that did not touch the wall. At higher interface levels, the liquid travelled along the wall and ϕ had a strong effect on $\dot{m}_{TP}$ resulting in an increase in $\dot{m}_{TP}$ with increasing $|\phi|$. New correlations were obtained to predict M and x as a function of H and ϕ, where M and H were defined by Equations (2.5) and (2.6).

For this same geometry, Ahmed et al. (2004) used point sink and finite branch analyses to develop models to predict h_{OGE}. The two models showed large deviations from one another at low $\mathrm{Fr}_{L,OGE}$ and better agreement at high $\mathrm{Fr}_{L,OGE}$. In the point sink model, h_{OGE} was independent of ϕ while the results from their finite branch model showed that for $-90° \le \phi \le 0°$ (Figure 2.3(a)), h_{OGE} increased with decreasing $|\phi|$, similar to the observations made by Bartley et al. (2008). Comparisons between the two models and Hassan's (1995) and Parrot et al.'s (1991) experimental data for ϕ = 0°, -45° and -90° showed good agreement.

Andaleeb et al. (2006) also developed point sink and finite branch models to predict h_{OGE} for inclined branches for ϕ = 0°, 45° and 90° (similar to Figure 2.3(b)) but in their models, the branch was attached perpendicular to a curved wall, instead of a flat wall. By comparing these two models it was shown that there is again large deviation at low $\mathrm{Fr}_{L,OGE}$ and better agreement at high $\mathrm{Fr}_{L,OGE}$. Their finite branch model showed relatively good agreement with Hassan's (1995) and Parrott et al.'s (1991) experimental data; however, Andaleeb et al.'s models predicted a significant increase in h_{OGE} with increasing ϕ; this is not consistent with the experimental findings from Bartley which showed that h_{OGE} was nearly independent of ϕ for this range of branch orientations.

2.3.3 Summary of Discharging Flow Through a Single Branch

There have been numerous experiments done to measure h_{OLE} and h_{OGE} for flow through vertical, horizontal and inclined branches and some experiments measured $\dot{m}_{TP}$ and x in the

branch. Based on these experimental results, empirical correlations have been developed to predict h_{OLE}, h_{OGE}, $\dot{m}_{TP}$ and x for these geometries. In addition, theoretical models have been developed to predict h_{OLE} and h_{OGE} for various single branch orientations; however, no theoretical models exist for predicting $\dot{m}_{TP}$ and x for interface heights between h_{OLE} and h_{OGE} for the case of discharging two-phase flow through a single branch.

2.4 Discharging Two-Phase Flow Through Multiple Branches

In an attempt to approach the multiple-branch-header problems, many studies have been conducted on two-phase flow from a large tank through multiple branches. A representative sample of the experimental studies on this topic is included in Table 2.4. In the dual branch experiments, two horizontal branches were located either one on top of the other, side-by-side or at an angle θ relative to one another. More recent experiments considered discharging flow through three branches located on a semi-circular wall. The experimental and theoretical studies on these geometries will be discussed throughout Sections 2.4.1 to 2.4.4.

2.4.1 Flow Through Two Horizontal Branches Located One On Top of the Other

Many experimental and theoretical studies have been conducted (most of them at the University of Manitoba) for two-phase flow from a large tank through two horizontal branches located one on top of the other, as shown in Figure 2.4. For this geometry, the upper branch is referred to as Branch A and the lower branch as Branch B and the branches are separated by a vertical distance L centre to centre.

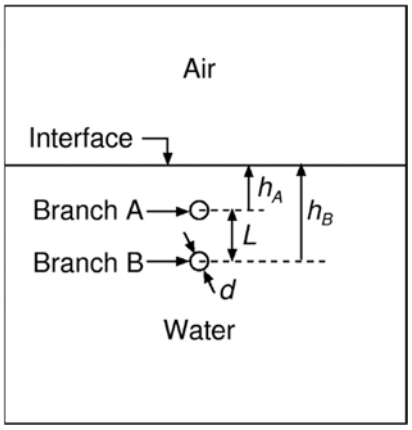

Figure 2.4 – Geometry for dual branches separated by a vertical distance L

Table 2.4 – A representative sample of the experimental studies on discharging two-phase flow through two or three branches

Author(s)	Wall Geometry (Flat/Pipe)	No. of Branches	Branch d (mm)	Branch Orientation	Fluids	Range of Parameters	Measured Quantities
Parrott et al. (1991)	flat	2	6.35	horizontal and located one on top of other	air-water	$P_0 = 510$ kPa; $1.5 \leq L/d \leq 6$; $0 \leq \mathrm{Fr}_L \leq 70$	$h_{OGE,A}$
Armstrong et al. (1992)	flat	2	6.35	horizontal and located one on top of other	air-water	$P_0 = 310$ kPa; $1.5 \leq L/d \leq 4$; $0 \leq \mathrm{Fr}_G \leq 32.1$	$h_{OLE,B}$
Hassan et al. (1996)	flat	2	6.35	horizontal and located one on top of other	air-water	$316 \leq P_0 \leq 517$ kPa; $40 \leq \Delta P \leq 235$ kPa; $1.5 \leq L/d \leq 8$; $1000 \leq R \leq 3000$ kg m$^{-1/2}$	h_{OGE}, h_{OLE}, $\dot{m}_{TP}$, x for both branches
Hassan et al. (1996)	flat	2	6.35	horizontal and located side by side	air-water	$316 \leq P_0 \leq 517$ kPa; $40 \leq \Delta P \leq 235$ kPa; $1.5 \leq L/d \leq 8$; $1000 \leq R \leq 3000$ kg m$^{-1/2}$	h_{OGE}, h_{OLE}, $\dot{m}_{TP}$, x for both branches
Hassan et al. (1997)	semicircular (D = 50.8 mm)	3	6.35	horizontal, 45° down and vertically down	air-water	316 kPa $\leq P_0 \leq 517$ kPa; $40 \leq \Delta P \leq 235$ kPa; $R = 1000$ kg m$^{-1/2}$	$\dot{m}_{TP}$, x at each branch for single, dual and triple discharge cases
Maier et al. (2001)	flat	2	6.35	horizontal and located an angle θ from one another	air-water	$310 \leq P_0 \leq 510$ kPa; $0 \leq \mathrm{Fr}_A \leq 70$; $0 \leq \mathrm{Fr}_B \leq 56.6$; $1.5 \leq L/d \leq 8$; θ = 0°, 10°, 30° and 60°	$h_{OGE,A}$, $h_{OLE,A}$
Ahmad and Hassan (2006)	semicircular (D = 50.8 mm)	3	6.35	horizontal, 45° down and vertically down	air-water	$206.8 \leq P_0 \leq 413.7$ kPa; $0 \leq \mathrm{Fr}_{L,A} \leq 100$; $0 \leq \mathrm{Fr}_{L,B} \leq 100$; $0 \leq \mathrm{Fr}_{L,C} \leq 100$	h_{OGE} for single discharge (Branches A, B, C), for dual discharge (A,B) and for triple discharge (A)
Bowden and Hassan (2008)	semicircular (D = 50.8 mm)	3	6.35	horizontal, 45° down and vertically down	air-water	$P_0 = 413.6$ kPa; $0 \leq \mathrm{Fr}_{G,A} \leq 20$; $0 \leq \mathrm{Fr}_{G,B}, \mathrm{Fr}_{G,C} \leq 26.4$	$h_{OLE,A}$, $h_{OLE,B}$ (single, dual and triple discharge cases)

In Parrott et al.'s (1991) experiments, the interface was located above Branch A and $h_{OGE,A}$ was measured for various values of $\mathrm{Fr}_{L,OGE,A}$, $\mathrm{Fr}_{L,OGE,B}$ and L/d. Their results showed that the branches had very little influence on each other at high L/d ($L/d > 6$) and as L/d decreased, the interaction between the branches increased. They also showed that for $L/d \leq 6$, $h_{OGE,A}$ increased with increasing $\mathrm{Fr}_{L,OGE,B}$ and under certain conditions, gas entrainment occurred through both branches simultaneously. Correlations were developed to predict $h_{OGE,A}/d$ as a function of $\mathrm{Fr}_{L,OGE,A}$, $\mathrm{Fr}_{L,OGE,B}$ and L/d.

In Armstrong et al.'s (1992) experiments, the interface was located below Branch B and $h_{OLE,B}$ was measured for various values of $\mathrm{Fr}_{G,OLE,A}$ and $\mathrm{Fr}_{G,OLE,B}$ and for various branch spacings L/d. Similar to the observations made by Parrott et al. (1991) for $h_{OGE,A}$, Armstrong et al.'s results showed that when the distance between the branches was high ($L/d = 4$), the branches had very little influence on each other and as L/d decreased, the interaction between the branches increased. Their study showed that for the range of L/d tested in this ($1.5 \leq L/d \leq 4$) study, when the interface was below both branches, Branch A assisted Branch B with liquid entrainment and therefore $|h_{OLE,B}|$ increased from the single branch case.

Hassan et al. (1996) extended the work of Parrott et al. (1991) and Armstrong et al. (1992) to measure h_{OLE}, h_{OGE}, $\dot{m}_{TP}$ and x at both the lower and upper branches for a range of P_0, ΔP, R and L/d. In this study ΔP was kept equal through each branch such that $\mathrm{Fr}_{G,OLE,A} = \mathrm{Fr}_{G,OLE,B}$ and $\mathrm{Fr}_{L,OGE,A} = \mathrm{Fr}_{L,OGE,B}$. Hassan et al. showed that when the interface was between the two branches, Branch B competed with Branch A for liquid and gas entrainment and therefore $|h_{OLE,A}|$ and $h_{OGE,B}$ decreased from the single branch results. Empirical correlations were developed by Hassan et al. to predict $|h_{OLE}|/d$ as a function of $\mathrm{Fr}_{G,OLE}$ and L/d (for both branches) and to predict h_{OGE}/d as a function of $\mathrm{Fr}_{G,OLE}$ (for both branches). For interface heights located between the onsets, Hassan et al. showed that for $L/d \leq 3$, the mass flow rate of gas, $\dot{m}_G$, through a particular branch decreased and the mass flow rate of liquid, $\dot{m}_L$, increased as the interface height, h,

increased from h_{OLE} to h_{OGE} for that branch. This resulted in an overall increase in $\dot{m}_{TP}$ with increasing h. When the dual branch results for $L/d \leq 3$ were compared with the single branch results they observed that the presence of an upper branch increased $\dot{m}_{TP}$ at the lower branch, while the addition of a lower branch decreased $\dot{m}_{TP}$ at the upper branch. Similar to previous observations, insignificant differences were found between the single branch results and the dual branch results for $L/d = 8$ and the results for Branch A were identical to the results for Branch B for this spacing. The deviation between the results for Branch A and B increased as L/d or R decreased or as ΔP increased. As was found for the single branch, the influences of ΔP and R were absorbed by plotting M versus H and x versus H for each branch where M and H are defined by Equations (2.5) and (2.6). The following empirical correlations were developed by Hassan et al. to predict $x(H, L/d, \rho_L/\rho_G)$ and $M(H, L/d)$ for each branch.

$$x_A = 0.2\exp\left[6H_A\left(1-D_1H_A\right)/\left(1-H_A\right)\right] + 0.8\left(1-H_A^2\right)^{1.3}\left[D_2\left(-0.0122+0.42/\left(1+\sqrt{\rho_L/\rho_G}\right)\right)\right]^{H_A} \tag{2.9}$$

$$x_B = 0.2\exp\left[6H_B\left(1-E_1H_B\right)/\left(1-H_B\right)\right] + 0.8\left(1-H_B^2\right)^{1.3}\left[E_2\left(-0.0122+0.42/\left(1+\sqrt{\rho_L/\rho_G}\right)\right)\right]^{H_B} \tag{2.10}$$

$$M_A = H_A^{\left[2+D_3\left(1-H_A^3\right)\right]}\exp\left[-1.84H_A^2\left(1-H_A^2\right)^{1.318}\right] \tag{2.11}$$

$$M_B = H_B^2\exp\left[-1.84H_B^2\left(1-H_B^2\right)^{E_3}\right] \tag{2.12}$$

where,

$$D_1 = 11.67 - 9.67\exp\left[-0.01\left(L/d\right)^3\right] \tag{2.13}$$

$$D_2 = 1 - 0.92\exp\left[-0.75\left(L/d\right)\right] \tag{2.14}$$

$$D_3 = 6.68\exp\left[-0.027\left(L/d\right)^4\right] \tag{2.15}$$

$$E_1 = 11.67 - 3.03\exp\left[-0.016(L/d)^3\right] \tag{2.16}$$

$$E_2 = 1 - 0.71\exp\left[-0.03(L/d)^4\right] \tag{2.17}$$

$$E_3 = 1.318 + 5.78\exp\left[-0.37(L/d)^2\right] \tag{2.18}$$

For the geometry shown in Figure 2.4, Armstrong et al. (1992) developed a theoretical model using an approach similar to that of Soliman and Sims (1992). The resulting model included two algebraic equations that solved for $|h_{OLE}|/L$ at Branch B as a function of $\mathrm{Fr}_{G,OLE,A}$ and $\mathrm{Fr}_{L,OLE,B}$. The results from their model show how $|h_{OLE}|/L$ increases with increasing either $\mathrm{Fr}_{G,OLE,A}$ or $\mathrm{Fr}_{L,OLE,B}$.

Other theoretical analyses have been performed to predict h_{OGE}/d at the upper branch for the case of two branches separated by a vertical distance L on a vertical wall by Ahmed et al. (2004) and on an inclined wall by Ahmed (2008). Both these studies followed the same approach as was done earlier for the case of a single branch by Ahmed et al. (2003) and showed that the point sink model and finite branch analysis were nearly identical at high $\mathrm{Fr}_{L,OGE}$ but deviated from each other at low $\mathrm{Fr}_{L,OGE}$. Since the majority of the experimental data was obtained for $\mathrm{Fr}_{L,OGE} >$ 10, both models showed similar agreement with the experimental results.

For interface heights between $h_{OLE,B}$ and $h_{OGE,A}$, Bartley et al. (2004) developed a theoretical model to predict the interface height, when the mass flow rates and qualities in each branch are known. Good agreement was found between the model and previous experimental results. However, in practice the designer is interested in solving for the mass flow rates and qualities at a known interface height and this model is therefore not sufficient.

2.4.2 Flow Through Two Horizontal Branches Located Side-by-Side

Hassan et al. (1996) performed experiments for discharging two-phase flow through two branches located side by side and separated by a distance L, as shown in Figure 2.5. For this geometry, Hassan et al.'s experiments measured h_{OLE}, h_{OGE}, $\dot{m}_{TP}$ and x at both branches for a range of P_0, ΔP, R and L/d, while maintaining $\mathrm{Fr}_{G,OLE,A} = \mathrm{Fr}_{G,OLE,B}$ and $\mathrm{Fr}_{L,OLE,A} = \mathrm{Fr}_{L,OLE,B}$. The

results showed that, for the entire range of parameters tested, h_{OLE}, h_{OGE}, $\dot{m}_{TP}$ and x were nearly identical for both branches. When the branches were spaced far apart (L/d = 8), the branches behaved as two independent branches and the results were close to the limiting case of a single branch. For L/d = 1.5, 2 and 3, the branches assisted one another with entrainment and h_{OLE} and h_{OGE} increased. Empirical correlations were developed based on the experimental results for h_{OLE}/d as a function of $\mathrm{Fr}_{G,OLE}$ and L/d and h_{OGE}/d as a function of $\mathrm{Fr}_{L,OGE}$ and L/d. For interface heights between the two onset heights and for L/d = 1.5, 2 and 3, results were compared with the single branch results and it was shown that for $h > 0$, $\dot{m}_G$ increased and $\dot{m}_L$ and $\dot{m}_{TP}$ decreased compared to the results from the single branch. For $h < 0$, $\dot{m}_G$ decreased and $\dot{m}_L$ and $\dot{m}_{TP}$ increased when compared to the single branch results. In these experiments, the influences of ΔP and R were absorbed by plotting the results in terms of M versus H and x versus H. When they compared their data plotted in terms of M versus H and x versus H with the single branch correlations defined by Equations (2.7) and (2.8), they found that these single branch correlations accurately predicted their data.

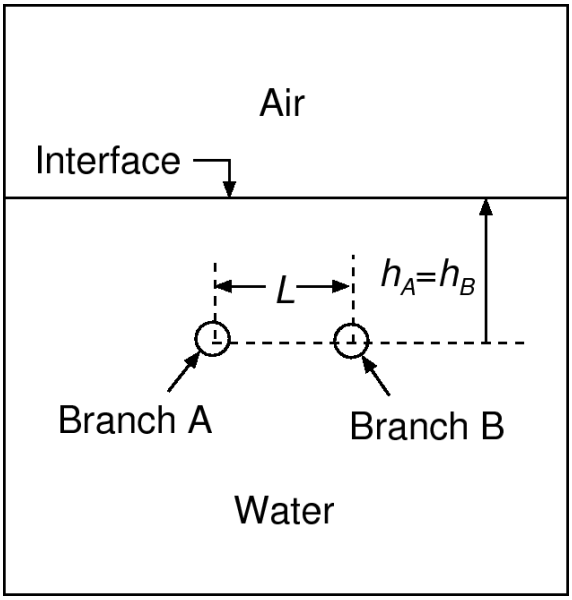

Figure 2.5 - Geometry for dual branches separated by a horizontal distance L

2.4.3 Flow Through Two Horizontal Branches Separated by a Distance L and an Angle θ

Experimental and theoretical studies were undertaken by Maier et al. (2001(a)) and Maier et al. (2001(b)), respectively, for the geometry shown in Figure 2.6 with two branches separated by a distance L and an angle θ. In Maier et al.'s experimental study, interface height measurements were taken for the OLE and the OGE at the primary branch, where the primary branch (Branch A in Figure 2.6) is the branch closest to the interface. The branch farthest from the interface is referred to as Branch B. For the OLE experiments, data was collected for angles of θ = 0° (side-by-side), 10°, 30° and 60°, measured counter clockwise from the horizontal. For this range of θ, a range of L/d, and a range of $Fr_{G,OLE,A}$ and $Fr_{G,OLE,B}$, $h_{OLE,A}$ was measured. The results showed that for L/d = 1.5 and 2, $\left|h_{OLE,A}\right|$ increased with an increase in $Fr_{G,OLE,A}$ or $Fr_{G,OLE,B}$ and for L/d = 8, $h_{OLE,A}$ did not depend on $Fr_{G,OLE,B}$. As L/d decreased, the results for $\left|h_{OLE,A}\right|$ increased due to Branch B assisting Branch A with liquid entrainment. They also showed that for a constant L/d, $\left|h_{OLE,A}\right|$ decreased as θ increased. In Maier et al.'s OGE experiments, data were collected for angles of θ = 0° (side by side), -10°, -30° and -60°. For L/d = 8, they showed that $\mathrm{Fr}_{L,OGE,B}$ had no effect on $h_{OGE,A}$. As either L/d decreased or $|\theta|$ decreased, $h_{OGE,A}$ increased. For both the OLE and OGE experiments, depending on the inclination angle θ, gas or liquid entrainment could be first observed at Branch A, Branch B or Branches A and B simultaneously.

The theoretical work of Maier et al. (2001(b)) consisted of developing an analytical solution to solve for $h_{OLE,A}$ for the same geometry used in their experiments. They developed two models: one using multiple point-sink analyses (similar to Craya (1949)) and one using a finite-branch model similar to what was done by Soliman and Sims (1992). The two models showed good agreement at high values of $\mathrm{Fr}_{L,OGE,A}$ or $\mathrm{Fr}_{L,OGE,B}$, but at low values of $\mathrm{Fr}_{L,OGE,A}$ or $\mathrm{Fr}_{L,OGE,B}$, the point-sink model does not give accurate predictions and the two models deviate from one another. Comparisons made by Maier et al. (2001(a)) between the finite-branch model and the experimental data showed good agreement.

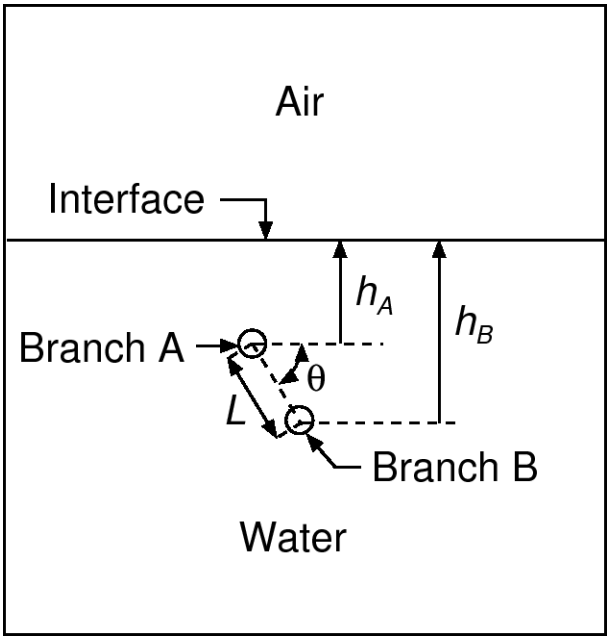

Figure 2.6 - Geometry for dual branches separated by a distance L and an angle θ

For this same geometry, Ahmed (2006) developed a point sink and finite branch model for solving $h_{OGE,1}/d$ using the same approach as for the case of a single branch by Ahmed et al. (2003) and showed that the two models were nearly identical at high $\mathrm{Fr}_{L,OGE}$ but deviated from each other at low $\mathrm{Fr}_{L,OGE}$. Their results agreed with Maier et al.'s (2001(a)) data to within 12%.

2.4.4 Flow Through Three Branches

In order to more closely model the CANDU header geometry, Hassan et al. (1997), Bowden and Hassan (2008), and Ahmad and Hassan (2006) performed experiments on discharging flow through three branches located on a semi-circular wall. The three branches in these experiments were orientated horizontally, vertically downwards, and at an angle of 45° from the horizontal, as shown in Figure 2.7.

The experiments by Hassan et al. (1997) focused mostly on measuring $\dot{m}_{TP}$ and x for a range of P_0 and ΔP. With all three branches activated, Hassan et al. showed that the flow through the downward Branch C did not have much effect on the flow from Branch A. The flow from

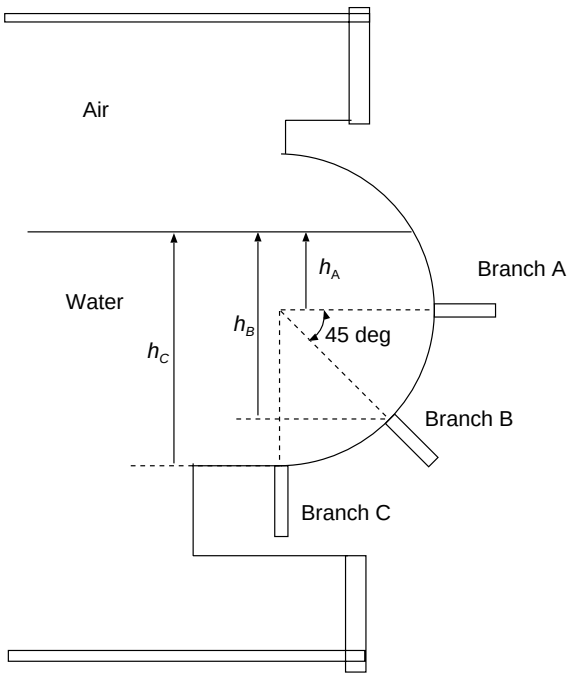

Figure 2.7 – Geometry for test section with three branches

Branch B however was strongly affected by the flow from Branches A and C: discharge from Branch A pulled gas away from Branch B but brought more liquid into Branch B while discharge from Branch C pulled liquid away from Branch B but brought more gas into Branch B. An interesting observation from their experiments was that the flow through Branch C was not affected by the flow through Branch A and/or Branch B. It was therefore concluded in their work that additional branches located on the other side of the wall, as is the case for a typical CANDU header, would also not be affected by the flow through A and B.

The effect of wall curvature on discharge through two branches was considered by Hassan et al. (1997) by comparing results for two branches located on a curved surface (Figure 2.7) with results for two branches located on a flat wall (Figure 2.4). The wall curvature was shown to have very little effect on the results for Branch A and a larger effect on the results for Branch B.

More recently, the onset of gas entrainment for discharging flow through three branches located on a semi-circular wall, as shown in Figure 2.7, was studied both experimentally by Ahmad and Hassan (2006) and theoretically by Saleh et al. (2011). Ahmad and Hassan measured h_{OGE} at Branch A and showed that with Branch A activated, activating Branches B and C resulted in an

increase in h_{OGE}. Therefore, Branches B and C assisted Branch A with entrainment. Saleh et al. (2011) developed a theoretical model to predict h_{OGE} at Branch A for the geometry shown in Figure 2.7. The Bernouilli equation was applied at the interface to equate the fluid energy at a stagnant point far from the branch with that at the point where the interface dips towards the branch. The branches were simulated as point-sinks and an expression was obtained for the critical height h_{OGE} as a function of $\mathrm{Fr}_{L,OGE,A}$, $\mathrm{Fr}_{L,OGE,B}$ and $\mathrm{Fr}_{L,OGE,C}$ and the location and angle of the secondary branch with respect to the primary branch. The predicted h_{OGE} was shown to be within 25% of the experimental data.

Bowden and Hassan's (2008) experiments focused on measuring h_{OLE} at Branches A and B for a range of $\mathrm{Fr}_{G,OLE,A}$, $\mathrm{Fr}_{G,OLE,B}$ and $\mathrm{Fr}_{G,OLE,C}$ for single, dual and triple discharging branches located on the side of a reservoir as shown in Figure 2.7. For triple discharge flow with the interface located beneath Branch A and above Branches B and C, the flow through Branches B and C assisted the onset of liquid entrainment at Branch A and $|h_{OLE}|$ increased compared to the single discharge case. With the interface located beneath Branch B, $|h_{OLE}|$ at Branch B increased when either $\mathrm{Fr}_{G,OLE,A}$ or $\mathrm{Fr}_{G,OLE,C}$ was increased. The observations that the branch(es) located beneath the interface assisted the primary branch with liquid entrainment was unexpected; branches beneath the interface are expected to pull liquid away from the interface, as was observed by Hassan et al. (1996) for dual branches located one on top of the other. Bowden and Hassan concluded that future flow field measurements are required to verify this observation.

2.4.5 Summary of Discharging Two-Phase Flow through Multiple Branches

In summary, for geometries with two branches located one-on-top of the other (Figure 2.4) and side by side (Figure 2.5) and for geometries with three branches (Figure 2.7), previous experimental studies have measured OLE, OGE and two-phase mass flow rate and quality results. For these geometries, theoretical models exist for predicting the OLE and OGE heights at the primary branch but no models exist for predicting the OLE and OGE heights at the secondary branch or for predicting $\dot{m}_{TP}$ and x for two-phase flow through the branches.

For the geometry with two branches separated by a distance L and an angle θ, previous experiments measured the OLE and the OGE heights at the primary branch and theoretical models exist to predict these parameters; however, no measurements or theoretical models exist for predicting the OLE and OGE heights at the secondary branch or the $\dot{m}_{TP}$ and x for interface heights located between the onset heights.

2.5 Conclusion

There are currently no theoretical models available for accurately predicting the two-phase flow distribution in geometries similar to a CANDU header or even in more simplified geometries with two-phase flow discharging from a stratified region through single, dual or triple branches. The few attempts at modelling the complicated CANDU header problem have not been successful at predicting the correct flow distribution through the branches. For the more simplified geometries, models exist to predict h_{OLE} and h_{OGE} and these models show good agreement with the experimental results; however, no theoretical models exist that are capable of predicting the mass flow rate and quality exiting through each branch for all interface heights.

From the literature reviewed, it appears that there is a need for a model to predict the two-phase mass flow rate and quality in each branch for discharging two-phase flow. There has been very little research done on this topic numerically and a proper assessment of any of the available commercial codes has not been done. For geometries with single and dual branches located one on top of the other and side by side, complete sets of experimental data are available for which a numerical model could be validated against; however, experimental results of $\dot{m}_{TP}$ and x are needed for the geometry shown in Figure 2.6 with two branches separated by a distance L and an angle θ.

Chapter 3

Experimental Investigation

3.1 Experimental Parameters

The geometrical and flow parameters that are relevant to this experimental investigation are shown in Figure 3.1. Two circular branches of equal diameter d are located on the side of a large reservoir (test section) containing stratified layers of water and air. The upper branch (Branch A) and the lower branch (Branch B) direct the flow to separators A and B, respectively, where the air and water are separated before their flow rates are measured. The front view in Figure 3.1 shows that the branch centrelines are separated by a distance L and an angle θ, measured relative to the horizontal plane. The interface heights, h_A and h_B are measured upwards from their respective branch centrelines such that h_A is positive if the interface is located above the centreline of Branch A and negative if it is located beneath the centreline of Branch A, and similarly for Branch B.

For each experiment, the air pressure inside the test section is maintained constant at P_0 and the pressures in separators A and B are maintained constant and equal to one another at $P_{S,A} = P_{S,B} = P_S$. The pressure difference from the test section to each of the separators is therefore constant and equal to $\Delta P = P_0 - P_S$. The resistances, R, in each of the lines were adjusted such that when the interface is low and single phase air flows through both branches, $\dot{m}_{G,A} = \dot{m}_{G,B}$ and when the interface is high and single phase water flows through each branch, $\dot{m}_{L,A} = \dot{m}_{L,B}$. The resistances will be kept constant throughout all the experiments for this study. For a constant R and under the above conditions, it is expected that the mass flow rates, $\dot{m}_{TP}$, and qualities, x, of the two-phase flow through each of the branches are dependent on L, θ, P_0, ΔP and h.

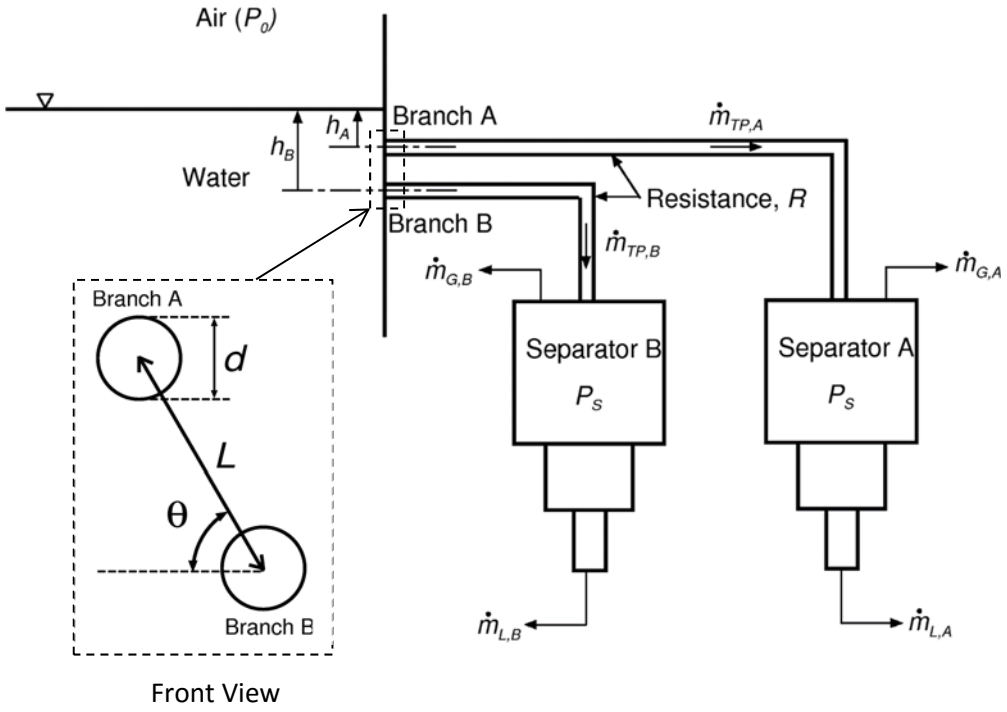

Figure 3.1 - Geometrical and flow parameters

For a fixed set of conditions (L, θ, P_0, ΔP, and R), Figure 3.2 shows how the mass flow rate through the branches varies with the interface height. For this graph, h_A was used for the x-axis for both Branch A and Branch B curves so the critical onset heights for Branch B, $h_{OLE,B}$ and $h_{OGE,B}$ are shown relative to Branch A, where $h_A = h_B - L\sin\theta$. When the interface is located high above Branch A, single phase water flows through both branches and $\dot{m}_{TP,A} = \dot{m}_{TP,B} = \dot{m}_{L,OGE,A} = \dot{m}_{L,OGE,B}$. As the interface is lowered, a critical height is reached where the onset of gas entrainment occurs at Branch A. At this instant, $h_A = h_{OGE,A}$ and $\dot{m}_{TP,A} = \dot{m}_{L,OGE,A}$. Lowering the interface further results in two-phase flow through Branch A ($\dot{m}_{TP,A} = \dot{m}_{L,A} + \dot{m}_{G,A}$), while the flow through Branch B is still single phase water ($\dot{m}_{TP,B} = \dot{m}_{L,OGE,B}$). As the interface is lowered further, a second critical height is reached where the onset of gas entrainment occurs at Branch B ($h_B = h_{OGE,B}$ and $\dot{m}_{TP,B} = \dot{m}_{L,OGE,B}$). With further lowering of the interface, two-phase flow is now present in both Branches A and B until a third

critical height is reached (onset of liquid entrainment at Branch A) where liquid stops flowing into Branch A at which time $h_A = h_{OLE,A}$ and $\dot{m}_{TP,A} = \dot{m}_{G,OLE,A}$, while two phases continue to flow through Branch B. Finally, with further lowering of the interface, a last critical height is reached where liquid stops flowing into Branch B ($h_B = h_{OLE,B}$ and $\dot{m}_{TP,B} = \dot{m}_{G,OLE,B}$). Beyond this point, only single phase gas flows into the branches. Note that the path of the $\dot{m}_{TP,A}$ and $\dot{m}_{TP,B}$ curves are shown only schematically for trend in Figure 3.2; the paths of these curves is, in general, not linear.

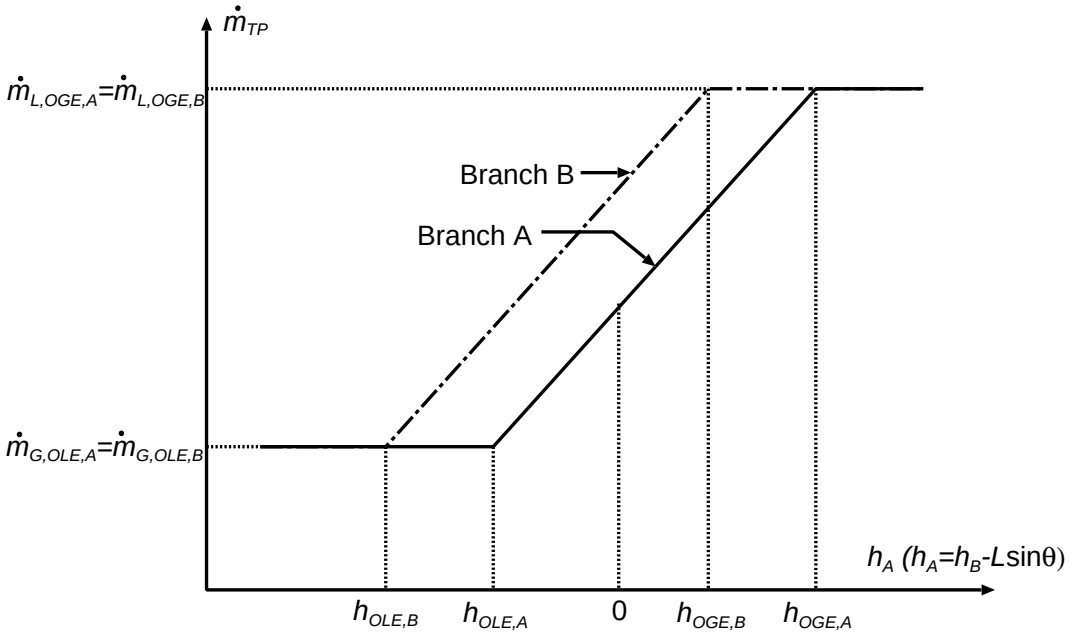

Figure 3.2 - Variation of $\dot{m}_{TP,A}$ and $\dot{m}_{TP,B}$ with h_A

3.2 Experimental Apparatus

3.2.1 Flow Loop

The experimental apparatus used in this study was first assembled and used by Parrott (1993) and later modified by Hassan (1995) and Bartley (2008). Before the apparatus could be used for the present work, several parts had to be replaced (pump, rotameters, pressure controller, etc.) and re-assembled. A schematic diagram of the apparatus is shown in Figure 3.3.

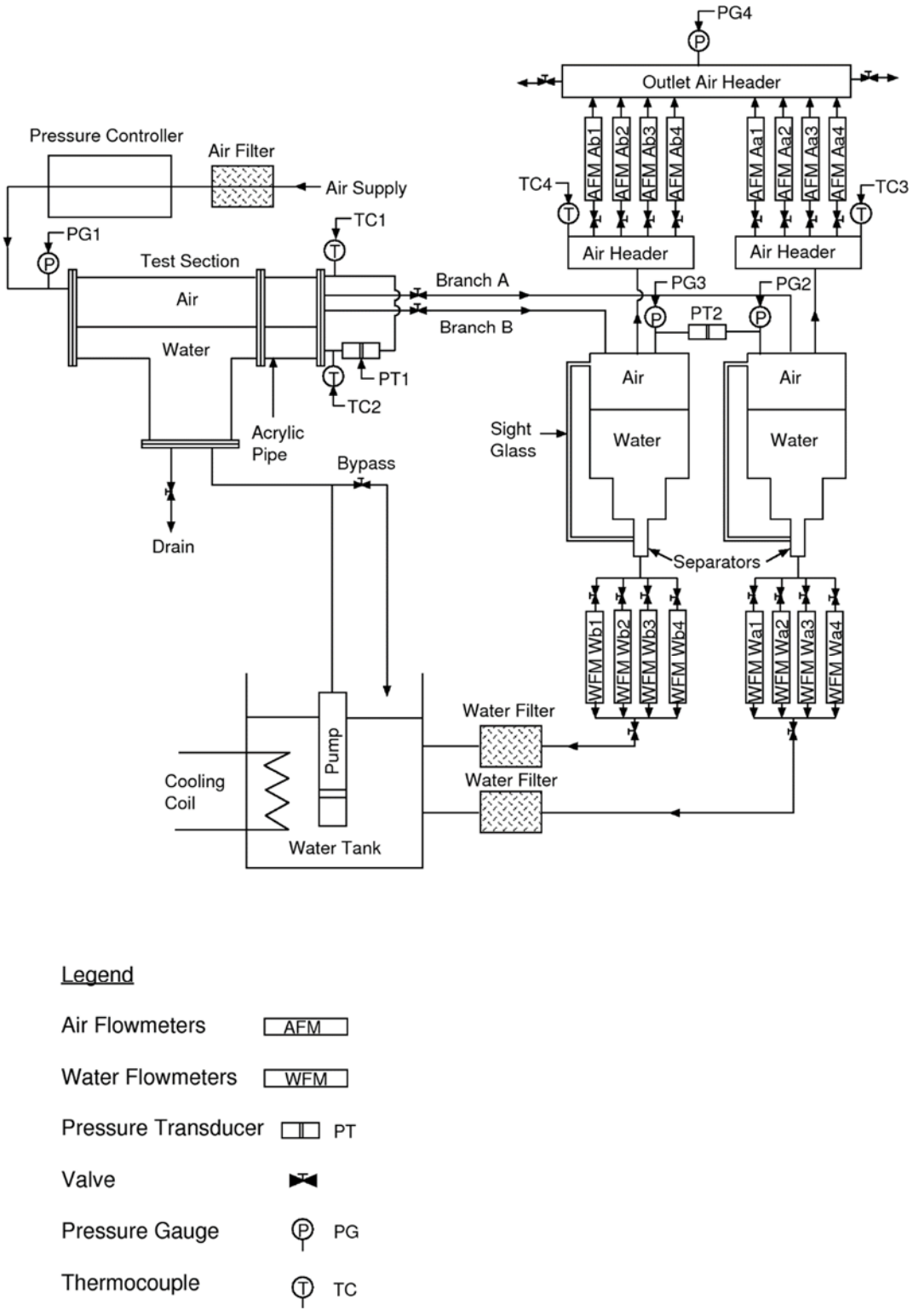

Figure 3.3 - Schematic of experimental apparatus

In this apparatus, distilled water was supplied to the bottom of the test section using a submersible pump (Franklin Electric FPS 4400). The flow rate of water to the test section was controlled by a valve connected to the by-pass line. A cooling coil in the water tank was used to maintain the water at constant temperature. Filtered air was supplied to the top of the test section and maintained at a steady pressure P_0 using a Fisher C1 pressure controller. A picture of the air supply piping and the test section is shown in Figure 3.4.

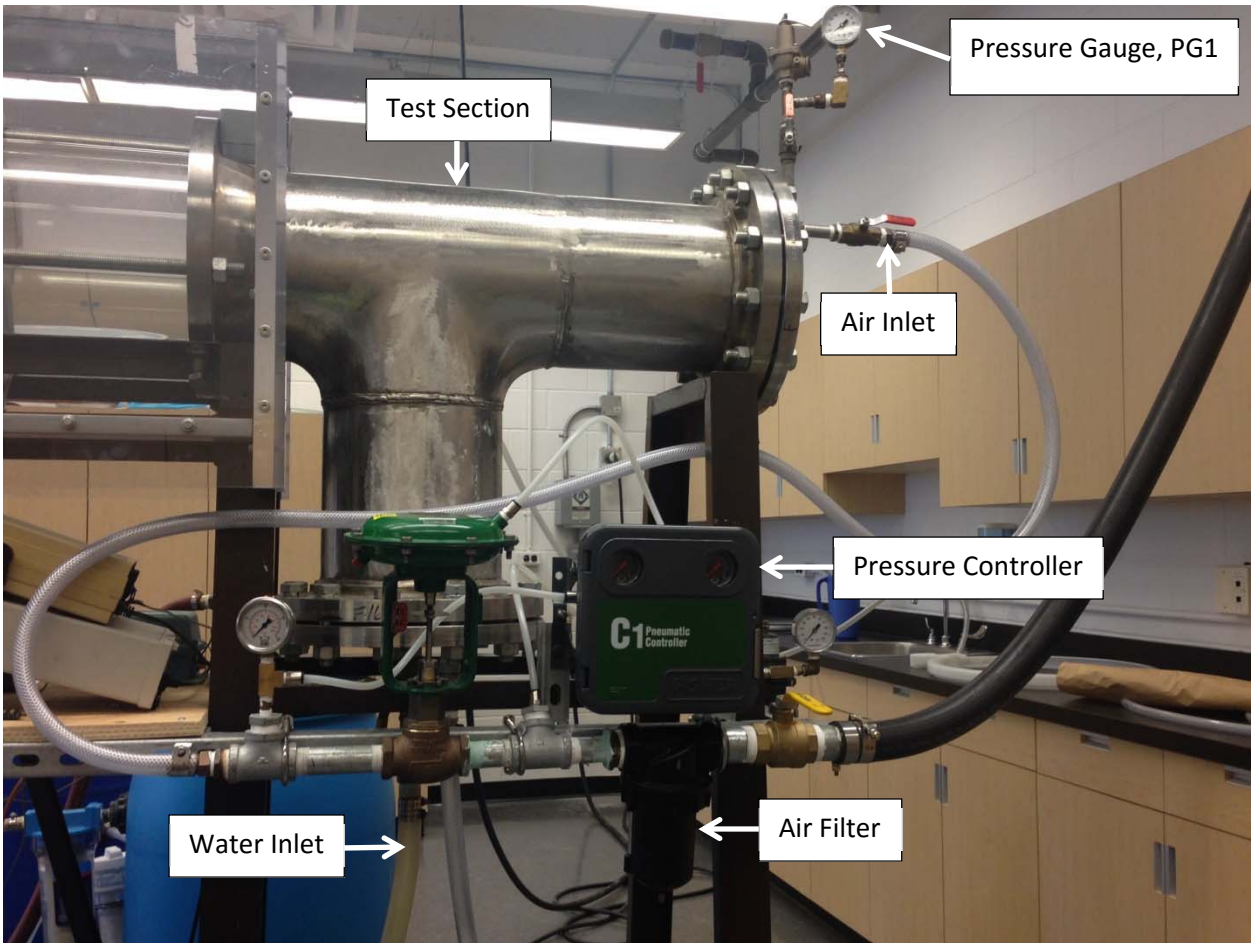

Figure 3.4 –Air supply piping and test section

Two pressure taps connected to a pressure transducer were installed on the outlet flange to measure the interface height in the test section. The flow leaving the test section was directed through Branches A and B to two separators which separated the air and water. A second pressure

transducer was connected to each separator to measure the pressure difference between them. The water leaving the bottom of each separator was directed to one of four water rotameters with overlapping ranges, before it was returned to the water tank. The air, leaving the top of each separator was directed into separate air headers and then passed through one of four air rotameters with overlapping ranges, where its flow rate was measured. The air from both sides was then combined into a common header before being released into the atmosphere. A muffler was used for the air exiting the outlet header to minimize the noise. Figure 3.5 shows a picture of Branches A and B from the test section to the separators and the air headers before and after the rotameters.

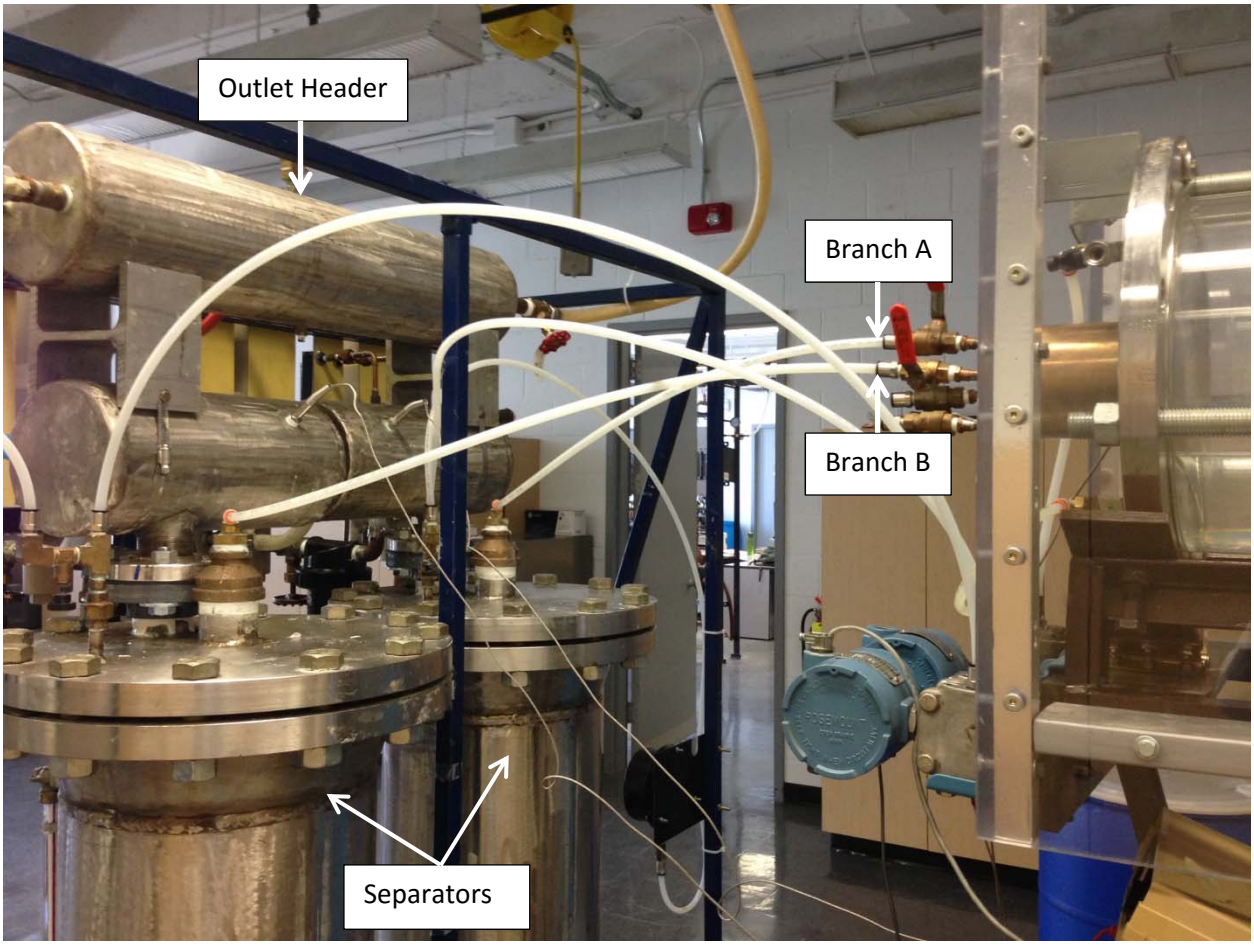

Figure 3.5 –Branches, separators and air headers

The temperature of the air and water in the test section and the air temperature in each air header were measured using Type T thermocouples (TC1 – TC4) connected to a digital thermocouple reader. All four thermocouples were calibrated at freezing point, room temperature

and boiling conditions. Bourdon pressure gauges were used to measure the pressure in the test section and in each separator and an Ashcroft digital pressure gauge was used to measure the pressure of air leaving the air flow meters. The pressure gauges were calibrated using an Ashcroft dead-weight testing device. Details of the thermocouple and pressure gauge calibrations can be found in Appendix A.

3.2.2 Test Section

The test section consists of a large tee-shaped reservoir containing stratified layers of water and air. The majority of the test section is fabricated with type 304 stainless steel, with an acrylic tube located near the outlet flange for visual observation of the flow phenomena. A picture of the acrylic portion of the test section is shown in Figure 3.6.

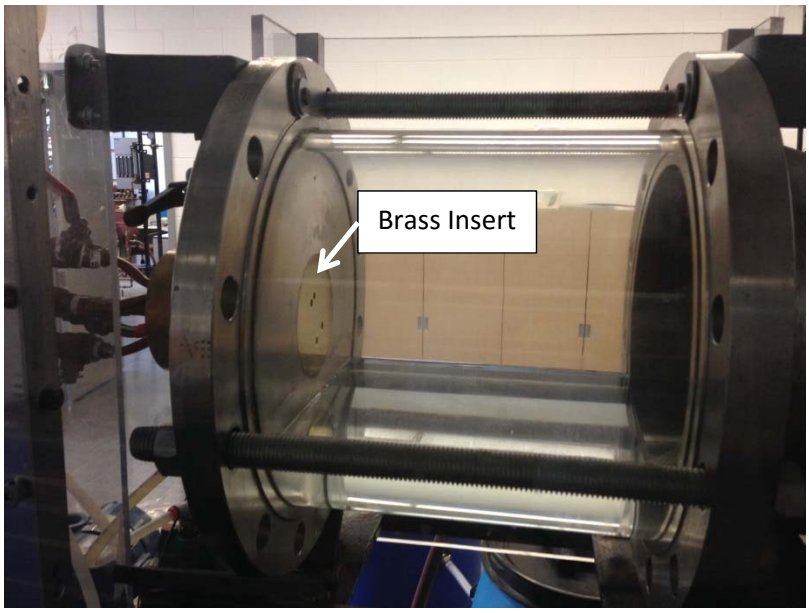

Figure 3.6 – Acrylic tube

Water entered the test section through twelve 12.7 mm diameter holes located in three rows of four around the circumference of a 25.4 mm diameter copper tube entering through the bottom flange of the test section and closed from the other end. This inlet tube was designed to help disperse the water entering the test section horizontally and, thus, prevent the formation of waves on the interface. Air entered the test section through the air inlet flange located at one end of the test section. In order to reduce the incoming air velocity and prevent waves or ripples from forming

on the interface, the air entered through four large outlet holes located on two sides of a triangular shaped dispersion box located inside the test section. Details of both the air inlet dispersion box and the water inlet tube can be found in Parrott (1993).

The discharging branches are two 6.35 mm diameter holes drilled through a brass block. Two brass blocks were machined for Maier's (1998) experiments to allow for branch spacing's of L/d = 1.5, 2, 3 and 8. Each orifice is 127 mm in length to ensure a straight length of 20 diameters before any bends or area changes occur. Long slots on the mounting flange allowed for the brass piece to be installed onto the outlet flange and rotate at various angles. The brass block containing branch spacings of 1.5 and 3 was used in these experiments and the layout is shown in Figure 3.7. A picture of the brass piece is shown in Figure 3.8.

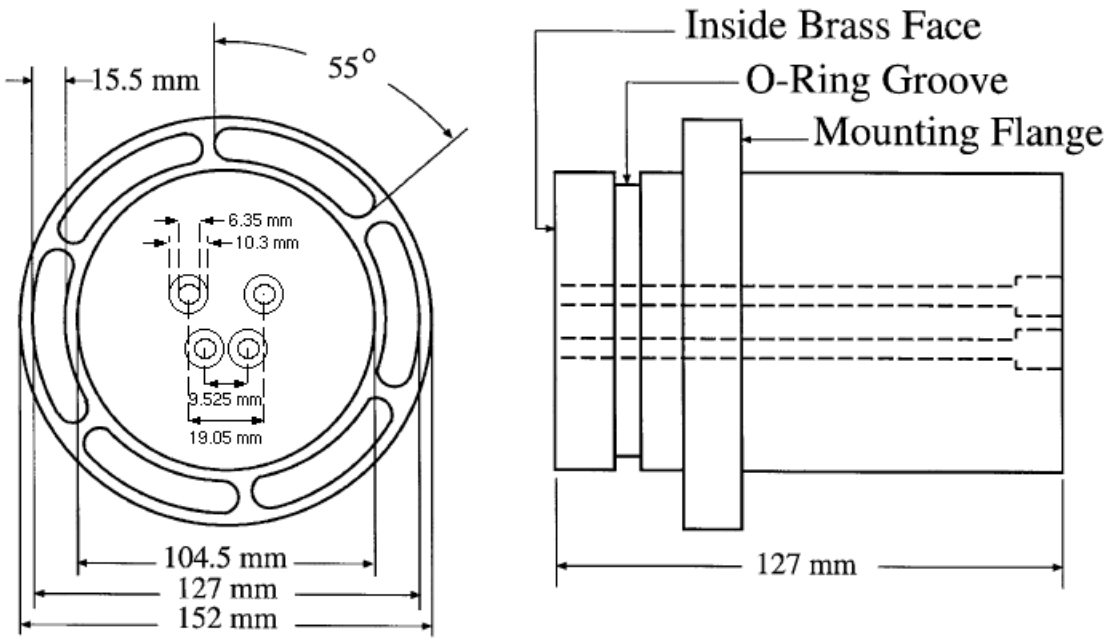

Figure 3.7 - Front and side views of the brass insert

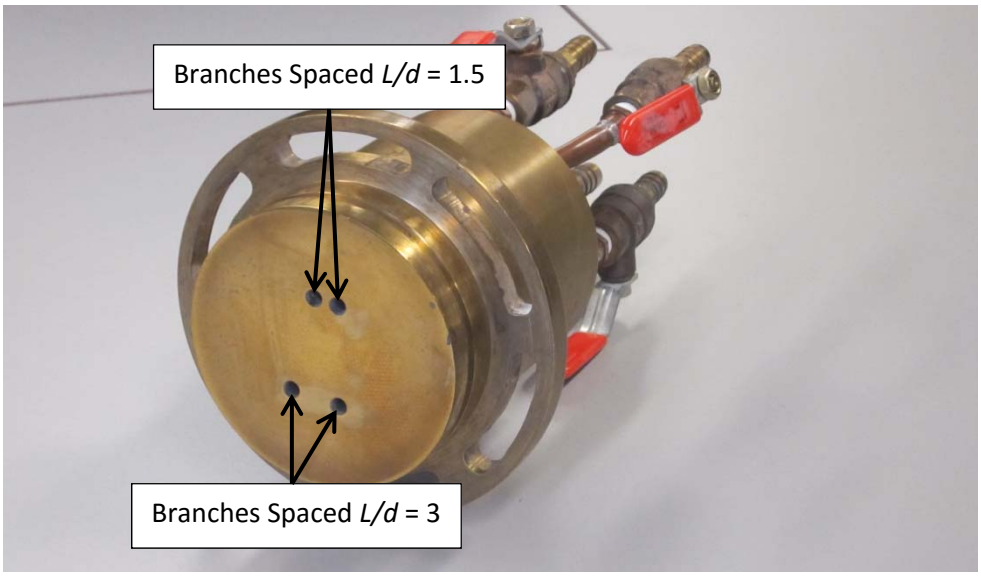

Figure 3.8 – Brass insert for test section

3.2.3 Separation Tanks

The two-phase flow leaving the test section through Branches A and B was directed to two stainless steel separators as shown in Figure 3.9. The flow entering each separator was split into two streams ending at 60 mm diameter nozzles located near the inside wall of the separators and angled to force the flow in a downward spiral such that the water flows downward along the wall and exits through the bottom of the separator and the air flows upwards and exits through the top. Clear glass tubes, 640 mm in length, were attached to the side of each separator to indicate the water level inside the separators. The separators were each made up of three sections of different cross sectional areas. The top section has a diameter of 327 mm and the water level was maintained in this section for high water flow rates, the water level was maintained in the middle section (143 mm diameter) for moderate water flow rates and the water level was maintained in the lowest and smallest section of the separator (60 mm diameter) for very small water flow rates. A smaller section was needed for smaller flow rates to detect inequalities (by monitoring the water level through the sight glass) between the flow rates entering and leaving the separators within a reasonable amount of time. If a large section is used for small or moderate flow rates, the water level inside the separator will change too slowly, making it hard to judge whether or not the water level is steady.

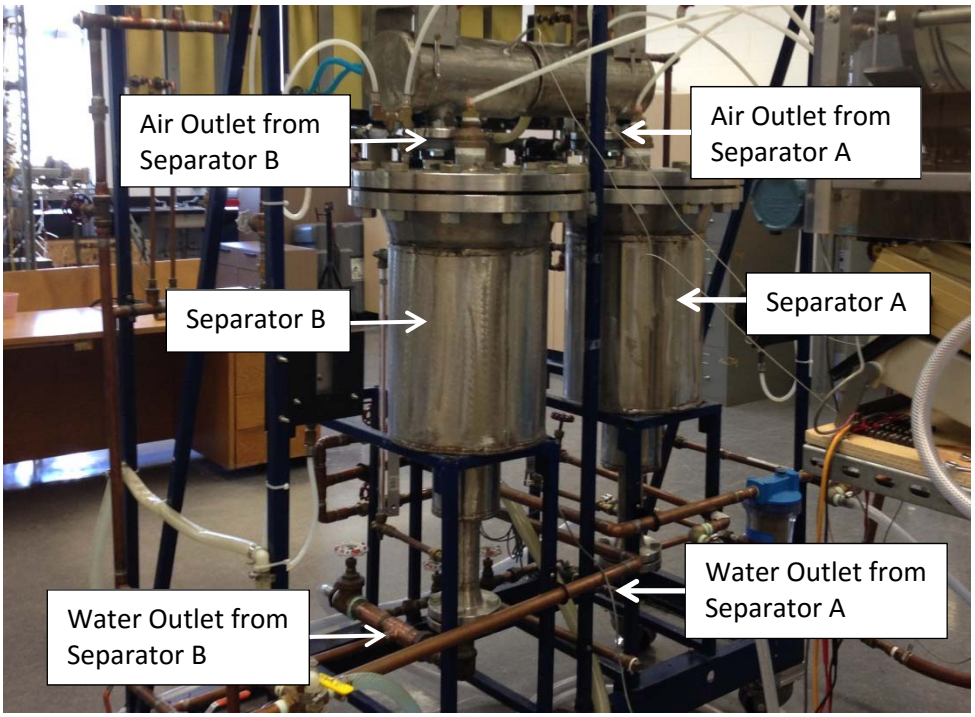

Figure 3.9 –Separators

In order to maintain the pressure in the separators equal to one another for all the experiments, a pressure tap was installed at the top of each separator and connected to a differential pressure transducer. The pressure transducer output was read continuously throughout the experiments and adjustments were made to ensure the pressure difference across the separators was near zero. Detailed figures of the separator can be found in Hassan (1995).

3.2.4 Flowrate Measurements

A picture of the water and air rotameters is shown in Figure 3.10. The water leaving the bottom of each separator was measured using one of four water rotameters with overlapping ranges connected in parallel. The flow through these rotameters was mainly controlled using the valve downstream of the rotameters. The make and capacities of each water rotameter are listed below.

- Wa4 and Wb4 - Cole-Parmer - N102-05, capacity = 93 STD mL/min
- Wa3 and Wb3 - Cole-Parmer - N044-40, capacity = 582 STD mL/min
- Wa2 and Wb2 – Brooks Instrument - R-8M-25-2, capacity = 4.00 STD L/min

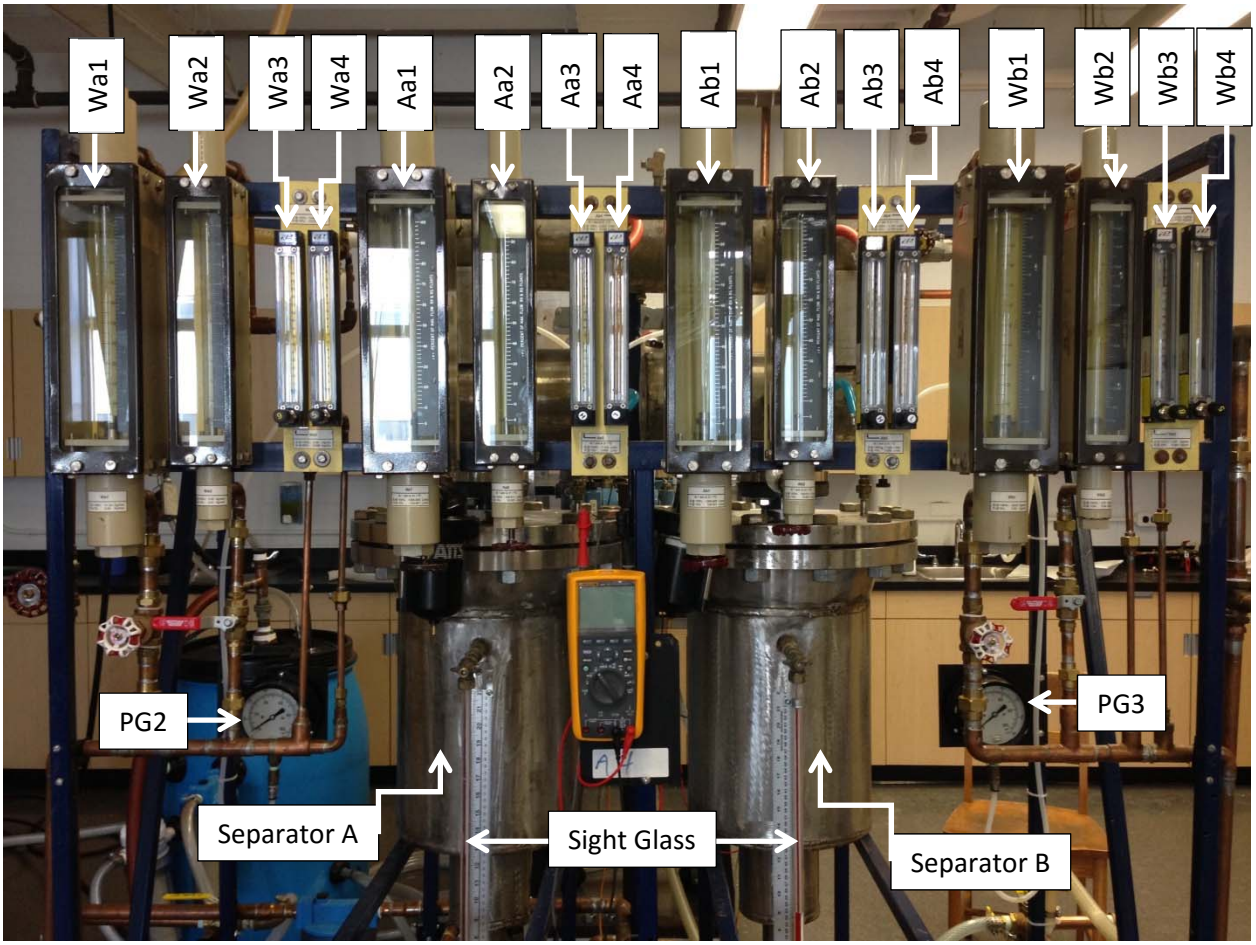

Figure 3.10 – Air and water rotameters

- Wa1 and Wb1 – Brooks Instrument - R-10M-2503, capacity = 41.0 STD L/min

These rotameters were all calibrated using a weigh and time method. Details of these calibrations can be found in Appendix A.

The flow rate of air leaving the top of each separator was measured using one of four air rotameters with overlapping ranges, connected in parallel. The make, model number and capacities of these rotameters are listed below:

- Aa4 and Ab4 – Cole-Parmer - N092-04, capacity = 2.3 STD L/min
- Aa3 and Ab3 – Cole-Parmer – N034-039, capacity = 16.4 STD L/min
- Aa2 and Ab2 – Brooks Instrument – R-8M-25-4, capacity = 165.3 STD L/min
- Aa1 and Ab1 – Brooks Instrument - R-10M-25-3, capacity = 1346 STD L/min

The pressure of air flow in the rotameters was obtained by measuring the pressure in the outlet air header using an Ashcroft digital pressure gauge. The pressures at these two locations are nearly equal. All eight air rotameters were calibrated in house using one of two wet-test meters for the lower flow rates and venturi tubes for the higher flow rates. Details of these calibrations can be found in Appendix A.

3.2.5 Liquid Level Measurement

Two pressure taps were installed on the outlet flange of the test section, one near the top into the air region, and the other near the bottom into the water region as shown in Figure 3.11. These pressure taps were connected to a differential pressure transducer to measure the height of the interface in the test section. The pressure transducer was calibrated using a water manometer to provide a measurement of 0 to 165 mm of water pressure over a range of 2 to 10 Volts. Because the pressure transducer is located L_{zero} = 217 mm below the desired zero elevation, the zero on the transducer was adjusted to give a reading of 2.0 Volts when applying a pressure of 217 mmH_2O and the maximum pressure at 10.0 Volts was therefore 382 mmH_2O (165 mmH_2O + 217 mmH_2O). When calibrating the pressure transducer, the following second order polynomial was found to fit the data:

$$P(\mathrm{mmH_2O}) = \gamma_1\left(E_L - \gamma_2 E_L^{\,2} - \gamma_3\right) \tag{3.1}$$

where γ_1 = 20.6188 mmH_2O/Volt, γ_2 = 8.29466x10^{-4} Volt^{-1}, γ_3 = 2.00416 Volt and E_L is the voltage reading. More details on this calibration can be found in Appendix A.

Equation (3.1) gives the height of the interface when the low side of the pressure transducer is exposed to air at atmospheric pressure, since these are the conditions under which the calibrations were performed. For higher test section pressures, the higher air density must be taken into consideration. The following equation was derived by Parrott (1993) for calculating the interface height for test section pressures above atmospheric and the derivation is explained in detail in his thesis:

$$h = \gamma_1\left(E_L - \gamma_2 E_L^2 - \gamma_3\right)\chi + L_{zero}(\chi - 1) - \gamma_1\left(E_{CL,atm} - \gamma_2 E_{CL,atm}^2 - \gamma_3\right) \tag{3.2}$$

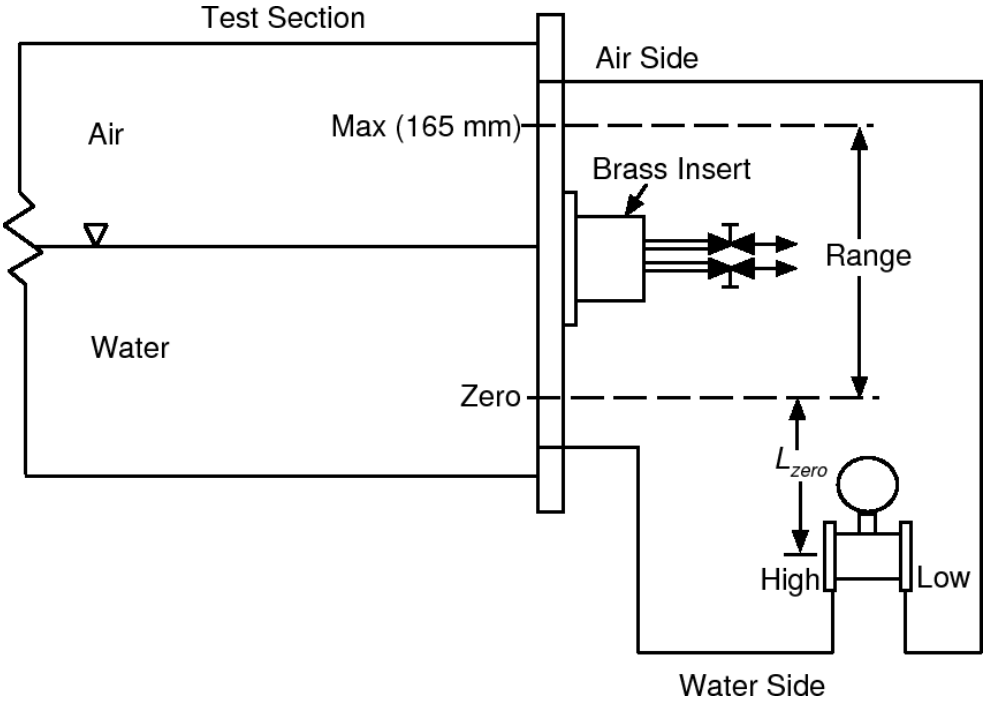

Figure 3.11 - Schematic of liquid level measurement

where h is in mmH2O. In Equation (3.2), $\chi = \frac{\rho_L - \rho_{G,atm}}{\rho_L - \rho_{G,0}}$, where $\rho_{G,atm}$ is the density of the gas at atmospheric conditions and $\rho_{G,0}$ is the density of the gas in the test section under pressurized conditions. The parameter L_{zero} is the height of the liquid between the high side of the pressure transducer and the zero location shown in Figure 3.11 and is equal to 217 mm. $E_{CL,atm}$ is the voltage reading for the branch centreline taken at atmospheric conditions; this will be discussed in the following paragraphs. For Branch A, Equation (3.2) was used by replacing h with h_A and $E_{CL,atm}$ with $E_{CL,atm,A}$ and for Branch B, Equation (3.2) was used by replacing h with h_B and $E_{CL,atm}$ with $E_{CL,atm,B}$.

For each angle of inclination and branch spacing, the voltage reading corresponding to the centreline of each branch was determined before running the experiments. This was done using the "needle method" used previously by Parrott (1993) and described in the following paragraph.

For each branch, the voltage readings corresponding to the top and the bottom of the branch were determined and the centreline voltage was taken as the average. The first step in this

procedure was to hang a needle into the test section some distance away from the outlet flange where the interface is flat (Parrott (1993) showed that the interface next to the wall is 3 mm higher than the flat interface far from the wall due to the meniscus effect). The needle was hung into the test section by attaching it to a string and feeding it through a metal rod inserted into the air pressure tap located on the outlet flange, as shown in Figure 3.12. For the voltage reading at the bottom of the branch, the tip of the needle was aligned with the bottom of the branch using a surveyor lens and the interface was slowly raised until the tip of the needle just touched the interface. The voltage reading was recorded at this instant as $E_{CL,atm,BOT}$ and the procedure was repeated at the top of the branch to obtain the voltage reading, $E_{CL,atm,TOP}$. The voltage corresponding to the center of the branch was then calculated as the average of these two voltages, $E_{CL,atm} = \left(\frac{E_{CL,atm,BOT} + E_{CL,atm,TOP}}{2} \right)$. It is important to note that this procedure must be done at atmospheric pressure, which was insured by maintaining the test section open to the atmosphere during the procedure.

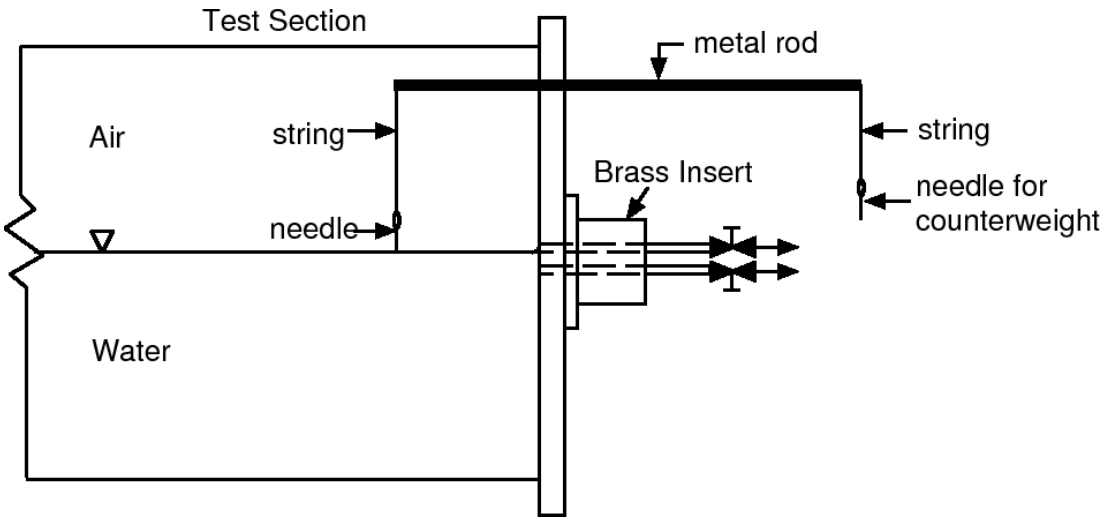

Figure 3.12 - Schematic of needle test set-up

3.2.6 Angle of Inclination Measurements

The angle of inclination, θ, between the two branches, is the angle between the horizontal plane and a line connecting the centrelines of the two branches such that at $\theta = 0°$, the branches are located side by side and at $\theta = 90°$, the branches are located one on top of the other. In order to measure this angle of inclination, a protractor was fit snugly around the circumference of the brass insert. The datum ($\theta = 0°$) was first established using a surveyor lens to ensure the tops and the bottoms of both branches are aligned with the horizontal. With the brass insert positioned for $\theta = 0°$, the zero on the protractor was aligned with a horizontal marking on the outlet flange. For all other angles, as the brass insert was rotated, the protractor rotated with it. The angle was then read as the protractor reading that aligned with the horizontal marking on the outlet flange.

3.3 Experimental Procedure

For each set of P_0, ΔP, L/d and θ, the following procedures were followed to first determine the onset of liquid entrainment mass flow rates ($\dot{m}_{G,OLE,A}$ and $\dot{m}_{G,OLE,B}$) and heights ($h_{OLE,A}$ and $h_{OLE,B}$), followed by the onset of gas entrainment mass flow rates ($\dot{m}_{L,OGE,A}$ and $\dot{m}_{L,OGE,B}$) and heights ($h_{OGE,A}$ and $h_{OGE,B}$) and finally the two-phase mass flow rates ($\dot{m}_{TP,A}$ and $\dot{m}_{TP,B}$) and corresponding interface heights (h_A and h_B) for approximately 25 interface heights between $h_{OLE,B}$ and $h_{OGE,A}$. Refer to Figure 3.3 for clarification of the labels used for the different measurement devices.

3.3.1 Procedure for Onset of Liquid Entrainment, OLE

1. The interface was first lowered to a height beneath the expected OLE height by draining water from the test section into the water tank.
2. The pump and cooling water were turned on with the bypass valve fully opened and the valve to the test section fully closed.
3. With the valves on both branches fully opened, the valves to rotameters Aa1 and Ab1 fully opened and the valves to all other air and water rotameters fully closed, the air supply valve was opened to allow air to flow into the apparatus.

4. The pressure in the test section was adjusted to the desired P_0 using the dial on the pressure controller and the pressure in the separators was adjusted to $P_S = P_0 - \Delta P$ using the valves on the outlet header. In order to obtain exactly zero pressure difference between the two separators, it was necessary to also slightly throttle the valves to Aa1 and/or Ab1.
5. Once the desired pressures were obtained in the test section and separators for single phase air flow through the branches, the air flow rates through rotameters Aa1 and Ab1, temperatures measured by the thermocouples TC1 to TC4 and the pressures measured in gauges PG1 to PG4 were recorded. These data were later used to calculate $\dot{m}_{G,OLE,A}$, $\dot{m}_{G,OLE,B}$, $\mathrm{Fr}_{G,OLE,A}$ and $\mathrm{Fr}_{G,OLE,B}$.
6. The water valve to the test section was then opened very slightly to let water into the test section thus raising the interface at a rate of 1 mm/min.
7. The interface was monitored through the acrylic section of the test section until water first started exiting through the lower branch (Branch B). At this instant, the voltage reading from the pressure transducer PT1 was recorded. This voltage reading was later used to calculate $h_{OLE,B}$.
8. Once these data were recorded, the valve to one of the Branch B water rotameters was opened fully and water flow through the rotameter was controlled using the valve downstream to maintain the water level inside the separator steady. With small water flow rates, the smallest rotameter was used (Wb4) and as the interface was raised and more water flowed through Branch B, larger and larger rotameters were used. Also, as more water flowed through Branch B, the water valve to the test section was adjusted to allow more flow into the test section.
9. As the water level was raised at a rate of 1 mm/min, the valves and dial controlling the pressures in the separators and the test section were continuously adjusted to maintain the pressures at the desired settings.
10. While monitoring the interface through the acrylic section, the voltage reading, E_L, from the pressure transducer (PT1), corresponding to the onset of liquid entrainment at Branch A was recorded immediately once water started exiting through the upper branch. This voltage was later used to calculate $h_{OLE,A}$.

3.3.2 Procedure for Onset of Gas Entrainment, OGE

1. Following the OLE at the upper branch, the water valve to one of the Branch A rotameters was opened fully and water flow through this rotameter was controlled using the valve downstream. Rotameter Wa4 was used initially for small water flow rates followed by Wa3, Wa2 and then Wa1 as the water flow rate through Branch A increased.
2. The interface was raised further by adjusting the water valve into the test section until it just passed the OGE height for Branch B. The valves and dial controlling the pressures in the test section and separators were continuously adjusted to maintain the pressures at the desired values and the water valves were adjusted to maintain the liquid in each separator at a constant level.
3. The interface was then lowered slowly at a rate of 1 mm/min while visually monitoring the flow through the bottom branch and maintaining the test section and separator pressures constant. The voltage reading, E_L, from the pressure transducer (PT1), corresponding to the onset of gas entrainment height at Branch B was recorded when gas was entrained into the bottom branch. The gas entrainment was at times intermittent at first, in which case the interface was lowered further until continuous entrainment occurred. The voltage corresponding to this continuous entrainment was later used to calculate $h_{OGE,B}$.
4. At interfaces above $h_{OGE,B}$, air no longer flows through Branch B and the valves to the Branch B air rotameters are closed. The pressure in the separator for Branch B will then be constant, as long as the water level inside that separator remains constant.
5. Step 2 was then repeated and the interface was raised above the OGE at Branch A. At this time, the valves to all the air rotameters are closed and single phase water flows through both branches. For all the cases in this study, the largest rotameters, Wa1 and Wb1, were required to measure single phase water flow through the branches.
6. The valves downstream of the water rotameters were adjusted until the water level inside each separator was constant.
7. The flow rates of water through the rotameters (Wa1 and Wb1), the temperatures (TC1 – TC4), and the pressures (PG1 – PG4) were then recorded. This data were later used to calculate $\dot{m}_{L,OGE,A}$, $\dot{m}_{L,OGE,B}$, $\mathrm{Fr}_{L,OGE,A}$ and $\mathrm{Fr}_{L,OGE,B}$.

8. The interface was then lowered slowly at a rate of 1 mm/min while visually monitoring the flow through the top branch. The voltage reading, E_L, from the pressure transducer (PT1), corresponding to the OGE height at Branch A was recorded when the gas first became continuously entrained into the upper branch. This voltage reading was later used to calculate $h_{OGE,A}$.

3.3.3 Procedure for Two-Phase Flow Measurements

1. Two-phase flow results were next obtained for approximately 25 interface heights between $h_{OLE,B}$ and $h_{OGE,A}$ by dividing this height into nearly equal intervals.
2. Starting from $h_{OGE,A}$, the interface was slowly lowered by adjusting the water valve upstream of the test section.
3. Once the desired height was obtained, the valves and dial controlling the pressures in the test section and separators were adjusted to the desired settings and the valves downstream of the rotameters were adjusted to obtain a constant water level in the separators. This was an iterative procedure since adjusting the pressures changed the interface height and vice versa. The pressure transducer between the separators was also monitored continuously to ensure near zero pressure difference between the separators.
4. Once the interface height, the pressures and the water level in the separators had remained steady for approximately 10 minutes, the following data were recorded:
    i. pressures in the test section, separators and outlet header (PG1 – PG4)
    ii. temperatures in the test section and each separator (TC1 – TC4)
    iii. air rotameter readings for both branches (Aa1 – Aa4 and Ab1 – Ab4)
    iv. water rotameter readings for both branches (Wa1 – Wa4 and Wb1 – Wb4)
    v. pressure transducer reading corresponding to interface height (PT1)

3.4 Data Reduction

Throughout the experiments, the data recorded for each test case included the air pressure and the temperature of water and air in the test section, the pressure and temperature of air in each separator, the pressure of air in the outlet header, the air and water rotameter readings for each branch and the voltage reading from the differential pressure transducer corresponding to the

interface height. From these data, the desired mass flow rates, throat velocities and Froude numbers and interface heights were calculated. The equations and methods described below for calculating the flow rates, velocities and Froude numbers are applicable to both Branches A and B but for simplicity, will be described only once for Branch A.

1. $\dot{m}_{L,A}$ Calculation: The mass flow rate of water through Branch A, $\dot{m}_{L,A}$, was interpolated using the calibration tables in Appendix A, Tables A.3 to A.6.

2. $\dot{m}_{G,A}$ Calculation: The mass flow rate of air through Branch A, $\dot{m}_{G,A}$, was calculated using the standard mass flow $\dot{m}_{G,A,STD}$ taken from the calibration tables in Appendix A and using the following equation:

$$\dot{m}_{G,A} = \dot{m}_{G,A,STD}\sqrt{\frac{\rho_{G,rot}}{\rho_{G,STD}}} \tag{3.3}$$

where $\rho_{G,STD}$ was taken as 1.19978 kg/m^3 and $\rho_{G,rot}$ was calculated using the ideal gas law:

$$\rho_{G,rot} = \frac{P_{rot}}{R_G T_{G,0}} \tag{3.4}$$

In Equation (3.4), P_{rot} is the pressure reading in the outlet air header (PG4), $T_{G,0}$ is the temperature of gas in the test section (TC1) and R_G is the gas constant for air ($R_G = 0.287$ kJ/kg K).

3. $V_{L,th,A}$ Calculation: The throat velocity in Branch A for single phase water, $V_{L,th,A}$, was required for calculating $\mathrm{Fr}_{L,OGE,A}$. The water density was evaluated at the water temperature in the test section. Its value was determined using linear interpolation in the water property table in Bergman, Lavine, Incropera and DeWitt (2011). The water velocity in the throat of the branch, $V_{L,th,A}$, was then calculated using the following equation:

$$V_{L,th,A} = \frac{\dot{m}_{L,A}}{\rho_L A} \tag{3.5}$$

4. $V_{G,th,A}$ Calculation: The throat velocity in Branch A for single phase air, $V_{G,th,A}$, was required for calculating $\mathrm{Fr}_{G,OLE,A}$. In order to calculate $V_{G,th,A}$, $\rho_{G,th,A}$ is also required, which depends on the throat pressure and temperature. These were determined using an energy balance for the flow of air between the upstream region of the test section and the throat location inside the branch.

$$C_p T_{G,0} + \frac{V_{G,0}^2}{2} = C_p T_{G,th,A} + \frac{V_{G,th,A}^2}{2} \tag{3.6}$$

The velocity of gas upstream, $V_{G,0}$, is assumed negligible and the velocity of the gas in the throat is:

$$V_{G,th,A} = \frac{\dot{m}_{G,A}}{\rho_{G,th,A} A} \tag{3.7}$$

where A is the cross sectional area and the throat density is calculated using the ideal gas law as:

$$\rho_{G,th,A} = \frac{P_{th,A}}{R_G T_{G,th,A}} \tag{3.8}$$

Isentropic expansion is assumed in the air between the upstream location in the test section and the throat and therefore the isentropic process equation is used:

$$T_{G,th,A} = T_{G,0}\left(\frac{P_{th,A}}{P_0}\right)^{\frac{n-1}{n}} \tag{3.9}$$

Where *n* is the ratio of specific heats and is equal to 1.4 for air. Using an initial guess for the throat pressure, $P_{th,A}$, Equations (3.6) to (3.9) were solved iteratively until Equation (3.6) was satisfied.

5. $\mathrm{Fr}_{G,OLE,A}$ Calculation: The gas Froude number for Branch A was then calculated using the following equation:

$$\mathrm{Fr}_{G,OLE,A} = V_{G,th,A}\sqrt{\frac{\rho_{G,th,A}}{gd\left(\rho_L - \rho_{G,th,A}\right)}} \tag{3.10}$$

6. $\mathrm{Fr}_{L,OGE,A}$ Calculation: The liquid Froude number for Branch A was calculated as:

$$\mathrm{Fr}_{L,OGE,A} = V_{L,th,A}\sqrt{\frac{\rho_L}{gd\left(\rho_L - \rho_{G,th,A}\right)}} \tag{3.11}$$

3.5 Experimental Uncertainty

The experimental uncertainty was calculated using the method of Kline and McClintock (1987). All the equations and detailed results for the uncertainties are included in Appendix B. The uncertainty in $\mathrm{Fr}_{G,OLE}$ ranges from $\omega_{\mathrm{Fr}_{G,OLE}} = \pm$ 3.3% to ± 5.6% and the uncertainty in $\mathrm{Fr}_{L,OGE}$ ranges from $\omega_{\mathrm{Fr}_{L,OGE}} = \pm$ 3.4% to ± 4.8%. Tables B.3 to B.7 show the uncertainty results for all cases of $\mathrm{Fr}_{G,OLE}$ and $\mathrm{Fr}_{L,OGE}$ tested in this study.

The uncertainties in mass flow rates, interface heights and qualities are shown in Tables B.8 to B.38 in Appendix B. For the two-phase mass flow rates through the branches, the maximum uncertainty in $\dot{m}_{TP}$ is $\omega_{\dot{m}_{TP}} = \pm$ 8.6%. The uncertainty in the interface height measurements ranges from ω_h = 0.21 to 0.22 mm and the maximum uncertainty in h/d is $\omega_{h/d}$ = 0.0566. Uncertainties were also calculated for the dimensionless parameters, M and H, and the quality x for branches A and B. The uncertainties in M and H increase as H decreases to a maximum of $\omega_M = \pm$ 24.4% and $\omega_H = \pm$ 11.2% at H = 0.1. Because the uncertainties are calculated as a percentage of the value of the parameter, at values lower than H = 0.1, the uncertainties are very high and are not included in the tables in Appendix B. The maximum uncertainty in the quality is $\omega_x = \pm$ 9.8%.

Chapter 4

Experimental Results and Discussion

4.1 Onset of Liquid Entrainment

4.1.1 Data Range for OLE

The onset of liquid entrainment data were collected for four different geometries by varying the spacing between the two branches, L/d, and the angle between the branches, θ. For each combination of L/d and θ, $h_{OLE,A}$ and $h_{OLE,B}$ data were collected for seven different Froude numbers over a range from $15 < \mathrm{Fr}_{G,OLE,A} < 40$, where $\mathrm{Fr}_{G,OLE,A} = \mathrm{Fr}_{G,OLE,B}$. This resulted in a total of 56 data points including 28 data points for $h_{OLE,A}$ and 28 data points for $h_{OLE,B}$. The Froude number was varied by varying the pressure in the test section, P_0, and/or the pressure difference, ΔP. The ranges of P_0, ΔP, L/d, and θ used to obtain the onset of liquid entrainment data are as follows:

- P_0 = 316 to 585 kPa
- ΔP = 40 to 300 kPa
- L/d = 1.5 and 3
- θ = 30° and 60°

4.1.2 Comparison of OLE Results with Previous Experimental Data

Before beginning the experimental investigation for the ranges defined in the Section 4.1.1, some preliminary experiments were done on cases where the two branches were located side by side (θ = 0°) and one on top of the other (θ = 90°). Results for $|h_{OLE,A}|/d$ and $|h_{OLE,B}|/d$ for these cases were compared against Hassan's (1995) correlation to ensure the apparatus was

producing accurate results and to validate the experimental procedure. Figures 4.1 and 4.2 show results at Branches A and B, respectively, for $\theta = 0°$ and $\theta = 90°$ for two combinations of P_0 and ΔP: $P_0 = 316$ kPa and $\Delta P = 40$ kPa; $P_0 = 517$ kPa and $\Delta P = 235$ kPa. The RMS deviation between the present data and the correlation for the eight data points shown in Figures 4.1 and 4.2 is 3.4%, which is within the range of experimental uncertainty.

4.1.3 Flow Phenomena for OLE

The flow phenomena observed during the onset of liquid entrainment at both the lower and upper branches will be discussed here. Pictures of the phenomena for $P_0 = 316$ kPa and $\Delta P = 123$ kPa are included to help describe the process. When the interface is located far beneath the bottom branch and single phase gas flows through the branches, the interface is flat. As the interface is raised, the liquid beneath the bottom branch opening starts to climb the wall until a stream of liquid suddenly forms and begins to flow through the branch. Regardless of the spacing or the angle between the branches, the shape of the interface is fairly consistent for the onset of liquid entrainment at the bottom branch. This can be observed in Figure 4.3 (a) to (d).

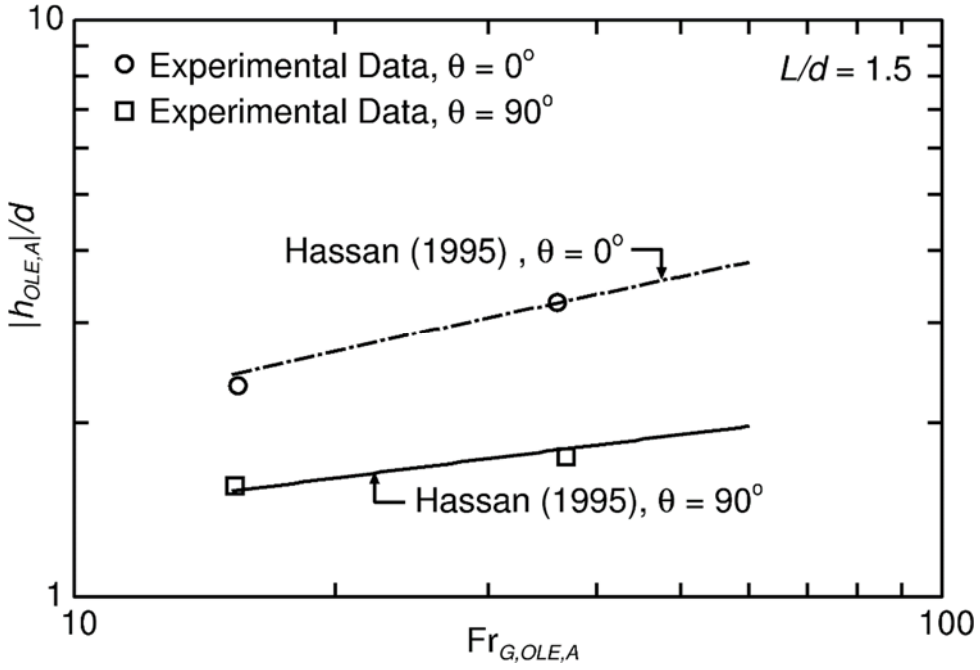

Figure 4.1 - Comparison of OLE data at Branch A with Hassan (1995) for $L/d = 1.5$

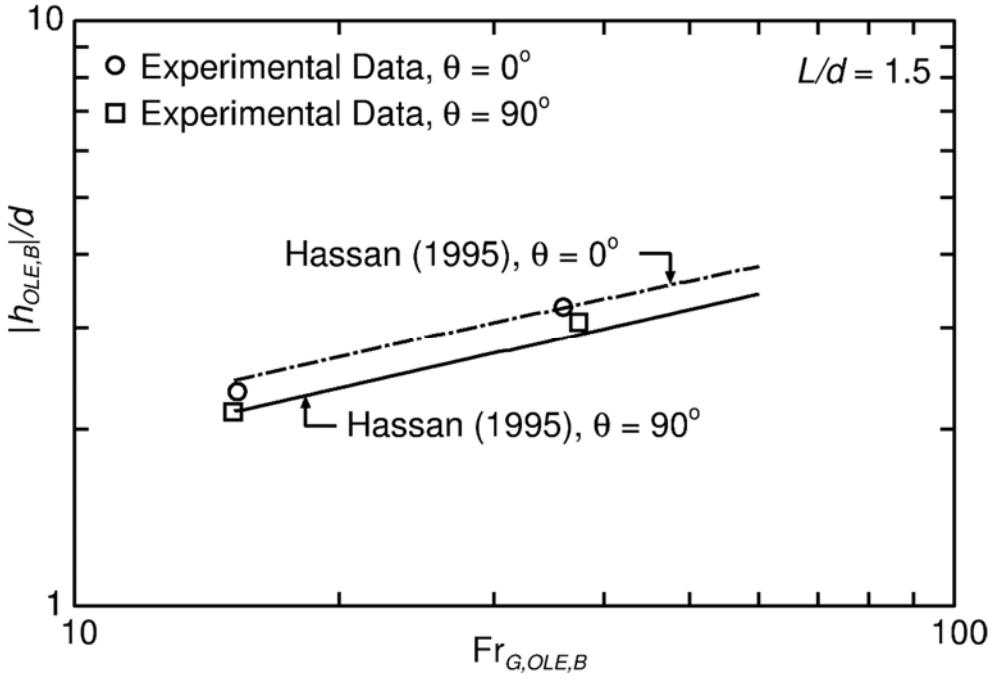

Figure 4.2 - Comparison of OLE data at Branch B with Hassan (1995) for $L/d = 1.5$

(a) $\theta = 30°$ and $L/d = 1.5$

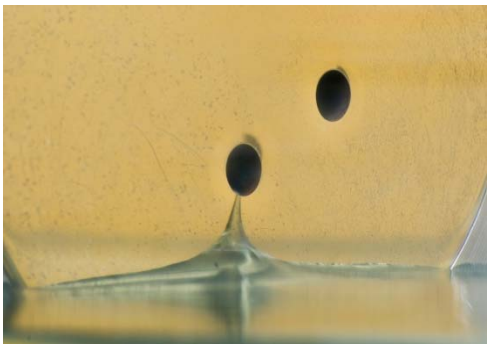

(b) $\theta = 30°$ and $L/d = 3$

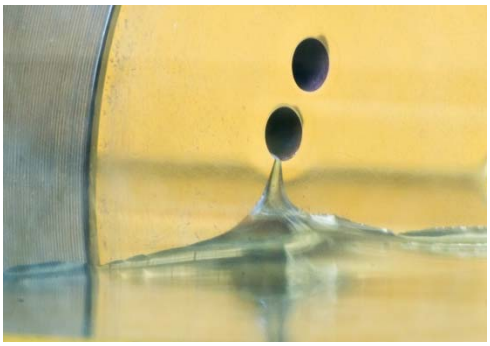

(c) $\theta = 60°$ and $L/d = 1.5$

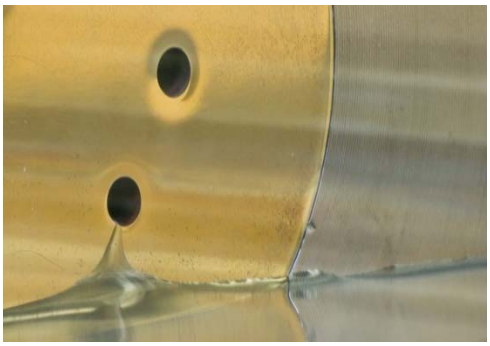

(d) $\theta = 60°$ and $L/d = 3$

Figure 4.3 - Photographs of OLEs at Branch B for $P_0 = 316$ kPa and $\Delta P = 123$ kPa

For the onset of liquid entrainment at the upper branch, the shape of the interface changes with θ and L/d. For $L/d = 1.5$, Figures 4.4 (a) and (c) show that there is only one peak in the interface under the branches and the liquid stream entering Branch A comes from the top of this peak. However, when the branches are spaced farther apart ($L/d = 3$) and for $\theta = 30°$, there are two separate peaks in the interface underneath the branches; one peak for liquid entrainment into Branch B and one for Branch A. The shape of the interface for $L/d = 3$ and $\theta = 30°$, as shown in Figure 4.4 (b), suggests that the branches are behaving as two independent branches for this geometry. In all three of the cases shown in Figures 4.4 (a) to (c), the onset of liquid entrainment at the upper branch occurs while the flat interface is still located beneath the bottom branch. For $L/d = 3$ and $\theta = 60°$, the flat interface is located above the bottom branch when the onset of liquid entrainment occurs at the upper branch and the liquid stream extends from the interface into the top branch opening at the onset, as shown in Figure 4.4 (d).

(a) $\theta = 30°$ and $L/d = 1.5$

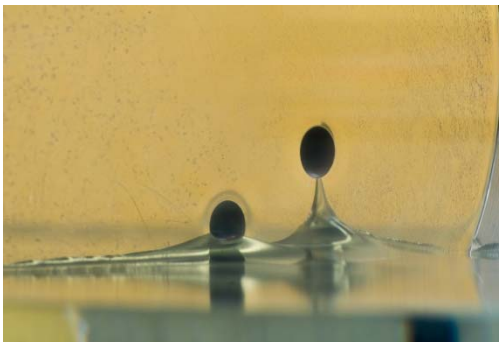

(b) $\theta = 30°$ and $L/d = 3$

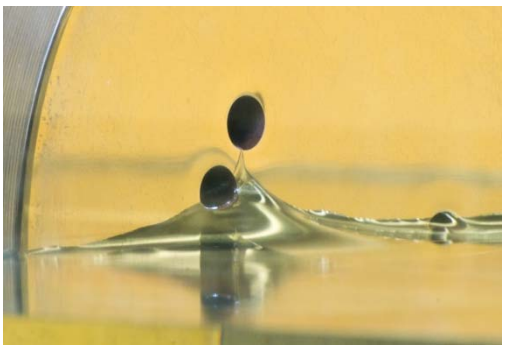

(c) $\theta = 60°$ and $L/d = 1.5$

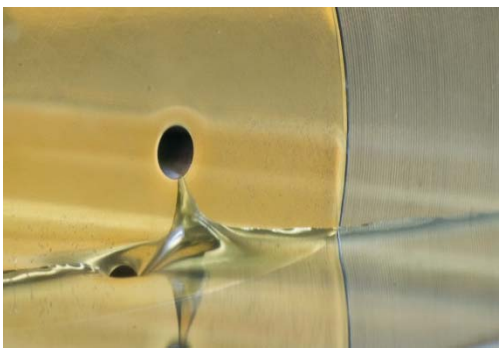

(d) $\theta = 60°$ and $L/d = 3$

Figure 4.4 - Photographs of OLEs at Branch A for $P_0 = 316$ kPa and $\Delta P = 123$ kPa

4.1.4 OLE Results and Correlations

The experimental results for the onset of liquid entrainment heights, $|h_{OLE,B}|/d$, at the bottom branch are plotted versus $\mathrm{Fr}_{G,OLE,B}$ in Figures 4.5 and 4.6. Figure 4.5 shows the experimental data for L/d = 1.5 and θ = 30° and 60° along with Hassan's (1995) correlation for this same branch spacing and angles of θ = 0° and 90°. Experimental data and correlations are presented for these same angles in Figure 4.6 but for L/d = 3. The experimental data show the correct trend of increasing $|h_{OLE,B}|/d$ with increasing $\mathrm{Fr}_{G,OLE,B}$. In both plots, the experimental results show that there is negligible effect of θ on the onset of liquid entrainment at the bottom branch between angles of 30° and 60°, while Hassan's (1995) correlations show that between θ = 0° and 90°, there is a slight decrease in the onset height with increasing θ (average difference of 11% for both L/d = 1.5 and 3).

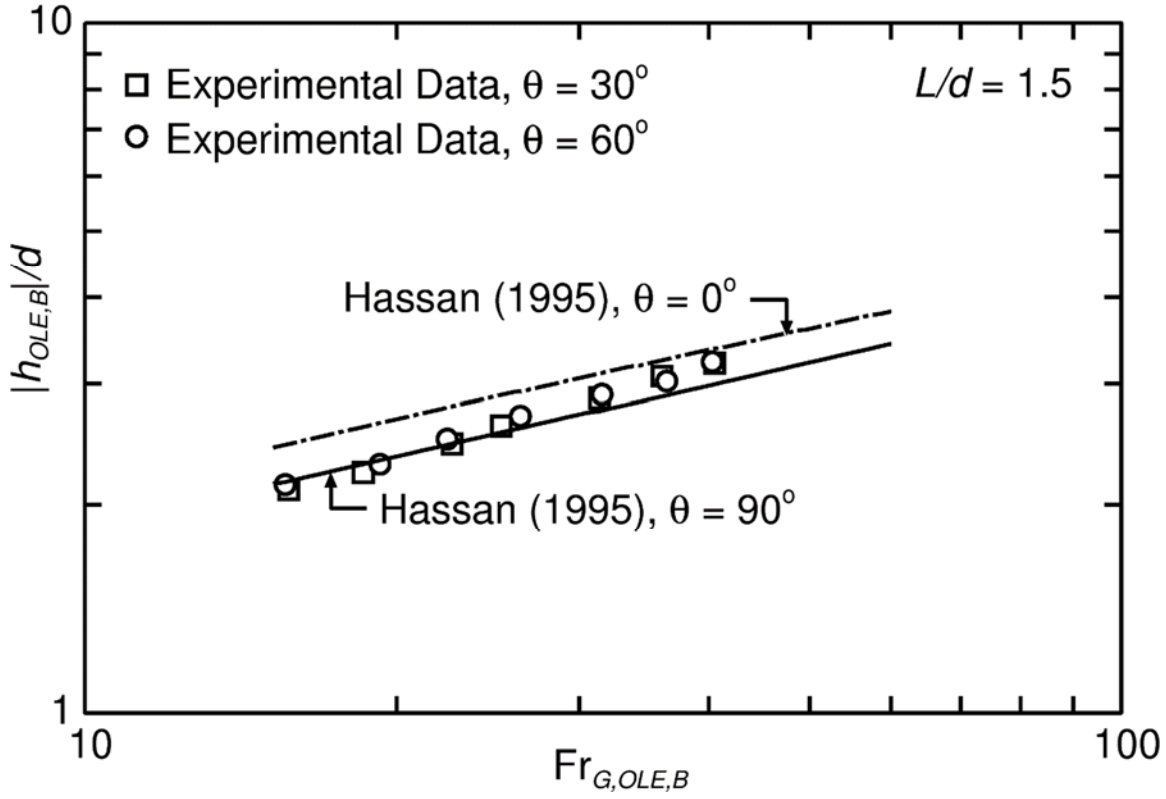

Figure 4.5 - OLE data and Hassan's (1995) correlations at Branch B for L/d = 1.5

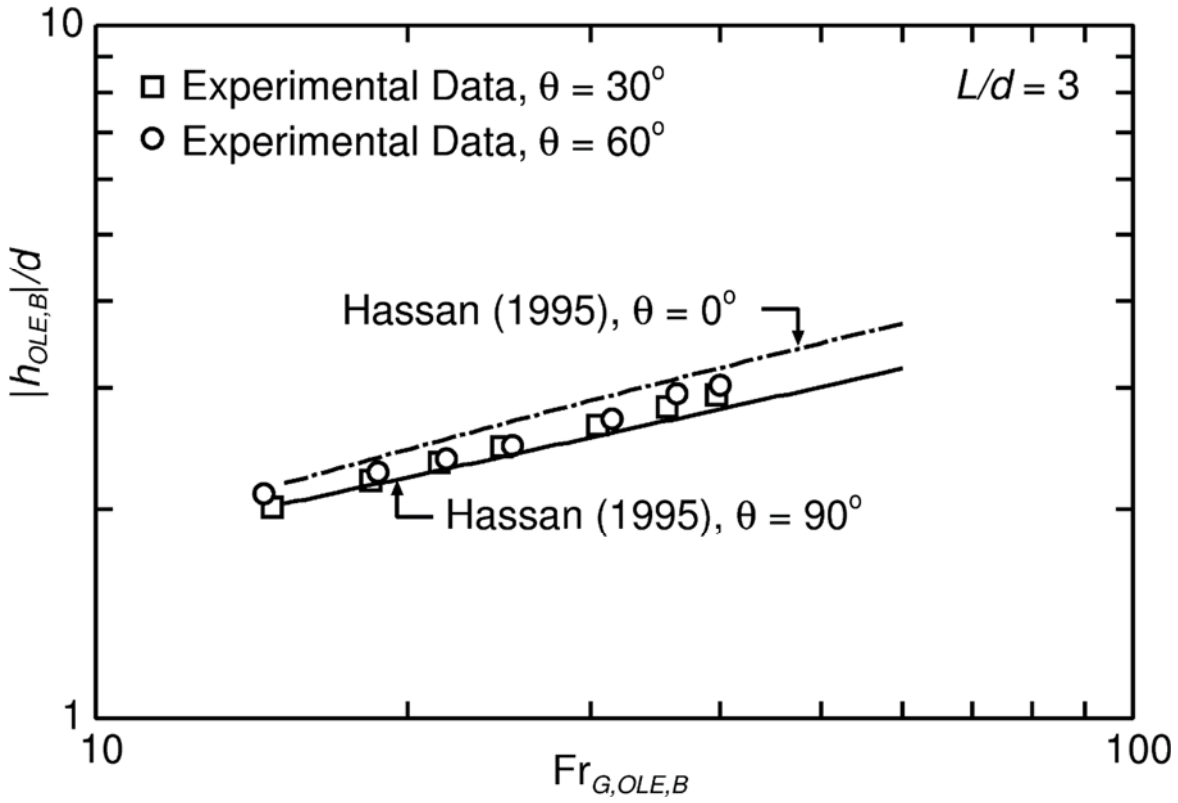

Figure 4.6 - OLE data and Hassan's (1995) correlations at Branch B for L/d = 3

The experimental data for the onset of liquid entrainment at Branch B were compared with Maier et al.'s (2001) theoretical model for θ = 30° and 60° in Figures 4.7 and 4.8, respectively. Both the experimental data and the analytical model plotted in these figures show that for both θ = 30° and 60°, $\left|h_{OLE,B}\right|/d$ increases with decreasing L/d. The upper branch provides more assistance to the lower branch with liquid entrainment as the spacing between the branches decreases. Excellent agreement was obtained between the experimental data and Maier et al.'s theoretical model for most of the data with slight deviations at low values of $\mathrm{Fr}_{G,OLE,B}$ for L/d = 3.

The angle between the branches has a more significant effect on the onset of liquid entrainment results at the upper branch, especially when the branches are located close together

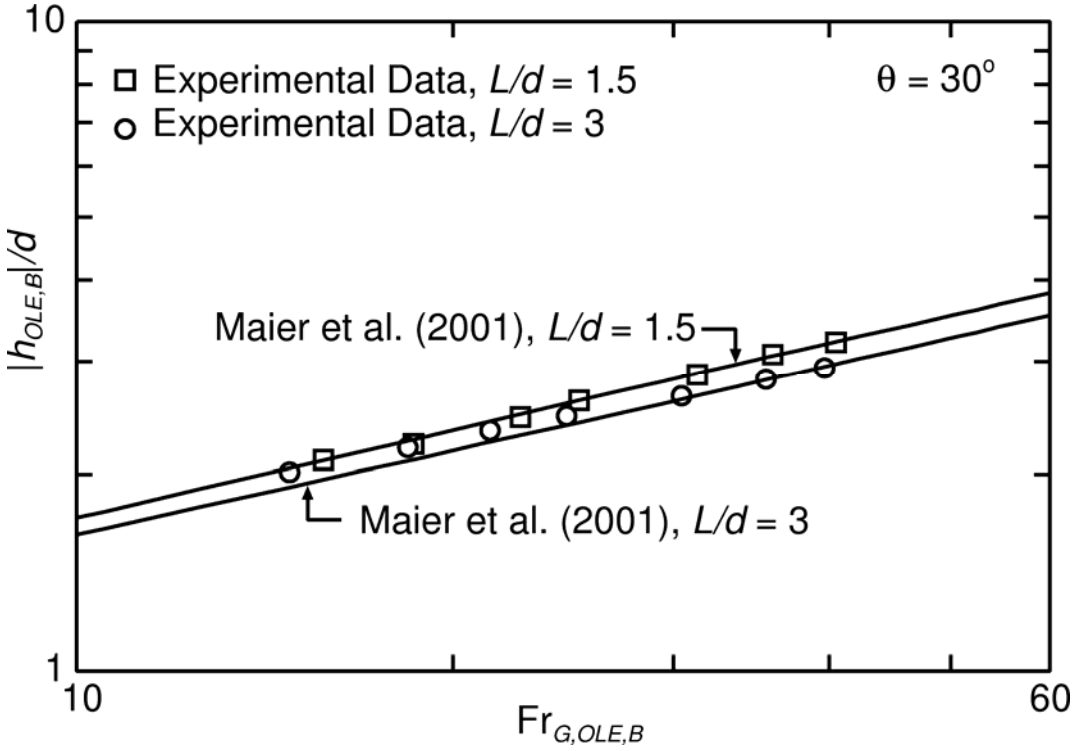

Figure 4.7 – Comparison of OLE data at Branch B with Maier et al. (2001) for θ = 30°

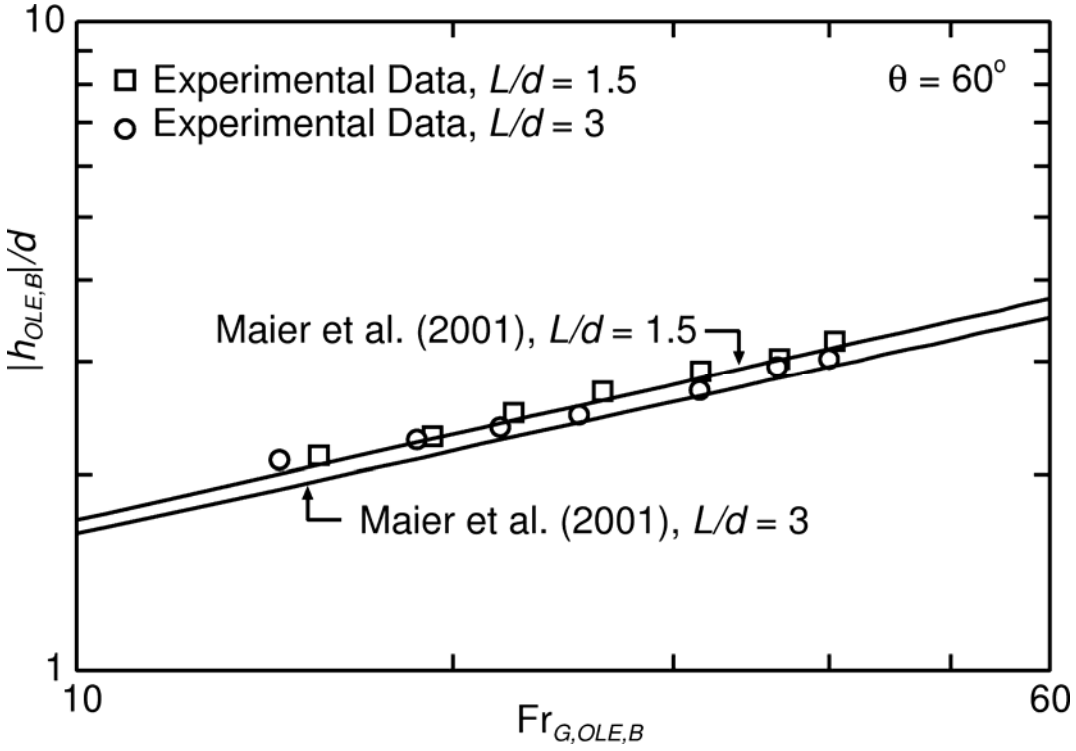

Figure 4.8 – Comparison of OLE data at Branch B with Maier et al. (2001) for θ = 60°

($L/d = 1.5$). Figure 4.9 shows the effect of θ on $|h_{OLE,A}|/d$ for $L/d = 1.5$. As θ increases, the lower branch competes with the upper branch for liquid entrainment and thus $|h_{OLE,A}|/d$ decreases. However, the change in $|h_{OLE,A}|/d$ with θ is not linear since the change between $\theta = 0°$ and $\theta = 60°$ is much smaller than the change between $\theta = 60°$ and $\theta = 90°$. With the branches located one on top of the other, they are now in direct competition for liquid entrainment as they are both pulling liquid from the same region near the wall between the two branches. Figure 4.10 shows that when the branches are located further apart ($L/d = 3$), the experimental data for $\theta = 30°$ and 60° shows negligible effect of θ on the onset height at the upper branch. However, Hassan's (1995) correlation does show a drop in $|h_{OLE,A}|/d$ from $\theta = 60°$ to $\theta = 90°$, probably due to the bottom branch competing with the upper branch for liquid entrainment at the higher angles.

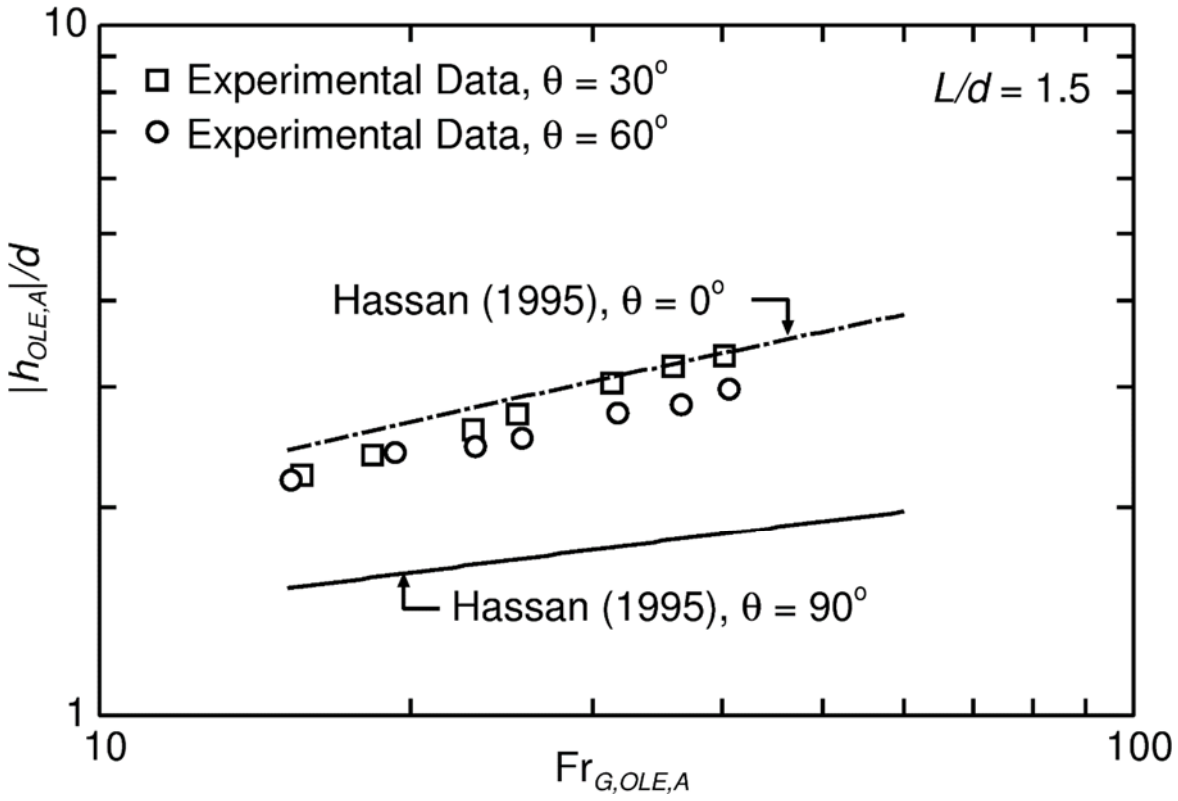

Figure 4.9 - OLE data and Hassan's (1995) correlations at Branch A for $L/d = 1.5$

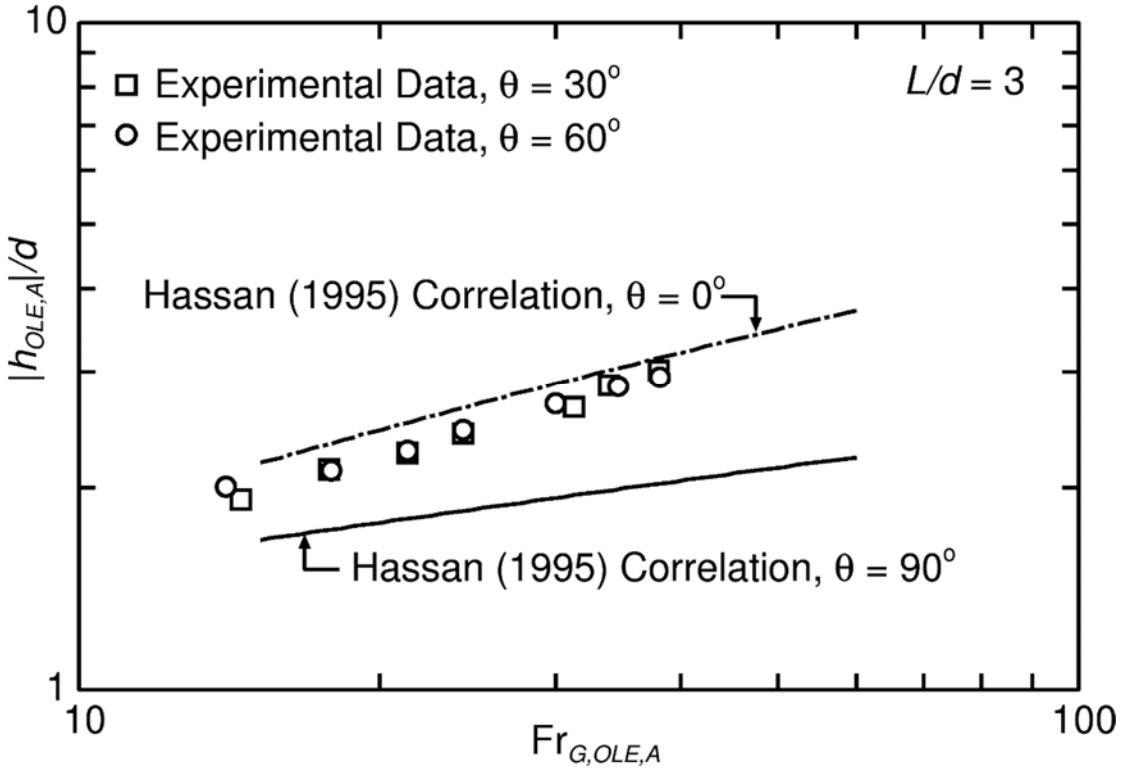

Figure 4.10 - OLE data and Hassan's (1995) correlations at Branch A for $L/d = 3$

The following empirical correlations were developed, using the nonlinear least-squares Marquardt-Levenberg algorithm, from the present experimental data and Hassan's experimental data for $\left|h_{OLE,A}\right|/d$ and $\left|h_{OLE,B}\right|/d$:

$$\left|h_{OLE,A}\right|/d = 0.625\mathrm{Fr}_{G,OLE,A}^{A_1} \tag{4.1}$$

$$\left|h_{OLE,B}\right|/d = 0.625\left(B_1\mathrm{Fr}_{G,OLE,B}\right)^{0.4} \tag{4.2}$$

where,

$$A_1 = 0.4\exp\left[-0.201\exp\left(-0.0838\left(\frac{L}{d}\right)^{1.637}\right)\cosh^2\theta + 0.404\exp\left(-0.13\left(\frac{L}{d}\right)^{1.413}\right)\cosh\theta\right] \tag{4.3}$$

and

$$B_1 = 1 + \exp\left[-0.683\left(\frac{L}{d}\right)^{0.408} \sin\theta - 0.219\left(\frac{L}{d}\right)^{1.091} \right] \tag{4.4}$$

These correlations are valid for L/d = 1.5 to 8, θ = 0° to 90°, and $\mathrm{Fr}_{G,OLE,A} = \mathrm{Fr}_{G,OLE,B}$ = 15 to 40 and show good agreement with the experimental data, as shown in Figures 4.11 and 4.12. These correlations also have the correct limits: as $L/d \to \infty$, the branches behave as single branches and the coefficient $A_1 \to 0.4$ and $B_1 \to$ 1 such that Equations 4.1 and 4.2 approach Craya's (1949) analytical solution, and as $L/d \to 0$, $B_1 \to 2$ and Equation 4.1 approaches Craya's single branch solution with twice the Froude number. The RMS deviation between the experimental data and the correlations is 4.2% for $|h_{OLE,A}|/d$ and 2.5% for $|h_{OLE,B}|/d$.

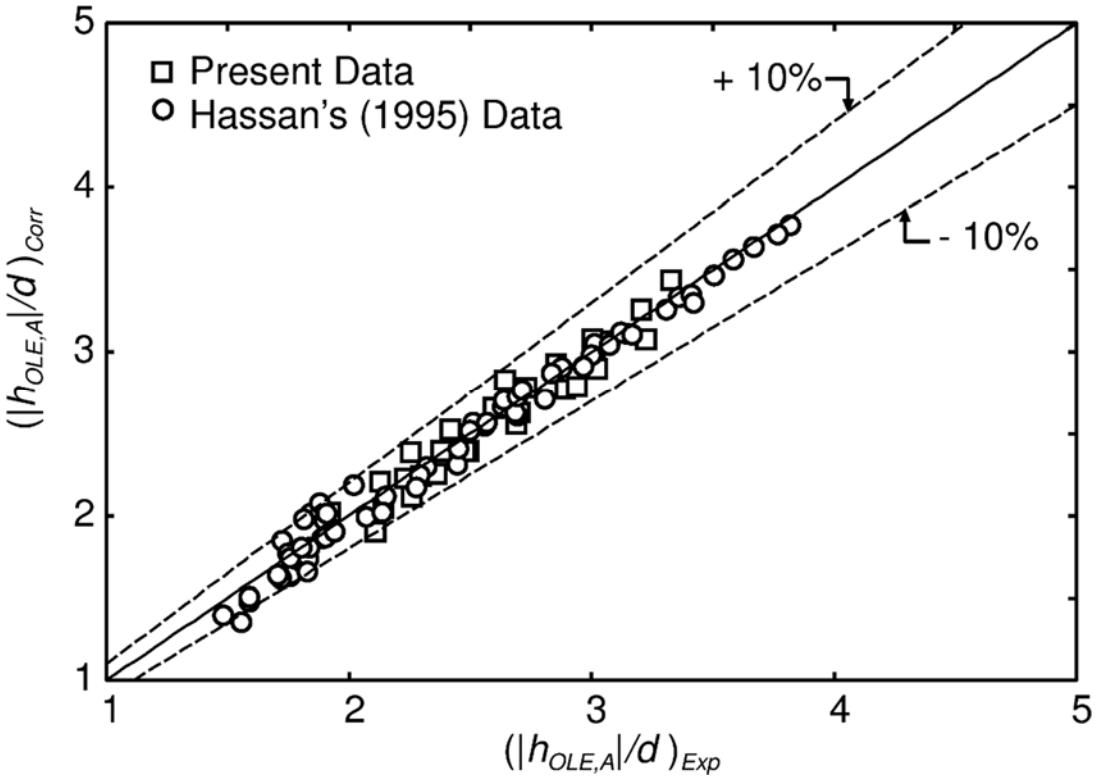

Figure 4.11 - Correlated versus measured values of $|h_{OLE,A}|/d$

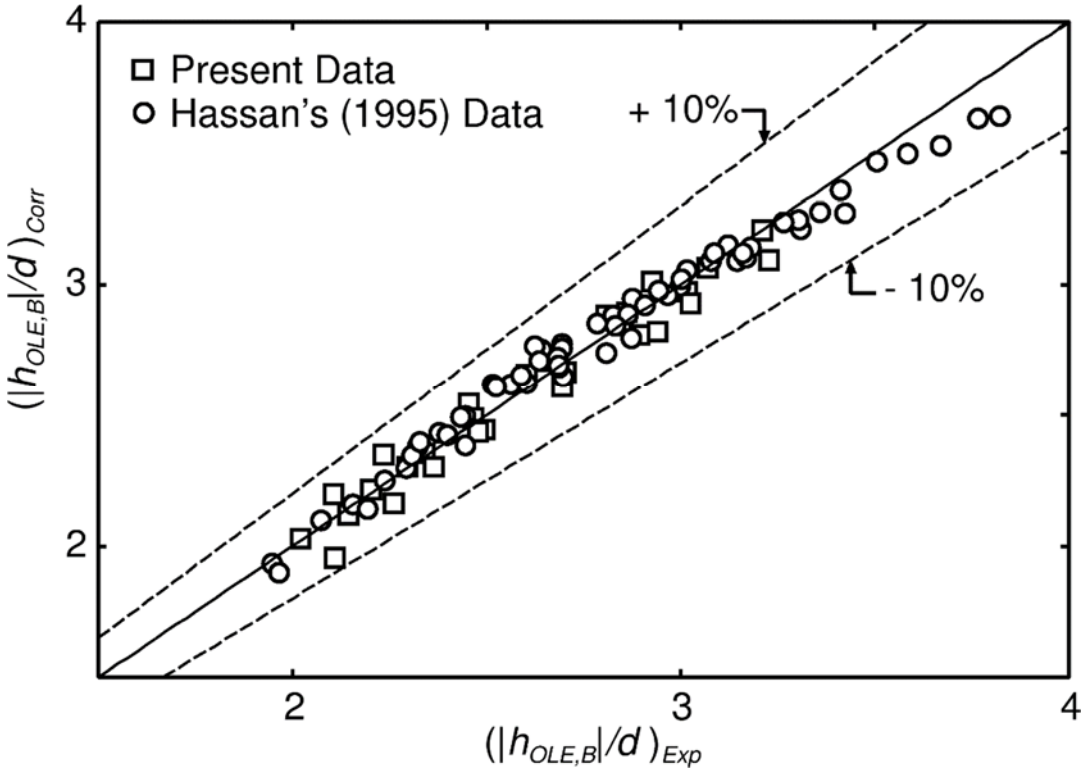

Figure 4.12 - Correlated versus measured values of $\left|h_{OLE,B}\right|/d$

4.2 Onset of Gas Entrainment

4.2.1 Data Range for OGE

The onset of gas entrainment height was measured for L/d = 1.5 and 3 and θ = 30° and 60° at each branch for seven different liquid Froude numbers between 15 and 50. In addition, data were also collected at four different liquid Froude numbers for θ = 90° and L/d = 1.5 and 3. Results for θ = 90° were previously obtained by Hassan (1995), however, since his criterion for OGE was different than for the present study (as will be discussed in Section 4.2.2), this geometry was included in the present study. To obtain the desired range of Froude numbers and geometries, the following range of conditions were required:

- P_0 = 316 to 585 kPa
- ΔP = 40 to 300 kPa
- L/d = 1.5 and 3

- θ = 30°, 60° and 90°

A total of 72 data points were collected including 36 data points for $h_{OGE,A}$ and $\mathrm{Fr}_{L,OGE,A}$ and 36 data points for $h_{OGE,B}$ and $\mathrm{Fr}_{L,OGE,B}$.

4.2.2 Comparison of OGE Results with Previous Experimental Data

Prior to obtaining data for the ranges defined in Section 4.2.1, experimental data were collected for the onset of gas entrainment at the upper and lower branches for the cases of two branches located side by side (θ = 0°) and one on top of the other (θ = 90°) for a branch spacing of L/d = 1.5. For these geometries, results for $h_{OGE,A}/d$ versus $\mathrm{Fr}_{L,OGE,A}$ and $h_{OGE,B}/d$ versus $\mathrm{Fr}_{L,OGE,B}$ were compared with Hassan's (1995) correlations as shown in Figures 4.13 and 4.14. At both the upper and lower branches it was found that the present results agreed well for θ = 0° with an RMS deviation of 3.6% between the present data and Hassan's correlation. For θ = 90°, however, the present results were consistently lower than the correlation with an RMS deviation of 12.5%. This deviation is due to how the onset condition was defined. In the present study, the onset of gas entrainment height is defined as the interface height at the instant when gas first becomes continuously entrained through the branch, while in Hassan's study, the onset of gas entrainment height was defined as the height of the interface when gas first began to enter the branch. It was observed in this study, as well as previous studies, that the gas flow into the branch is often intermittent for some time before continuous entrainment occurs. Results from Maier (1998) showed that the difference between the interface height when the gas first enters the branch and when continuous entrainment occurs can be significant at higher θ. It was therefore concluded that the Hassan correlation accurately predicts the present onset of gas entrainment data at θ = 0°, but at θ = 90°, new data were required.

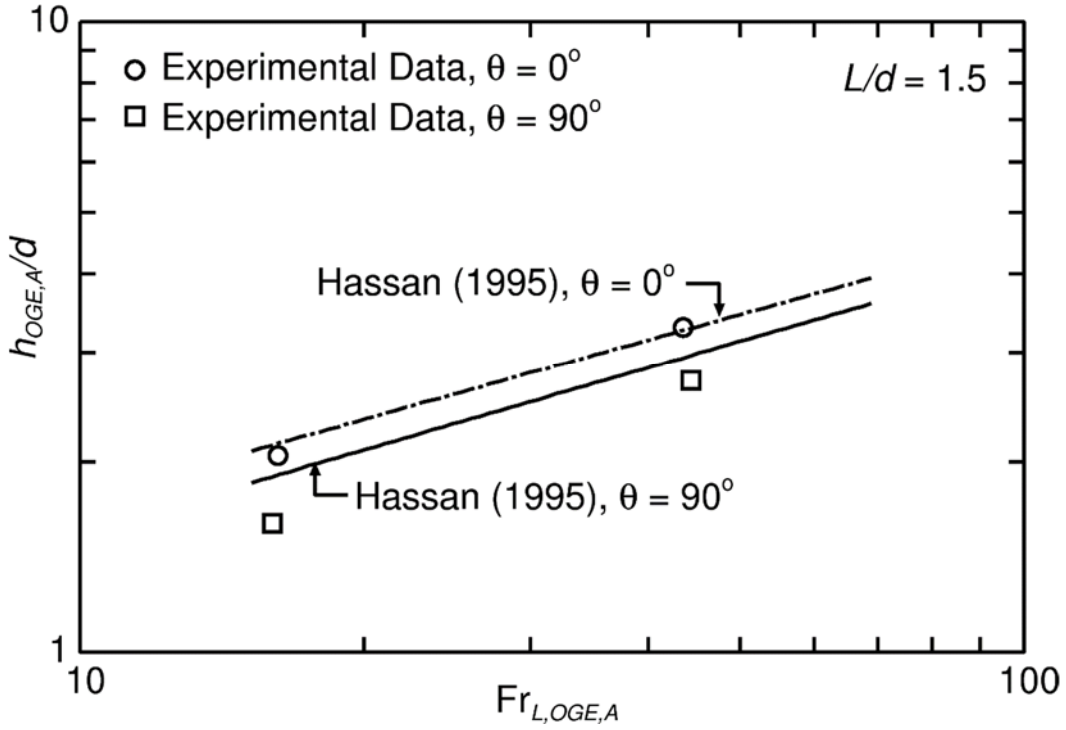

Figure 4.13 - Comparison of OGE data at Branch A with Hassan (1995) for $L/d = 1.5$

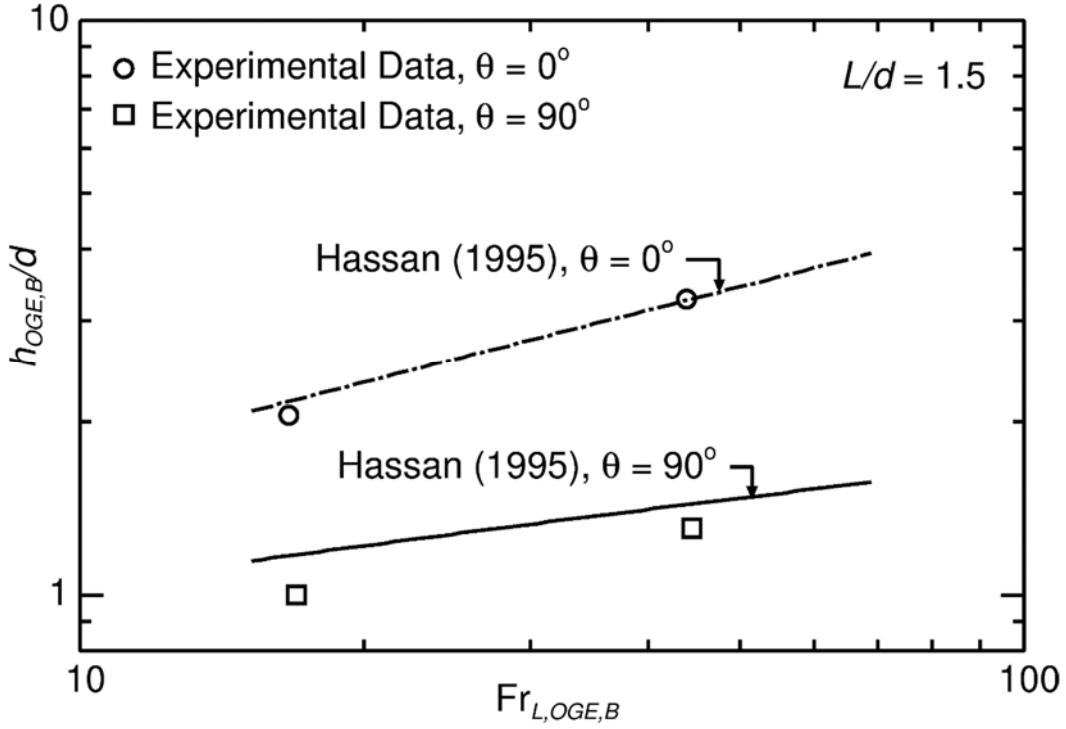

Figure 4.14 - Comparison of OGE data at Branch B with Hassan (1995) for $L/d = 1.5$

4.2.3 Flow Phenomena for OGE

Figures 4.15 and 4.16 are pictures of the onset of gas entrainment phenomenon at the upper and lower branches, respectively for $P_0 = 316$ kPa and $\Delta P = 123$ kPa. In order to capture the gas cones in these photographs, the pictures were taken from beneath the interface, looking through the water. This caused the picture to distort with the image above the interface shifted to the right relative to the image beneath the interface.

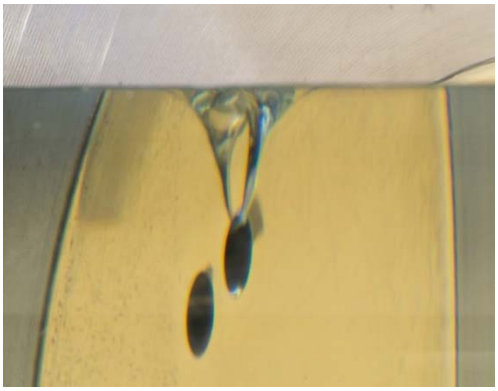

(a) $\theta = 30°$ and $L/d = 1.5$

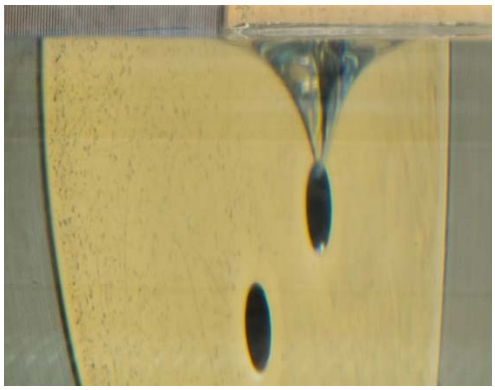

(b) $\theta = 30°$ and $L/d = 3$

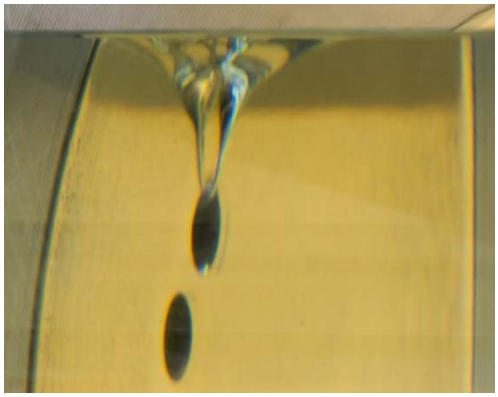

(c) $\theta = 60°$ and $L/d = 1.5$

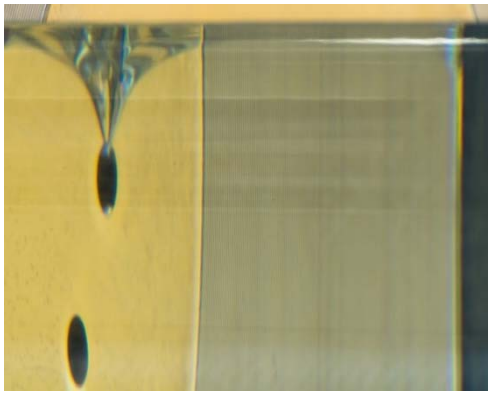

(d) $\theta = 60°$ and $L/d = 3$

Figure 4.15 - Photographs of OGEs at Branch A for $P_0 = 316$ kPa and $\Delta P = 123$ kPa

For the onset of gas entrainment at the upper branch, when the interface was located far above the upper branch, the interface was flat. As the interface was lowered, a dip appeared in the interface above the upper branch near the wall. When the critical height was reached, a gas cone

formed and a stream of gas extended from the dip in the interface towards the branch entrance. Figure 4.15 (a) to (d) show how the gas cone appears for all four combinations of L/d = 1.5 and 3 and θ = 30° and 60°; there is minimal difference in the shape of the interface between these four geometries. Note that in Figure 4.15 (a) to (d) there is a reflection of the gas cone in the brass piece making it appear as if there are two cones extending from the interface to the branch inlet when in reality there is only one gas cone.

More variation was observed in the shape of the interface for the onset of gas entrainment at the lower branch. In the photographs shown in Figure 4.16 (a) to (d) it was difficult to capture the shape of the interface since the gas cone at Branch B blocked the view of Branch A, especially for θ = 60°.

For L/d = 1.5, the onset of gas entrainment at the lower branch occurred when the interface was still located above the top branch, as shown in Figures 4.16 (a) and (c) for θ = 30° and 60°, respectively. As the interface was lowered to $h_{OGE,B}$, a gas cone extended from the region above and to the right of Branch B (where the interface was dipped down due to gas entrainment into the upper branch) towards the bottom branch opening. Figures 4.16 (b) and (d) show the gas entrainment into the bottom branch for L/d = 3 and θ = 30° and 60°, respectively. For L/d = 3 and θ = 30°, the onset of gas entrainment into Branch B occurs when the interface is located above the top of Branch A, as can be seen in Figure 4.16 (b). For this onset, the gas cone extends from a region above the branch where the interface is nearly flat, suggesting that the branches are behaving more independently for this geometry. For L/d = 3 and θ = 60° (Figure 4.16 (d)), the onset of gas entrainment at the lower branch occurs when the interface height is between the two branches. With Branch A above the interface and Branch B below the interface, the distortion caused by photographing through the water makes it appear as if Branch A has shifted to the right, while in reality these branches are spaced as was shown in Figure 4.15 (d). Under these conditions, the interface rises underneath Branch A as liquid flows into the upper branch and dips down above Branch B as gas is entrained into the lower branch. It is difficult to speculate from the shape of the interface whether or not the branches are influencing each other for these conditions.

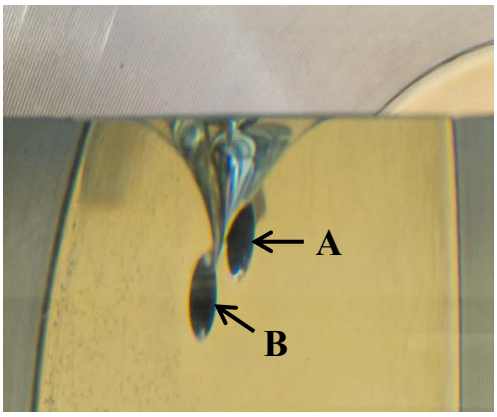

(a) $\theta = 30°$ and $L/d = 1.5$

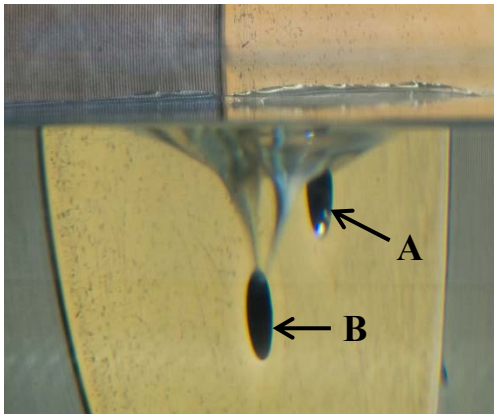

(b) $\theta = 30°$ and $L/d = 3$

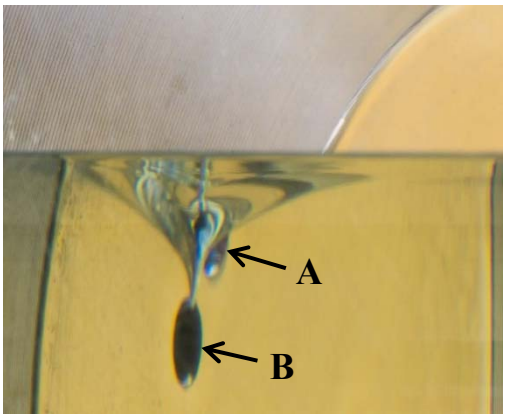

(c) $\theta = 60°$ and $L/d = 1.5$

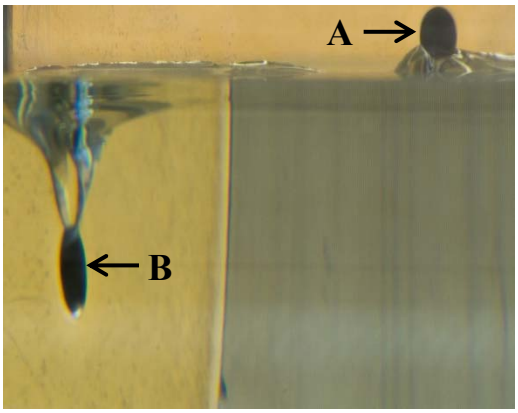

(d) $\theta = 60°$ and $L/d = 3$

Figure 4.16 - Photographs of OGEs at Branch B for $P_0 = 316$ kPa and $\Delta P = 123$ kPa

4.2.4 OGE Results and Correlations

Figures 4.17 and 4.18 show the experimental results for $h_{OGE,A}/d$ versus $\mathrm{Fr}_{L,OGE,A}$ for $\theta =$ 30°, 60° and 90° and $L/d = 1.5$ and 3, respectively, along with Hassan's (1995) correlation for $\theta = 0°$. In Figure 4.17, for $L/d = 1.5$, the results show that there are small differences between the results for $\theta = 60°$ and 90° but the general trend is for the onset height to increase with decreasing θ from $\theta = 60°$ to 0°. As θ decreases towards zero, the distance between the bottom branch and the interface drops and the bottom branch aids the top branch more with gas entrainment. This trend is also observed in Figure 4.18 for $L/d = 3$ but for that case, there is

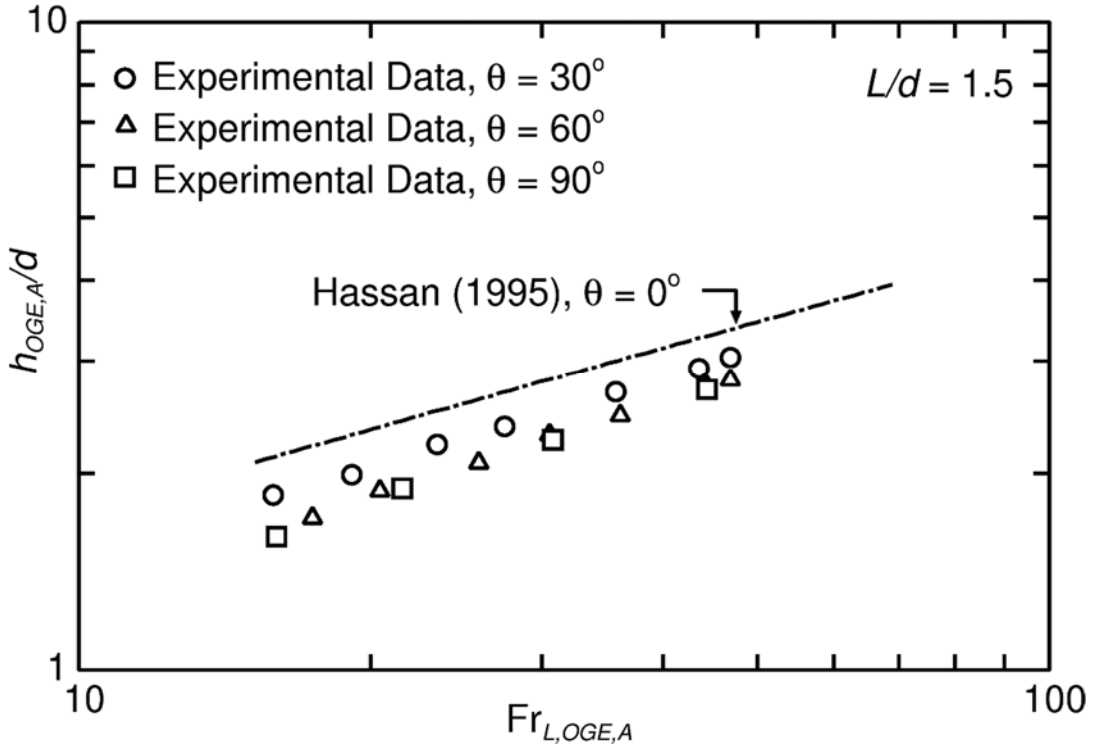

Figure 4.17 - OGE data and Hassan's (1995) correlation at Branch A for $L/d = 1.5$

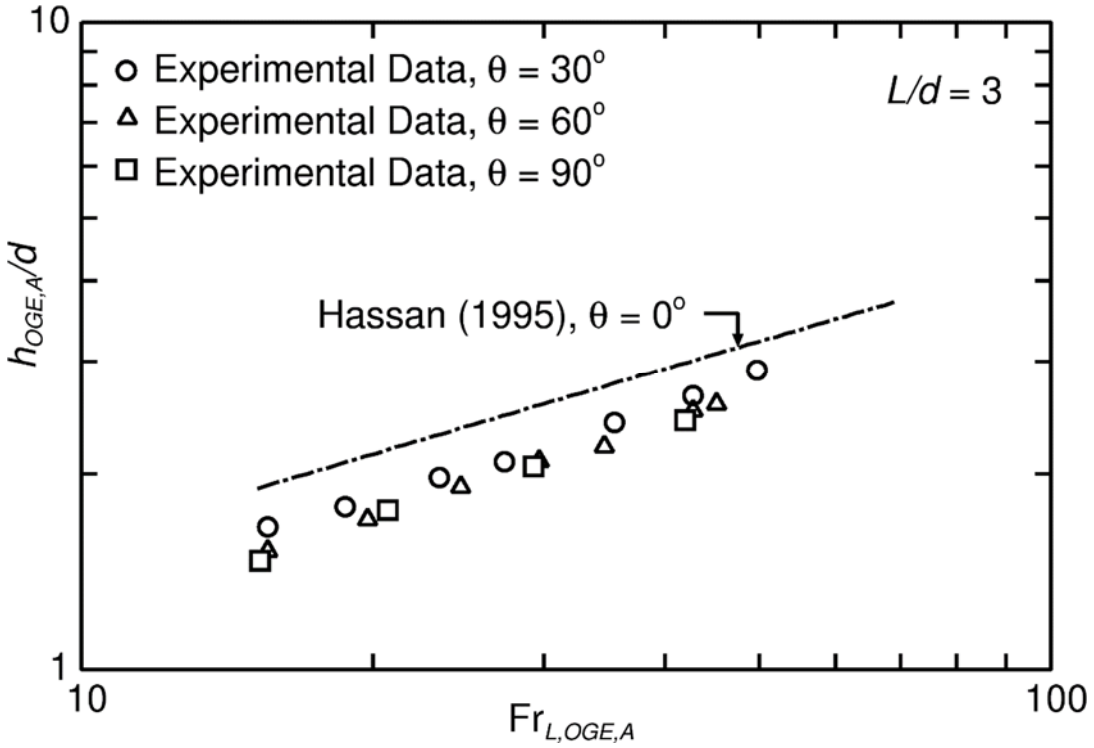

Figure 4.18 - OGE data and Hassan's (1995) correlation at Branch A for $L/d = 3$

less difference in the results for θ = 30° and 60° but still a slight increase in $h_{OGE,A}/d$ when θ drops to zero.

For the onset of gas entrainment at the bottom branch, the experimental results for $h_{OGE,B}/d$ versus $\mathrm{Fr}_{L,OGE,B}$ for θ = 30°, 60° and 90° are plotted in Figures 4.19 and 4.20 for L/d = 1.5 and 3, respectively, along with Hassan's (1995) correlation for θ = 0°. The results show that $h_{OGE,B}/d$ decreases with increasing θ. At θ = 0°, Branch A is located beside Branch B and is assisting Branch B with gas entrainment while when θ = 90°, Branch A is located directly above Branch B and is competing with Branch B for gas entrainment. Between these two limits, the upper branch provides more assistance (or less competition) to the lower branch with gas entrainment as θ decreases.

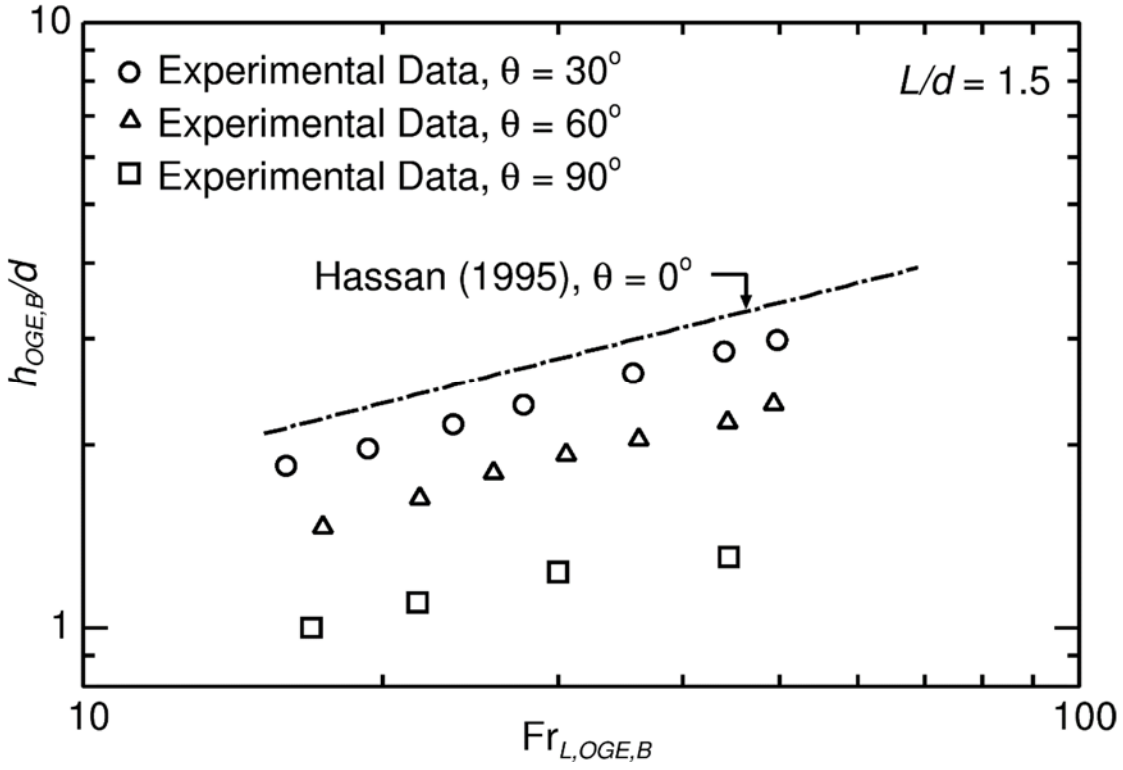

Figure 4.19 - OGE data and Hassan's (1995) correlation at Branch B for L/d = 1.5

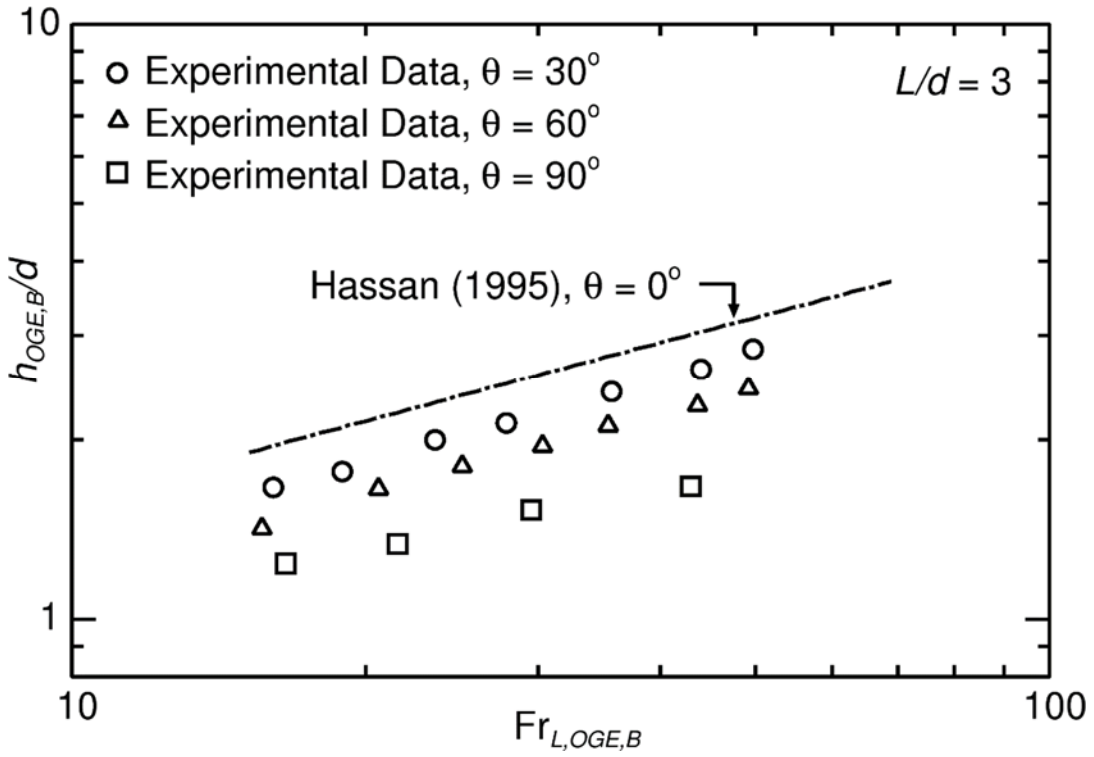

Figure 4.20 - OGE data and Hassan's (1995) correlation at Branch B for $L/d = 3$

Empirical correlations for $h_{OGE,A}/d$ and $h_{OGE,B}/d$ were developed based on the present data for $\theta = 30°$, 60° and 90° and Hassan's (1995) data for $\theta = 0°$. The correlations (Equations (4.5) to (4.9)) are valid over the ranges from $L/d = 1.5$ to 8, $\theta = 0°$ to 90° and $\mathrm{Fr}_{L,OGE,A} = \mathrm{Fr}_{L,OGE,B} = 15$ to 50.

$$h_{OGE,A}/d = 0.626\left(A_2^{0.4} + \mathrm{A}_3^{0.4}\right)\mathrm{Fr}_{L,OGE,A}^{0.4} \tag{4.5}$$

$$h_{OGE,B}/d = 0.626\mathrm{Fr}_{\mathrm{L,OGE,B}}^{B_2} \tag{4.6}$$

where,

$$A_2 = 2\exp\left[\left(-0.975\sin\theta - 0.485\right)\left(\frac{L}{d}\right)^{1.516-0.771\sin\theta}\right] \tag{4.7}$$

$$A_3 = 1 - \exp\left(-0.025\left(\frac{L}{d}\right)^2\right) \tag{4.8}$$

and,

$$B_2 = 0.4\exp\left[1.274\cos\theta\left(\frac{L}{d}\right)^{-0.895} - 1.014\left(\frac{L}{d}\right)^{-0.747}\right] \tag{4.9}$$

Equations (4.5) to (4.9) converge to the correct limits for large and small L/d. As $L/d \to \infty$, Equations (4.5) and (4.6) approach the single branch correlations of Lubin and Springer (1967) and Micaelli and Memponteil (1989) and as $L/d \to 0$, Equation (4.5) approaches the single branch correlations of Lubin and Springer and Micaelli and Memponteil with twice the Froude number. These equations show good agreement with the experimental data, as shown in Figures 4.21 and 4.22 with an RMS deviation of 4.8% for $h_{OGE,A}/d$ and 5.8% for $h_{OGE,B}/d$.

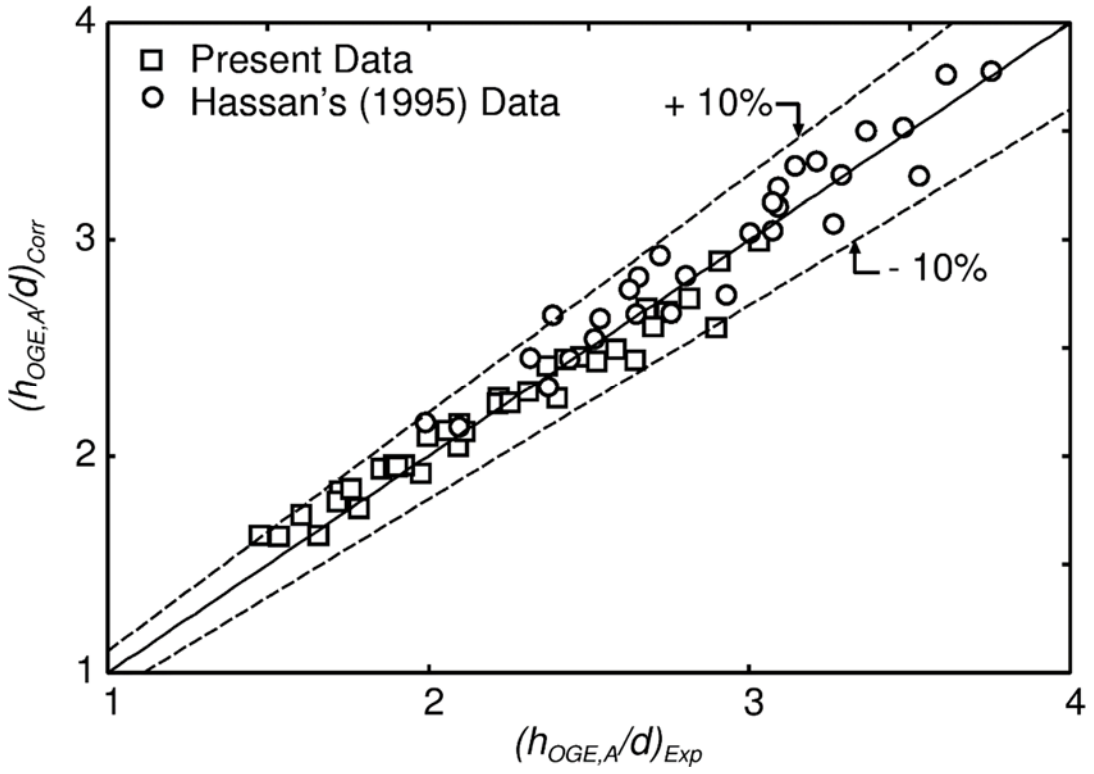

Figure 4.21 - Correlated versus measured values of $h_{OGE,A}/d$

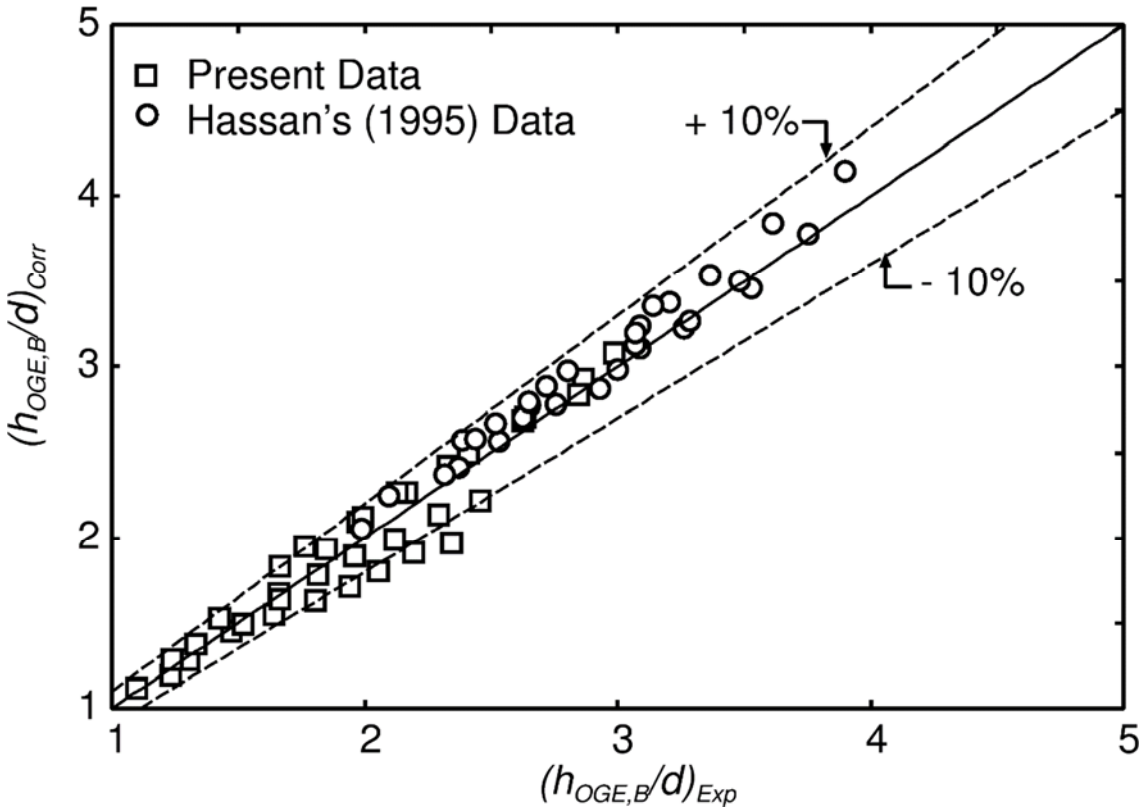

Figure 4.22 - Correlated versus measured values of $h_{OGE,B}/d$

4.3 Two-Phase Flow

4.3.1 Data Range for Two-Phase Flow

Experimental data were collected for the 16 combinations of P_0, ΔP, L/d and θ shown in Table 4.1. For each of these combinations, flow rate, temperature, pressure and interface height measurements were taken at approximately 25 interface heights located between $h_{OLE,B}$ and $h_{OGE,A}$. This resulted in approximately 400 data points, not including the additional cases for comparison purposes as will be discussed in the following section.

Table 4.1 - Experimental matrix for two-phase flow

Case #	θ	L/d	P_0 (kPa)	ΔP (kPa)
1	30°	1.5	316	40
2				123
3			517	97
4				235
5		3	316	40
6				123
7			517	97
8				235
9	60°	1.5	316	40
10				123
11			517	97
12				235
13		3	316	40
14				123
15			517	97
16				235

4.3.2 Comparison of Two-Phase Flow Results with Previous Experimental Data

As was done for the onset of liquid and gas entrainment data, preliminary experiments were run to collect two-phase flow data for a geometry that was previously tested by Hassan (1995) to validate the procedure and ensure the apparatus was producing accurate results. For this purpose, experimental results were obtained outside the range of conditions shown in Table 4.1 for L/d = 1.5 and θ = 0°. For this geometry, data were collected for the lowest P_0 and ΔP combination from Hassan's work (P_0 = 316 kPa and ΔP = 40 kPa) and the highest P_0 and ΔP (P_0 = 517 kPa and ΔP = 235 kPa). Since the branch resistance, R, in this study did not match exactly any of

the branch resistances in Hassan's study, results for the dimensionless mass flow rate M and quality x versus H were compared with Hassan's correlations for $\theta = 0°$, where M and H are defined by Equations (2.5) and (2.6), respectively, and the correlations for $M(H)$ and $x(H)$ are defined by Equations (2.7) and (2.8). Hassan showed that the effects of R are negligible when the results are plotted this way.

Figures 4.23 and 4.24 show the experimental data for M versus H and x versus H, respectively for dual branches with $L/d = 1.5$ and $\theta = 0°$, along with Hassan's (1995) correlation for this geometry. When the branches are located side by side as is the case here, the results should be identical for Branches A and B as can be observed in the figures. These plots also show that the effects of P_0 and ΔP are absorbed when plotted this way and that the experimental data is in excellent agreement with Hassan's correlations. It was therefore concluded that the apparatus was producing accurate results and the correct procedure was being used.

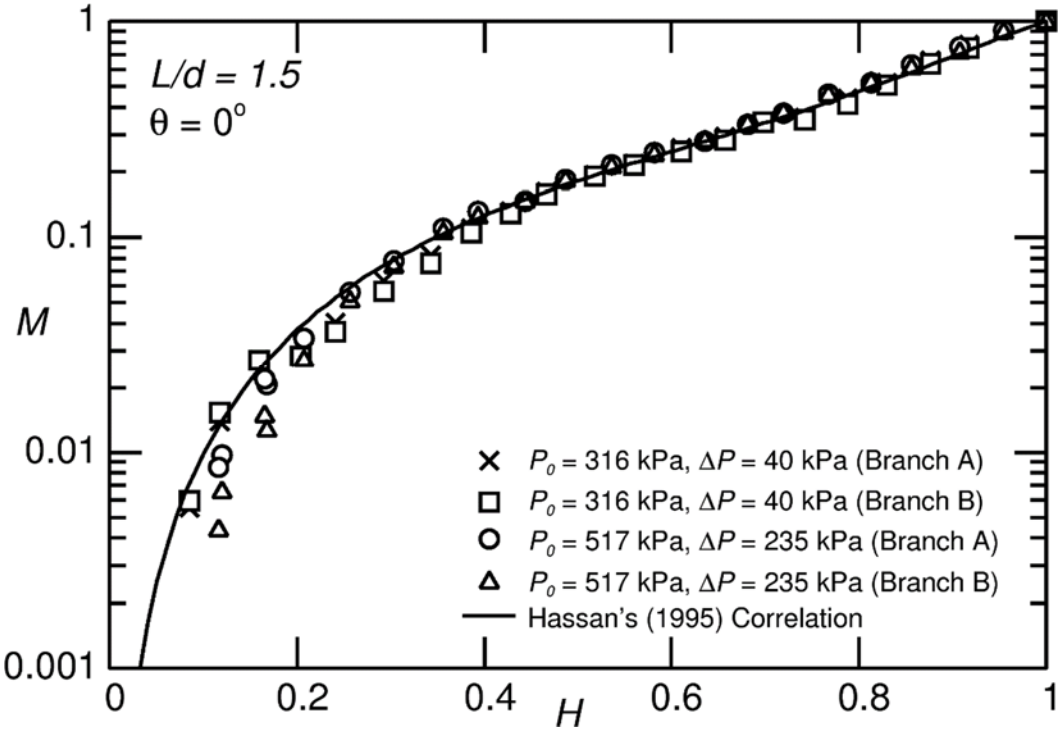

Figure 4.23 - Comparison of results for M versus H with Hassan (1995) for $\theta = 0°$

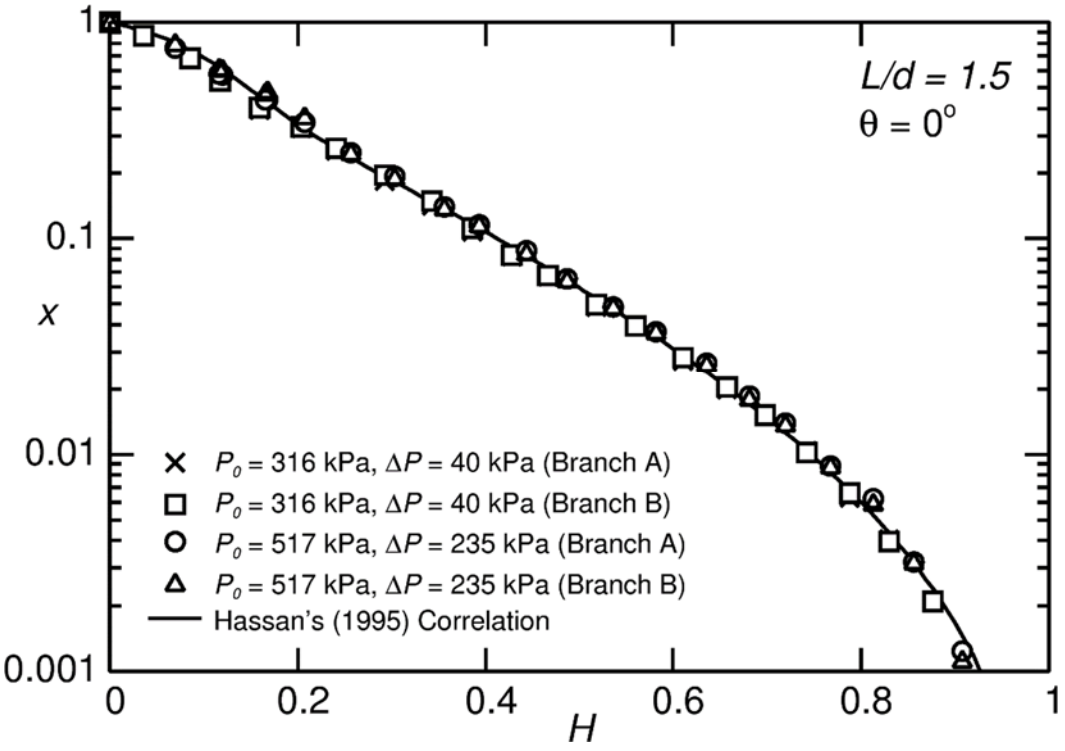

Figure 4.24 - Comparison of results for x versus H with Hassan (1995) for $\theta = 0°$

4.3.3 Two-Phase Flow Results and Correlations

The following Sections 4.3.3.1 to 4.3.3.5 include results that show the variation in the two-phase mass flow rate and quality as the interface height varies from $h_{OLE,B}$ to $h_{OGE,A}$. A single case is first discussed to show these trends for Branches A and B together in one graph (Section 4.3.3.1). Following this, the effect of certain parameters on the results will be analyzed by plotting multiple cases together, including the effects of P_0 and ΔP (Section 4.3.3.2), the effect of L/d (Section 4.3.3.3) and the effect of θ (Section 4.3.3.4). Section 4.3.3.5 presents the correlations developed from the experimental results for the dimensionless parameters M_A, M_B, x_A and x_B. The data for all 16 cases are included in Appendix C.

4.3.3.1 *Two-Phase Flow Results for Case 1*

Results for $\dot{m}_{TP}$ versus h_A for Branches A and B are plotted in Figure 4.25 for Case 1 where $P_0 = 316$ kPa, $\Delta P = 40$ kPa, $L/d = 1.5$ and $\theta = 30°$. The data points corresponding to the onsets of liquid and gas entrainment are indicated by filled in black squares for Branch A and filled

in black circles for Branch B. Starting at the right end of the plot, as h_A decreases, the onset of gas entrainment occurs first at the upper branch followed by a decrease in $\dot{m}_{TP,A}$ with decreasing h_A as more and more gas is entrained into Branch A. The onset of gas entrainment at the lower branch occurs within approximately a 5 mm drop in the interface height following the OGE at Branch A. As h_A decreases further, $\dot{m}_{TP}$ decreases in both branches but is always higher at Branch B because more liquid is flowing through that branch. Near the left hand side of the plot, as h_A decreases, the onset of liquid entrainment height is reached for the upper branch first; a further decrease in h_A results in single phase air flowing through Branch A. Finally, the onset of liquid entrainment height is reached for the lower branch and single phase air flows through both branches. Although the shape of the $\dot{m}_{TP}$ versus h_A curves will change from one case to another, the overall trends discussed here apply to all cases tested in this study.

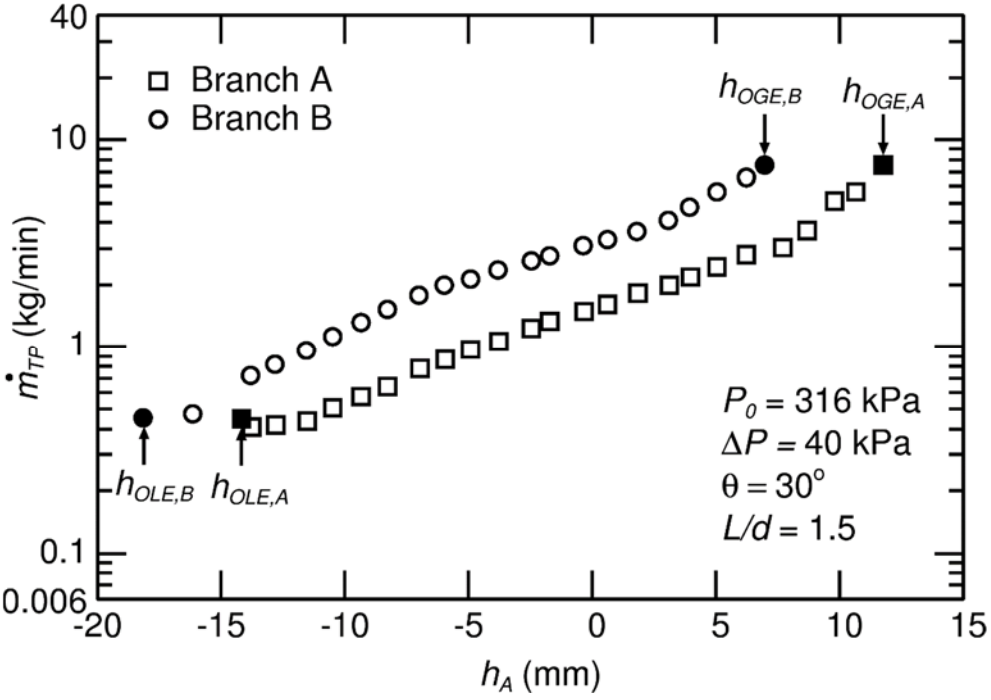

Figure 4.25 - $\dot{m}_{TP}$ versus h_A for Case 1

Figure 4.26 shows results for x versus h_A for Branches A and B for this same case (Case 1). This plot shows that for the same interface height, h_A, the quality in Branch A is always higher than the quality in Branch B. This trend is also consistent for all the cases tested in this study because Branch A is always located above Branch B and ΔP is equal for both branches.

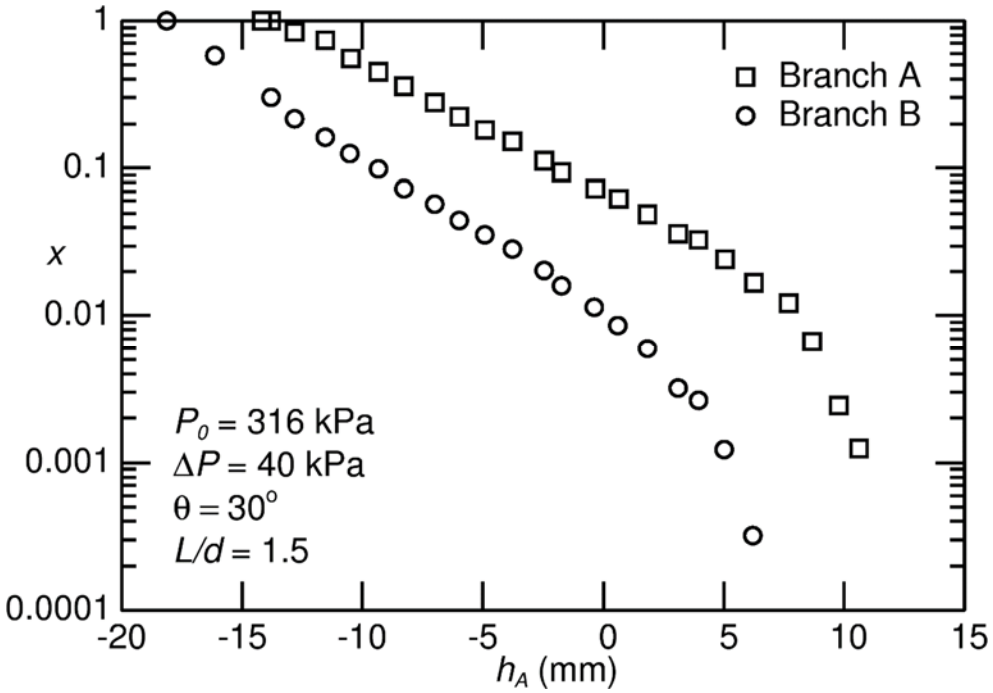

Figure 4.26 - x versus h_A for Case 1

4.3.3.2 Effect of ΔP and P_0 on Two-Phase Flow Results

Figures 4.27 to 4.30 show the effect of ΔP on $\dot{m}_{TP}$ and x versus h at Branches A and B using the results from Case 1 (ΔP = 40 kPa) and Case 2 (ΔP =123 kPa), where P_0 = 316 kPa, L/d =1.5 and θ = 30° in both cases. The first and last data points in each of the curves represent the onset of liquid and gas entrainment results, respectively. In all four figures, the data points extend further along the *x*-axis in both directions as ΔP increases since $|h_{OLE,A}|$, $|h_{OLE,B}|$, $h_{OGE,A}$ and $h_{OGE,B}$ increase with increasing ΔP. From Figures 4.27 and 4.28 it can be observed that in general, the mass flow rate increases with increasing ΔP.

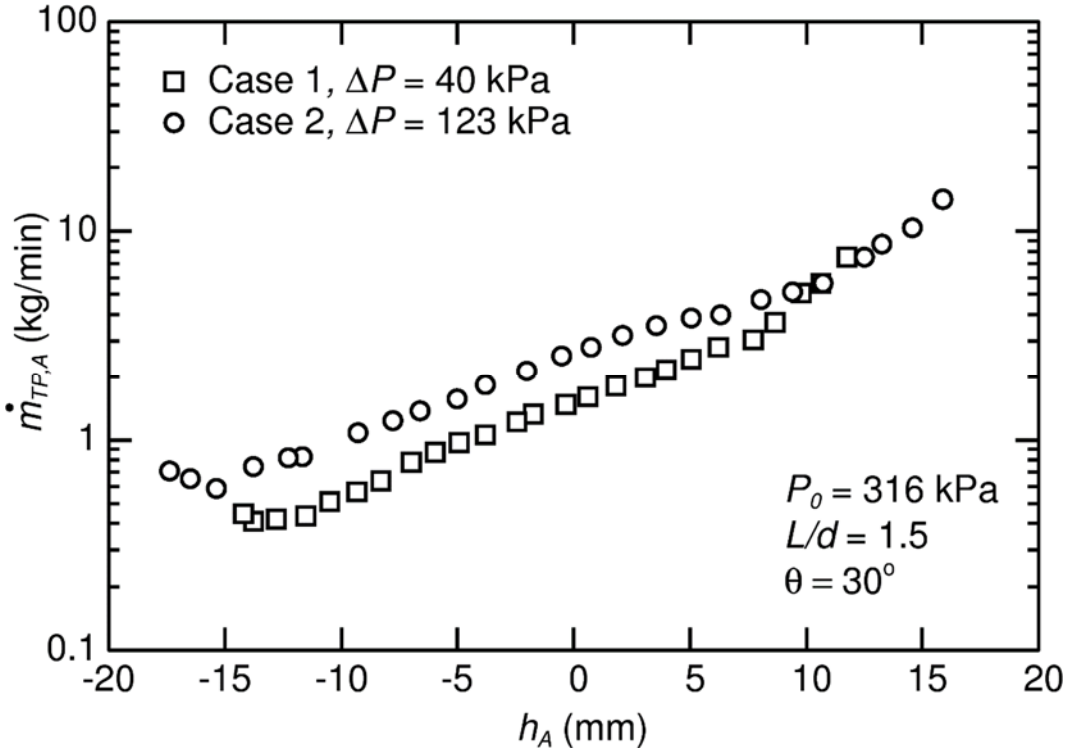

Figure 4.27 - Experimental results for $\dot{m}_{TP,A}$ versus h_A for Cases 1 and 2

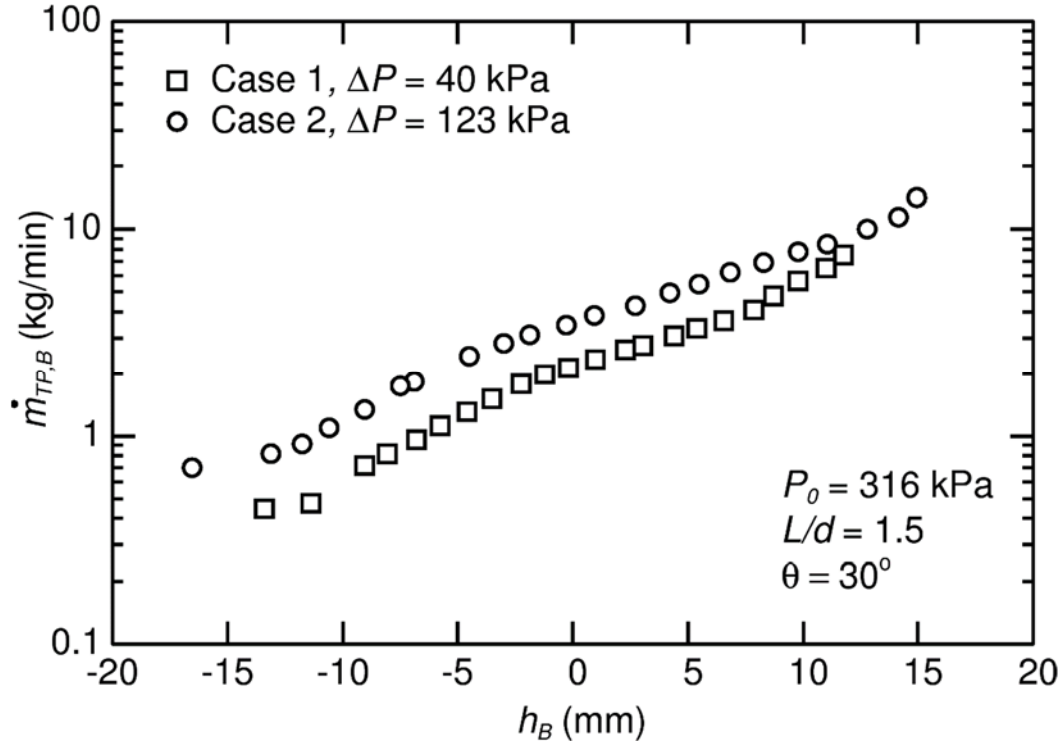

Figure 4.28 - Experimental results for $\dot{m}_{TP,B}$ versus h_B for Cases 1 and 2

The results for $x_A(h_A)$ and $x_B(h_B)$ for Cases 1 and 2, as shown in Figures 4.29 and 4.30 cross; x_A and x_B decrease with increasing ΔP at low interface heights but increase with increasing ΔP at high interface heights. The results cross due to the magnitudes of the onset heights. To explain this clearly, a simplified schematic of x versus h is shown in Figure 4.31. At low values of h ($h < h_{OLE}$), the flow through the branch is single phase gas for both Cases 1 and 2 and x = 1. As h increases past h_{OLE}, the quality x starts to decrease as liquid enters the branch; the start occurs at a lower h (or higher $|h|$) for Case 2 than for Case 1 due to the higher ΔP. As h increases further, x continues to decrease for both Cases 1 and 2 until the OGE. For $h > h_{OGE}$, single phase liquid flows through the branch and $x = 0$. The OGE occurs first (at lower h) for Case 1 due to the lower ΔP, and in order to satisfy the condition of $x = 0$ at h_{OGE}, the data for Case 1 must cross the data for Case 2.

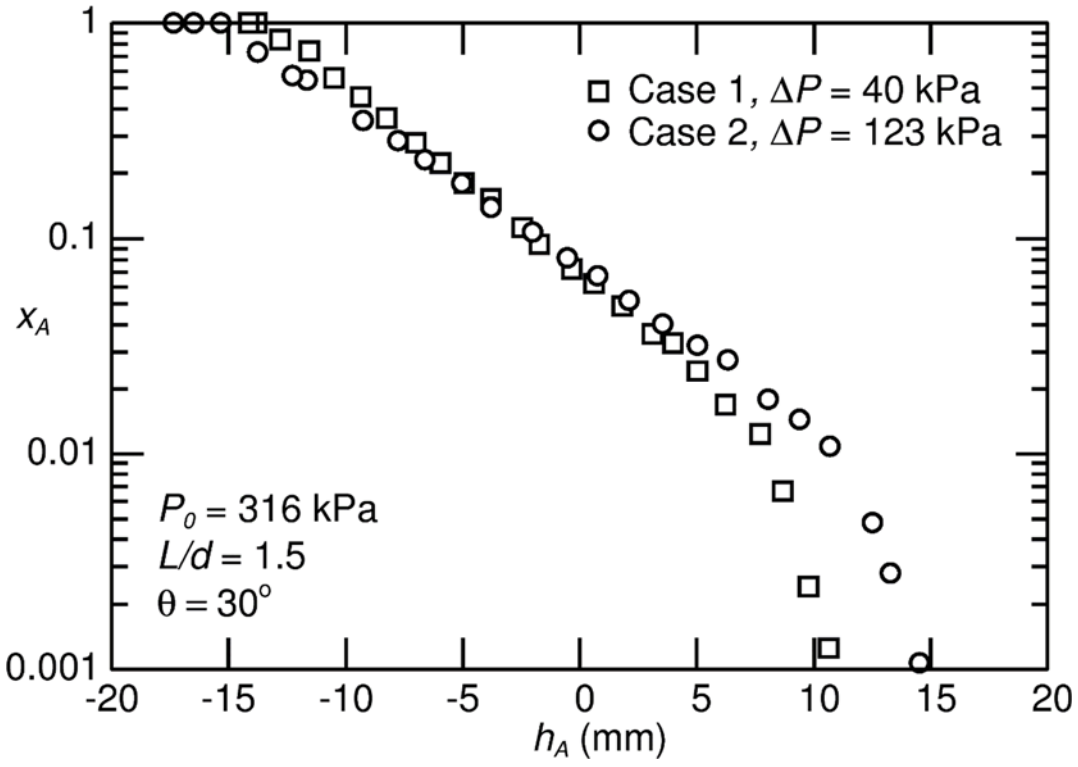

Figure 4.29 - Experimental results for x_A versus h_A for Cases 1 and 2

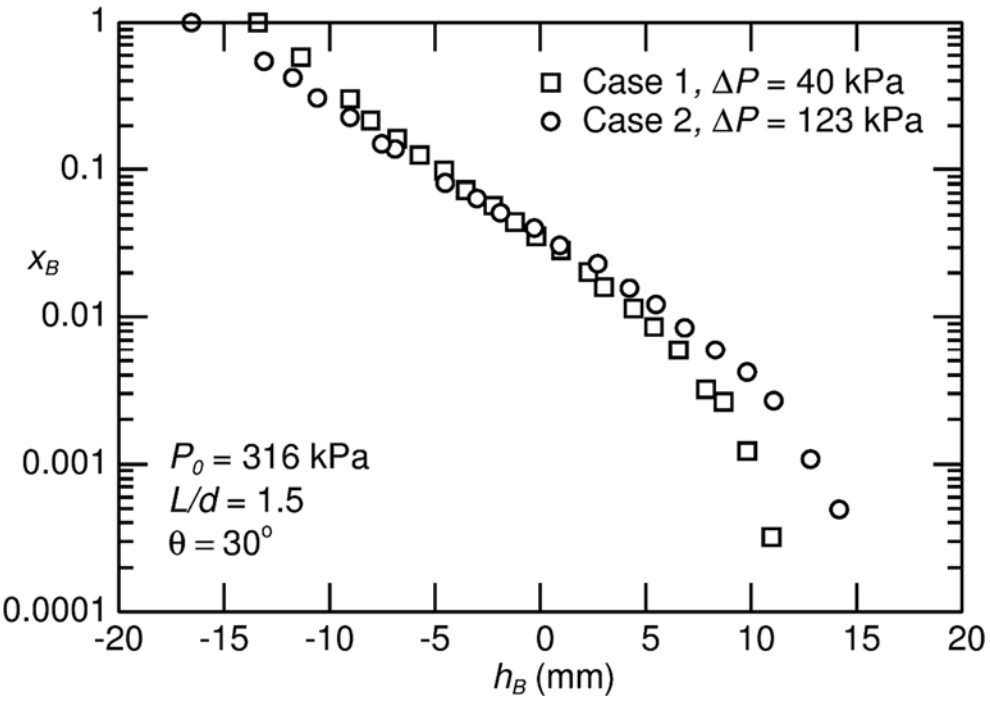

Figure 4.30 - Experimental results for x_B versus h_B for Cases 1 and 2

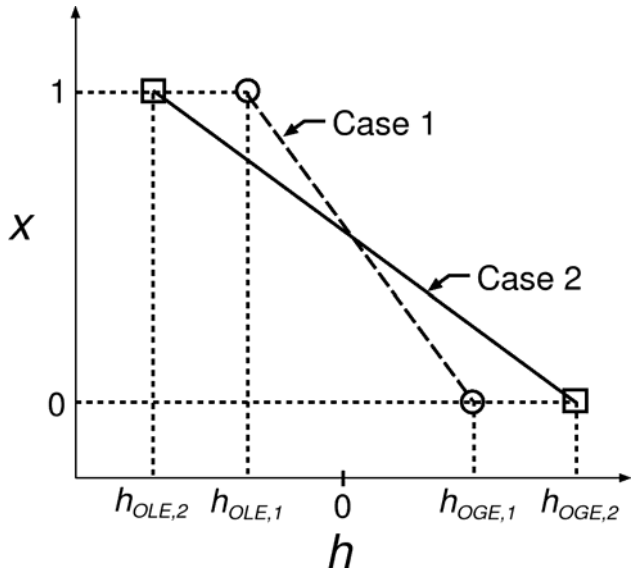

Figure 4.31 – Schematic of crossing x versus h curves for Cases 1 and 2

When the results for Cases 1 and 2 are plotted using the dimensionless variables M, x and H, Figures 4.32 to 4.35 show that the effect of ΔP is absorbed for $\theta = 30°$ and $L/d = 1.5$. This same observation was found to be true for the other three geometries tested ($\theta = 30°$ and $L/d = 3$; $\theta = 60°$ and $L/d = 1.5$; $\theta = 60°$ and $L/d = 3$).

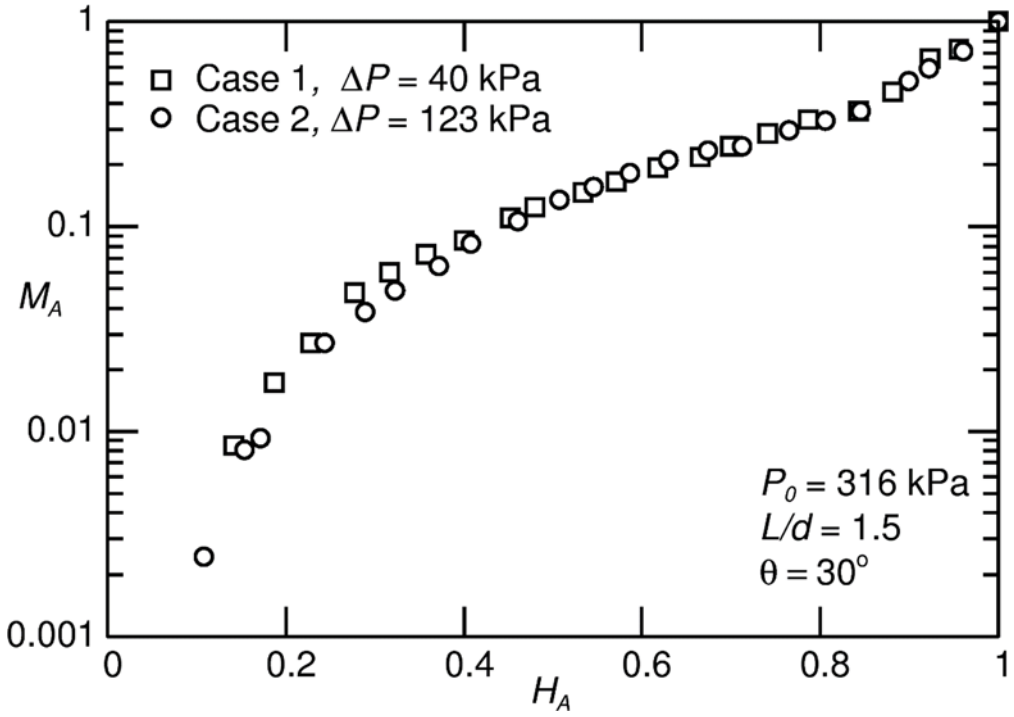

Figure 4.32 - Experimental results for M_A versus H_A for Cases 1 and 2

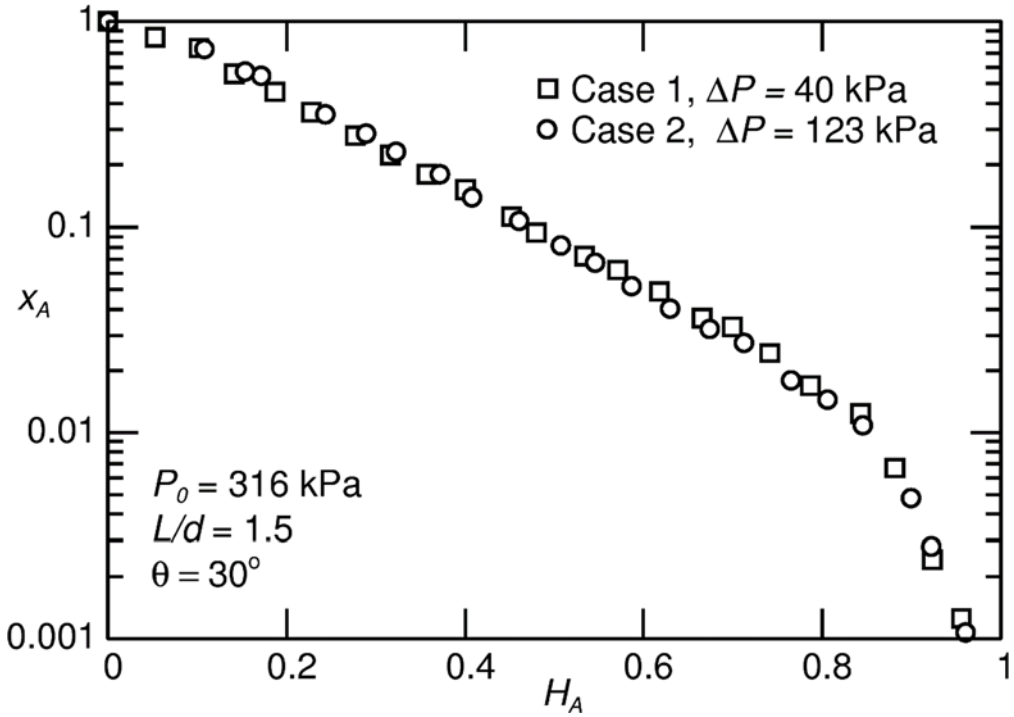

Figure 4.33 - Experimental results for x_A versus H_A for Cases 1 and 2

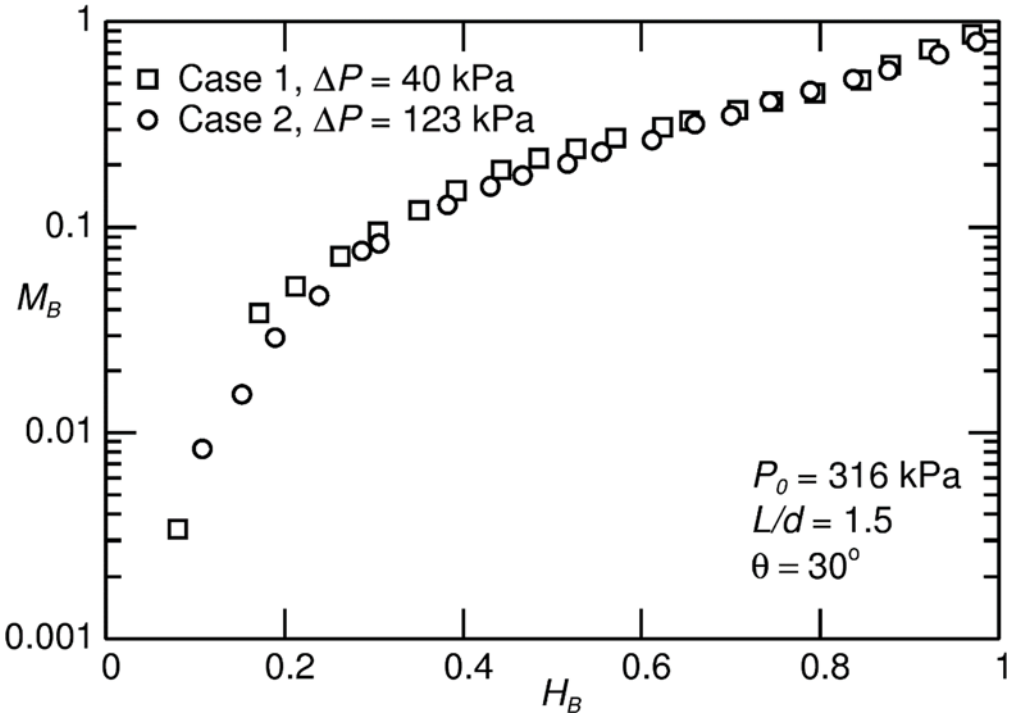

Figure 4.34 - Experimental results for M_B versus H_B for Cases 1 and 2

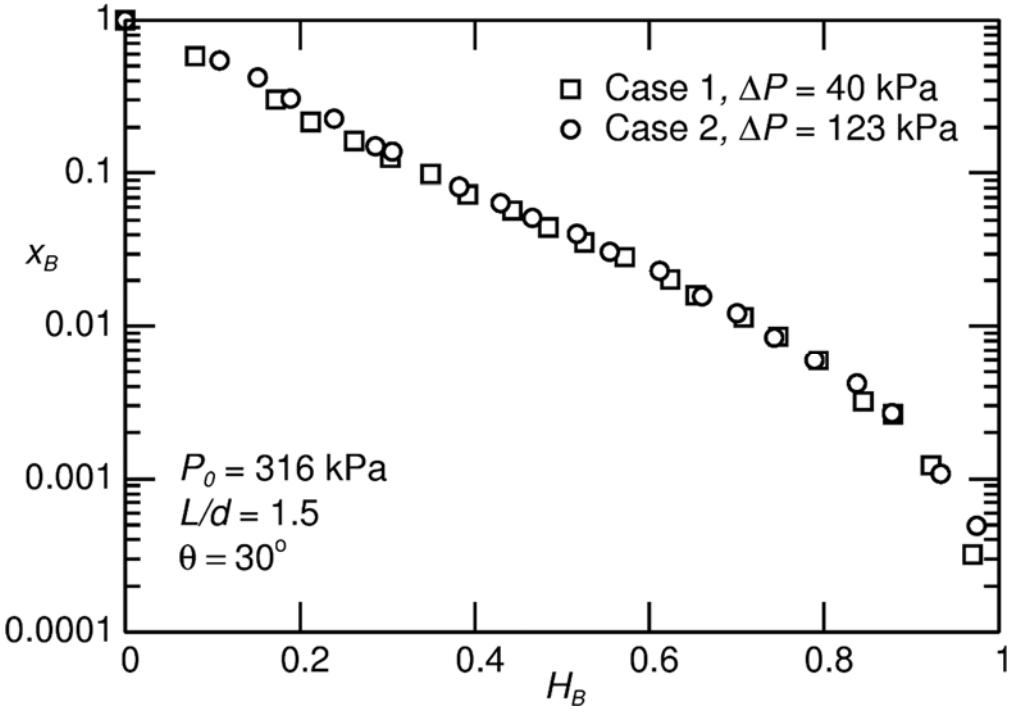

Figure 4.35 - Experimental results for x_B versus H_B for Cases 1 and 2

Dimensionless results for M and x versus H for Cases 1 to 4, which are for the same geometry ($\theta = 30°$ and $L/d = 1.5$) but various combinations of P_0 and ΔP, are plotted in Figures 4.36 to 4.39. In Cases 1 and 2, P_0 = 316 kPa and in Cases 3 and 4, P_0 = 517 kPa. Since it was already proven that the results collapse onto one curve for the same P_0 and various ΔP values, the results shown in the following figures use the same symbol for Cases 1 and 2 (open square) and for Cases 3 and 4 (open circle) to show whether the effect of P_0 is also absorbed when the results are plotted in terms of the dimensionless variables M, x and H.

In Figures 4.36 and 4.38, the effect of P_0 on the mass flow rate results appears to be absorbed when plotted as M versus H for both Branches A and B. However, for the quality at Branch A, x_A, as shown in Figure 4.37, the results for P_0 = 316 kPa are consistently lower than the results for P_0 = 517 kPa. This difference was also observed by Hassan (1995) and was accounted for by including the density ratio, ρ_L / ρ_G, in his correlations for x. Figure 4.39 shows that the results for x_B are again slightly lower for P_0 = 316 kPa. This difference, however, is minimal. These same observations were also true for the other three branch geometries.

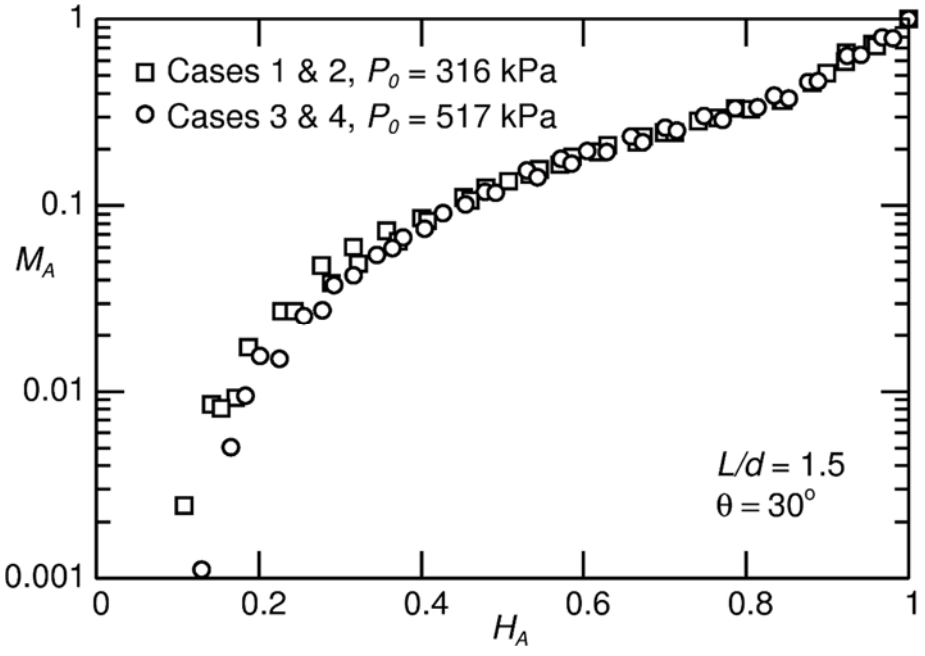

Figure 4.36 - Experimental results for M_A versus H_A for Cases 1 to 4

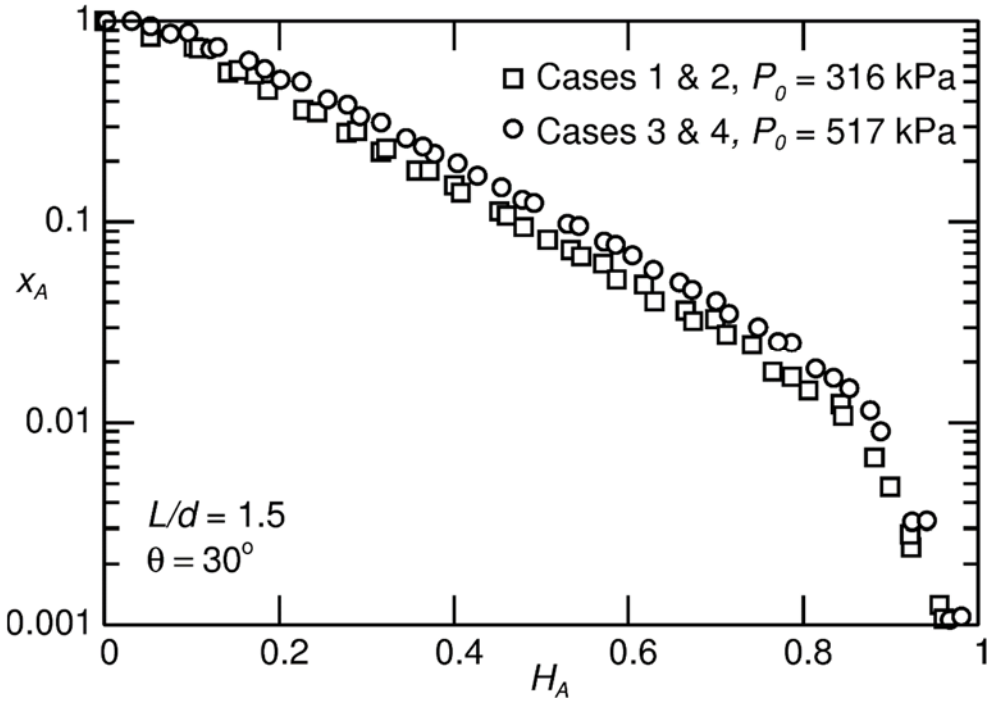

Figure 4.37 - Experimental results for x_A versus H_A for Cases 1 to 4

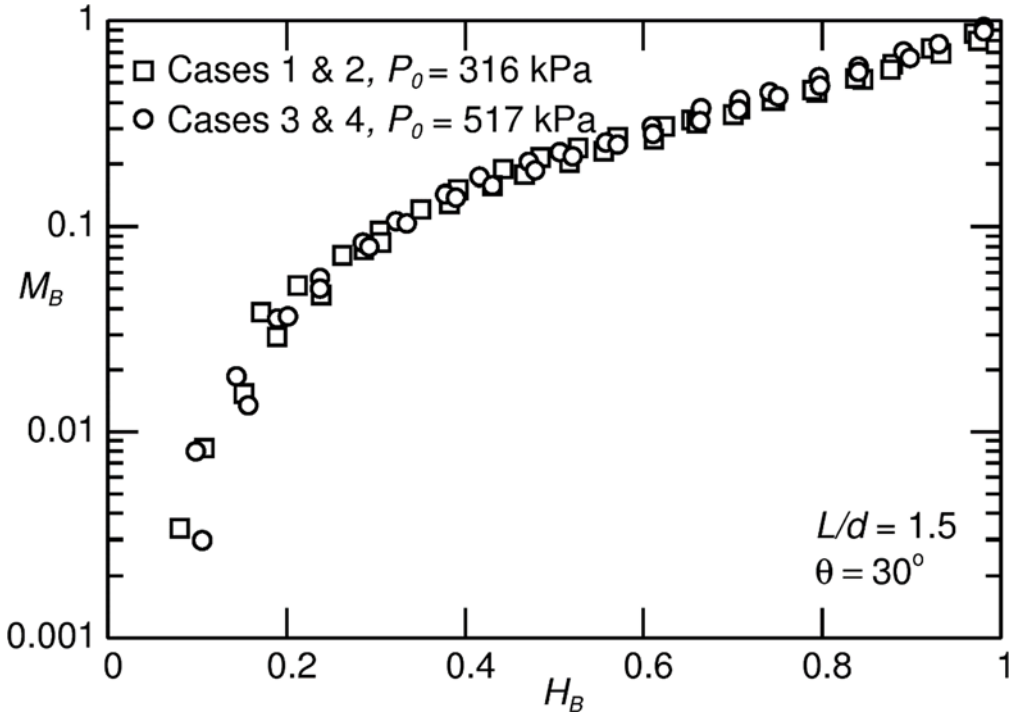

Figure 4.38 - Experimental results for M_B versus H_B for Cases 1 to 4

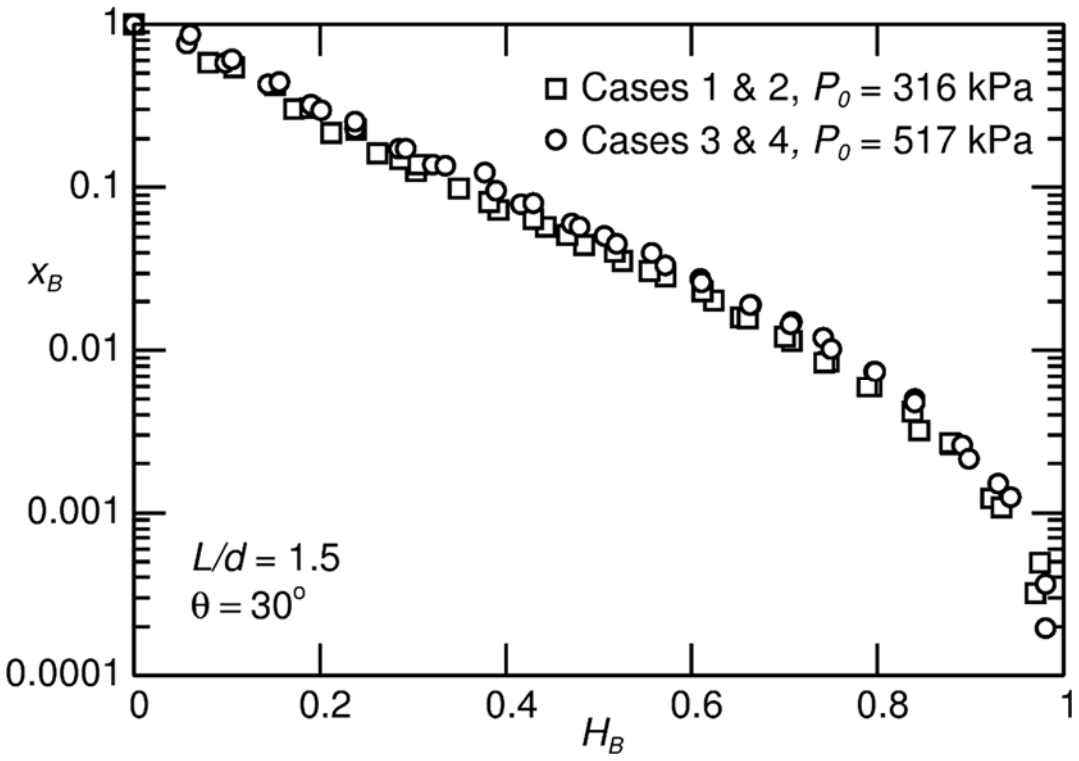

Figure 4.39 - Experimental results for x_B versus H_B for Cases 1 to 4

4.3.3.3 Effect of L/d on Two-Phase Flow Results

Previous studies showed that for discharging two-phase flow through two branches with θ = 0° and 90°, the branches became more independent and had less influence on one another as L/d increased. Such trend was examined in this study for θ = 30° and 60° by analyzing results of $\dot{m}_{TP}$ versus h at Branches A and B together on one plot and results for x versus h at Branches A and B together on one plot. When the branches are behaving as two independent branches, the results for $\dot{m}_{TP,A}$ (and x_A) versus h_A fall on top of the results for $\dot{m}_{TP,B}$ (and x_B) versus h_B, while when the branches are influencing one another the results of $\dot{m}_{TP}$ (and x) versus h at Branch A will differ from those at Branch B.

For L/d = 1.5, the results for $\dot{m}_{TP}$ and x versus h from all 8 cases tested in this study showed that the branches have less influence on one another as ΔP and θ decreased. Sample results for L/d = 1.5 of the two extreme cases with the highest ΔP and θ (Case 12) and the lowest ΔP and θ (Case 1) are plotted in Figures 4.40 to 4.43. Note that for the remainder of this chapter,

$\dot{m}_{TP}$ and x on the vertical axis represent $\dot{m}_{TP,A}$ and x_A, respectively, for the Branch A results and $\dot{m}_{TP,B}$ and x_B, respectively, for the Branch B results. Similarly, the interface height h on the horizontal axis represents h_A for the Branch A results and h_B for the Branch B results. Figure 4.40 shows that for L/d = 1.5 and the case with the highest ΔP and θ (Case 12), there is a large deviation between the $\dot{m}_{TP}$ results at Branches A and B; the $\dot{m}_{TP,B}$ results are significantly higher than the $\dot{m}_{TP,A}$ results. Similarly, there is a large deviation between the results for x versus h at Branches A and B, as shown in Figure 4.41. These observations indicate that the branches are highly dependent on one another for Case 12.

Figures 4.42 and 4.43 show results for $\dot{m}_{TP}$ and x versus h, respectively, for the case with the lowest ΔP and θ (Case 1) for L/d = 1.5. These plots show that there is still some deviation between the results at Branches A and B; however, the differences are much less than they were for Case 12. Therefore, for L/d = 1.5, the branches are influenced by one another for all cases tested in this study.

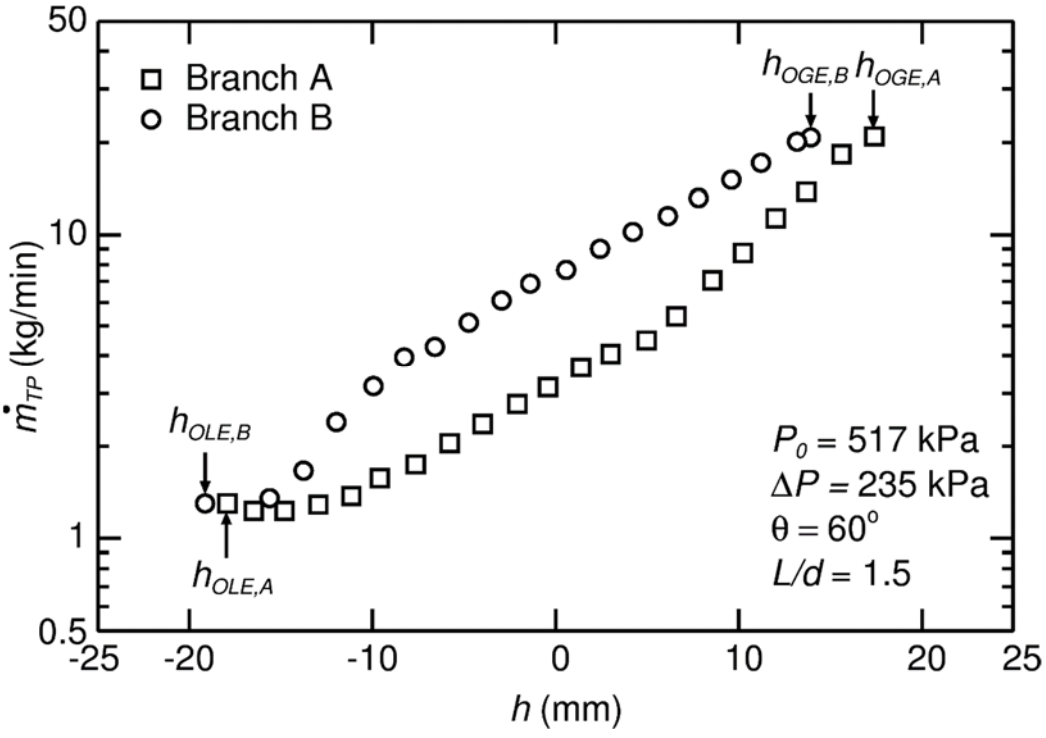

Figure 4.40 - $\dot{m}_{TP}$ versus h at Branches A and B for Case 12

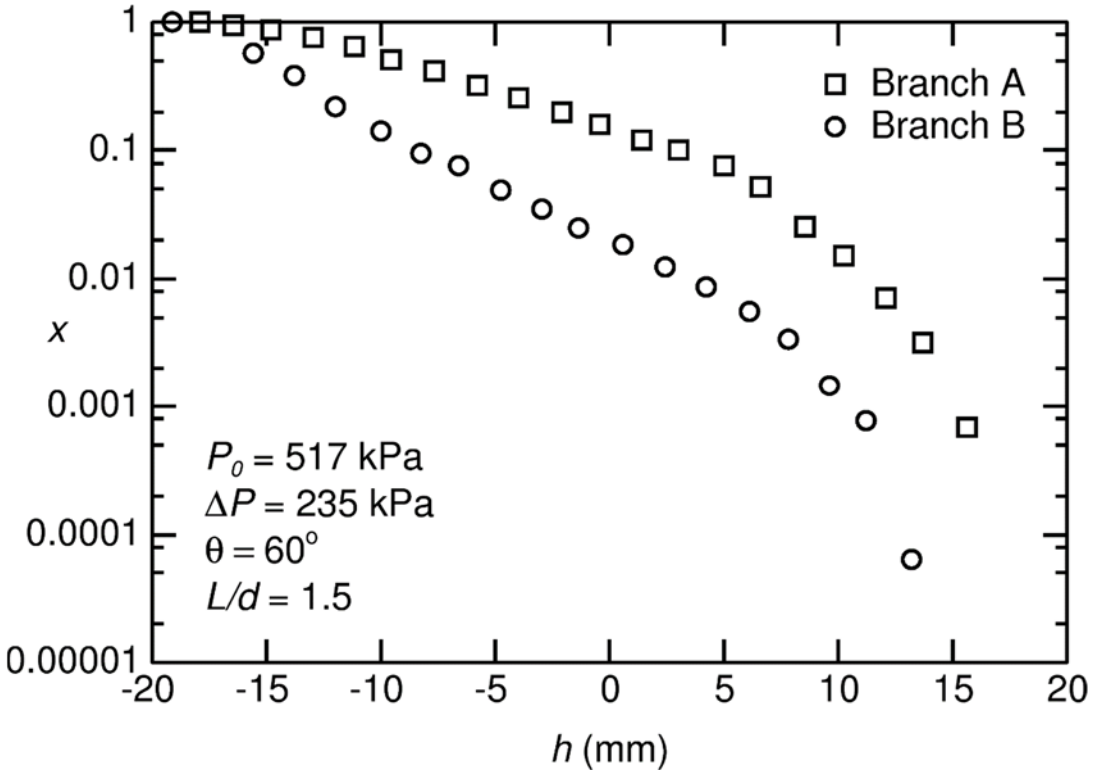

Figure 4.41 - x versus h at Branches A and B for Case 12

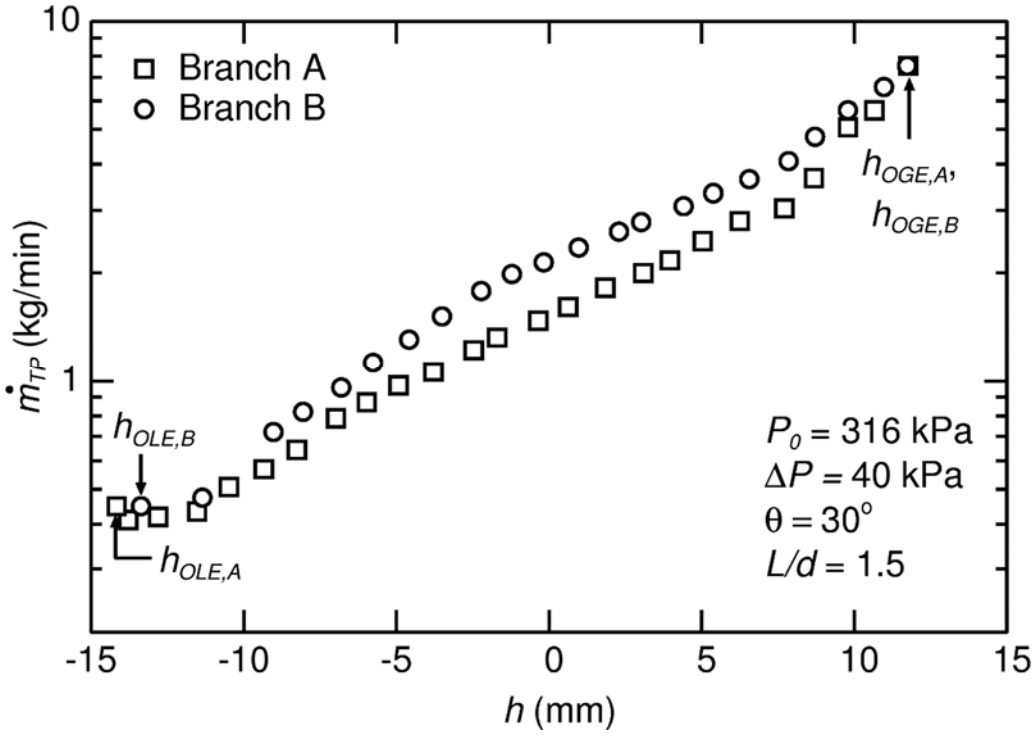

Figure 4.42 - $\dot{m}_{TP}$ versus h at Branches A and B for Case 1

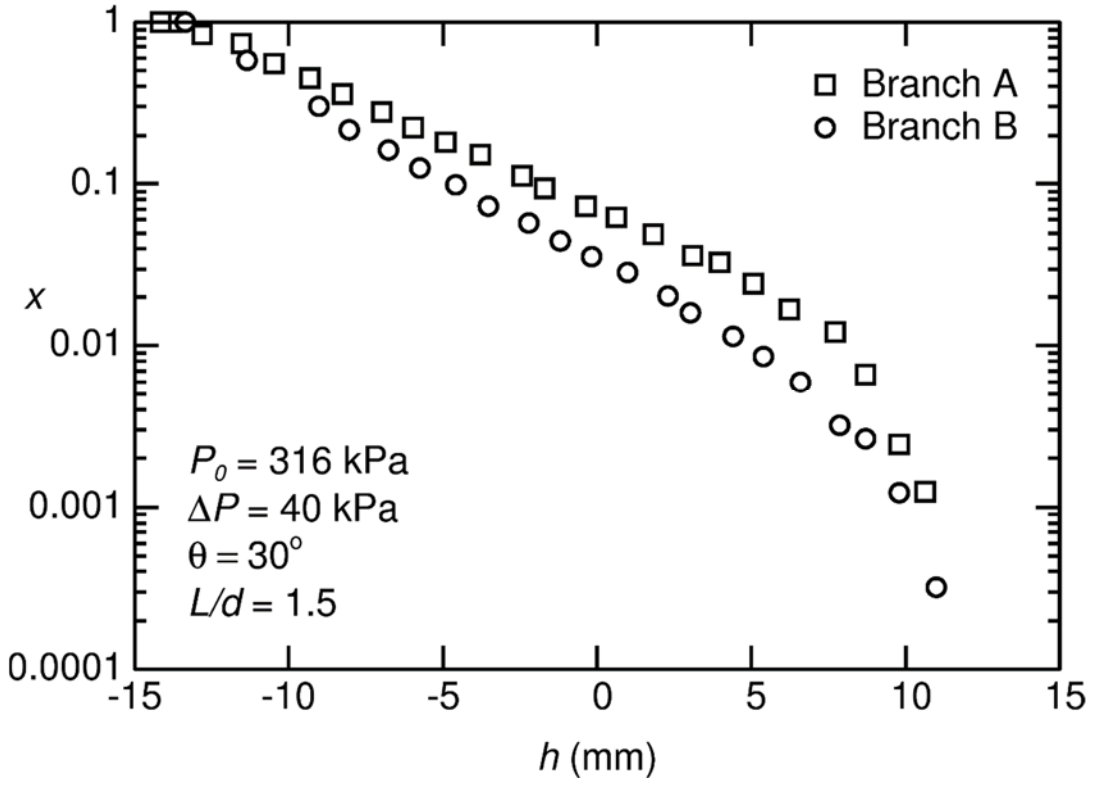

Figure 4.43 - x versus h at Branches A and B for Case 1

The effect of L/d on these results is observed by plotting results for L/d = 3 for the same values of P_0, ΔP and θ used in Figures 4.40 to 4.43. The $\dot{m}_{TP}$ and x versus h results for Case 16 for L/d = 3, P_0 = 517 kPa, ΔP = 235 kPa and θ = 60° are plotted in Figures 4.44 and 4.45, respectively. By comparing these results to those for Case 12 shown in Figures 4.40 and 4.41 where L/d = 1.5, it is observed that there is less deviation between the results at Branches A and B for L/d = 3 and thus the branches do influence each other but to a lesser degree than Case 12. For L/d = 3 and as ΔP and θ decreased, the branches became practically independent of one another; this is observed in the results for Case 5 shown in Figures 4.46 and 4.47. In these figures, the results for Branch A are very close to the results for Branch B indicating the branches have very little influence on one another.

It is concluded from the above results that the influence of L/d on $\dot{m}_{TP}$ and x at Branches A and B is dependent on ΔP and θ, with this effect decreasing as ΔP and θ decrease.

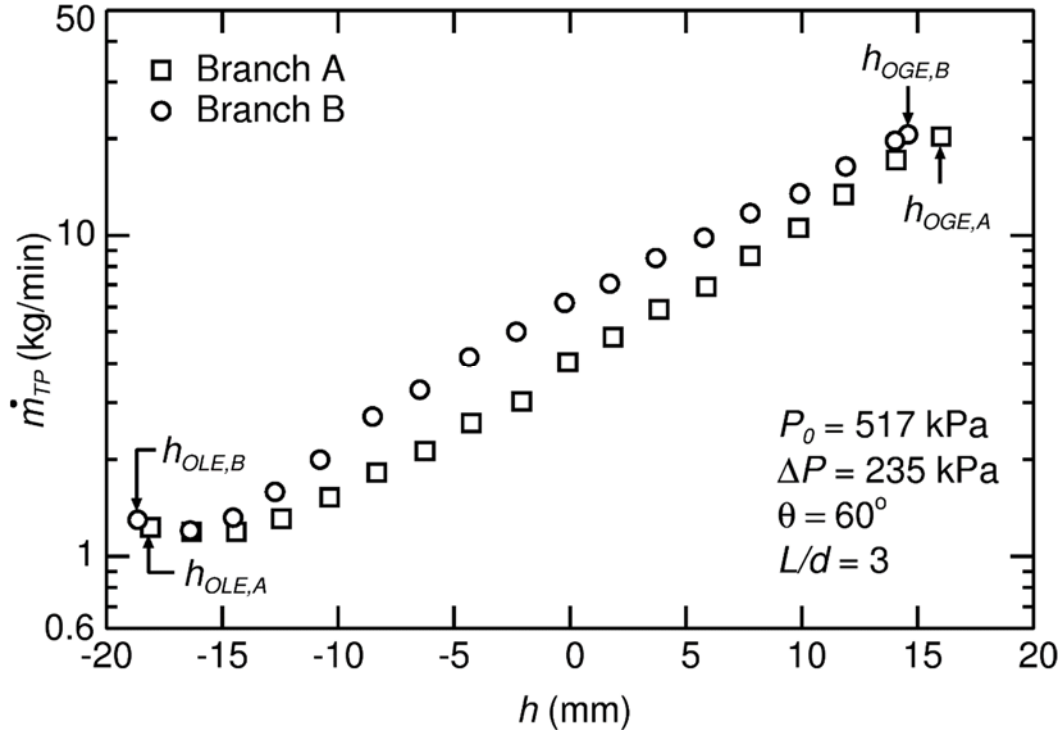

Figure 4.44 - $\dot{m}_{TP}$ versus h at Branches A and B for Case 16

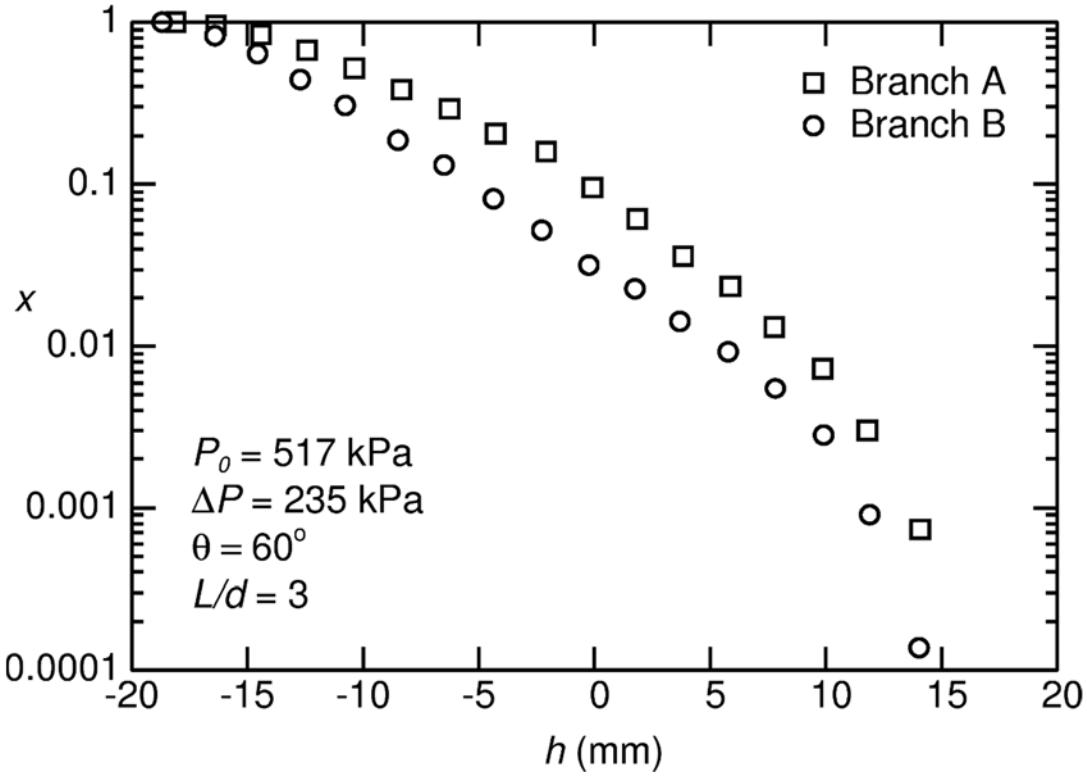

Figure 4.45 - x versus h at Branches A and B for Case 16

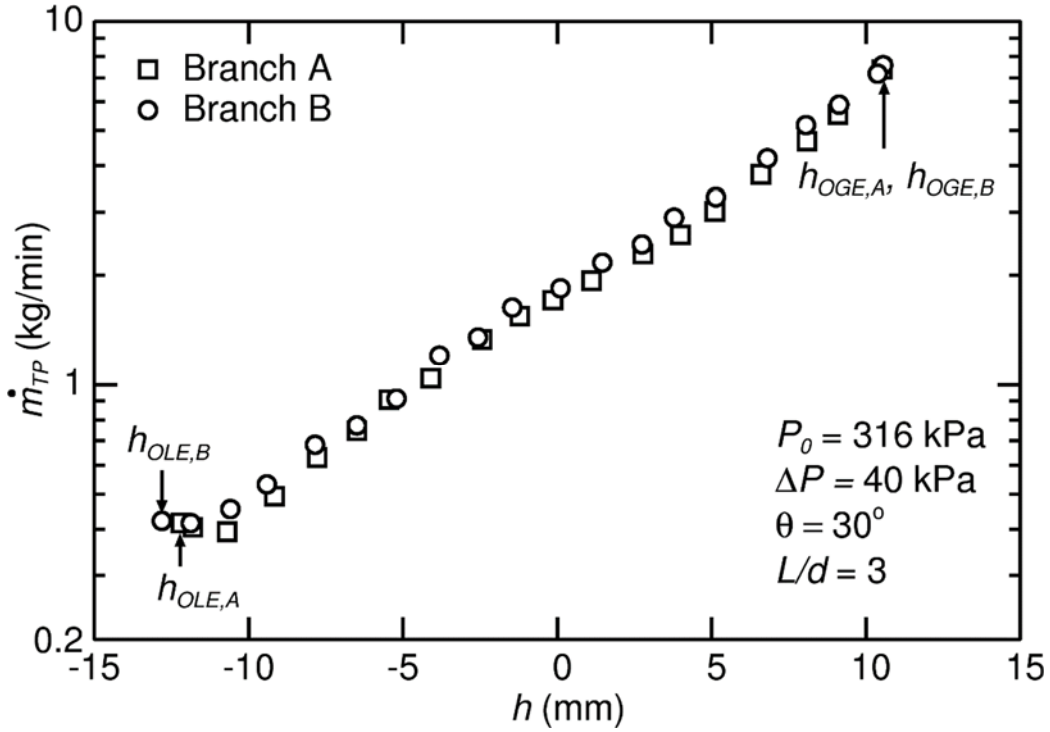

Figure 4.46 - $\dot{m}_{TP}$ versus h at Branches A and B for Case 5

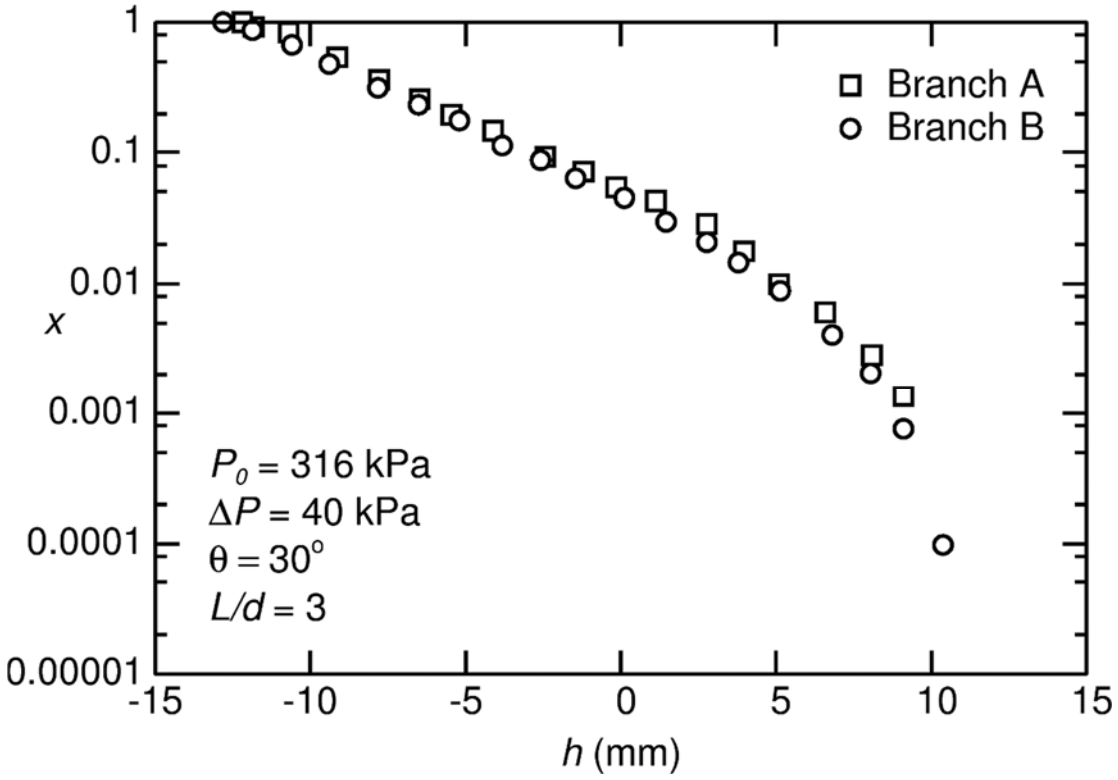

Figure 4.47 - x versus h at Branches A and B for Case 5

4.3.3.4 Effect of θ on the Two-Phase Flow Results

In the previous section (Section 4.3.3.3), the results showed that the branches become more independent of one another with increasing L/d and decreasing ΔP and θ. In order to examine more closely the effect of θ on the results, experimental results are now plotted for one combination of P_0, ΔP and L/d for θ = 30° (Figures 4.48 and 4.49) and 60° (Figures 4.50 and 4.51), along with results from Hassan's (1995) correlation for θ = 90°.

As was previously discussed in Section 2.4.1, Hassan (1995) developed correlations for M_A, M_B, x_A and x_B. During the course of the present study, it was determined that there was a large deviation between Hassan's experimental data and his correlation for M_A. After consulting with the author on this matter, it was concluded that there was likely a typographical error in the coefficients presented in his thesis and journal publications. A new correlation was therefore fit to Hassan's data for M_A. This new correlation, shown below in Equations (4.10) to (4.12), will be used in all the plots in this thesis to represent Hassan's mass flow data at Branch A for θ = 90° instead of Equations (2.11) and (2.15).

$$M_A = H_A^{(2+A_4)} \exp\left[-1.84 H_A^{\,2}\left(1 - H_A^{\,2}\right)^{A_5}\right] \tag{4.10}$$

where,

$$A_4 = \exp\left(-1.662\left(\frac{L}{d}\right) + 2.584\right) \tag{4.11}$$

and,

$$A_5 = 1.318 + 1.9\left(\frac{L}{d}\right)^{-2.066} \tag{4.12}$$

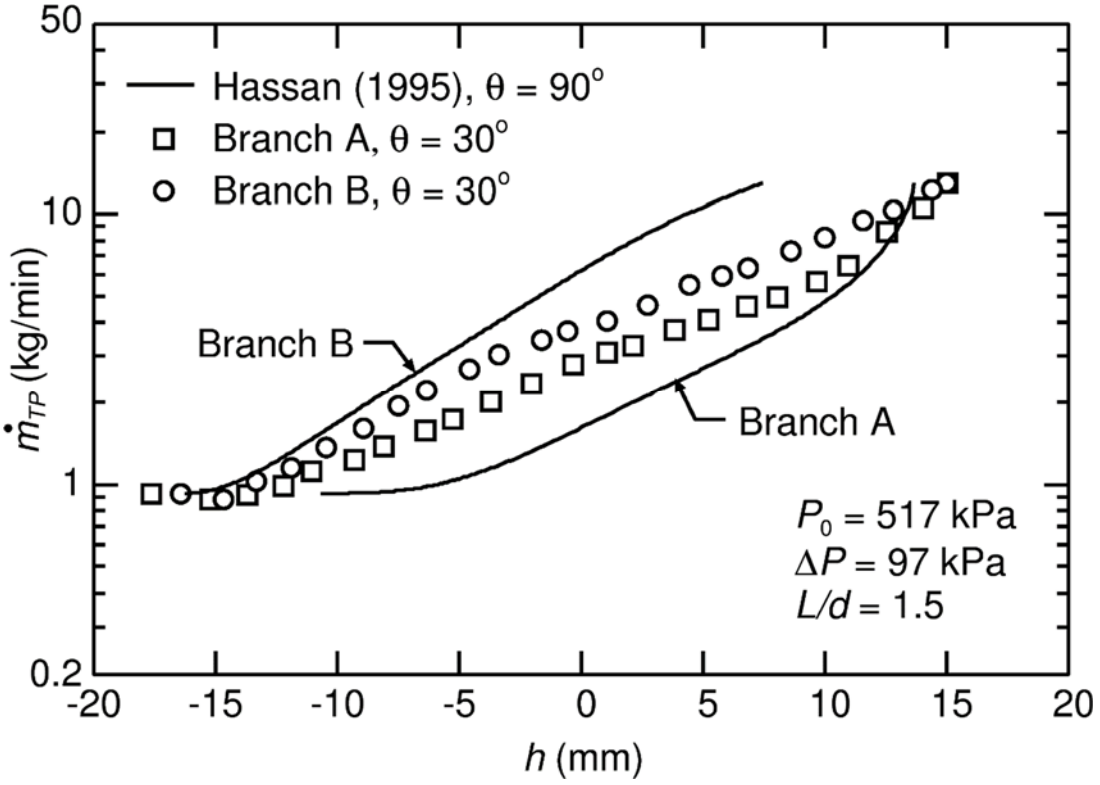

Figure 4.48 - $\dot{m}_{TP}$ versus h at Branches A and B for Case 3

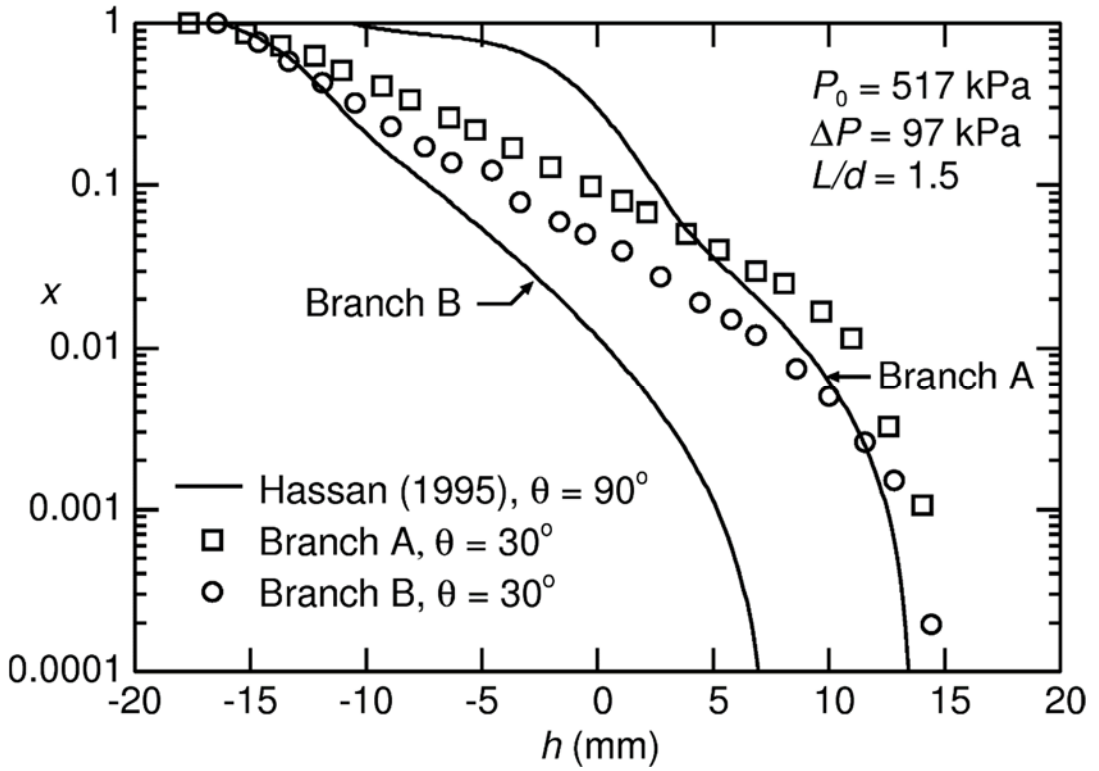

Figure 4.49 - x versus h at Branches A and B for Case 3

Figures 4.48 and 4.49 show experimental results for $\dot{m}_{TP}$ versus h and x versus h, respectively, at Branches A and B for P_0 = 517 kPa, ΔP = 97 kPa, L/d = 1.5 and θ = 30° (Case 3) along with Hassan's (1995) correlations for θ = 90°. To extract $\dot{m}_{TP}$ and h from the dimensionless quantities M and H in Hassan's correlations, Equations (2.5) and (2.6) were used with $h_{OLE,A}$, $h_{OLE,B}$, $h_{OGE,A}$ and $h_{OGE,B}$ calculated using Hassan's onset height correlations and $\dot{m}_{G,OLE,A}$, $\dot{m}_{G,OLE,B}$, $\dot{m}_{L,OGE,A}$ and $\dot{m}_{L,OGE,B}$ taken from the present data. Figures 4.50 and 4.51 clearly show how the branches have more influence on one another with increasing θ; i.e. the deviation between the results at Branches A and B increases with increasing θ. For the same combination of P_0, ΔP and L/d, Figures 4.50 and 4.51 show $\dot{m}_{TP}$ versus h and x versus h results for θ = 60° (Case 11), along with Hassan's correlations for θ = 90°. The results at Branches A and B for θ = 60° show more deviation from one another than was observed for θ = 30°, but less deviation than the results for θ = 90°.

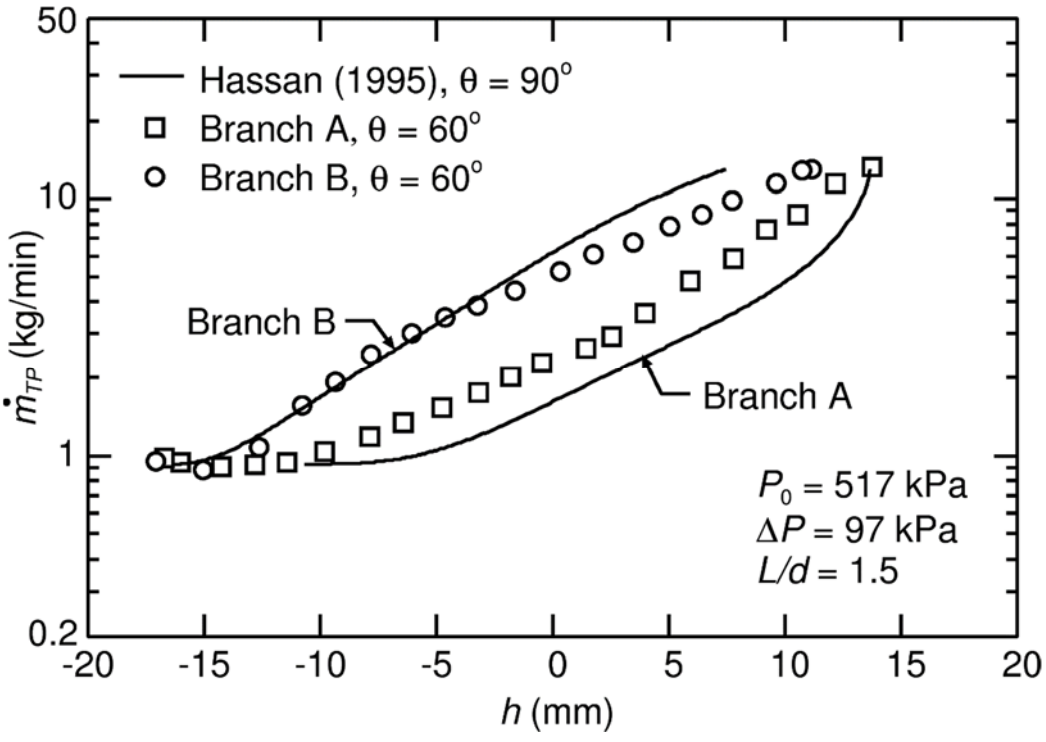

Figure 4.50 - $\dot{m}_{TP}$ versus h at Branches A and B for Case 11

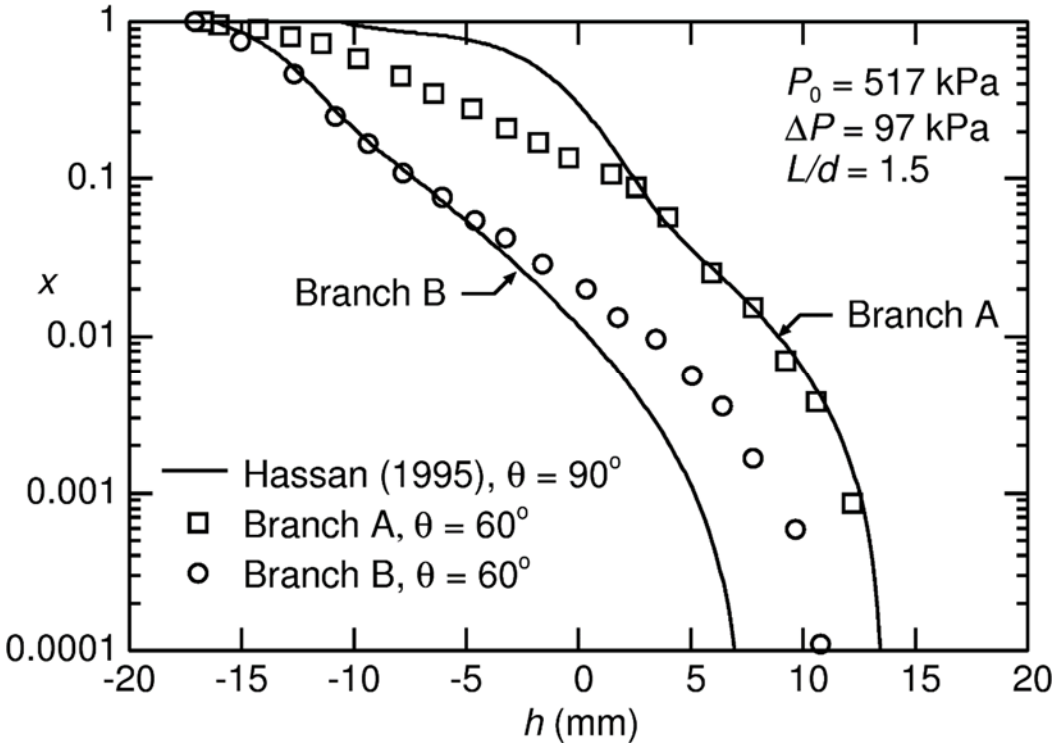

Figure 4.51 - x versus h at Branches A and B for Case 11

The effect of θ can also be observed by plotting the experimental results at Branch A for $\theta = 30°$ and 60° together on one plot, along with Hassan's (1995) correlation for $\theta = 90°$. Figures 4.52 and 4.53 show results for $\dot{m}_{TP,A}$ versus h_A and x_A versus h_A, respectively for Cases 4 and 12 with $P_0 = 517$ kPa, $\Delta P = 235$ kPa, and $L/d = 1.5$. The results in these figures show that at low values of h_A, $\dot{m}_{TP,A}$ decreases and x_A increases with increasing θ. This trend occurs due to $|h_{OLE,A}|$ increasing with decreasing θ and thus more liquid enters the branch at lower θ. However, in both $\dot{m}_{TP,A}$ and x_A plots, as h_A increases, the curves cross right before the onset of gas entrainment height. This crossing is not visible between the $\theta = 30°$ data and the $\theta = 90°$ curve in Figure 4.53 since it occurs at $x_A = 0$, which is not possible to plot on a logarithmic scale. The crossing curves in these figures can be explained more clearly using the schematics shown in Figures 4.54 and 4.55. The three sets of results plotted in Figures 4.52 and 4.53 have the same limits for $\dot{m}_{TP,A}$ and x_A at the onsets of liquid and gas entrainment. In addition, the magnitudes of the OLE and OGE interface heights increase with decreasing θ. To satisfy both these conditions, the results are forced to cross as shown in Figures 4.54 and 4.55.

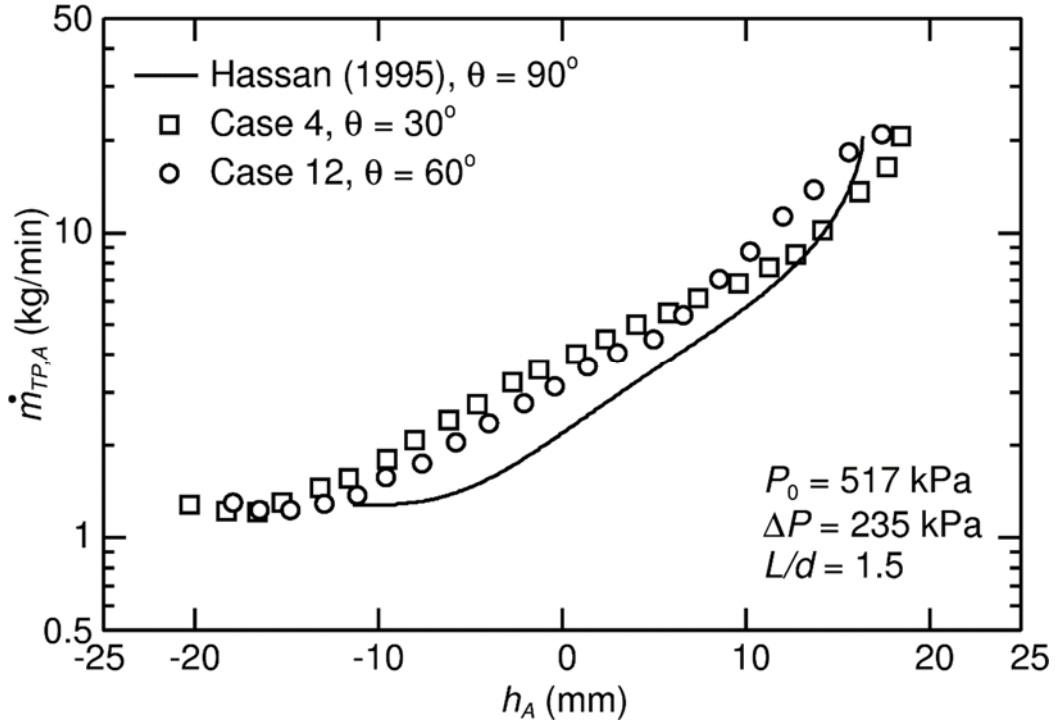

Figure 4.52 - $\dot{m}_{TP,A}$ versus h_A for θ = 30°, 60° and 90°

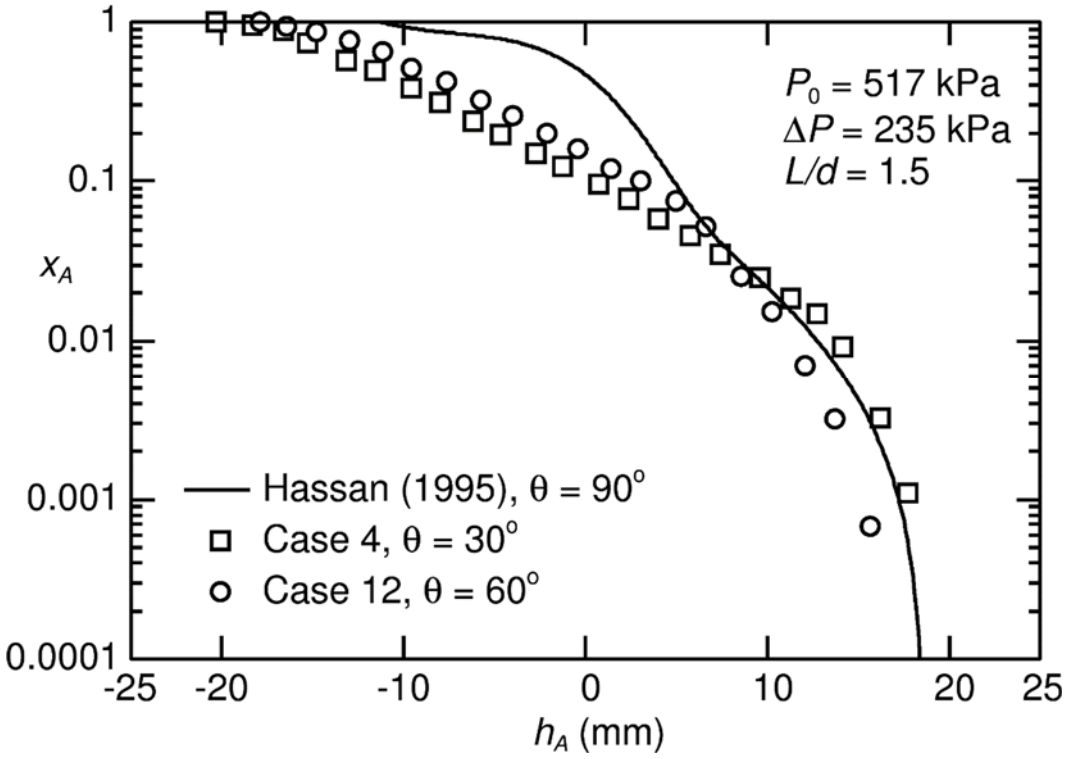

Figure 4.53 - x_A versus h_A for θ = 30°, 60° and 90°

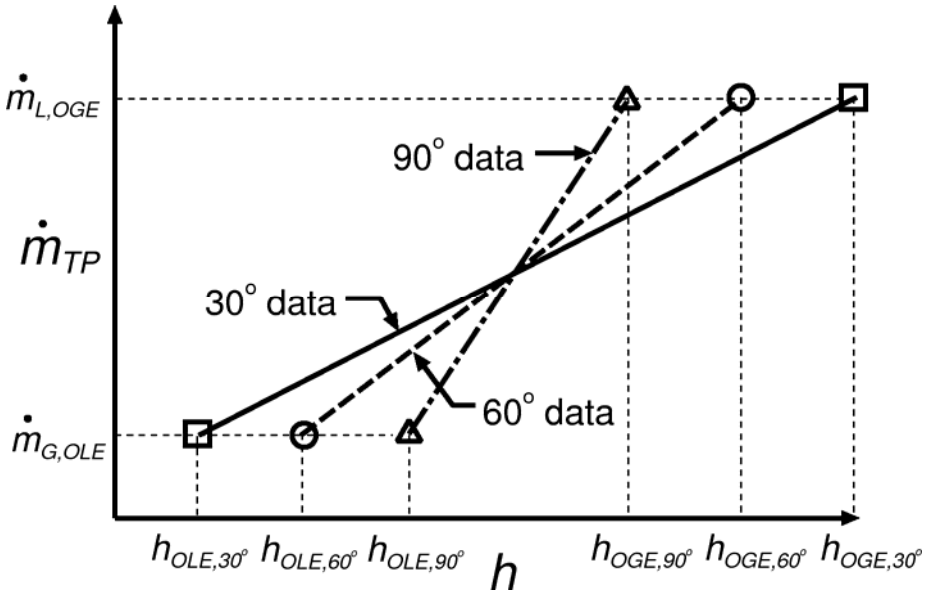

Figure 4.54 - Schematic of $\dot{m}_{TP}$ versus h at Branch A for θ = 30°, 60° and 90°

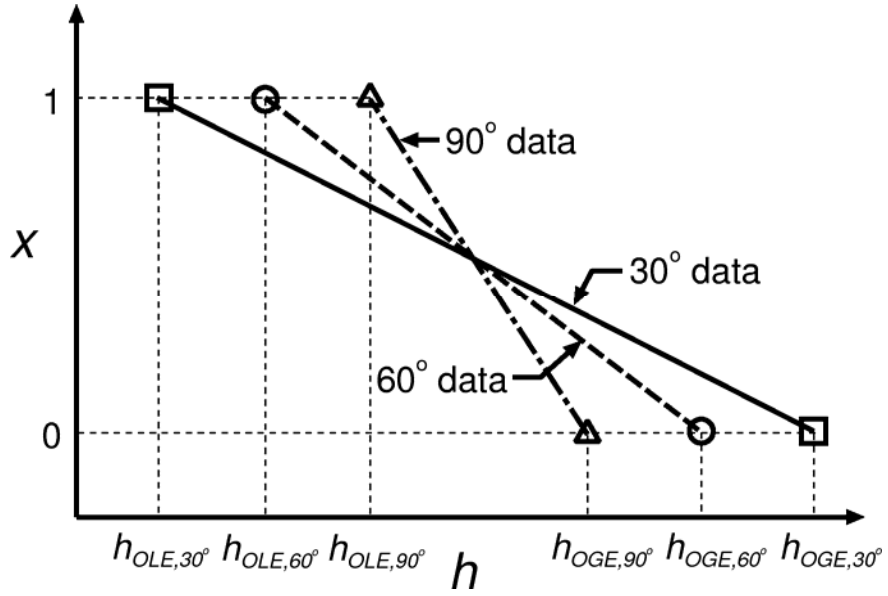

Figure 4.55 – Schematic of x versus h at Branch A for θ = 30°, 60° and 90°

Figures 4.56 and 4.57 show results for $\dot{m}_{TP,B}$ versus h_B and x_B versus h_B, respectively, for Cases 4 and 12, along with Hassan's (1995) correlation for θ = 90°. From these results it can be seen that at higher values of h_B, $\dot{m}_{TP,B}$ increases and x_B decreases with increasing θ. Starting

from the far right end of the horizontal axis in Figures 4.56 and 4.57, as the interface height decreases, the onset of gas entrainment occurs much sooner for the lower θ, resulting in more gas flow through the branch and a smaller flow rate. Because the onset of liquid entrainment heights are so similar for all values of θ, the results converge near the onset of liquid entrainment heights.

The experimental results at θ = 30° and 60° are now plotted in terms of the dimensionless variables M_A versus H_A, x_A versus H_A, M_B versus H_B and x_B versus H_B for P_0 = 517 kPa and ΔP = 97 kPa in Figures 4.58 to 4.61 for L/d = 1.5 and in Figures 4.62 to 4.65 for L/d = 3. Included in these figures are Hassan's (1995) correlations for θ = 0° and 90°. For θ = 90°, it was preferable to use Hassan's data for M_A, rather than the correlation.

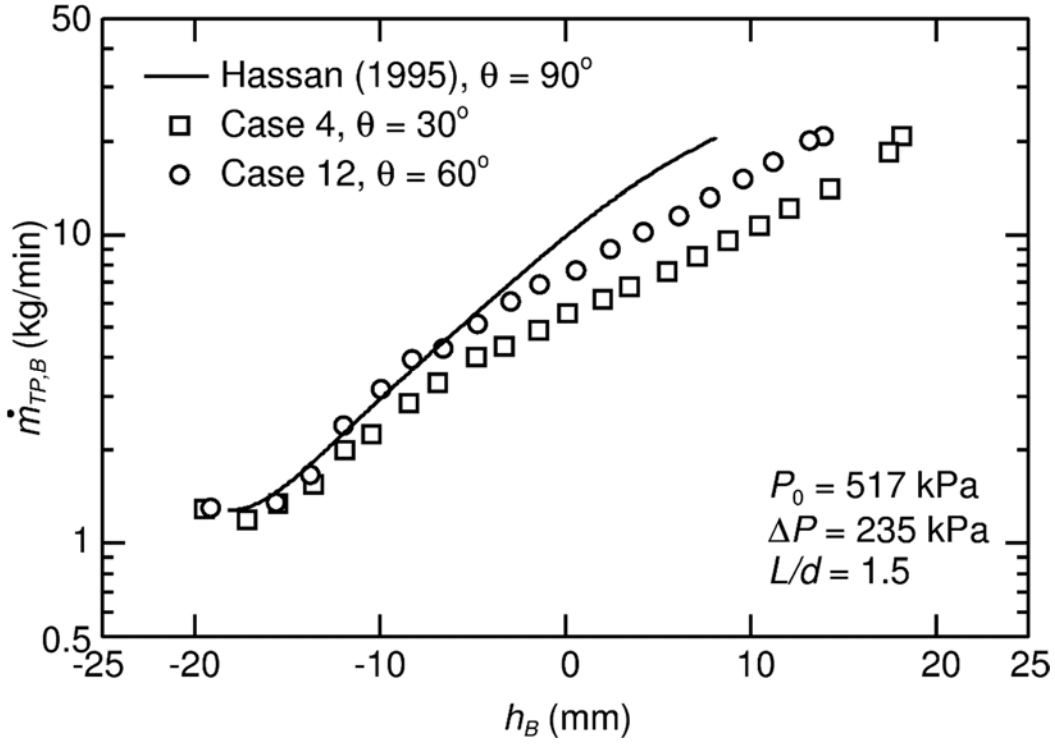

Figure 4.56 - $\dot{m}_{TP,B}$ versus h_B for θ = 30°, 60° and 90°

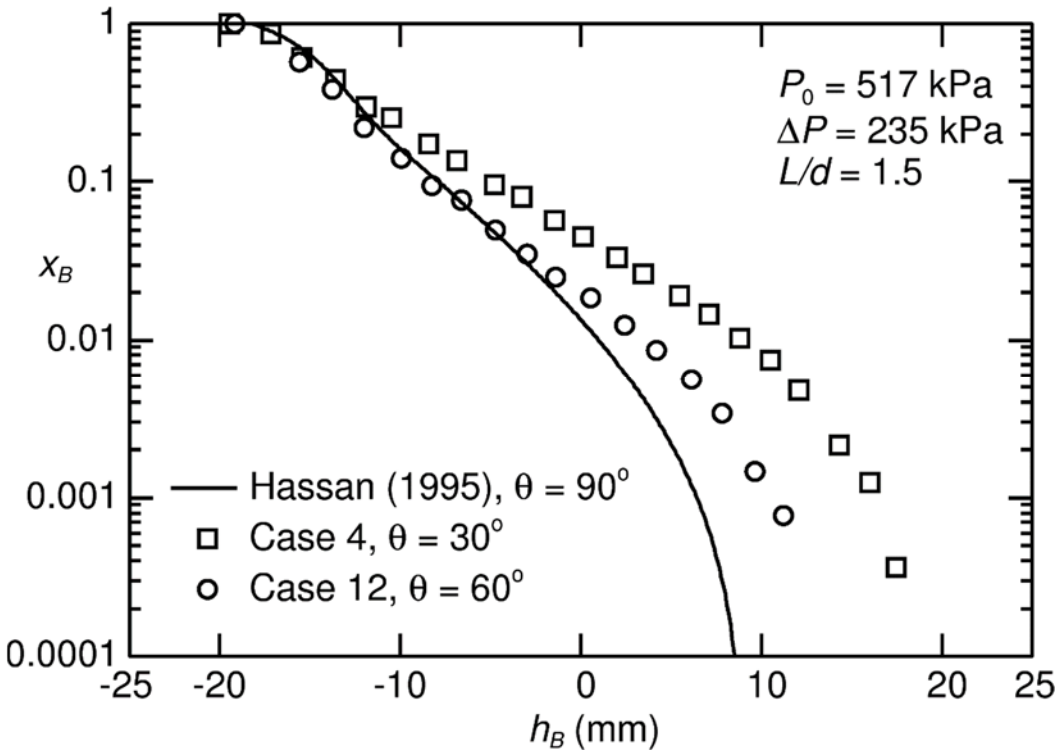

Figure 4.57 - x_B versus h_B for θ = 30°, 60° and 90°

For L/d = 1.5, Figure 4.58 shows the experimental data for M_A versus H_A for Cases 3 and 11 from the present work along with data set no. 3-8 from Hassan (1995) for θ = 90° and Hassan's correlation for θ = 0°. From these results it can be seen that at low values of H_A (H_A < 0.4), M_A decreases with increasing θ. Within the range of 0.4 < H_A < 0.8, the data for θ = 30, 60 and 90° cross, similar to what was seen with the dimensional plots, while the correlation for θ = 0° remains above the rest of the data. At high values of H_A (H_A > 0.8), M_A increases with increasing θ between θ= 30° and 90°. Results for x_A versus H_A are shown in Figure 4.59 for these same cases. At low H_A, x_A increases with increasing θ and the data for θ = 30 and 60° and the correlation for θ = 90° cross between H_A = 0.4 and 0.8, as also occurred with the M_A data for these same cases. For H_A > 0.8, x_A decreases with increasing θ from θ = 30 to 90°. For θ = 0°, x_A remains the lowest and M_A remains the highest for all values of H_A.

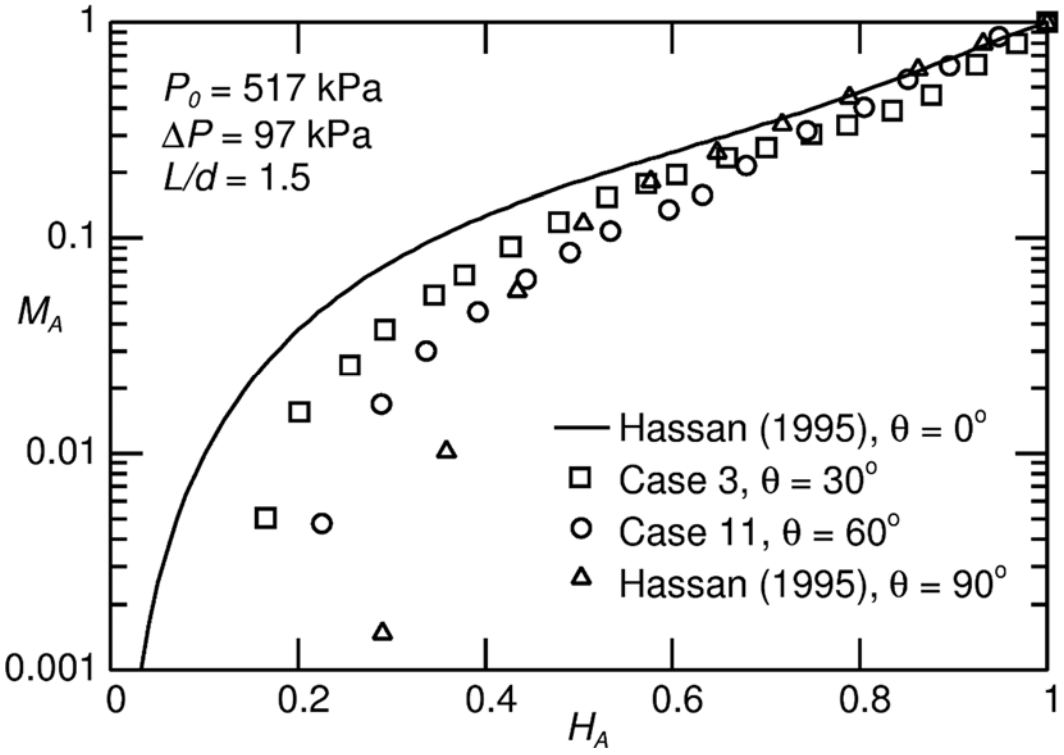

Figure 4.58 - Experimental results for M_A versus H_A for Cases 3 and 11

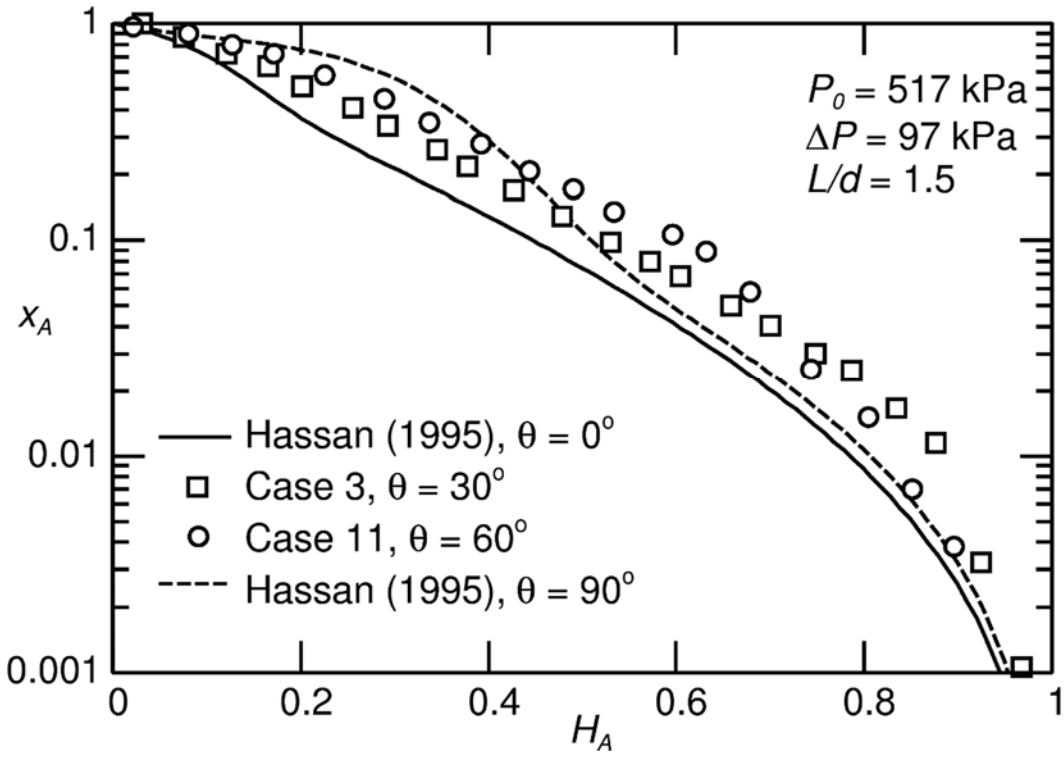

Figure 4.59 - Experimental results for x_A versus H_A for Cases 3 and 11

The dimensionless results for M_B and x_B versus H_B are shown in Figures 4.60 and 4.61 for Cases 3 and 11. For Branch B, there is much less effect of θ on the results compared to Branch A. At high values of H_B ($H_B > 0.7$), M_B increases slightly and x_B decreases slightly with increasing θ. At moderate values of H_B ($0.3 < H_B < 0.7$), there is negligible difference between the results for $\theta = 30$, 60 and 90°, while for $\theta = 0°$ M_B is lower and x_B is higher for this range of H_B. At low values of H_B, the results converge onto the same curve for all values of θ.

In general, for $L/d = 3$, Figures 4.62 to 4.65 show that there is less effect of θ on the dimensionless parameters than was observed for $L/d = 1.5$. For the upper branch, the results for M_A versus H_A (Figure 4.62) follow the same trend of increasing M_A with decreasing θ at low values of H_A, as was observed for $L/d = 1.5$; however, at high values of H_A the data collapse onto the same curve for all values of θ. The results for x_A versus H_A (Figure 4.63)

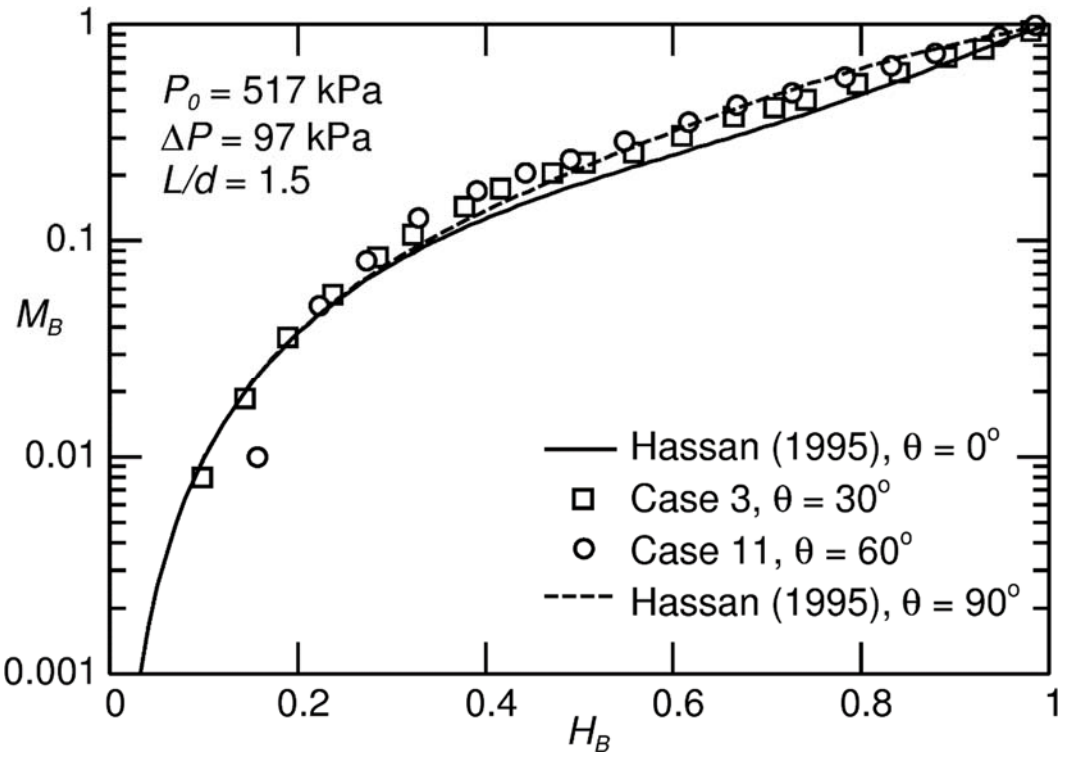

Figure 4.60 - Experimental results for M_B versus H_B for Cases 3 and 11

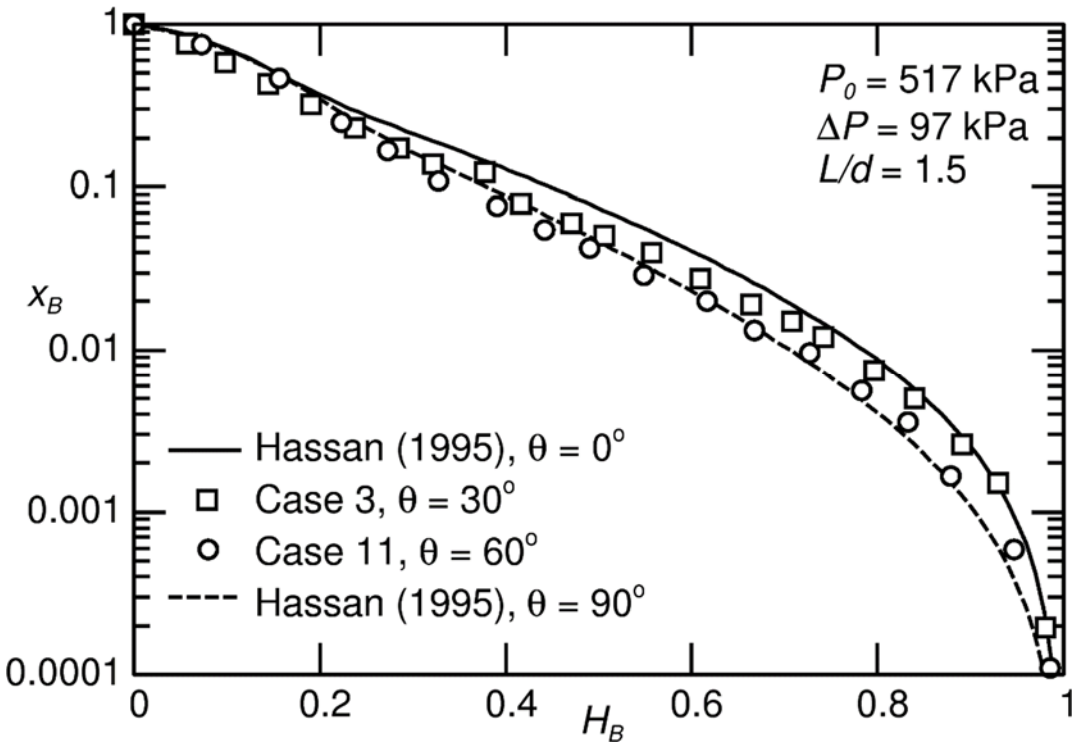

Figure 4.61 - Experimental results for x_B versus H_B for Cases 3 and 11

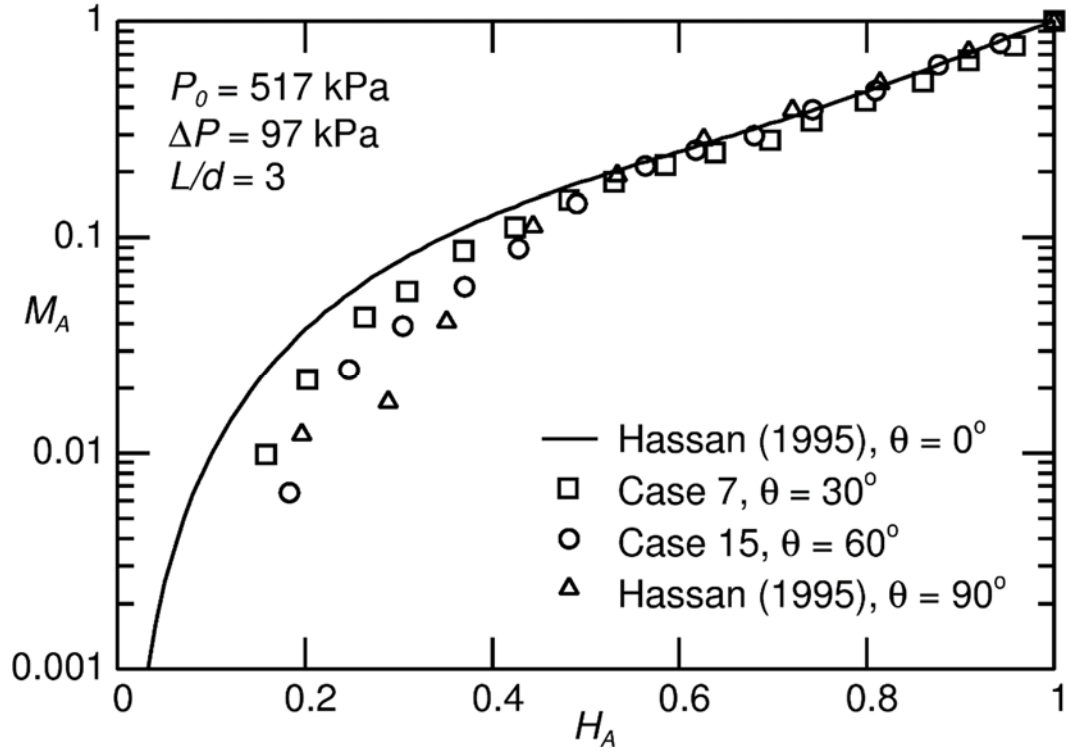

Figure 4.62 - Experimental results for M_A versus H_A for Cases 7 and 15

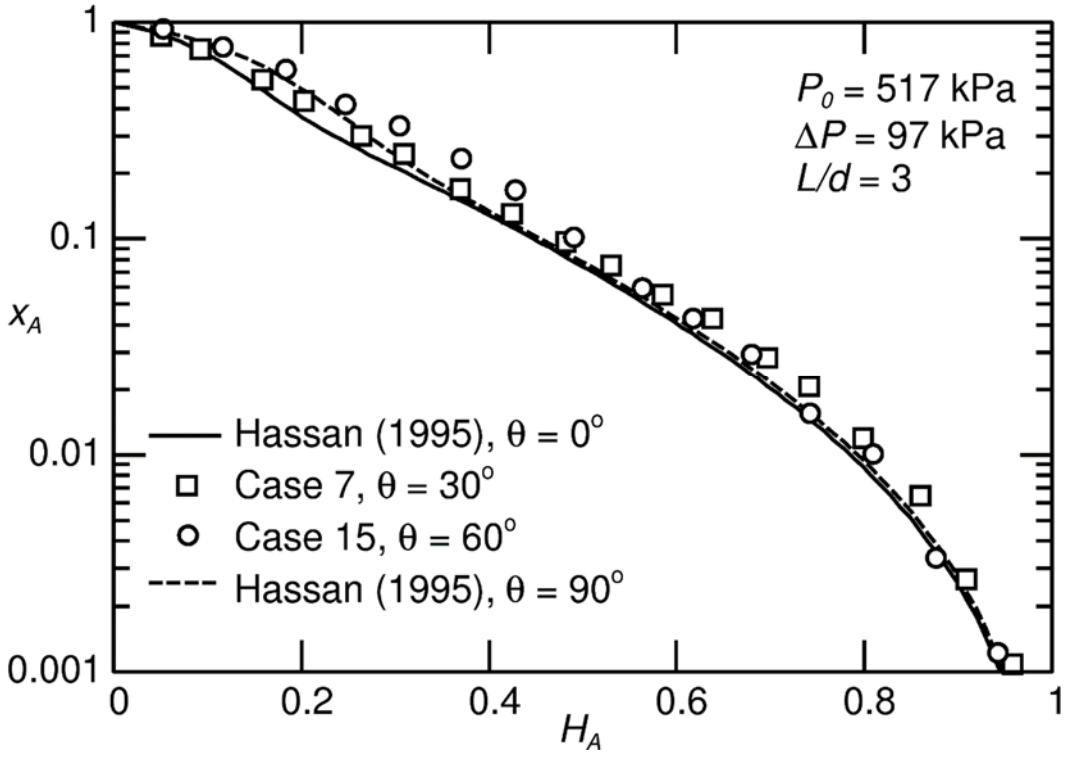

Figure 4.63 - Experimental results for x_A versus H_A for Cases 7 and 15

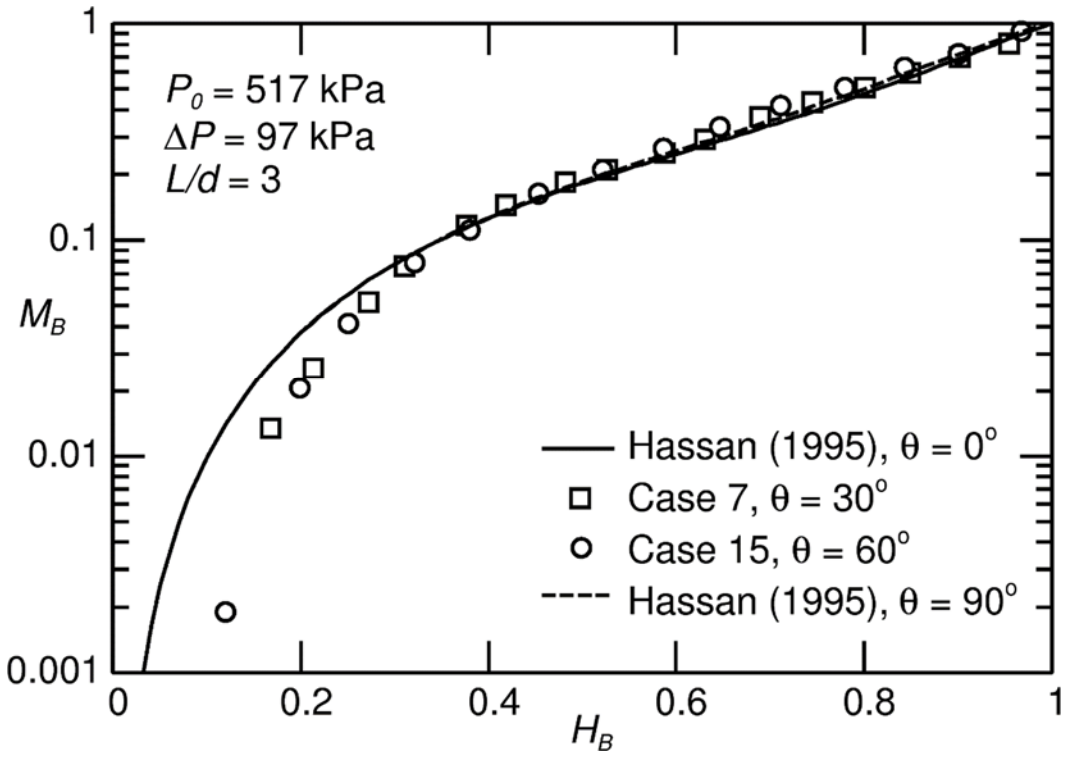

Figure 4.64 - Experimental results for M_B versus H_B for Cases 7 and 15

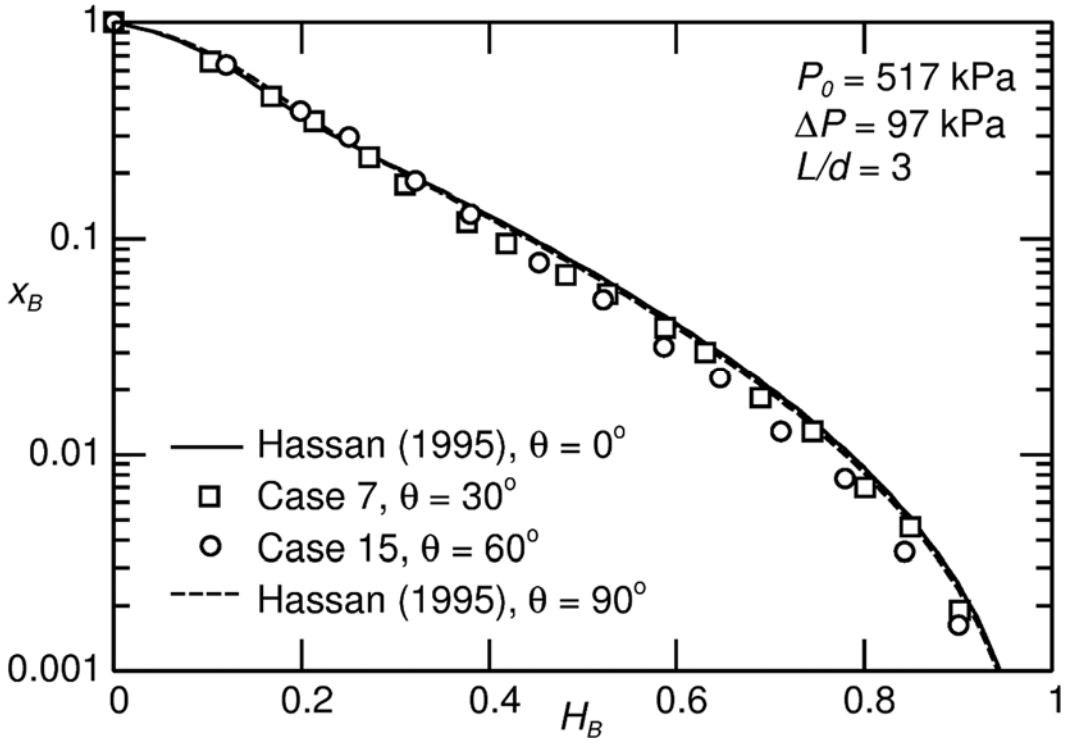

Figure 4.65 - Experimental results for x_B versus H_B for Cases 7 and 15

deviate slightly with θ at low values of H_A, but converge onto the same curve at high values of H_A. At the lower branch and for L/d = 3, the effect of θ appears to be absorbed when the results are plotted as M_B versus H_B (Figure 4.64) and x_B versus H_B (Figure 4.65).

4.3.3.5 M and x *Correlations*

Based on the present experimental data for Cases 1 to 16 and the correlations developed by Hassan (1995) for θ = 0 and 90°, empirical correlations were developed for $M_A(H_A, L/d, \theta)$, $M_B(H_B, L/d, \theta)$, $x_A(H_A, L/d, \theta, (\rho_L/\rho_G))$ and $x_B(H_B, L/d, \theta, (\rho_L/\rho_G))$. The correlations are valid over the following ranges:

- P_0 = 316 to 517 kPa
- ΔP = 40 to 235 kPa
- θ = 0 to 90°
- L/d = 1.5 to ∞

For these correlations, the angle between the branches must be measured from the horizontal line through the center of the bottom branch towards the line connecting the centerlines of the two branches. Facing the branch inlet, this angle must be measured counter clockwise when the upper branch is located towards the right as shown in Figure 4.66 (a) and must be measured clockwise when the upper branch is located towards the left, as shown in Figure 4.66(b).

(a) (b)

Figure 4.66 – Measurement schematic for θ used in correlations

The resulting correlations take the same form as Hassan's correlations and the coefficients converge to the correct limits for $\theta = 0$ and 90° and as $L/d \to \infty$.

<u>M_A Correlation</u>

$$M_A = H_A^{(2+A_4)} \exp\left[-1.84 H_A^{\,2}\left(1 - H_A^{\,2}\right)^{A_5}\right] \tag{4.13}$$

where,

$$A_4 = \sin\theta \exp\left[\sinh\theta\left(-0.722\left(\frac{L}{d}\right)+1.123\right)\right] \tag{4.14}$$

$$A_5 = 1.318 + \sin\theta\left(7.873\sin\theta - 5.973\right)\left(\frac{L}{d}\right)^{2.085\sin(1.635\theta)-3.197} \tag{4.15}$$

As $L/d \to \infty$ or when $\theta = 0°$, $A_4 \to 0$ and $A_5 \to 1.318$ and Equation (4.13) converges to Hassan's single branch correlation for M_A (Recall that Hassan showed excellent agreement between the single branch correlations and the experimental results for dual branches with θ =

0°). When θ = 90°, Equation (4.13) converges to Equation (4.10) (the new correlation fit to Hassan's data for M_A at θ = 90°). Figure 4.67 shows the agreement between the experimental results for M_A and the correlations; good agreement was found with an RMS deviation of 11.4% between the limits of $0.1 \le M_A \le 1$ and 19.0% between the limits of $0.01 \le M_A \le 1$.

<u>M_B Correlation</u>

$$M_B = H_B{}^2 \exp\left[-1.84 H_B{}^2 \left(1 - H_B{}^2\right)^{B_3 + B_4 H_B}\right] \tag{4.16}$$

where,

$$B_3 = 1.318 + 5.78 \sin\theta \exp\left[-0.37\left(\frac{L}{d}\right)^2 (\sin\theta)^{-2.101\left(\frac{L}{d}\right)^{-0.854}} - 4.551\left(\frac{L}{d}\right)^{-0.911} \cos\theta\right] \tag{4.17}$$

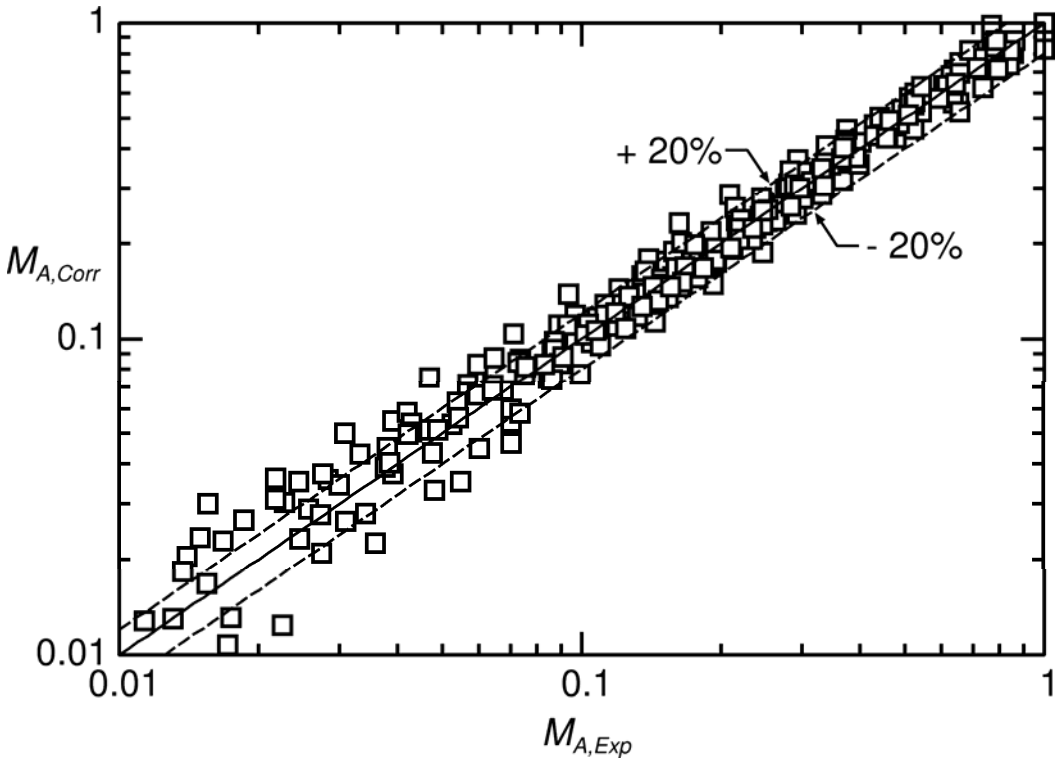

Figure 4.67 - Predicted versus Measured Values of M_A

$$B_4 = -39.94\cos\theta(\sin\theta)^{2.664}\left(\frac{L}{d}\right)^{-1.134\sin\theta-0.803} \tag{4.18}$$

As $L/d \to \infty$ or when θ = 0°, $B_3 \to 1.318$ and $B_4 \to 0$ and Equation (4.16) is equivalent to Hassan's single branch correlation for M_B. When θ = 90°, $B_3 \to 1.318 + 5.78\sin\theta\exp\left[-0.37\left(\frac{L}{d}\right)^2\right]$ and $B_4 \to 0$ and Equation (4.16) becomes the dual branch equation for M_B, developed by Hassan for θ = 90°. Between these limits of θ = 0 and 90°, the correlation shows excellent agreement with the experimental data for Cases 1 to 16 with an RMS deviation of 8.1% between the limits of $0.1 \le M_B \le 1$ and 14.1% between the limits of $0.01 \le M_B \le 1$. Figure 4.68 shows the agreement between the experimental data and the present correlations.

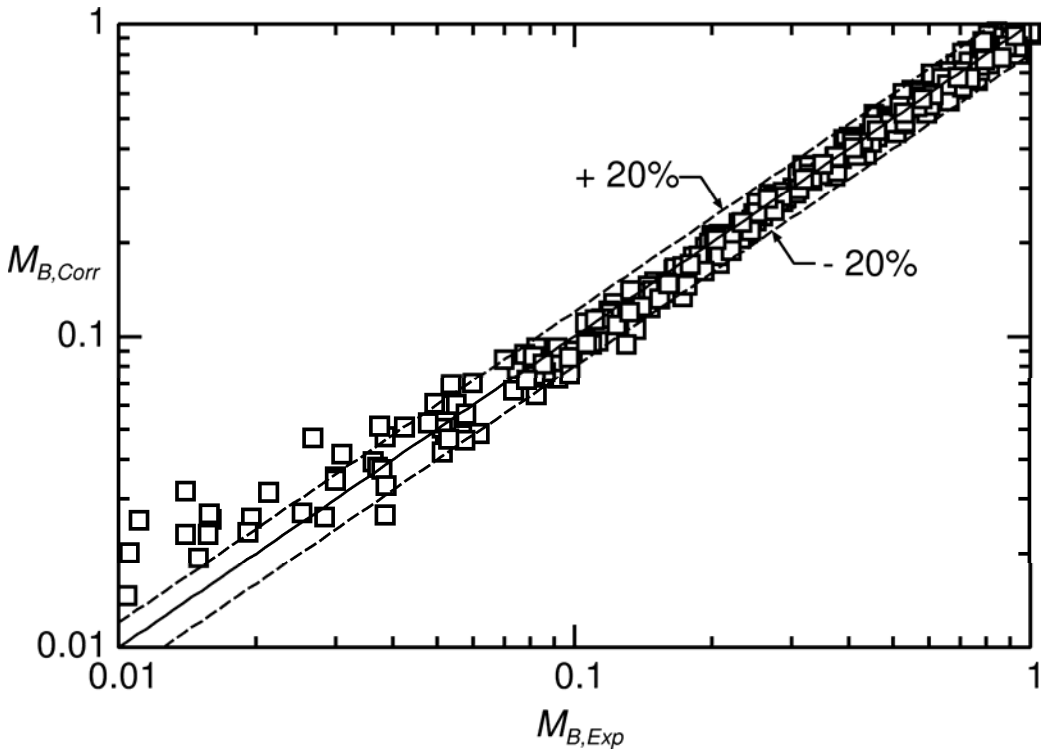

Figure 4.68 - Predicted versus measured values of M_B

x_A Correlation

$$x_A = 0.2\exp\left[6H_A\frac{(1-A_6H_A)}{(1-H_A)}\right] + 0.8\left(1-A_7{H_A}^2\right)^{1.3}\left(A_8E\right)^{H_A} \tag{4.19}$$

where,

$$A_6 = 11.67 - 9.67\sin\theta\exp\left[-0.01\left(\frac{L}{d}\right)^3 + \cos\theta\left[\left(0.883\left(\frac{L}{d}\right)-1.468\right)\theta - 0.0859\left(\frac{L}{d}\right)^{2.279}\right]\right] \tag{4.20}$$

$$A_7 = \exp\left[134.229\left(\frac{L}{d}\right)^{-6.343}\cos\theta(\sin\theta)^{46.701-14.411\frac{L}{d}}\right] \tag{4.21}$$

$$A_8 = 1 + 0.92\sin\theta\exp\left[-0.75\frac{L}{d} + \cos\theta\left(6.792\left(\frac{L}{d}\right)^{-0.953}\theta^{1.546-0.534\frac{L}{d}}\right)\right] \tag{4.22}$$

$$E = -0.0122 + 0.42/\left[1+\sqrt{\rho_L/\rho_G}\right] \tag{4.23}$$

At the limit of $L/d \to \infty$ or when $\theta = 0°$, $A_6 \to 11.67$, $A_7 \to 1$ and $A_8 \to 1$ and Equation (4.19) is equivalent to Hassan's single branch correlation for x_A. When θ = 90° , $A_6 \to 11.67 - 9.67\exp\left[-0.01\left(\frac{L}{d}\right)^3\right]$, $A_7 \to 1$ and $A_8 \to 1 + 0.92\exp\left[-0.75\frac{L}{d}\right]$ and Equation (4.19) becomes Hassan's correlation for x_A for $\theta = 90°$. For Cases 1 to 16, this correlation agrees well with the experimental data, as shown in Figure 4.69, with an RMS deviation of 19.1% between the limits of $0.01 \le x_A \le 1$ and 24.0% between the limits of $0.001 \le x_A \le 1$.

x_B Correlation

$$x_B = 0.2\exp\left[6H_B\frac{(1-B_5H_B)}{(1-H_B)}\right] + 0.8\left(1-{H_B}^2\right)^{1.3}\left(B_6E\right)^{H_B} \tag{4.24}$$

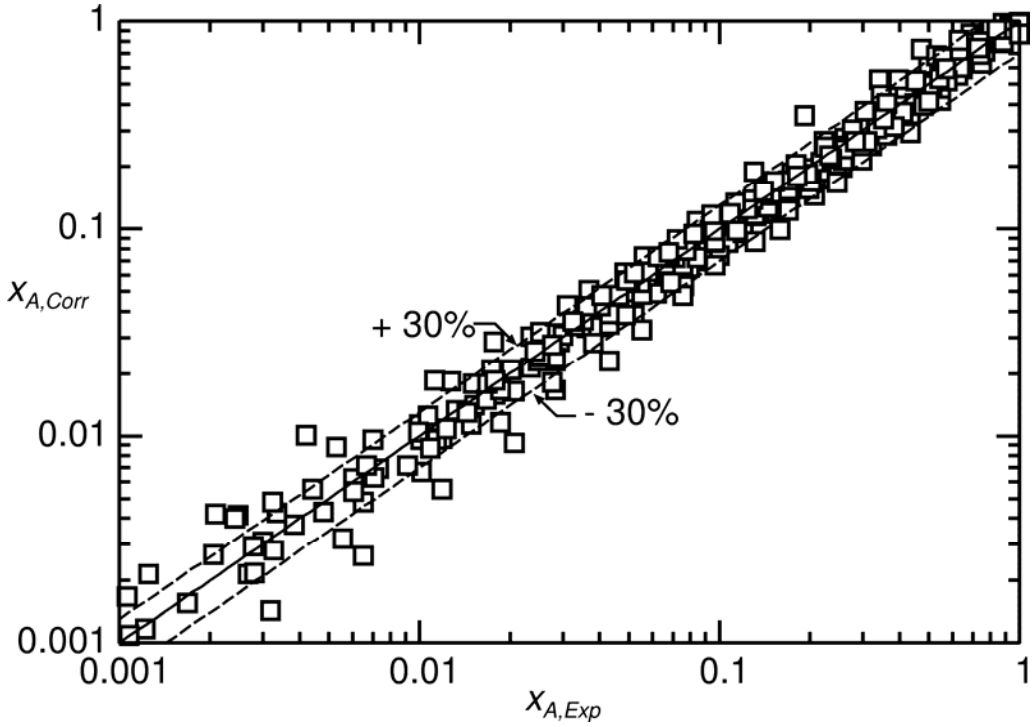

Figure 4.69 - Predicted versus measured values of x_A

where,

$$B_5 = 11.67 - 3.03\sin\theta\exp\left[-0.016\left(\frac{L}{d}\right)^3 + 1.108\left(\frac{L}{d} - 1.448\right)\cos\theta\right] + 89.415\left(\frac{L}{d}\right)^{-1.657}(\cos\theta)^{2.25}\sin\theta \tag{4.25}$$

$$B_6 = 1 - 0.71\sin\theta\exp\left[-0.03\left(\frac{L}{d}\right)^4 + \cos\theta\left(0.793\theta\left(\frac{L}{d}\right)^{1.614} - 1.332\left(\frac{L}{d}\right)^{-0.331}\right)\right] \tag{4.26}$$

The correlation for x_B also converges to the correct correlations at the limit of $L/d \to \infty$ and for $\theta = 0$ and 90°. For $L/d \to \infty$ and $\theta = 0°$, $B_5 \to 11.67$ and $B_6 \to 1$ and Equation (4.24) becomes Hassan's single branch correlation for x_B. For $\theta = 90°$, $B_5 = 11.67 - 3.03\exp\left[-0.016\left(\frac{L}{d}\right)^3\right]$ and $B_6 = 1 - 0.71\exp\left[-0.03\left(\frac{L}{d}\right)^4\right]$ and the correlation equals Hassan's dual branch correlation for x_B

for $\theta = 90°$. Figure 4.70 shows that the agreement between the correlation and the experimental data is good with an RMS deviation of 17.2% between the limits of $0.01 \le x_B \le 1$ and 18.8% between the limits of $0.001 \le x_B \le 1$.

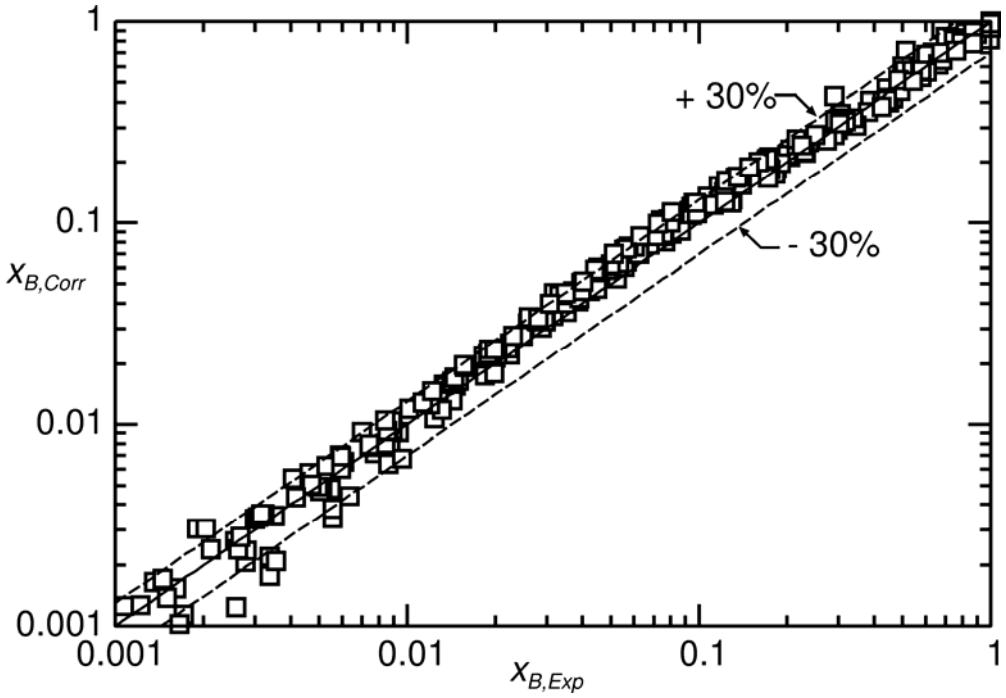

Figure 4.70 - Predicted versus measured values of x_B

4.4 Experimental Repeatability

In addition to the comparisons that were made with previous experimental data and correlations, an effort was made to further ensure the accuracy of the present data by conducting some repeatability experiments. These repeatability tests included experiments for both critical onset heights as well as experiments for two-phase flow and the results are shown in Tables 4.2 to 4.4. Table 4.2 shows three repeatability experiments: one for $h_{OLE,B}/d$ and two for $h_{OLE,A}/d$. As can be seen from this table, the maximum deviation in h_{OLE}/d is 1.82%. Table 4.3 shows that for the two repeatability experiments conducted for the onset of gas entrainment at the lower branch, the maximum deviation in $h_{OGE,B}/d$ was only 1.6%. Finally, Table 4.4 shows results for two different repeatability tests for cases where two phases flowed through each branch. For these tests, the percent deviation in the two-phase mass flow rates, $\dot{m}_{TP}$, and qualities, x, ranged from

0.84% to 5.8%. The small deviations found from these repeatability tests further confirm the accuracy of the results.

Table 4.2 – Repeatability of h_{OLE}/d for $P_0 = 316$ kPa, $\Delta P = 40$ kPa, and $\theta = 60°$

L/d	$h_{OLE,A}/d$	$h_{OLE,B}/d$	$Fr_{G,OLE,A}$	$Fr_{G,OLE,B}$	% deviation in h_{OLE}/d
3	-	-2.0844	14.20	14.47	1.8%
	-	-2.1230	14.05	14.51	
3	-2.0137	-	14.04	14.50	0.33%
	-2.0202	-	14.20	14.47	
1.5	-2.2017	-	15.99	15.62	0.15%
	-2.1984	-	15.33	15.17	

Table 4.3 – Repeatability of h_{OGE}/d for $P_0 = 316$ kPa, $\Delta P = 40$ kPa, and $\theta = 60°$

L/d	$h_{OGE,B}/d$	$Fr_{L,OGE,B}$	% deviation in h_{OGE}/d
3.00	1.4041	15.61	1.6%
	1.4269	15.61	
1.50	1.4133	17.01	0.53%
	1.4209	17.34	

Table 4.4 – Repeatability of two-phase data for $P_0 = 316$ kPa, $\Delta P = 40$ kPa, $L/d = 1.5$ and $\theta = 30°$

h_B/d	h_A/d	$\dot{m}_{TP,A}$ (kg/s)	x_A	$\dot{m}_{TP,B}$ (kg/s)	x_B	% deviation in $\dot{m}_{TP,A}$	% deviation in x_A	% deviation in $\dot{m}_{TP,B}$	% deviation in x_B
0.355	-0.392	1.937E-02	0.117	4.506E-02	0.019	5.1%	-3.6%	3.4%	5.3%
0.361	-0.386	2.041E-02	0.113	4.358E-02	0.020				
1.054	0.307	2.875E-02	0.050	5.704E-02	0.006	5.1%	2.9%	5.8%	0.84%
1.036	0.289	3.028E-02	0.049	6.056E-02	0.006				

4.5 Closure

Throughout the experimental investigation, data were collected for the onset of liquid and gas entrainment interface heights and the two-phase mass flow rates for discharging two-phase flow from a stratified region through two horizontal branches. For the OLE experiments, results were obtained for L/d = 1.5 and 3, θ = 30° and 60° and $\mathrm{Fr}_{G,OLE,A} = \mathrm{Fr}_{G,OLE,B}$ = 15 to 40. The results showed that for both L/d = 1.5 and 3, there is very little effect of θ on the OLE at Branch B. However, for the OLE at Branch A, as θ increases Branch B competes more with Branch A for liquid entrainment and $\left|h_{OLE,A}\right|/d$ decreases; this effect of θ on $\left|h_{OLE,A}\right|/d$ decreases as L/d increases. Empirical correlations were developed based on the present data and Hassan's (1995) data to predict $\left|h_{OLE,A}\right|/d$ and $\left|h_{OLE,B}\right|/d$. The developed correlations showed excellent agreement with the data with RMS deviations of 4.2% and 2.5% for $\left|h_{OLE,A}\right|/d$ and $\left|h_{OLE,B}\right|/d$, respectively, for L/d = 1.5 to 8, θ = 0° to 90° and $\mathrm{Fr}_{G,OLE,A} = \mathrm{Fr}_{G,OLE,B}$ = 15 to 40.

For the OGE, data were obtained for L/d = 1.5 and 3, θ = 30°, 60° and 90°, and $\mathrm{Fr}_{G,OLE,A} = \mathrm{Fr}_{G,OLE,B}$ = 15 to 50. For the OGE at Branch A, as θ decreases, Branch B provides more assistance to Branch A with gas entrainment and $h_{OGE,A}/d$ increases. A larger effect of θ was observed for the OGE at Branch B. As θ increases, Branch A competes more with Branch B for gas entrainment and $h_{OGE,B}/d$ decreases. These trends were observed for both values of L/d, however, θ has less effect on $h_{OGE,A}/d$ and $h_{OGE,B}/d$ as L/d increases. From the present data and Hassan's (1995) data, empirical correlations were developed to predict $h_{OGE,A}/d$ and $h_{OGE,B}/d$ with an RMS deviation of 4.8% and 5.8%, respectively, from the data over the range of L/d = 1.5 to 8, θ = 0° to 90° and $\mathrm{Fr}_{G,OLE,A} = \mathrm{Fr}_{G,OLE,B}$ = 15 to 50.

For interface heights between $h_{OLE,B}$ and $h_{OGE,A}$, results were obtained for 16 data sets with the following ranges of parameters: P_0 = 316 and 517 kPa; ΔP = 40 to 235 kPa; L/d = 1.5 and 3; and θ = 30° and 60°. For this range of parameters, the effects of ΔP, L/d and θ on $\dot{m}_{TP}$ and x results were analyzed and the following observations were made:

- For both Branches A and B, as ΔP increases, $\dot{m}_{TP}$ increases and x decreases at low values of h and increases at high values of h.
- When the results were plotted in terms of the dimensionless parameters M versus H or x versus H, the effects of ΔP were absorbed.
- The effect of L/d on the two-phase flow distribution in the branches is dependent on both ΔP and θ but in general, as L/d increases, the branches have less influence on one another.
- The branches have less influence on one another as θ or ΔP decrease.
- For both Branches A and B, at high values of h, $\dot{m}_{TP}$ decreases and x increases as θ increases.
- For Branch A, at low values of h_A, $\dot{m}_{TP,A}$ increases and x_A decreases with increasing θ.
- For Branch B, at low values of h_B, θ has very little effect on $\dot{m}_{TP,B}$ and x_B because $h_{OLE,B}$ is nearly independent of θ.

Empirical correlations were developed to predict M_A, M_B, x_A and x_B. The correlations show good agreement with the experimental data for P_0 = 316 to 517 kPa, ΔP = 40 to 235 kPa, θ = 0 to 90° and L/d = 1.5 to ∞.

Chapter 5

Numerical Model Description

5.1 Model Geometries

A total of five different geometries were modelled in this study for two-phase discharge from a large rectangular tank; three of these geometries included a single branch on the side of the tank and two of the geometries included two side branches. Table 5.1 lists each of the geometries, the number of branches, the angle between the branches, θ (for dual branches only), the length of the branch(es) divided by the branch diameter, L_B / d, the shape of the branch cross section, and the spacing between the branches divided by the branch diameter, L / d.

Table 5.1 - Geometries modelled

Geometry	Number of Branches	θ	L_B / d	Branch Cross Section	L / d
G1	1	NA	20	Square	-
G2	1	NA	200	Square	-
G3	1	NA	200	Circular	-
G4	2	90°	200	Circular	1.5
G5	2	30°	200	Circular	1.5

Figures 5.1 and 5.2 show side and front views of the single branch geometries modelled in this study. These geometries consist of a large rectangular tank (720 mm x 246 mm x 125 mm) with a small side branch of square cross section (6 mm x 6 mm) for Geometries G1 and G2 and of circular cross section (d = 6 mm) for Geometry G3. Air and water at 25°C are contained in the tank with a flat interface. The height of the interface, h, is measured from the centreline of the branch (h is positive if the interface is located above the branch centreline and negative if the interface is located beneath the branch centreline). The length of the branch differs for the three

single branch geometries from $L_B / d = 20$ for G1 to $L_B / d = 200$ for G2 and G3. For all three of the single branch geometries, only half the tank and branch were modelled due to symmetry along the centreplane of the reservoir at z = 62.5 mm.

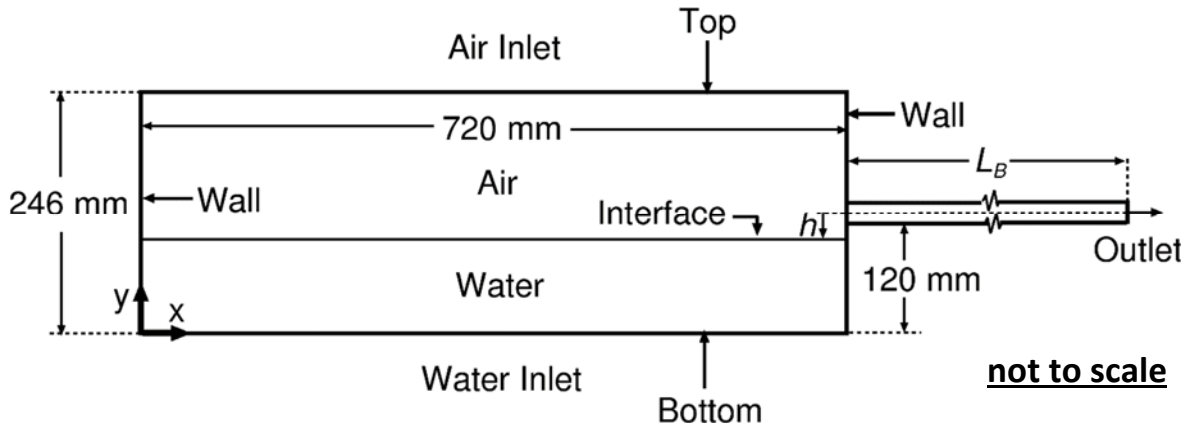

Figure 5.1 - Geometry of single branch models (G1 to G3) – side view

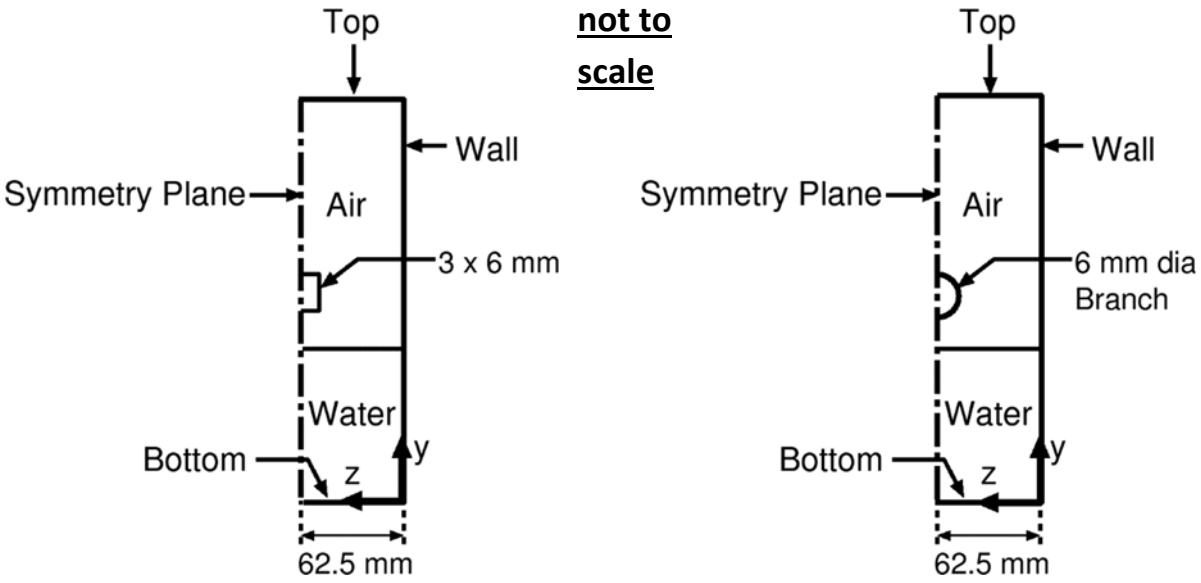

(a) Square branch cross section (G1 and G2) (b) Circular branch cross section (G3)

Figure 5.2 – Geometry of single branch models (G1 to G3) – front views

The geometries with two branches are shown in Figures 5.3 and 5.4. Stratified layers of air and water are contained in the tank with two circular side branches (d = 6.35 mm) separated by a distance of L/d = 1.5 and an angle θ. For Geometry G4, the branches are located one on top of the other such that θ = 90°, as shown in Figure 5.4 (a) and for Geometry G5, the branches are located at an angle of θ = 30° from one another, as shown in Figure 5.4 (b). For the geometries with two branches, the upper branch is always referred to as Branch A and the lower branch as Branch B. As shown in Figure 5.4 (a) and (b), the interface height, h_A, is measured from the centreline of Branch A to the interface, such that h_A is positive if the interface is located above the Branch A centreline and negative if it is located beneath the Branch A centreline. Similarly, the interface height, h_B, is measured from the centreline of Branch B towards the interface, such that it is positive if it is located above the Branch B centreline and negative if it is located beneath the Branch B centreline. For the dual branch geometry with θ = 90°, half the tank and branch were modelled due to symmetry along the centreplane. However, for the dual branch geometry with θ = 30°, symmetry conditions could not be used and the entire width of the geometry was modelled.

The numerical model was set up differently depending on the type of flow phenomena under investigation. These investigations were split up into three categories: the OLE Analysis, the OGE Analysis and the Two-Phase Flow Analysis. The following discussion focuses on the geometries with a single branch but these same procedures can be applied to the geometries with two branches. When differences exist between the single and dual branch procedures, these differences will be discussed.

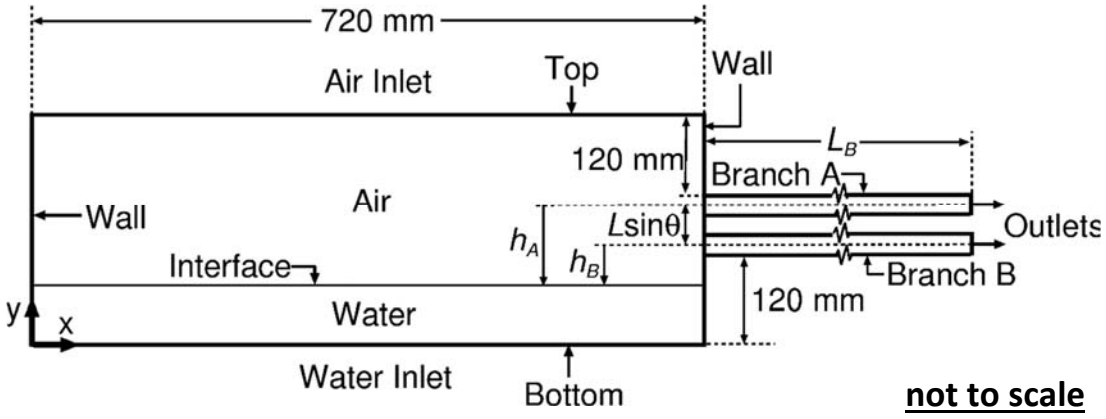

Figure 5.3 – Geometry of dual branch models (G4 and G5) – side view

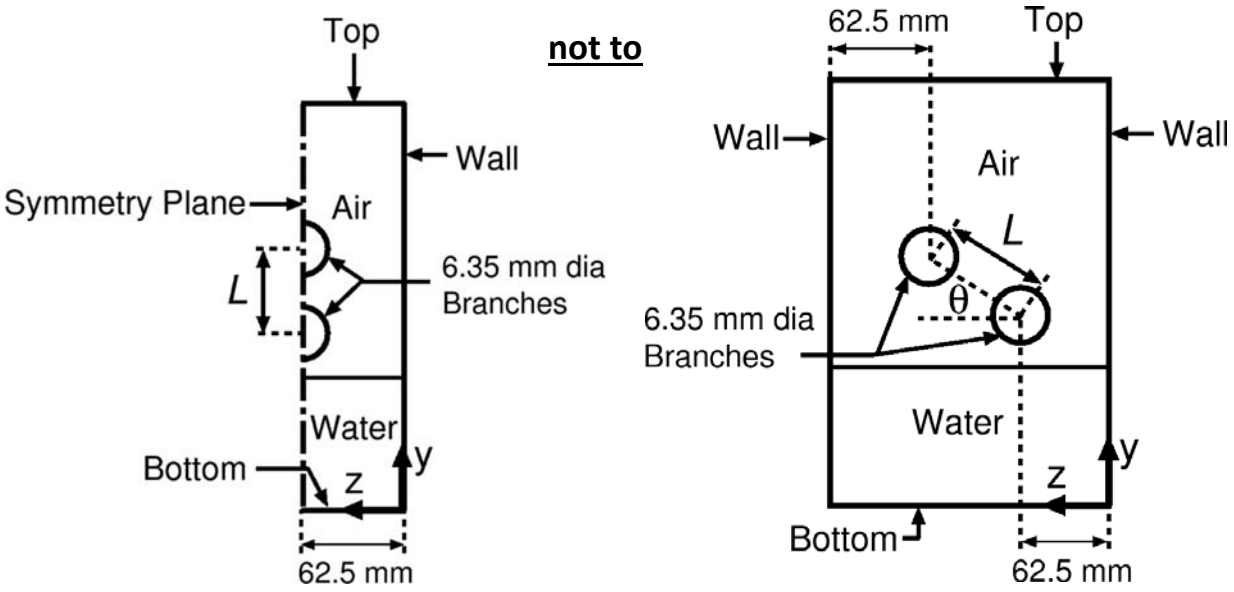

(a) θ = 90° (G4) (b) θ = 30° (G5)

Figure 5.4 – Geometry of dual branch models (G4 and G5) – front views

OLE Analysis

In order to obtain results for the OLE, water was introduced slowly through the bottom of the tank raising the interface level at a rate of 1 mm/min. Starting from a converged steady-state solution with an interface sufficiently lower than the branch, a transient solution was advanced until liquid started to flow into the branch. This was determined by monitoring the air volume fraction at the bottom of the branch inlet, $\alpha_{G,BB}$, on the symmetry plane for Geometries G1 to G4. For Geometry G5 with two branches and θ = 30°, the locations where the air volume fraction was monitored for Branches A and B were offset slightly from the branches' centreplanes to capture the exact location where liquid first started entering the branch. These locations were selected by monitoring the air volume fraction contours from the transient results and observing the location around the circumference of the branch opening where the air volume fraction first started deviating from 1; this occurred at the same location for all cases of ΔP. For Branch A, this location was shifted 40° from the bottom of Branch A in the counter-clockwise direction and for Branch B, this location was shifted 21° from the bottom of Branch B in the clockwise direction. A schematic is included in Figure 5.5 to help clarify the location where the air volume fractions, $\alpha_{GA,BBI}$ and $\alpha_{GB,BBI}$, for Branches A and B, respectively, were monitored for Geometry G5, where

the subscript BBI refers to the branch bottom for the inclined geometry (G5). The value for the monitored air volume fraction remained constant at 1 until the onset of liquid entrainment occurred, at which time it just started dropping below 1. At this instant, the onset of liquid entrainment was declared and the value of h, which is defined as the location where $\alpha_G = \alpha_L =$ 0.5 and is measured far from the branch inlet at z = 62.5 mm, was taken as h_{OLE}.

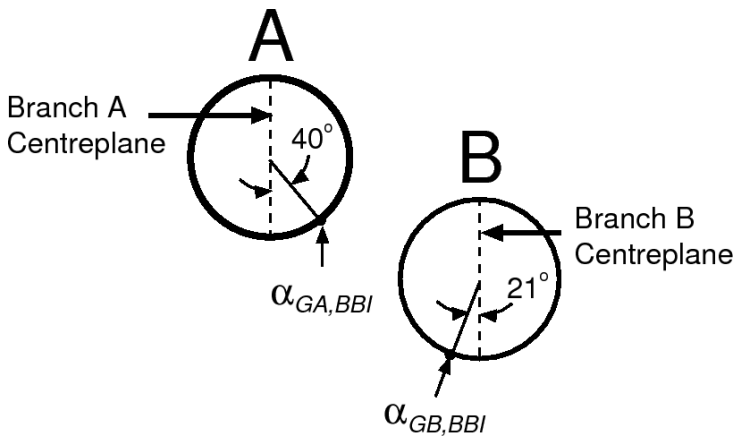

Figure 5.5 - Locations where $\alpha_{GA,BBI}$ and $\alpha_{GB,BBI}$ were measured during OLE Analysis for Geometry G5

OGE Analysis

For the tests designed to determine the critical height for the OGE, water was introduced through the bottom of the tank at a rate equal to 99% of the rate exiting through the branch(es), thus slowly lowering the interface height. Starting from a converged steady-state solution with an interface sufficiently higher than the branch under consideration, a transient solution was advanced past the OGE and the value of h at the timestep corresponding to the OGE was taken as h_{OGE}. The timestep at which the OGE occurred was determined by monitoring the air volume fraction at the top of the branch inlet on the symmetry plane, $\alpha_{G,BT}$, for Geometries G1 to G4 and the mass flow rate of gas through the branch, $\dot{m}_G$, versus time, τ, for Geometries G1 to G5, just before and after the OGE. For Geometry G5, the air volume fraction, $\alpha_{GA.BTI}$, was monitored at the top of Branch A on the centreplane because this was the location where $\alpha_{GA.BTI}$ first started deviating from zero. For Branch B, the location where the air volume fraction, $\alpha_{GB.BTI}$, was monitored was

shifted 19.5° counter-clockwise from the top of the branch, as shown in Figure 5.6, to capture the exact location where air first started entering the branch. This location was selected by monitoring the air volume fraction contours from the transient results and observing the location around the circumference of the branch opening where the air volume fraction first started deviating from zero; this occurred at the same location for all values of ΔP. More details on the selection procedure for the timestep corresponding to the OGE will be discussed in Section 6.1.2.

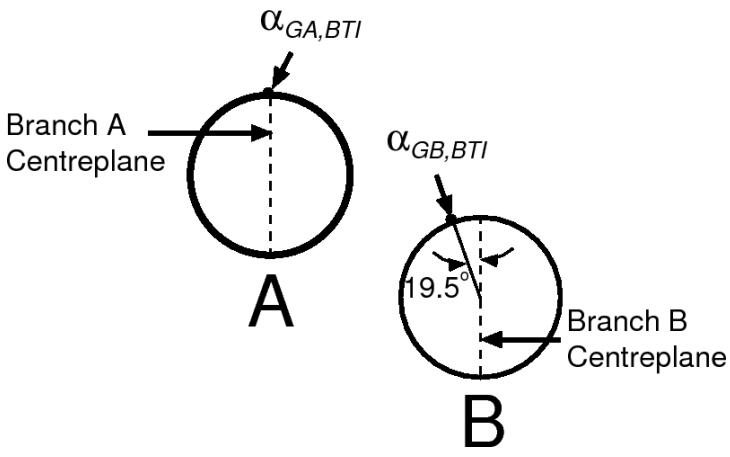

Figure 5.6 - Locations where $\alpha_{GA,BTI}$ and $\alpha_{GB,BTI}$ were measured during OLE Analysis for Geometry G5

Two-Phase Flow Analysis

For tests involving two-phase flow through the branch, a steady state solution was performed for each case where a steady value of h was specified as an initial condition such that $h_{OLE} < h < h_{OGE}$. Water was introduced into the bottom of the tank at a rate that was successively adjusted to match the water flow rate exiting the branch(es).

5.2 Multiphase Flow Models in ANSYS CFX

The problem defined in Section 5.1 was solved using ANSYS CFX version 14.5 and 15.0. The models available in ANSYS CFX for modelling multiphase flow can be separated into two distinct models: an Eulerian-Eulerian multiphase model and a Lagrangian Particle Tracking multiphase model. The Lagrangian Particle Tracking model is used when the flow consists of dispersed phases which are discretely distributed in a continuous phase. Since this thesis focuses

on two-phase flows where both phases are continuous, the Lagrangian Particle Tracking Model will not be discussed.

Within the Eulerian-Eulerian model, two different sub-models are available: the homogeneous model and the inhomogeneous model. In these models, a volume of fluid method is used in which the volume fraction of each fluid is tracked throughout the domain and sums to unity in each control volume. With the homogeneous model, the fields for velocities (u, v and w); for turbulent kinetic energy (k); for eddy dissipation rate (ε) and for properties (density ρ and viscosity μ) are shared by the phases and represent volume-averaged values. With the inhomogeneous model, on the other hand, each fluid has its own velocities, turbulence quantities and properties, and the fluids interact by interfacial transfer terms.

In the early stages of the investigation, attempts were made at using the homogeneous model for modelling a steady-state case for Geometry G1 with $\mathrm{Fr}_{G,OLE}$ = 7.74 and an interface height of h = -10.8 mm. This interface height was expected to be well below the OLE height based on Craya's (1949) correlation defined in Equation (2.1). For these conditions, the model did not converge after over 11,000 iterations; the mass flow rates of liquid and gas at the outlet were oscillating with no sign of leveling off. Figure 5.7 (a) shows air volume fraction contours plotted on the symmetry plane from the results obtained using the homogeneous model after 11,400 iterations. The red region in these figures represents mostly air with α_G between 0.975 and 1 and the blue region represents mostly water with α_G between 0 and 0.025. The air volume fraction contours show that air is forming in the region below the interface near the wall underneath the branch inlet and the interface has climbed the wall underneath the branch resulting in significant amounts of water exiting through the branch when the interface is lower than the expected onset height.

When using the inhomogeneous free surface model for this same case, a converged solution was attained after only 8800 iterations with stratified layers of liquid and gas inside the tank, as shown in Figure 5.7 (b). The inhomogeneous model also produced results that were in better agreement with previous experimental data and correlations, as will be shown later. The inhomogeneous model was therefore selected for this study.

Three different sub-models exist in the inhomogeneous model: particle model, mixture model and free surface model. These three models differ in the way that they model the interfacial area density (interfacial area per unit volume) required to calculate the interphase drag

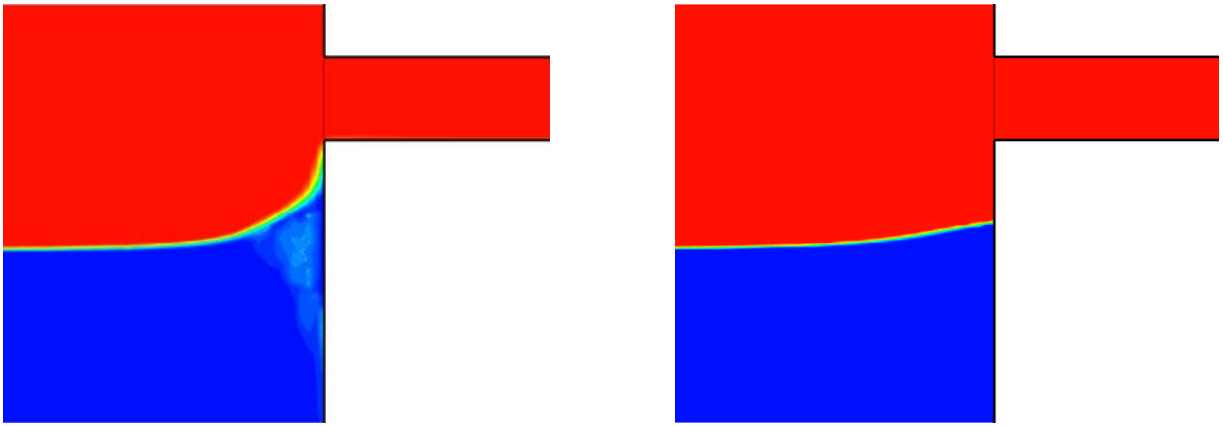

(a) Homogeneous model (b) Inhomogeneous model

Figure 5.7 – Comparison of air volume fraction contours from homogeneous and inhomogeneous models for $\mathrm{Fr}_{G,OLE} = 7.74$ and $h = -10.8$ mm

force that appears in the momentum equations. The free surface model is recommended by ANSYS Inc. (2013) for two-phase flows where a distinct interface exists between the two-phases and was the model used in this study.

5.3 Governing Equations for the Inhomogeneous Model

For the inhomogeneous free surface model, 14 equations are required to solve for the following 14 variables at each node: the velocities in the liquid and gas regions, u_{Li} and u_{Gi} (for all three components in the x, y and z directions corresponding to i = 1, 2 and 3, respectively), the volume fractions, α_L and α_G, and the pressures P_L and P_G, and the turbulence kinetic energy and dissipation rate in each phase. The 14 equations used to solve for these variables include: one continuity equation (for either the liquid or gas), six momentum equations (three for liquid and three for gas), two volume conservation equations, one pressure constraint, two turbulence kinetic energy equations (one in each phase), and two dissipation rate equations (one in each phase).

Only one of the following two continuity equations is used to solve for the volume fraction of one of the phases:

Liquid Continuity

$$\frac{\partial}{\partial t}\left(\alpha_L \rho_L\right)+\frac{\partial}{\partial x_i}\left(\alpha_L \rho_L u_{Li}\right)=0 \tag{5.1}$$

Gas Continuity

$$\frac{\partial}{\partial t}\left(\alpha_G \rho_G\right)+\frac{\partial}{\partial x_i}\left(\alpha_G \rho_G u_{Gi}\right)=0 \tag{5.2}$$

The following liquid and gas momentum equations are used to solve for the liquid and gas velocities:

Liquid Momentum (3 Equations for i = 1, 2 and 3)

$$\begin{aligned}\frac{\partial}{\partial t}\left(\alpha_L \rho_L u_{Li}\right)+\frac{\partial}{\partial x_j}\left(\alpha_L \rho_L u_{Li} u_{Lj}\right)-\frac{\partial}{\partial x_j}\left(\alpha_L \mu_{eff,L}\left(\frac{\partial u_{Li}}{\partial x_j}+\frac{\partial u_{Lj}}{\partial x_i}\right)\right)= \\ -\alpha_L \frac{\partial P_L}{\partial x_i}+S_{b,Li}+F_L+M_{Li}{}^{D}\end{aligned} \tag{5.3}$$

Gas Momentum (3 Equations for i = 1, 2 and 3)

$$\begin{aligned}\frac{\partial}{\partial t}\left(\alpha_G \rho_G u_{Gi}\right)+\frac{\partial}{\partial x_j}\left(\alpha_G \rho_G u_{Gi} u_{Gj}\right)-\frac{\partial}{\partial x_j}\left(\alpha_G \mu_{eff,G}\left(\frac{\partial u_{Gi}}{\partial x_j}+\frac{\partial u_{Gj}}{\partial x_i}\right)\right)= \\ -\alpha_G \frac{\partial P_G}{\partial x_i}+S_{b,Gi}+F_G+M_{Gi}{}^{D}\end{aligned} \tag{5.4}$$

In Equations (5.3) and (5.4), $\mu_{eff,L}$ and $\mu_{eff,G}$ are the effective viscosities of the liquid and gas, respectively, $S_{b,Li}$ and $S_{b,Gi}$ represent the buoyancy sources in the liquid and gas, F_L and F_G are the surface tension forces and $M_{Li}{}^{D}$ and $M_{Gi}{}^{D}$ are the interphase drag forces. These terms are defined as:

$$\mu_{eff,L} = \mu_L + \mu_{TL} \tag{5.5}$$

$$\mu_{eff,G} = \mu_G + \mu_{TG} \tag{5.6}$$

$$S_{b,Li} = (\rho_L - \rho_{ref})g_i \tag{5.7}$$

$$S_{b,Gi} = (\rho_G - \rho_{ref})g_i \tag{5.8}$$

$$F_L = -F_G = (-\sigma_{LG}\nabla \cdot n_{LG} n_{LG} + \nabla_s \sigma_{LG})\delta_{LG} \tag{5.9}$$

$$M_{Li}^{\ D} = -M_{Gi}^{\ D} = C_D \rho A_{LG} |u_{Gi} - u_{Li}|(u_{Gi} - u_{Li}) \tag{5.10}$$

In Equations (5.5) and (5.6), μ_{TL} and μ_{TG} are the eddy viscosities of the liquid and gas, respectively. In Equations (5.7) and (5.8), the reference density, ρ_{ref} was specified as 1.185 kg/m^3 (air at 100 kPa and 21°C) and g is the gravitational acceleration (g_2 = -9.81 m/s^2, $g_1 = g_3 = 0$). In Equation (5.9), the surface tension coefficient, σ_{LG} for water in contact with air is 0.0728 N/m, the interface delta function is defined as $\delta_{LG} = |\nabla \alpha_{LG}|$ and is zero away from the interface, n_{LG} is the interface normal vector pointing from the primary fluid (water) to the secondary fluid (air), and ∇_s is the gradient operator on the interface. In Equation (5.10), the mixture density, ρ, is defined by the following:

$$\rho = \alpha_L \rho_L + \alpha_G \rho_G \tag{5.11}$$

The drag coefficient, C_D, in Equation (5.10) was found to have a significant effect on the onset results but minimal effect on the two-phase mass flow rate and quality results. The default setting in CFX for this parameter is 0.44 and is based on interfaces between a continuous phase and spherical particles of another phase. Because the interface in this study does not take this form, the drag coefficient was adjusted from the default setting. The value for C_D was determined by solving the onset of liquid entrainment height for one value of ΔP and then adjusting C_D until the results from the numerical model agreed with Craya's (1949) analytical solution. This resulted in a drag coefficient of 0.05 which was then kept constant for all the computations in this study. The interfacial area density in Eq. (5.10), A_{LG}, is defined by the following equation for the free surface model:

$$A_{LG} = \left| \frac{\partial \alpha_L}{\partial x} + \frac{\partial \alpha_L}{\partial y} + \frac{\partial \alpha_L}{\partial z} \right| \tag{5.12}$$

The following volume conservation equations are required to solve for the volume fraction of the second phase (Equation (5.13)) and the pressure of one of the phases (Equation (5.14)). Equation (5.13) enforces that the volume fractions of the two phases sum to unity in each control volume and Equation (5.14) combines the continuity equations (Equations (5.1) and (5.2)) with Equation (5.13).

Volume Conservation Equations

$$\alpha_L + \alpha_G = 1 \tag{5.13}$$

$$\frac{1}{\rho_L}\left(\frac{\partial}{\partial t}\rho_L \alpha_L + \frac{\partial}{\partial x_i}\rho_L \alpha_L u_{Li} \right) + \frac{1}{\rho_G}\left(\frac{\partial}{\partial t}\rho_G \alpha_G + \frac{\partial}{\partial x_i}\rho_G \alpha_G u_{Gi} \right) = 0 \tag{5.14}$$

The liquid and gas pressures are equated to give one final constraint to solve for the pressure of the second phase.

Pressure Constraint

$$P_L = P_G = P \tag{5.15}$$

The two-equation $k-\varepsilon$ model was used to model turbulence in both phases of the flow and the turbulent viscosity, kinetic energy, and dissipation rate equations are shown below for the liquid and gas regions.

Liquid Eddy Viscosity, μ_{TL}

$$\mu_{TL} = C_\mu \rho_L \left(\frac{{k_L}^2}{\varepsilon_L} \right) \tag{5.16}$$

Gas Eddy Viscosity μ_{TG}

$$\mu_{TG} = C_\mu \rho_G \left(\frac{{k_G}^2}{\varepsilon_G} \right) \tag{5.17}$$

Liquid Turbulence Kinetic Energy, k_L

$$\frac{\partial(\alpha_L \rho_L k_L)}{\partial t} + \frac{\partial}{\partial x_j}\left(\alpha_L\left(\rho_L u_{Lj} k_L - \left(\mu_L + \frac{\mu_{TL}}{\sigma_k}\right)\frac{\partial k_L}{\partial x_j}\right)\right) = \alpha_L\left(P_{TL} - \rho_L \varepsilon_L\right) \quad (5.18)$$

Gas Turbulence Kinetic Energy, k_G

$$\frac{\partial(\alpha_G \rho_G k_G)}{\partial t} + \frac{\partial}{\partial x_j}\left(\alpha_G\left(\rho_G u_{Gj} k_G - \left(\mu_G + \frac{\mu_{TG}}{\sigma_k}\right)\frac{\partial k_G}{\partial x_j}\right)\right) = \alpha_G\left(P_{TG} - \rho_G \varepsilon_G\right) \quad (5.19)$$

Liquid Dissipation Rate, ε_L

$$\frac{\partial(\alpha_L \rho_L \varepsilon_L)}{\partial t} + \frac{\partial}{\partial x_j}\left(\alpha_L\left(\rho_L u_{Lj} \varepsilon_L - \left(\mu_L + \frac{\mu_{TL}}{\sigma_\varepsilon}\right)\frac{\partial \varepsilon_L}{\partial x_j}\right)\right) = \alpha_L \frac{\varepsilon_L}{k_L}\left(C_{\varepsilon 1} P_{TL} - C_{\varepsilon 2} \rho_L \varepsilon_L\right) \quad (5.20)$$

Gas Dissipation Rate, ε_G

$$\frac{\partial(\alpha_G \rho_G \varepsilon_G)}{\partial t} + \frac{\partial}{\partial x_j}\left(\alpha_G\left(\rho_G u_{Gj} \varepsilon_G - \left(\mu_G + \frac{\mu_{TG}}{\sigma_\varepsilon}\right)\frac{\partial \varepsilon_G}{\partial x_j}\right)\right) = \alpha_G \frac{\varepsilon_G}{k_G}\left(C_{\varepsilon 1} P_{TG} - C_{\varepsilon 2} \rho_G \varepsilon_G\right) \quad (5.21)$$

In Equations (5.16) to (5.21), $C_\mu = 0.09$, $C_{\varepsilon 1} = 1.44$, $C_{\varepsilon 2} = 1.92$, $\sigma_k = 1.0$, $\sigma_\varepsilon = 1.3$ and the turbulence production for the liquid and gas are:

$$P_{TL} = \mu_{TL}\left(\frac{\partial u_{Li}}{\partial x_j} + \frac{\partial u_{Lj}}{\partial x_i}\right)\frac{\partial u_{Li}}{\partial x_j} - \frac{2}{3}\frac{\partial u_{Lk}}{\partial x_k}\left(3\mu_{TL}\frac{\partial u_{Lk}}{\partial x_k} + \rho_L k_L\right) \quad (5.22)$$

$$P_{TG} = \mu_{TG}\left(\frac{\partial u_{Gi}}{\partial x_j} + \frac{\partial u_{Gj}}{\partial x_i}\right)\frac{\partial u_{Gi}}{\partial x_j} - \frac{2}{3}\frac{\partial u_{Gk}}{\partial x_k}\left(3\mu_{TG}\frac{\partial u_{Gk}}{\partial x_k} + \rho_G k_G\right) \quad (5.23)$$

5.4 Boundary and Initial Conditions

For all five geometries shown in Figures 5.1 to 5.4, the walls of the tank and branch(es) were treated as no slip walls and for the Geometries G1 to G4, a symmetry boundary condition was applied on the *x-y* plane at $z = 62.5$ mm. The scalable wall function, developed by ANSYS CFX, was used with the *k-ε* model equations. The scalable wall function is similar to the standard

wall function but limits the value of y^+ to 11.06 such that all mesh points are forced to fall outside the viscous sublayer. The boundary conditions applied to the top and bottom of the tank and at the outlet of each branch will be discussed in Sections 5.4.1 to 5.4.3, respectively.

5.4.1 Boundary Condition at the Top of the Tank

In the terminology used by CFX, an "opening" boundary condition was specified at the top of the tank with a steady pressure of P_0 for all the geometries modelled in this study. In CFX, an "opening" allows fluid to flow both into and out of the domain; however, in the present work, once a fully converged solution was attained the air flow across this entire boundary was always entering the domain.

At the top of the tank, the turbulence intensity was set to 1%; for this intensity, CFX specifies (μ_T / μ)=1. This low intensity was selected since the Re_G at this boundary was always below 4540. To check the effect of this boundary condition, the model was also solved using both a low intensity of 1% and a moderate intensity of 5% for the case with the highest Re_G; negligible differences were observed between these results.

5.4.2 Boundary Condition at the Bottom of the Tank

The boundary condition at the bottom of the tank depended on the type of phenomena under consideration. For the OLE analysis described in Section 5.1, the bottom of the tank was specified as an inlet with a normal speed of 1 mm/min. For the OGE analysis, the bottom of the tank was specified as a wall with zero slip and for the two-phase flow analysis the bottom of the tank was specified as an inlet with a mass flow rate of water, $\dot{m}_{L,in}$, that was successively adjusted to match the water flow rate exiting the branch(es), $\dot{m}_{L,out}$, using the following equation:

$$\dot{m}_{L,in}^{i} = m_{L,in}^{i-1} + 0.1\left(m_{L,out}^{i-1} - m_{L,in}^{i-1}\right) \tag{5.24}$$

where the superscript *i* indicates the current iteration and *i*-1 indicates the previous iteration.

When the bottom of the tank was specified as an inlet for the OLE and two-phase flow analyses, the turbulence intensity was set to 1% at this boundary. A low turbulence intensity was selected due to the low Reynolds numbers at this inlet ($\mathrm{Re}_L < 1854$).

5.4.3 Boundary Condition at a Branch Outlet

For all five geometries, an "outlet" with a specified relative static pressure was set at each branch outlet. For the steady-state and transient analyses using Geometries G1 to G3 and for the transient analyses using Geometries G4 and G5, a constant outlet relative static pressure of zero (relative to atmospheric pressure) was specified. For the steady-state analyses using Geometries G4 and G5, the model convergence showed better behaviour when the outlet relative static pressure was specified to drop linearly from P_0 to zero over the first 5000 iterations. Because the outlet pressure is zero, P_0 in the numerical model is equal to ΔP.

5.4.4 Initial Conditions

For the steady-state analyses, the following initial conditions were specified:

- The air and water velocities were set to zero everywhere in the domain.
- The interface height was set to the desired height by specifying the air volume fractions above that height as 1 and below that height as 0.
- The pressure was specified as P_0 in the air region and varied hydrostatically in the water region.
- The turbulence intensity was set to 1% and (μ_T / μ)=1 was set everywhere in the domain.

For the transient OLE and OGE analyses, a steady-state solution was used as the initial conditions.

5.5 Properties

In this study, air was treated as an ideal gas with μ_G = 1.831 x 10^{-5} N·s/m^2 and the density and dynamic viscosity of water were taken at 25 °C and 1 atmosphere to be ρ_L = 997 kg/m^3 and μ_L = 8.899 x 10^{-4} N·s/m^2, respectively.

5.6 Mesh and Discretization Schemes

5.6.1 Mesh

Using ANSYS ICEM software, the geometries shown in Figures 5.1 to 5.4 were divided into a number of control volumes using a block-structured, hexahedral mesh; sample portions of the mesh are shown in Figures 5.8 to 5.11 for Geometries G1, G3, G4 and G5, respectively. The mesh for Geometry G2 is identical to the mesh for Geometry G1 with the exception of a longer branch and is therefore not shown here. For all branch geometries, the mesh was refined in the *y*-direction in the areas above or below the branch where the interface was expected to be located and in the *x*-direction towards the branch inlet. For the geometries with a circular branch cross section, the grid was also refined in the *z*-direction towards the branch inlet. The grids shown in Figures 5.8 to 5.11 were used when the interface was located below the branch centreline (or below the Branch A centreline for dual branch geometries), which is why the mesh is refined more in the region beneath the branch. When the interface was located above the branch centreline, the refined region was located above the branch and the overall number of nodes was the same. These figures also show that the geometries with a round branch cross section required more nodes across the branch in the *y* and *z* directions than were required for the geometries with a square cross section.

Grid independence tests were conducted for the Geometries G1, G3 and G5 in order to assess the accuracy of the numerical results. For the geometries with a single branch (G1 and G3), Tables 5.2 and 5.3 show results of the mass flow rate of liquid at the branch outlet, $\dot{m}_L$, and the mass flow rate of gas at the branch outlet, $\dot{m}_G$, using coarse, medium and fine meshes. These tables also show how the execution time increases as the mesh is refined. The results for Geometry G1 (Table 5.2), corresponding to h = -14.98 mm and P_0 = 120 kPa, show that the deviation between the medium and the fine meshes is 1.43% in $\dot{m}_L$ and 0.11% in $\dot{m}_G$. Based on these small deviations it was decided to use a mesh size of 1.2 M nodes in generating results for this geometry. For Geometry G2, this same mesh was used with the addition of a branch extension connected to the branch outlet. The axial spacings of the extension were the same as for the short portion of the branch and there was a one-to-one node correspondence at the interface between the main grid and the branch extension. For Geometry G3 (Table 5.3), results corresponding to h = - 6.89 mm and P_0 = 120 kPa show that the deviation between the medium and fine meshes is 2.97% in $\dot{m}_L$ and

1.93% in $\dot{m}_G$. Based on these results, the mesh with 2.8 M nodes was selected, as a compromise between accuracy and execution time.

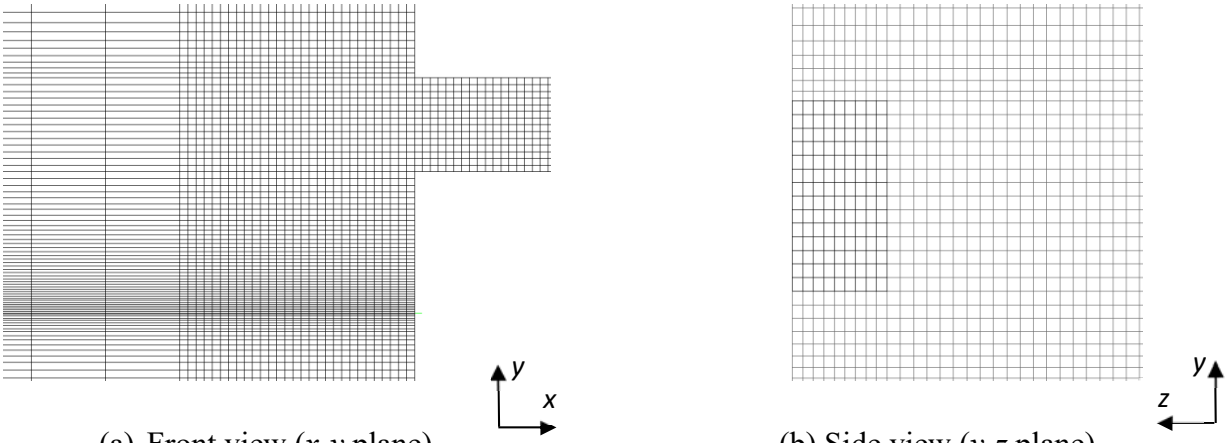

(a) Front view (*x*-*y* plane) (b) Side view (*y*-*z* plane)

Figure 5.8 - Cropped views of a sample medium mesh for Geometry G1

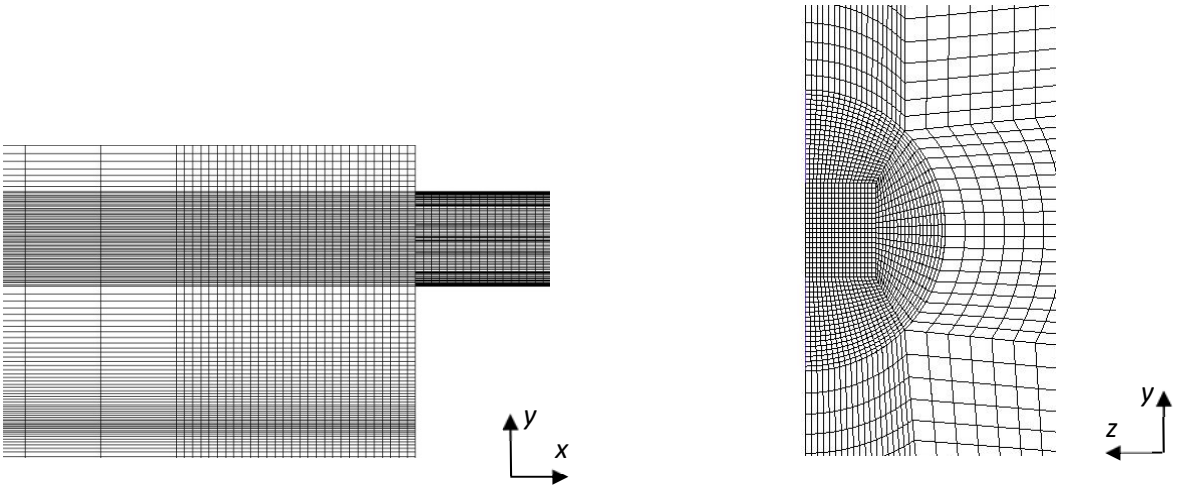

(a) Front view (*x*-*y* plane) (b) Side view (*y*-*z* plane)

Figure 5.9 - Cropped views of a sample medium mesh for Geometry G3

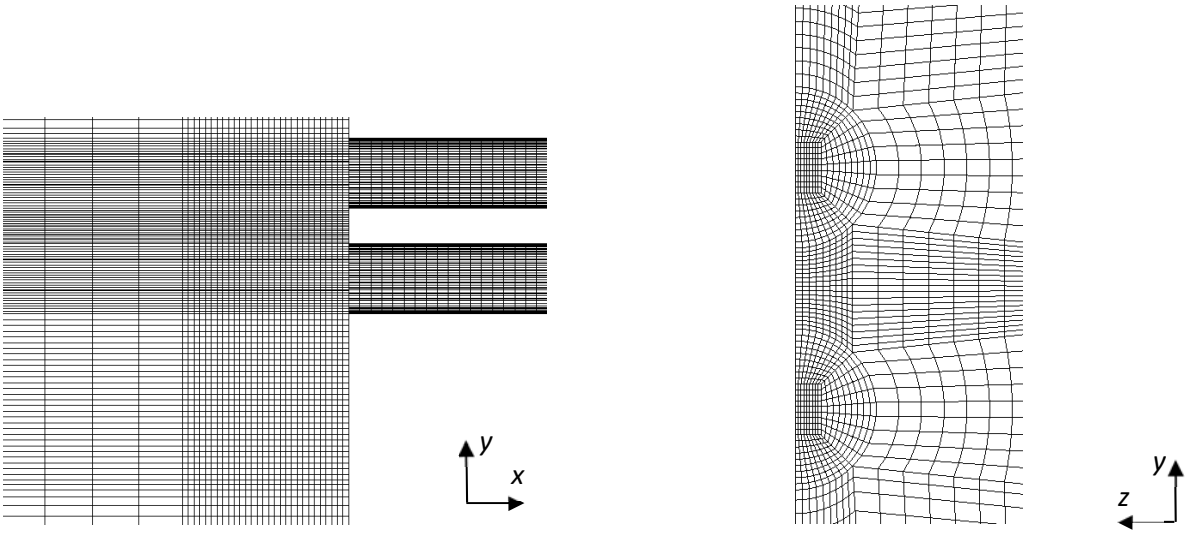

(a) Front view (*x*-*y* plane) (b) Side view (*y*-*z* plane)

Figure 5.10 - Cropped views of a sample medium mesh for Geometry G4

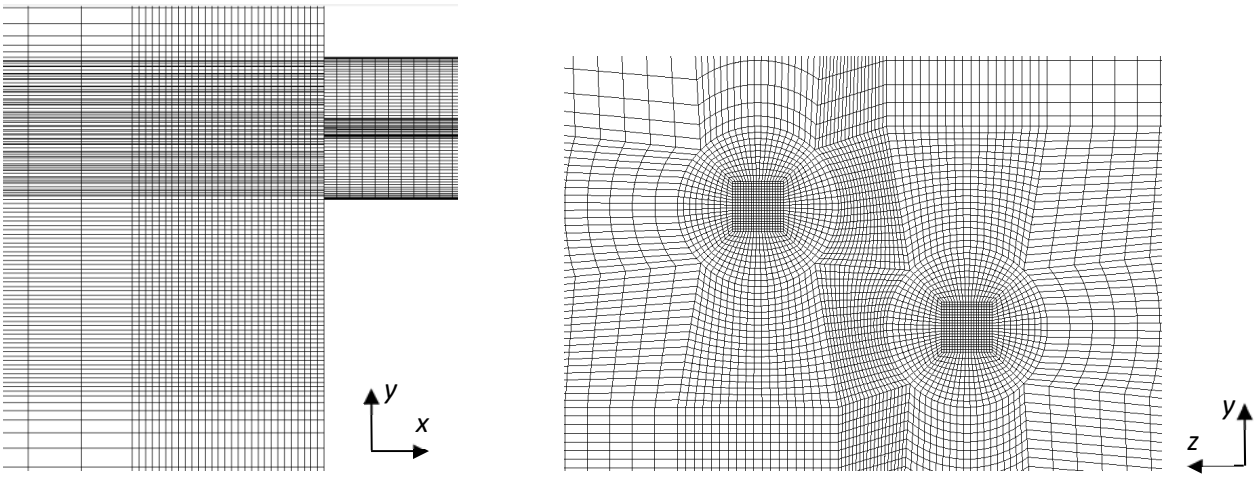

(a) Front view (*x*-*y* plane) (b) Side view (*y*-*z* plane)

Figure 5.11 - Cropped views of a sample medium mesh for Geometry G5

The grid independence results for the geometry with two inclined branches (G5) for h_A = -6.53 mm and P_0 = 120 kPa are shown in Table 5.4. For this geometry, the grid spacing was increased in the tank far away from the branch inlet compared to the single branch grids to keep the total number of nodes to a minimum since symmetry conditions could not be used. The results show that the medium and fine mesh results for the mass flow rate of liquid at the branch outlet deviate by 0.94% and 0.17% for Branches A and B, respectively, and the results for the mass flow

rate of gas at the branch outlet deviate by 0.81% and 0.11% for Branches A and B, respectively. Based on these small deviations, the medium mesh with 1.9 M nodes was selected for this geometry. The mesh for Geometry G4 used approximately the same sized control volumes as were used for Geometry G5 with a total of 1.3 M nodes for Geometry G4.

Table 5.2 - Grid independence results for Geometry G1 for h = -14.98 mm and P_0 = 120 kPa

Mesh	$\dot{m}_L$ (kg/min)	$\dot{m}_G$ (kg/min)	Estimate of Execution Time with 8 Cores (days)
Course (0.86 M nodes)	0.1960	0.3612	7.50
Medium (1.2 M nodes)	0.1770	0.3549	16.05
Fine (3.3 M nodes)	0.1745	0.3545	52.18

Table 5.3 - Grid independence results for Geometry G3 for h = -6.89 mm and P_0 = 120 kPa

Mesh	$\dot{m}_L$ (kg/min)	$\dot{m}_G$ (kg/min)	Estimate of Execution Time with 8 Cores (days)
Course (1.2 M nodes)	0.3674	0.1105	12.18
Medium (2.8 M nodes)	0.4477	0.1139	34.68
Fine (5.0 M nodes)	0.4347	0.1161	51.97

Table 5.4 - Grid independence results for Geometry G5 for h_A = -6.53 mm and P_0 = 120 kPa

Mesh	$\dot{m}_{L,A}$ (kg/min)	$\dot{m}_{L,B}$ (kg/min)	$\dot{m}_{G,A}$ (kg/min)	$\dot{m}_{G,B}$ (kg/min)	Estimate of Execution Time with 8 Cores (days)
Course (1.0 M nodes)	2.8728	7.0209	0.1557	0.0011	5.81
Medium (1.9 M nodes)	3.1542	7.5019	0.1477	0.0569	7.93
Fine (4.5 M nodes)	3.1841	7.5144	0.1489	0.0570	16.8

5.6.2 Discretisation Schemes

ANSYS CFX uses a finite volume method in which the governing equations are discretised by integrating each equation over a three-dimensional control volume. Figure 5.12 shows how a typical two-dimensional control volume is constructed in CFX. The solid lines connecting the nodes make up four elements surrounding the node. A control volume (represented by the shaded area in Figure 5.12) is created around each node by connecting the element centres.

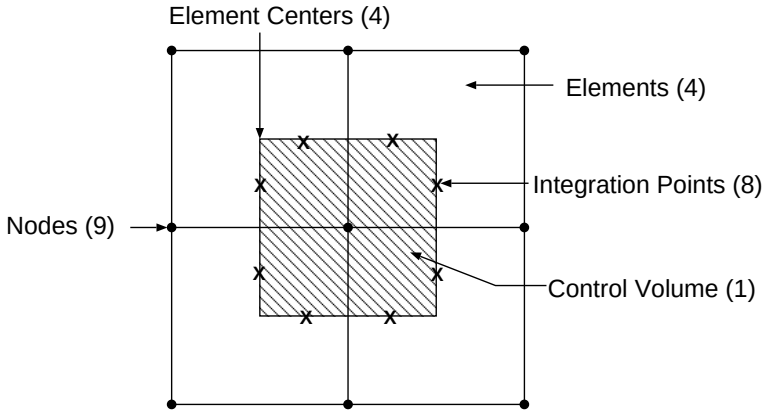

Figure 5.12 – Typical two-dimensional control volume in CFX

In CFX, all solution variables and fluid properties are stored at the nodes. Diffusion terms are discretised using standard finite element derivative approximations. The high resolution advection scheme based on the work of Barth and Jespersen (1989) was used on the advection terms in the discretised momentum equation and a second order backward Euler scheme was used on the transient terms. To help capture the interface, the free surface model uses a compressive differencing scheme on the advection terms in the continuity equation, as described by Zwart et al. (2003). The discretised equations are then solved using a fully coupled solution approach in which the velocity, pressure and volume fraction equations are solved simultaneously. Computations were performed in double precision using parallel computing with the MeTiS partitioning method and additive correction multigrid was used to accelerate convergence.

5.7 Timestep and Convergence Criteria

For multiphase flow it is often difficult to obtain low algebraic equation residuals due to small spurious waves in certain locations of the domain. Therefore, in this study, convergence was declared when the global mass and momentum imbalances were less than 0.01%, when the mass flow rates of liquid and gas at the branch outlets had leveled off to a near constant value (less than 1% change over 1000 iterations), and when the velocity and volume fraction at a selection of points (5 points spaced 1 mm apart in the *y*-direction across each branch opening and 4 points spaced 24 mm apart in the *x*-direction along the branch centrelines immediately after the inlet) had leveled off to a near constant value (less than 1% change over 1000 iterations). Due to the large number of equations that were solved, small timesteps of $1x10^{-4}$ seconds were required for the steady-state cases. For the steady-state cases for the geometries with two branches (G4 and G5), an even smaller timestep of $1x10^{-7}$ was used initially to avoid divergence and the timestep was increased linearly to $1x10^{-4}$ over 1000 iterations and then kept at this value for the remainder of the run. For the transient runs, timesteps between $1x10^{-3}$ and $1x10^{-2}$ seconds were used. With timesteps larger than these, the solution would diverge. During the transient runs, five iterations were performed at each time step. Increasing the number of iterations per timestep to ten for Geometry G3 with P_0 = 120 kPa resulted in a difference of only 0.3% in h_{OLE} and 0.04% in h_{OGE}; therefore, five iterations was considered sufficient for these analyses.

Chapter 6

Numerical Results and Discussion

6.1 Introduction

The numerical results presented in this chapter are divided into five main sections. The first section (6.2) presents the results for Geometry G3 where two-phase flow discharges from a large tank through a single circular branch of length $L_B / d = 200$. Following this, the effect of the branch cross section on the critical heights at the OLE and OGE and on the two-phase flow results will be discussed in Section 6.3 by comparing the results for Geometries G2 and G3, with square and circular branch cross sections, respectively. The effect of the branch length will then be discussed in Section 6.4 by comparing results for Geometries G1 and G2, with branch lengths of $L_B / d = 20$ and 200, respectively, and square branch cross sections. For geometries with two branches, Section 6.5 presents results for Geometry G5, where the branches are separated by a distance of $L / d = 1.5$ and an angle of $\theta = 30°$ and Section 6.6 presents results for Geometry G4, where the branches are located one-on-top of the other. The total number of cases solved with varying P_0 and h for each of the five geometries is as follows:

- Geometry G1: 31 Cases (4 OLE, 4 OGE and 23 two-phase)
- Geometry G2: 33 Cases (7 OLE, 4 OGE and 22 two-phase)
- Geometry G3: 32 Cases (8 OLE, 4 OGE and 20 two-phase)
- Geometry G4: 18 Cases (2 OLE, 2 OGE and 14 two-phase)
- Geometry G5: 44 Cases (4 OLE, 4 OGE and 36 two-phase)

The numerical results for all five geometries are tabulated in Appendix D.

6.2 Results for Geometry with Single Circular Branch (G3)

Numerical results will first be presented and discussed for the Geometry G3 consisting of a large tank with a single circular branch ($L_B / d = 200$). For this geometry, the OLE, OGE and two-phase flow results will be discussed in Sections 6.2.1, 6.2.2 and 6.2.3, respectively.

6.2.1 OLE Results for Geometry G3

For Geometry G3 with a single circular branch, the onset of liquid entrainment height, h_{OLE}, was determined at eight different values of P_0, each corresponding to a different gas Froude number, $\mathrm{Fr}_{G,OLE}$, where,

$$\mathrm{Fr}_{G,OLE} = \frac{\dot{m}_{G,OLE}}{A_c \sqrt{gd\rho_G(\rho_L - \rho_G)}} \tag{6.1}$$

where A_c is the cross sectional area of the branch. Results were obtained at P_0 = 0.015, 0.1, 1, 4, 12, 35, 120 and 400 kPa which corresponded to $\mathrm{Fr}_{G,OLE}$ = 0.23, 0.61, 2.06, 4.32, 7.71, 13.19, 22.55, and 36.46, respectively. Figure 6.1 (a) to (c) shows the air volume fraction contours on the symmetry plane from the transient results for $\mathrm{Fr}_{G,OLE}$ = 22.55. The red region in these figures represents mostly air ($0.975 < \alpha_G < 1$) and the blue region represents mostly water ($0.975 < \alpha_L < 1$). The interface region between α_G = 0.975 and α_L = 0.975 is approximately 1.5 mm thick. It can be seen that, in Figure 6.1 (a) when h = -14.205 mm, the interface is located far beneath the branch inlet and $\alpha_{G,BB}$ = 1. By raising the interface slightly to h = -14.189 mm, as indicated in Figure 6.1 (b), the water has climbed the wall slightly but $\alpha_{G,BB}$ is still equal to 1. Almost instantaneously after this timestep, the water climbed the wall underneath the branch inlet further (Figure 6.1 (c)) and $\alpha_{G,BB}$ dropped from 1 to 0.997, indicating that a small amount of water was exiting the branch. This phenomenon was taken as the OLE and was observed to occur suddenly (within a 0.002 mm rise of the interface from Figure 6.1 (b) to (c)), consistent with previous experimental observations (e.g., Bartley et al., 2008; Hassan, 1995; Armstrong et al., 1992).

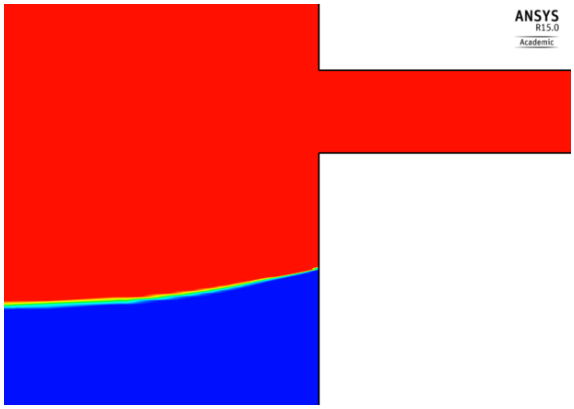

(a) $\alpha_{G,BB} = 1$ and h = -14.205 mm

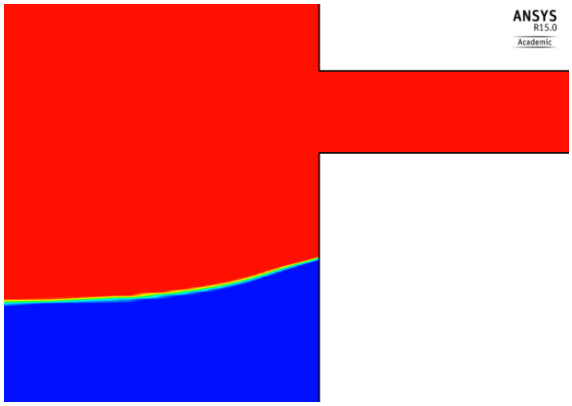

(b) $\alpha_{G,BB} = 1$ and h = -14.189 mm

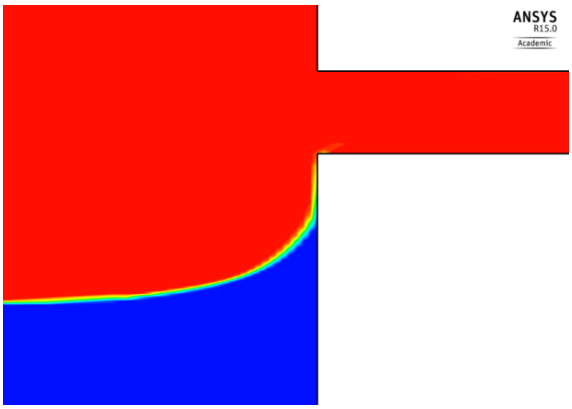

(c) $\alpha_{G,BB} = 0.997$ and h = -14.187 mm

Figure 6.1 - Air volume fraction contours for Geometry G3 for $\mathrm{Fr}_{G,OLE}$ = 22.55 near the OLE

Results of pressure and air volume fraction from the numerical results were used to provide some insight into the balance of forces in the liquid region under the branch inlet immediately before the onset of liquid entrainment. Figure 6.2 is a schematic of the interface beneath the branch inlet, shortly before the OLE. The location where the interface meets the wall will be referred to as IU and the location at the wall corresponding to the height of the flat interface far from the wall is IL.

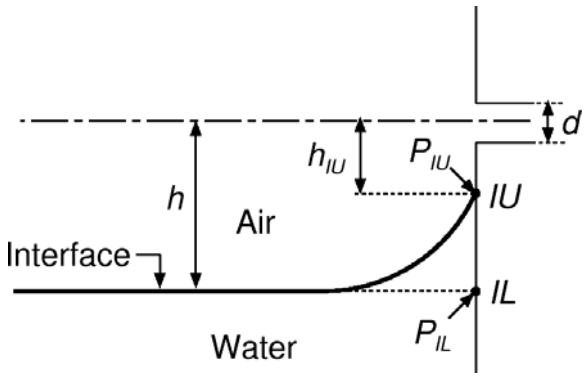

Figure 6.2 - Schematic of interface near OLE

In Figure 6.3 (a) and (b), the pressure difference, $P_{IL} - P_{IU}$, and $\alpha_{G,BB}$ are plotted versus the hydrostatic pressure difference, $\rho_L g\Delta h$, where $\Delta h = \left|h - h_{IU}\right|$. The data points plotted in these figures correspond to results at consecutive time steps, spaced 1×10^{-3} seconds apart, just before the onset of liquid entrainment occurs. In Figure 6.3 (a), the model was solved with no surface tension effects; therefore, before the onset of liquid entrainment occurs and while the velocity of the water underneath the branch is zero, the pressure difference and hydrostatic head are approximately balanced (i.e., $P_{IL} - P_{IU} \approx \rho_L g\Delta h$). As the interface is raised, the fluid climbs the wall and $P_{IL} - P_{IU}$ increases uniformly with $\rho_L g\Delta h$ until the onset of liquid entrainment is approached, at which time P_{IU} suddenly drops and $P_{IL} - P_{IU} >> \rho_L g\Delta h$. The air volume fraction, $\alpha_{G,BB}$, is equal to 1 until the onset of liquid entrainment occurs, at which time the air volume fraction first drops below 1; this first drop in $\alpha_{G,BB}$ coincides with the timestep just before $P_{IL} - P_{IU}$ begins to increase rapidly. The results shown in Figure 6.3 (b) were obtained by including surface tension effects in the model. The addition of surface tension slightly modifies the balance between $P_{IL} - P_{IU}$ and $\rho_L g\Delta h$ and causes Δh to increase relative to the case with no surface tension; however, the start of the sharp increase in $P_{IL} - P_{IU}$ is still coincident with the condition of $\alpha_{G,BB}$ deviating from 1. The onset of liquid entrainment height was therefore defined as the interface height when the air volume fraction first drops below 1 and is indicated by the solid black circles and squares in Figure 6.3 (a) and (b).

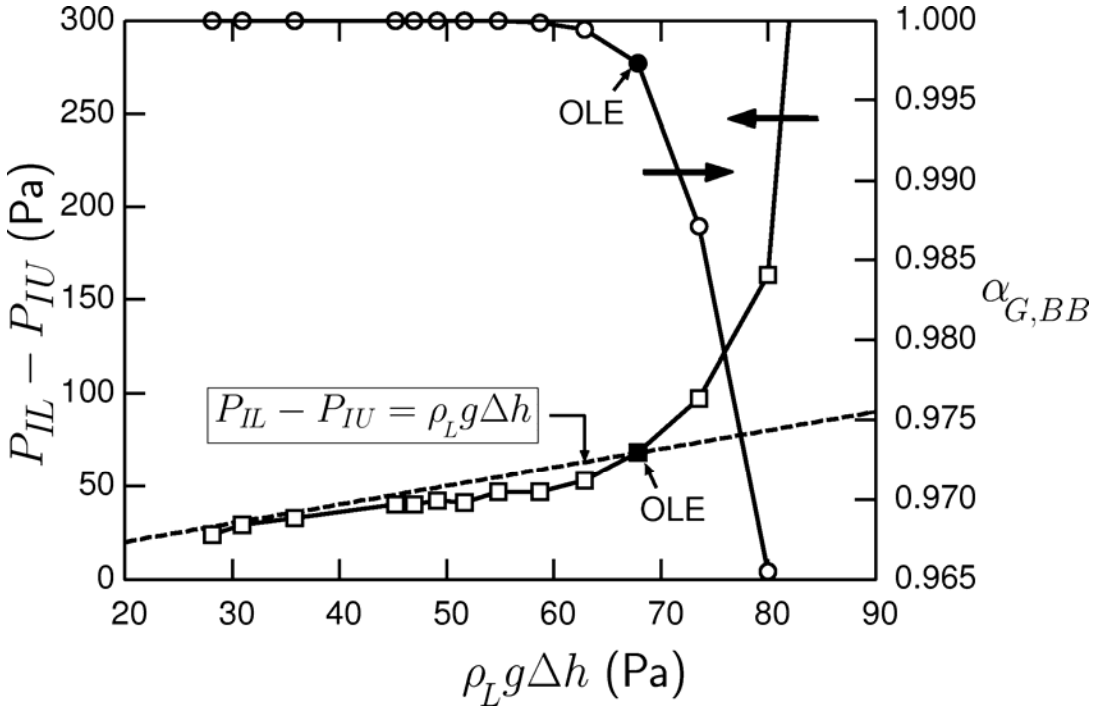

(a)

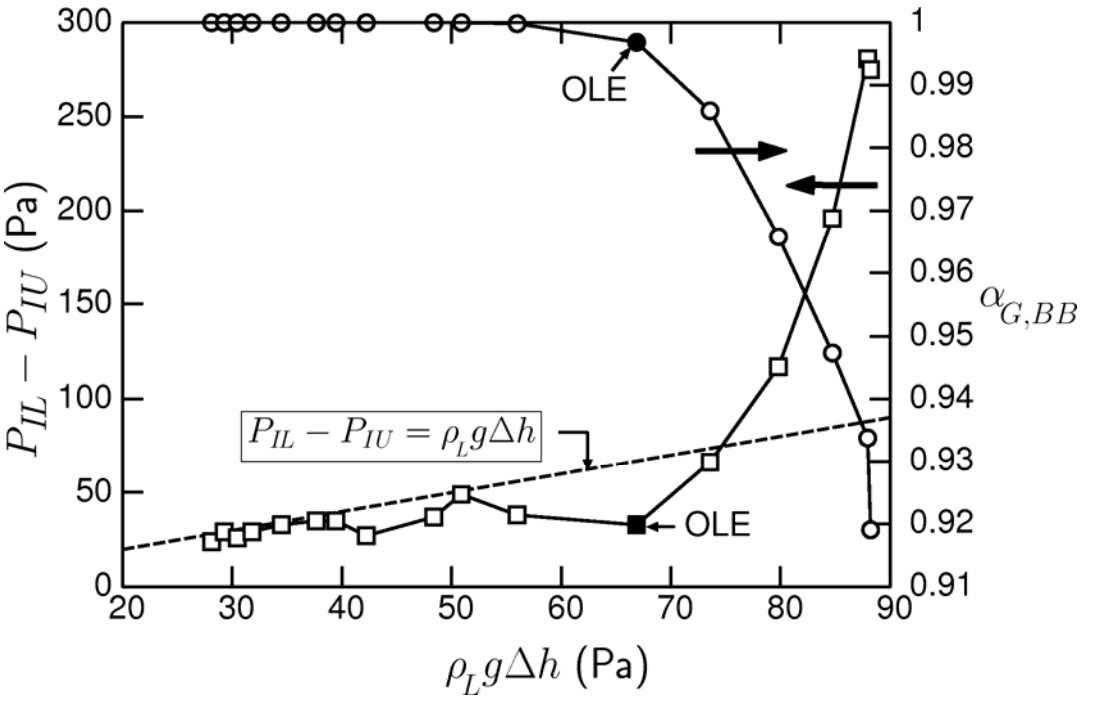

(b)

Figure 6.3 - Pressure difference, hydrostatic pressure and air volume fraction for $Fr_{G,OLE}$ = 22.55 near the OLE

The results for $|h_{OLE}|/d$ are plotted versus $\mathrm{Fr}_{G,OLE}$ in Figure 6.4, along with the theoretical models developed by Craya (1949) and Soliman and Sims (1992), the correlation developed by Yonomoto and Tasaka (1988), and a correlation based on the present numerical results. From this figure it can be observed that the present numerical data agree well with all the equations at higher $\mathrm{Fr}_{G,OLE}$ and agree well with Soliman and Sims' model at low $\mathrm{Fr}_{G,OLE}$. As $\mathrm{Fr}_{G,OLE}$ approaches zero, it is expected that $|h_{OLE}|/d$ will tend to approach 0.5. This limit is accurately represented by the present data and the Soliman and Sims' model, which simulated the branch as an opening of finite diameter. The theoretical model developed by Craya and later adjusted by Yonomoto and Tasaka; however, was derived by simulating the branch as a point sink and therefore, $|h_{OLE}|/d \rightarrow 0$ as $\mathrm{Fr}_{G,OLE} \rightarrow 0$. The following equation was fit to the numerical data using non-linear least squares and is shown as a solid black line in Figure 6.4:

$$|h_{OLE}|/d = 0.5\left(1 + 7.727\,\mathrm{Fr}_{G,OLE}{}^{2.058}\right)^{0.184} \tag{6.2}$$

This equation shows excellent agreement with the numerical data with an RMS deviation of 2.3%. At the limit of $\mathrm{Fr}_{G,OLE} \rightarrow 0$, Equation (6.2) reduces to the correct limit of $|h_{OLE}|/d = 0.5$ and as $\mathrm{Fr}_{G,OLE}$ becomes large, Equation (6.2) takes the form of Equation (2.1) with $C_1 = 0.728$ and $C_2 = 0.379$.

6.2.2 OGE Results for Geometry G3

Onset of gas entrainment results were obtained for Geometry G3 at four different pressures, P_0 = 12, 35, 120 and 400 kPa, corresponding to liquid Froude numbers of $\mathrm{Fr}_{L,OGE}$ = 7.62, 13.58, 26.51 and 51.13, respectively, where $\mathrm{Fr}_{L,OGE}$ is given by:

$$\mathrm{Fr}_{L,OGE} = \frac{\dot{m}_{L,OGE}}{A_c\sqrt{gd\rho_L(\rho_L - \rho_G)}} \tag{6.3}$$

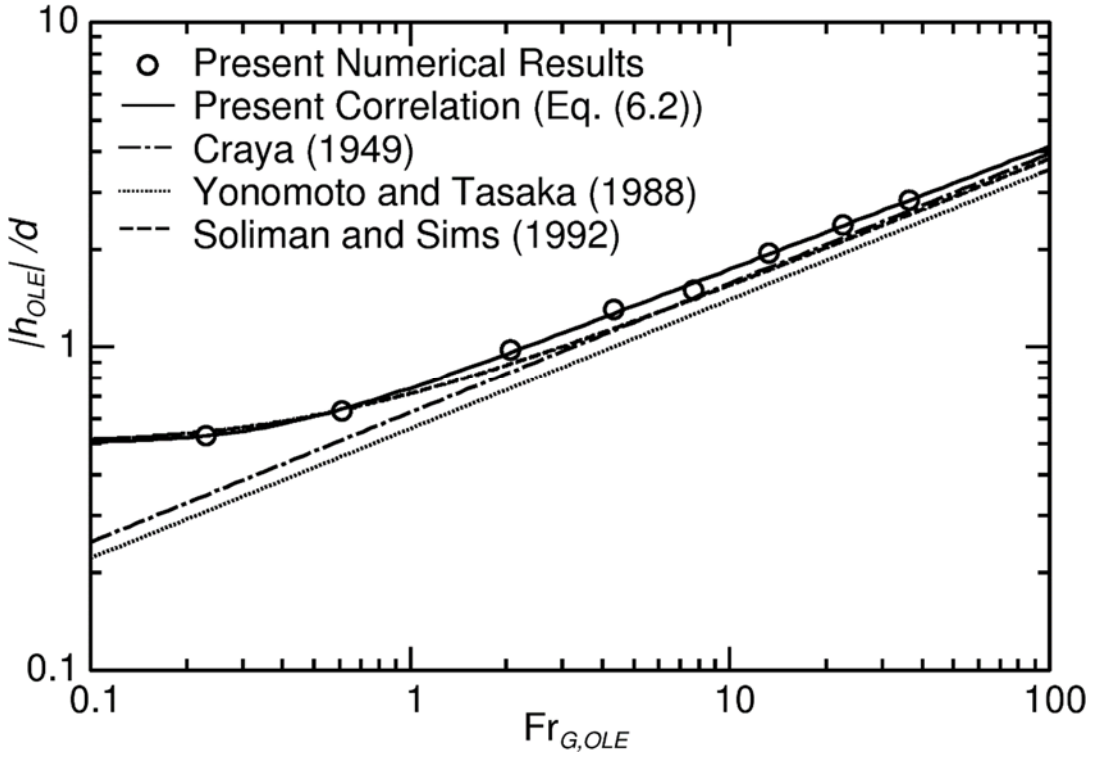

Figure 6.4 - Interface height at the onset of liquid entrainment for Geometry G3

In order to illustrate the appearance of the phenomena as predicted by the CFD code, the OGE results were taken at four different time steps. Time $\tau_1 = 0$ seconds was selected as a datum during the transient OGE simulations and times τ_2, τ_3 and τ_4 correspond to 0.5, 0.75 and 1 second, respectively; these times are separated by 25 time steps in the transient solution. Figure 6.5 (a) to (d) shows the results for the air volume fraction contours on the symmetry plane for $\mathrm{Fr}_{L,OGE} = 26.51$ at times τ_1, τ_2, τ_3 and τ_4. The red region in these figures represents nearly 100% air ($0.975 \leq \alpha_G \leq 1$) and the colours of the contours follow a rainbow pattern with decreasing α_G down to blue at $\alpha_G = 0.025$. Grey was selected for the colour of the region with nearly 100% water ($0 \leq \alpha_G \leq 0.025$) to highlight the cone that is beginning to form in Figure 6.5 (b). Values for the air volume fraction at the top of the branch inlet along the symmetry plane, $\alpha_{G,BT}$, are shown next to the contours. As the flat interface approaches the onset height, the interface near the wall dips above the branch inlet (Figure 6.5 (a)). With a slight decrease in the interface height, a gas cone begins to form beneath the interface near the wall but does not yet reach the branch inlet (Figure 6.5 (b)). As the interface is lowered further, the gas cone extends from the interface to the branch

inlet without fully contacting the wall (Figure 6.5 (c)). A very slight drop further in the interface height causes the gas cone to break through the liquid and the air to flow freely along the wall above the branch as it enters the branch inlet (Figure 6.5 (d)).

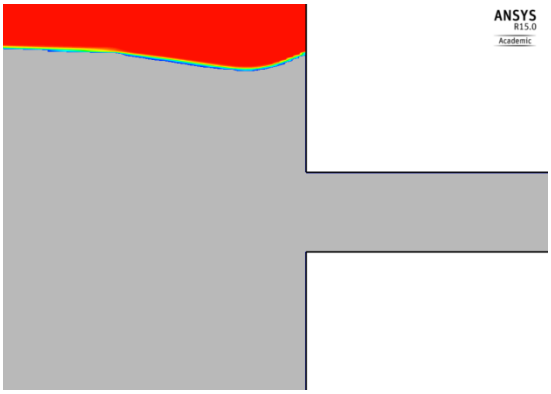

(a) $\tau = \tau_1$, $\alpha_{G,BT} = 0$, $h = 12.333$ mm

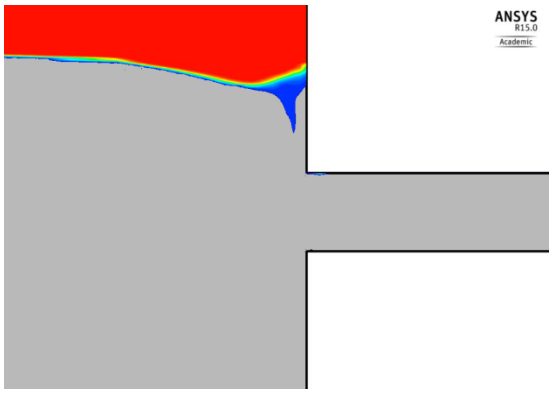

(b) $\tau = \tau_2$, $\alpha_{G,BT} = 0.013771$, $h = 12.139$ mm

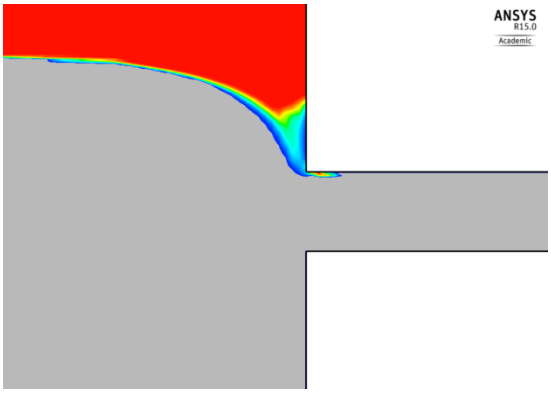

(c) $\tau = \tau_3$, $\alpha_{G,BT}$ =0.18805, h =11.895 mm

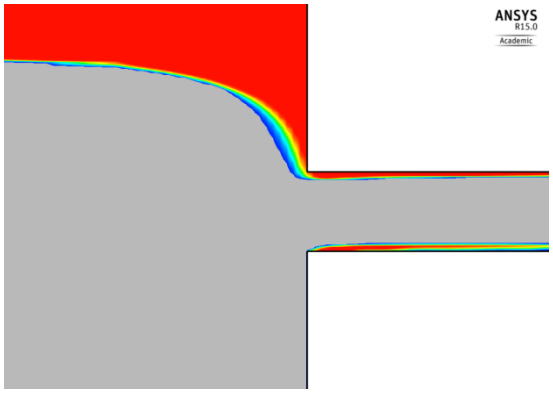

(d) $\tau = \tau_4$, $\alpha_{G,BT}$ =0.91482, h =11.890 mm

Figure 6.5 - Air volume fraction contours for Geometry G3 for $\mathrm{Fr}_{L,OGE} = 26.51$ near the OGE

The selection of the timestep corresponding to the OGE was determined by monitoring $\alpha_{G,BT}$ and the mass flow rate of gas through the branch, $\dot{m}_G$, versus time, τ, just before and after the OGE. A sample of these results is shown in Figure 6.6 for $\mathrm{Fr}_{L,OGE} = 26.51$ (the case shown in Figure 6.5). The times τ_1 to τ_4 corresponding to Figure 6.5 (a) to (d) are labelled on the *x*-axis of the figures. In a typical run, both $\alpha_{G,BT}$ and $\dot{m}_G$ fluctuated just above zero for some time before

they rose sharply, as shown in Figure 6.6. The results for $\alpha_{G,BT}$ and $\dot{m}_G$ were monitored in each test run and the OGE height was then taken as the height of the flat interface at the timestep just before the start of the sharp increase in $\alpha_{G,BT}$ and $\dot{m}_G$. There is an element of judgement involved in selecting the timestep corresponding to the OGE; however, the precise selection does not have a significant effect on the result for h_{OGE}/d. For the case shown in Figures 6.5 and 6.6, from τ_2 to τ_3 (25 timesteps), h decreased by only 0.244 mm which corresponds to h/d = 0.04. Also, the OGE phenomenon occurs very quickly; $\alpha_{G,BT}$ rose from 0.1 to 0.83 in just 0.09 seconds. For this case, the time at which the OGE occurred was selected as τ_3 and h_{OGE} = 11.895 mm.

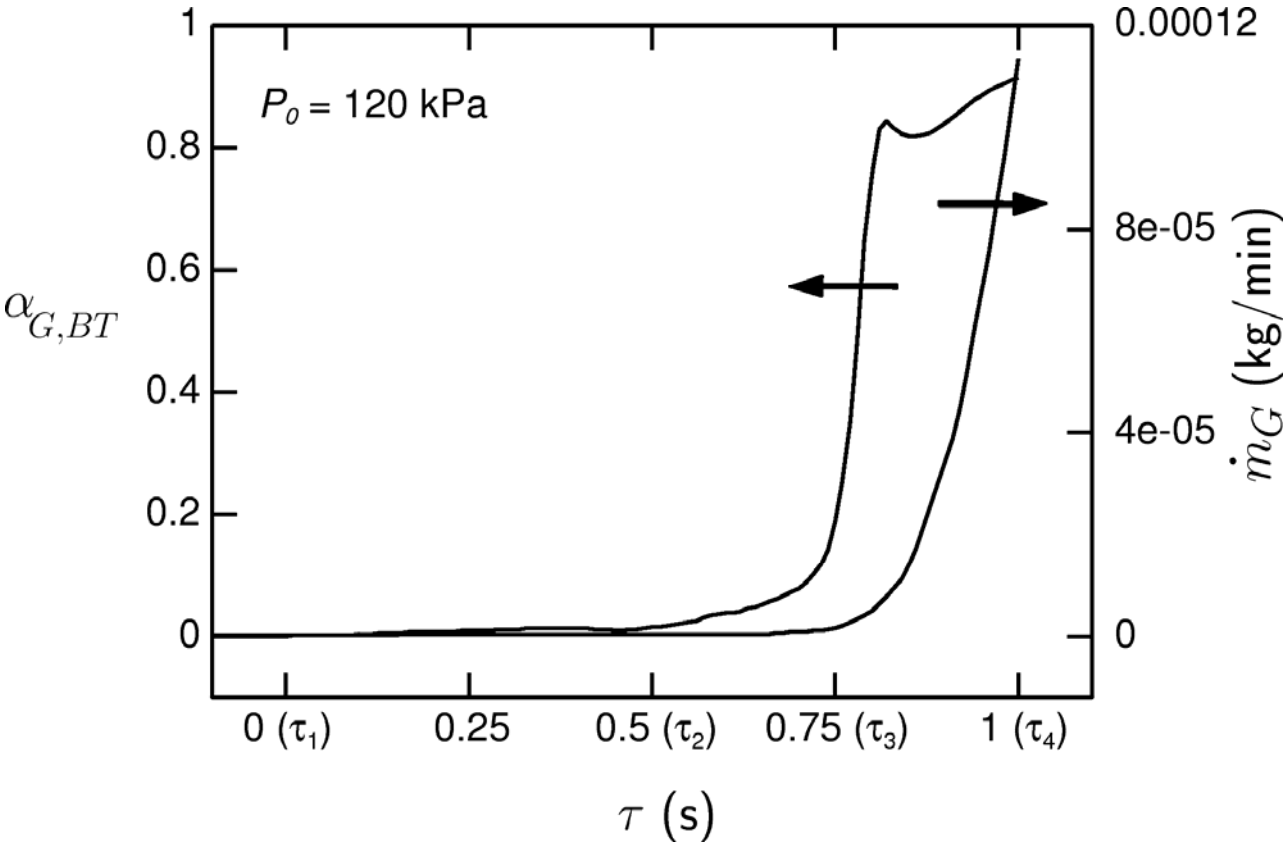

Figure 6.6 - Transient results of $\alpha_{G,BT}$ and $\dot{m}_G$ versus timestep near the OGE for Geometry G3

Insight into the formation of the gas cone can be obtained by observing the pressure contours on an x-y plane located 2.5 mm away from the symmetry plane (z = 60 mm). These contours are plotted in Figure 6.7 parts (a) to (d) at these same four timesteps, τ_1, τ_2, τ_3 and τ_4, in

the region near the branch inlet. Before the OGE (τ_1), the pressure just below the interface increases from 3 Pa relative to P_0 (contour level 3) to 11 Pa (contour level 4) before decreasing towards the branch inlet. This region of increasing pressure just below the interface would inhibit the formation of a gas cone because there is no clear path between the interface and the branch inlet where the pressure is decreasing continuously. At τ_2 (Figure 6.7 (b)), the interface has dropped slightly and the pressure in the region beneath the interface has dropped; however, there is still no clear path of continuously decreasing pressure from the interface to the branch opening. Figure 6.7 (c) shows that at τ_3, although there is still a high pressure region next to the wall above the branch, there is now an obvious path of decreasing pressure from the interface dip to the branch inlet. This path of decreasing pressure allows gas to flow into the branch while the high pressure region next to the wall prevents the gas from flowing along the wall; this explains the formation of a gas cone at τ_3 as was observed in Figure 6.5 (c). These observations support the selection of τ_3 as the time at which the OGE occurred. After the OGE, at τ_4, Figure 6.7 (d) shows that the high pressure region next to the wall above the branch has disappeared and there is a continuous path of decreasing pressure from the air to the branch inlet as air flows freely into the branch.

Figure 6.8 shows the numerical results of h_{OGE}/d versus $Fr_{L,OGE}$ along with the correlations of Micaelli and Memponteil (1989), Yonomoto and Tasaka (1988) and Hassan (1995). The numerical data were fitted by the following equation, which is shown in Figure 6.8 as a solid line:

$$h_{OGE}/d = 0.560\mathrm{Fr}_{L,OGE}^{0.399} \tag{6.4}$$

From Figure 6.8 it can be seen that the present results are consistent with existing empirical correlations. Equation (6.4) agrees well with the numerical results with an RMS deviation of 3.1% and is very close to Hassan's correlation.

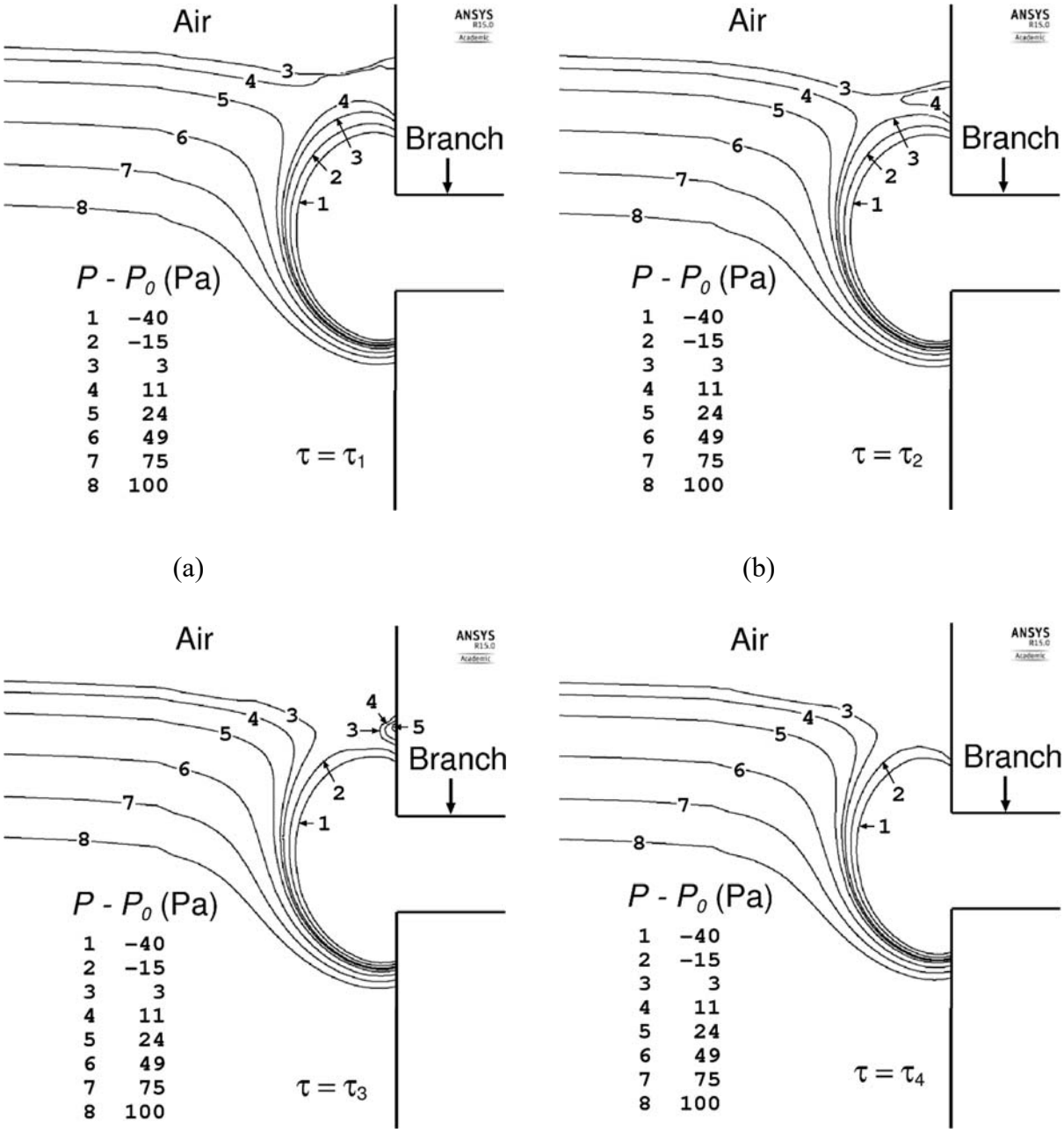

(a) (b)

(c) (d)

Figure 6.7 - Pressure contours for Geometry G3 for $\mathrm{Fr}_{L,OGE} = 26.51$

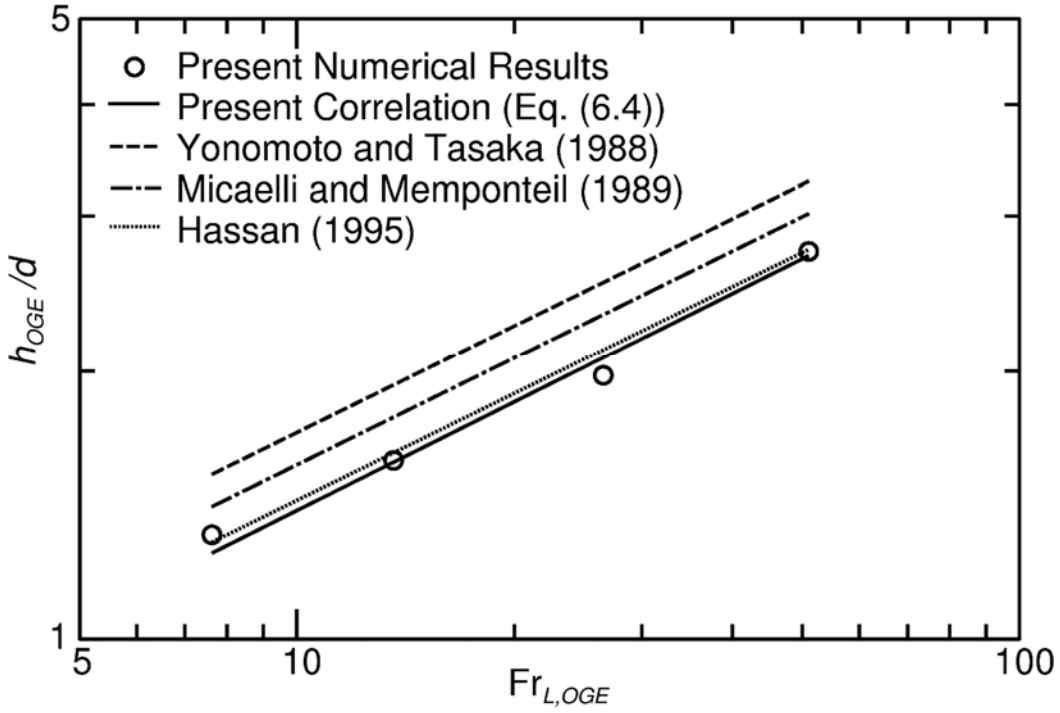

Figure 6.8 - Interface height at the onset of gas entrainment for Geometry G3

6.2.3 Two-Phase Flow Results for Geometry G3

For tests involving two-phase flow through a single circular branch, results for the total mass flow rate, $\dot{m}_{TP}$, and mixture quality, x, at the branch outlet were obtained for various interface heights at two tank pressures: P_0 = 35 kPa and 120 kPa. Figure 6.9 shows $\dot{m}_{TP}$ versus h for the two values of P_0. For each P_0, data are presented from $h = h_{OLE}$ to $h = h_{OGE}$. From this figure it can be seen that as P_0 increases, $\dot{m}_{TP}$ increases for the same interface height. As well, h_{OGE} and $|h_{OLE}|$ increase as P_0 increases.

The present numerical results for P_0 = 35 kPa and 120 kPa are plotted in Figure 6.10 in terms of M versus H and in Figure 6.11 in terms of x versus H, where M and H are defined by Equations (2.5) and (2.6). The correlations developed by Hassan (1995) are shown in these figures as solid lines. From these figures it can be seen that the effect of P_0 on the numerical results is absorbed when the data are plotted using the dimensionless parameters. In addition, the present numerical results show very good agreement with the Hassan correlations.

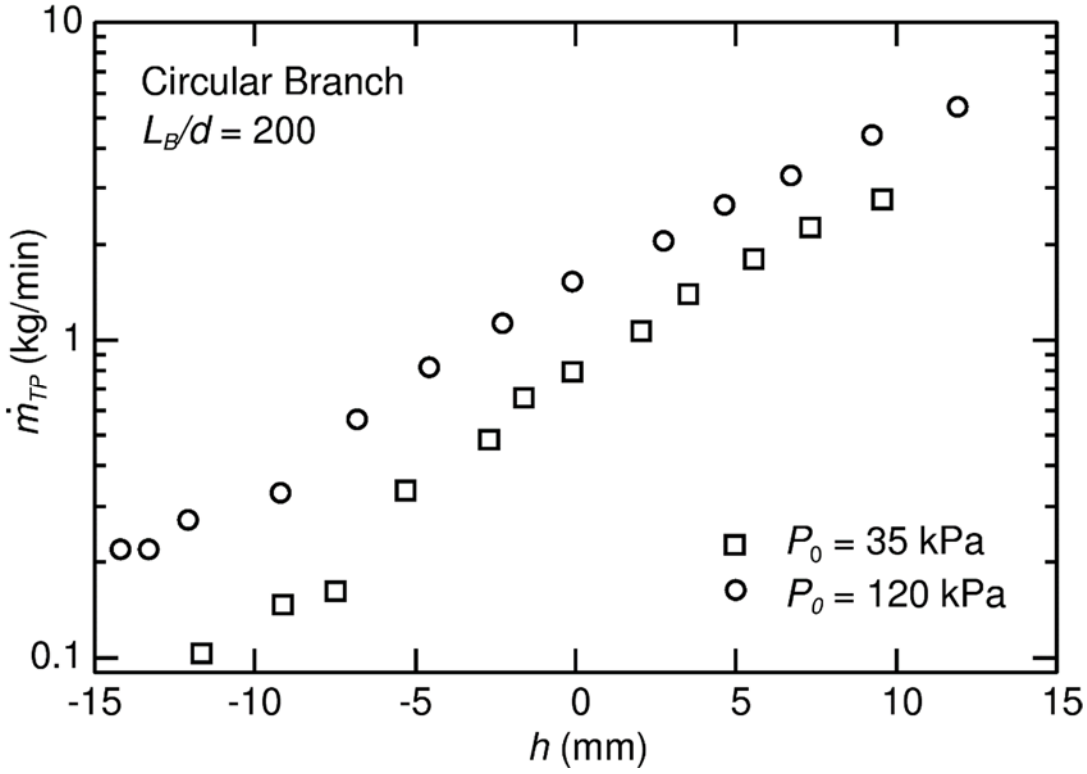

Figure 6.9 - $\dot{m}_{TP}$ versus h for P_0 = 35 and 120 kPa for Geometry G3

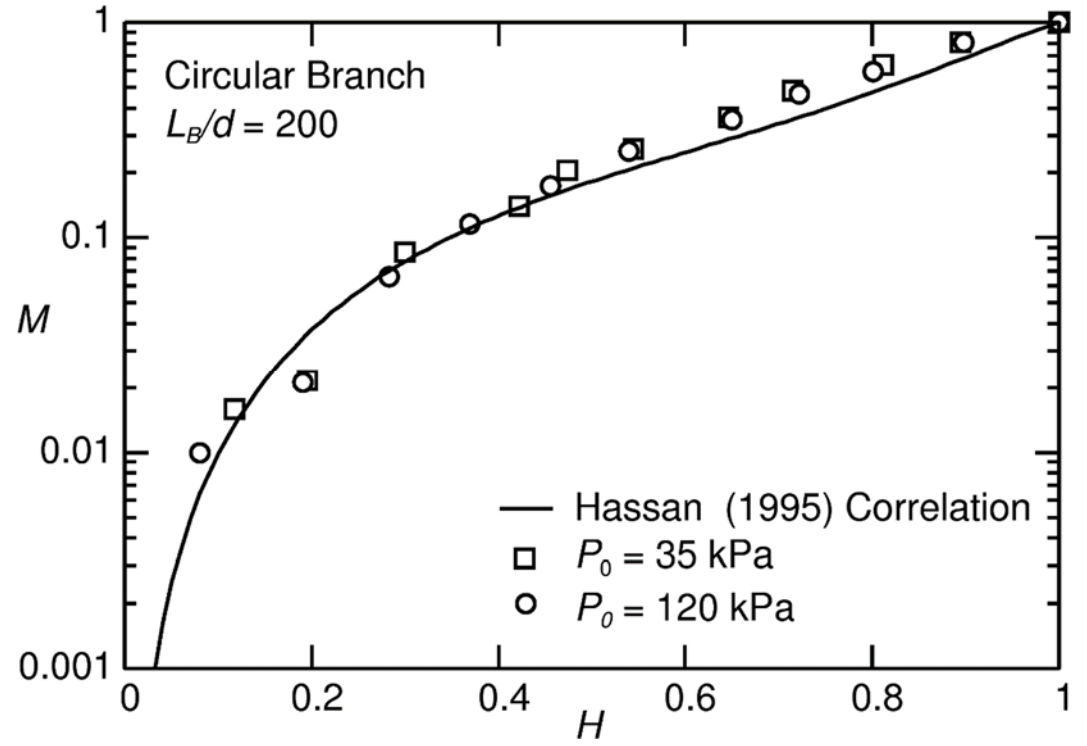

Figure 6.10 - M versus H for P_0 = 35 and 120 kPa for Geometry G3

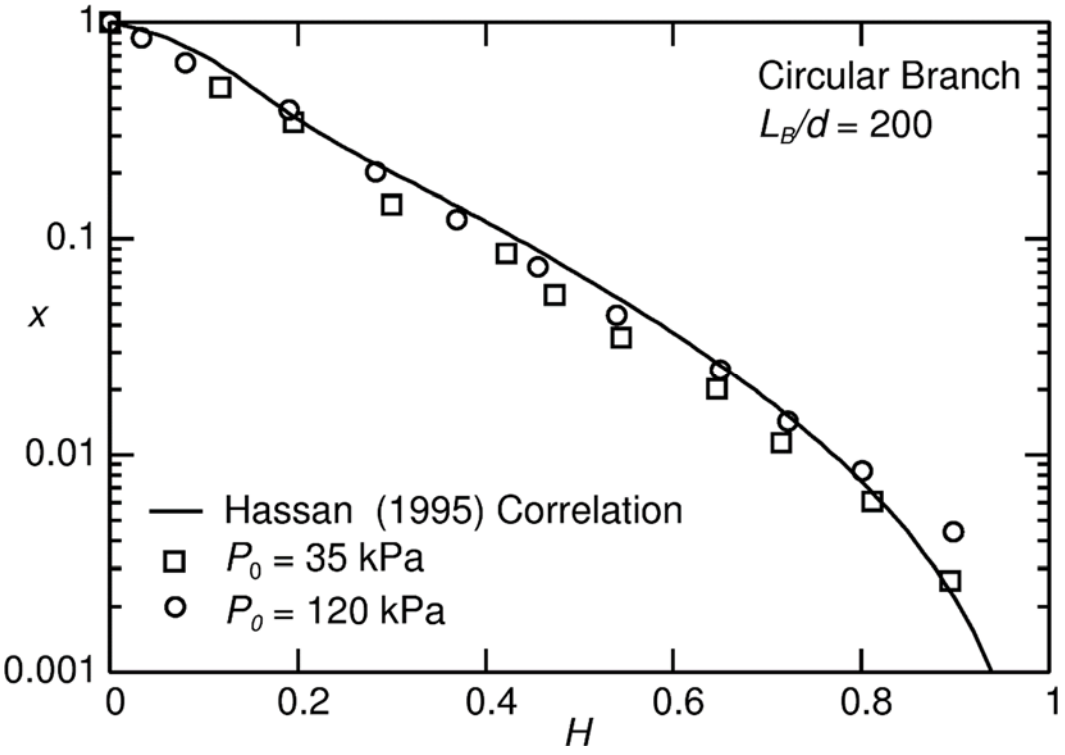

Figure 6.11 - x vs. H for P_0 = 35 and 120 kPa for Geometry G3

6.2.4 Summary of Results for Geometry G3

The results obtained for the critical heights h_{OLE} and h_{OGE} and the mass flow rate $\dot{m}_{TP}$ and quality x of the two-phase discharge agreed well in magnitude and trend with existing experimental data. In addition, the numerical model provides additional results that have not been obtained experimentally, including pressure contours and force balances at the onsets of gas and liquid entrainment, respectively. These results provided insight into the flow characteristics just before the onsets. It is therefore concluded that for Geometry G3, ANSYS CFX is capable of predicting the correct flow phenomena.

6.3 The Effect of Branch Cross Section on Single Branch Results

In order to analyse the effects of the branch cross section on the OLE, OGE and two-phase flow results, the numerical results for Geometries G2 and G3 are compared. Geometries G2 and G3 are identical with the exception of the branch in Geometry G2 has a square cross section (6 mm x 6 mm) and the branch in Geometry G3 has a circular cross section (d = 6 mm).

Results of $|h_{OLE}|/d$ versus $\mathrm{Fr}_{G,OLE}$ from both Geometries G2 and G3 are compared in Figure 6.12. For the geometry with a square branch, a hydraulic diameter of 6 mm was used for d on the vertical axis of this figure, and in the equation used to calculate $\mathrm{Fr}_{G,OLE}$ (Equation (6.1)). The results show that for $\mathrm{Fr}_{G,OLE} > 5$, $|h_{OLE}|/d$ is approximately 10% higher for the geometry with the square branch compared to the geometry with the circular branch. One possible explanation for this is that the suction through the corners of the square branch inlet helps with earlier liquid entrainment. As $\mathrm{Fr}_{G,OLE} \rightarrow 0$, Figure 6.12 shows that $|h_{OLE}|/d \rightarrow 0.5$ for both geometries.

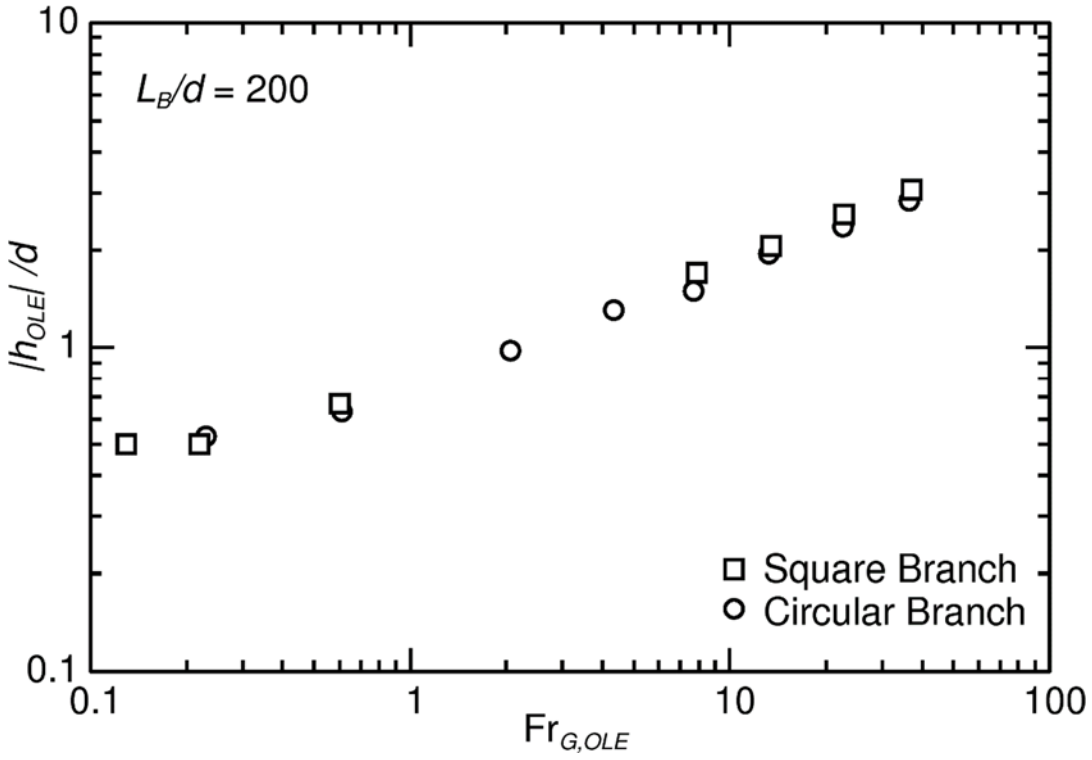

Figure 6.12 - Effect of branch cross section on $|h_{OLE}|/d$ versus $\mathrm{Fr}_{G,OLE}$

The effect of the branch cross section on the OGE results of h_{OGE}/d versus $\mathrm{Fr}_{L,OGE}$ is shown in Figure 6.13. Similar to the OLE results, h_{OGE}/d is approximately 10% higher for the geometry with the square branch compared to the geometry with the circular branch.

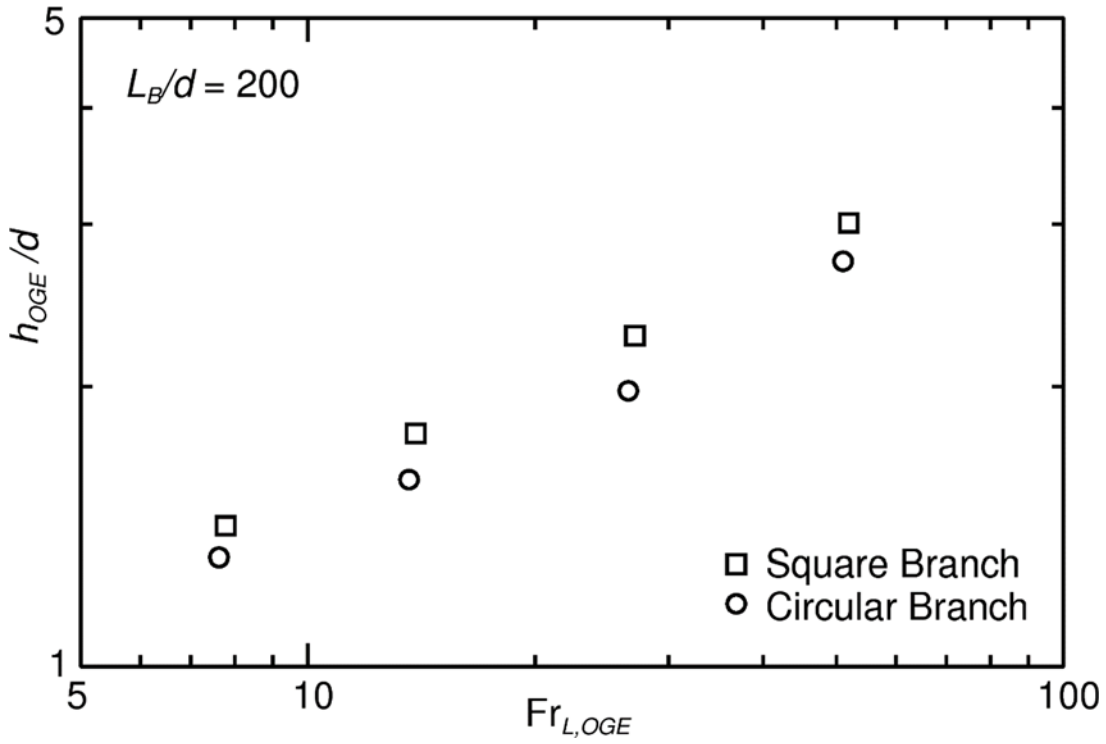

Figure 6.13 - Effect of branch cross section on h_{OGE}/d versus $\mathrm{Fr}_{L,OGE}$

Results for $\dot{m}_{TP}$ versus h are plotted in Figure 6.14 for Geometries G2 and G3 for P_0 = 120 kPa to show the effect of the branch cross section on the two-phase flow results. From this figure it can be seen that for the same h, $\dot{m}_{TP}$ is slightly higher for the geometry with the square branch compared to the geometry with the circular branch. The larger mass flow rates in the square branch may be a result of the larger cross sectional area.

The numerical results for the cases plotted in Figure 6.14 are plotted again in Figure 6.15 in terms of M versus H, and in Figure 6.16 in terms of x versus H, along the single branch correlations of Hassan (1995) for a single circular branch. These results show that when the numerical data are plotted in terms of the dimensionless parameters, the effect of the branch cross section is mostly absorbed and both sets of data agree well with Hassan's correlations.

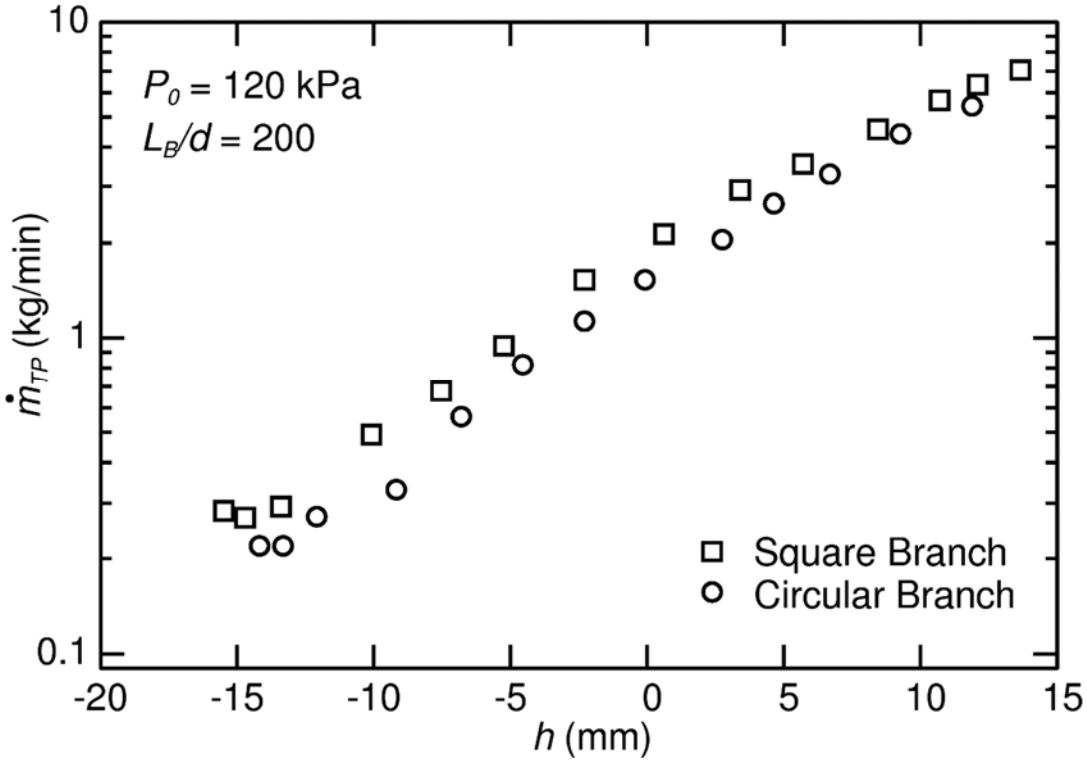

Figure 6.14 - Effect of branch cross section on $\dot{m}_{TP}$ versus h for P_0 = 120 kPa

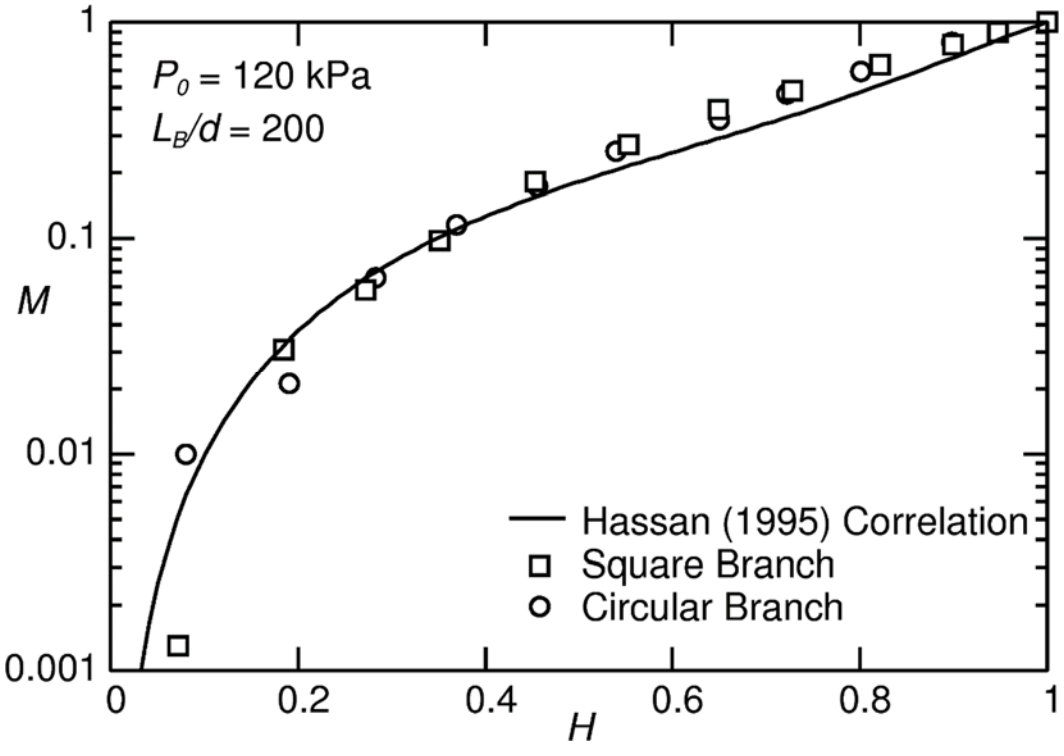

Figure 6.15 - Effect of branch cross section on M versus H for P_0 = 120 kPa

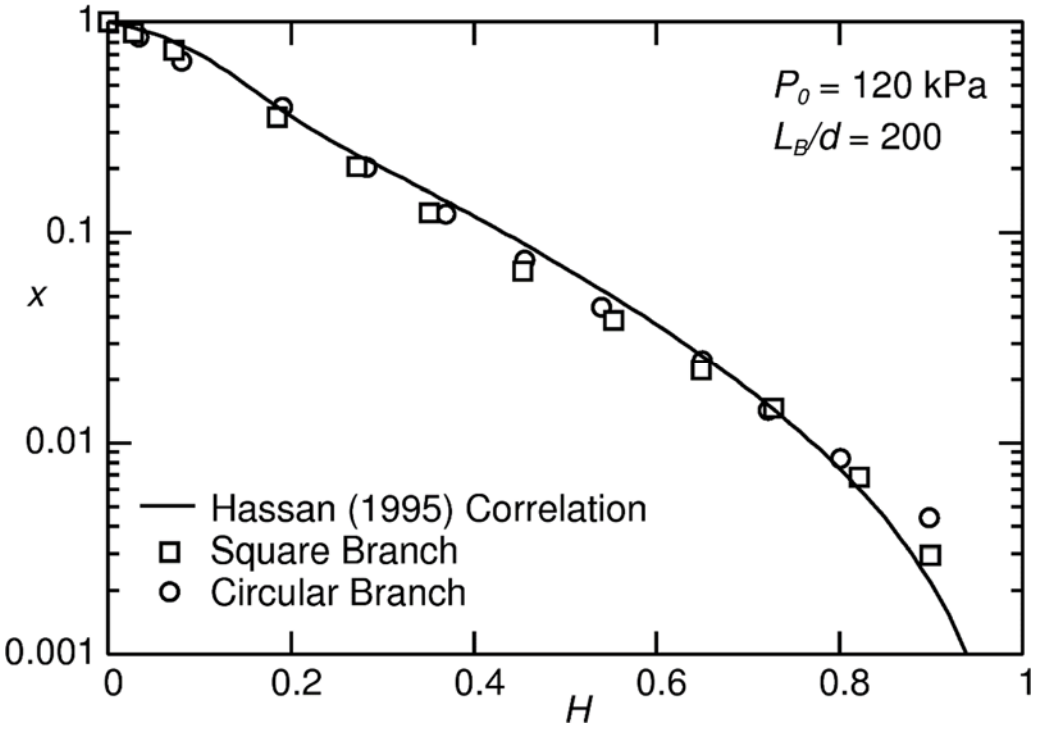

Figure 6.16 - Effect of branch cross section on x versus H for P_0 = 120 kPa

In summary, the numerical results show that a square branch cross section slightly increases the magnitudes of the onset of liquid and gas entrainment critical heights and increases the two-phase mass flow rate through the branch when compared with the circular branch cross section. However, the effect of the branch cross section is largely absorbed when the results are plotted as M versus H and x versus H and the results agree well with previous experimental correlations.

6.4 The Effect of Branch Length on Single Branch Results

The effect of the branch length on the OLE, OGE and two-phase flow results is analyzed by comparing results for Geometry G1 which has a single short square branch (L_B / d = 20) with results from Geometry G2 which has a single long square branch (L_B / d = 200). Aside from the branch length, these two geometries are identical.

For the OLE and OGE, results for Geometries G1 and G2 of $|h_{OLE}|/d$ versus $\mathrm{Fr}_{G,OLE}$ and h_{OGE}/d versus $\mathrm{Fr}_{L,OGE}$ are plotted in Figures 6.17 and 6.18, respectively. These results show that the effect of the branch length is small for the OLE and negligible for the OGE.

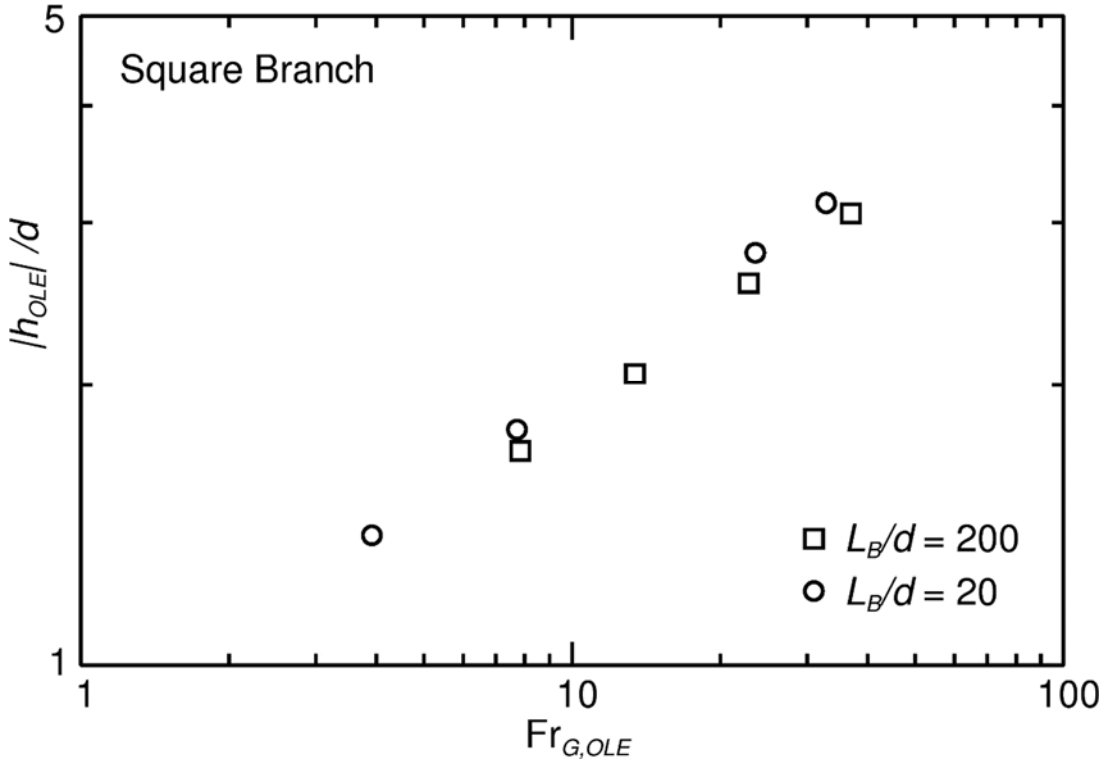

Figure 6.17 - Effect of branch length on $|h_{OLE}|/d$ versus $Fr_{G,OLE}$

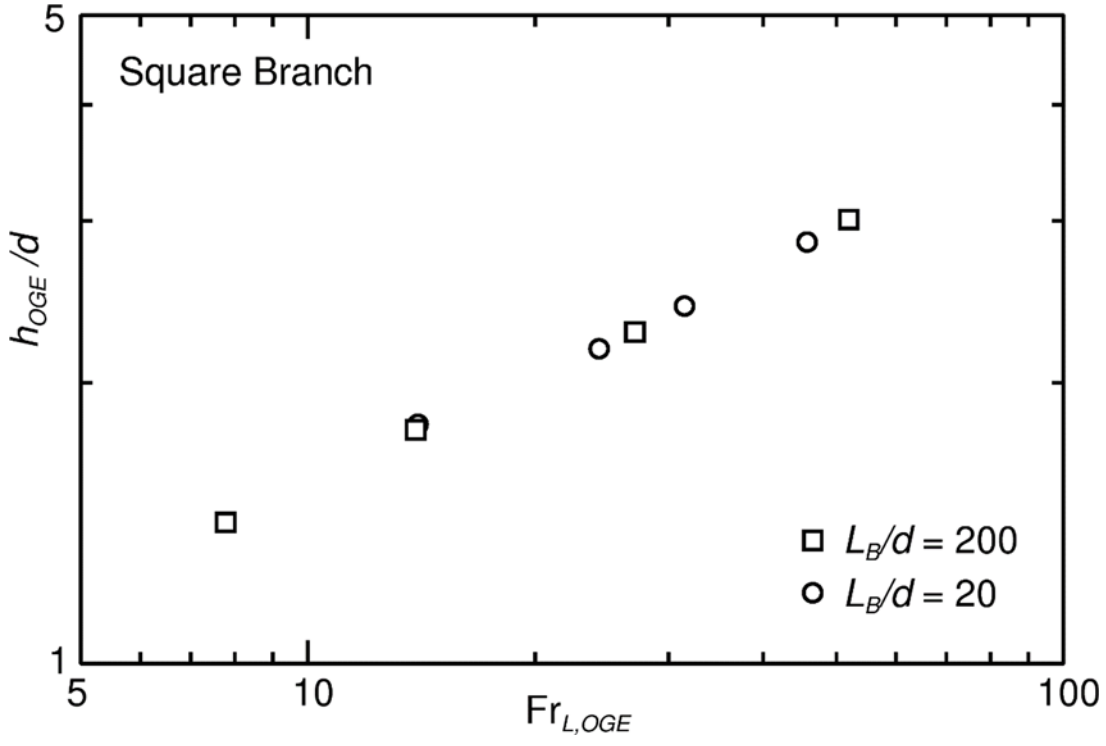

Figure 6.18 - Effect of branch length on h_{OGE}/d versus $Fr_{L,OGE}$

The two-phase flow results of $\dot{m}_{TP}$ versus h for Geometries G1 and G2 with P_0 = 120 kPa are plotted in Figure 6.19. These results show that the mass flow rate decreases with increasing branch length; this trend was expected because increasing the branch length is equivalent to increasing the resistance in the branch.

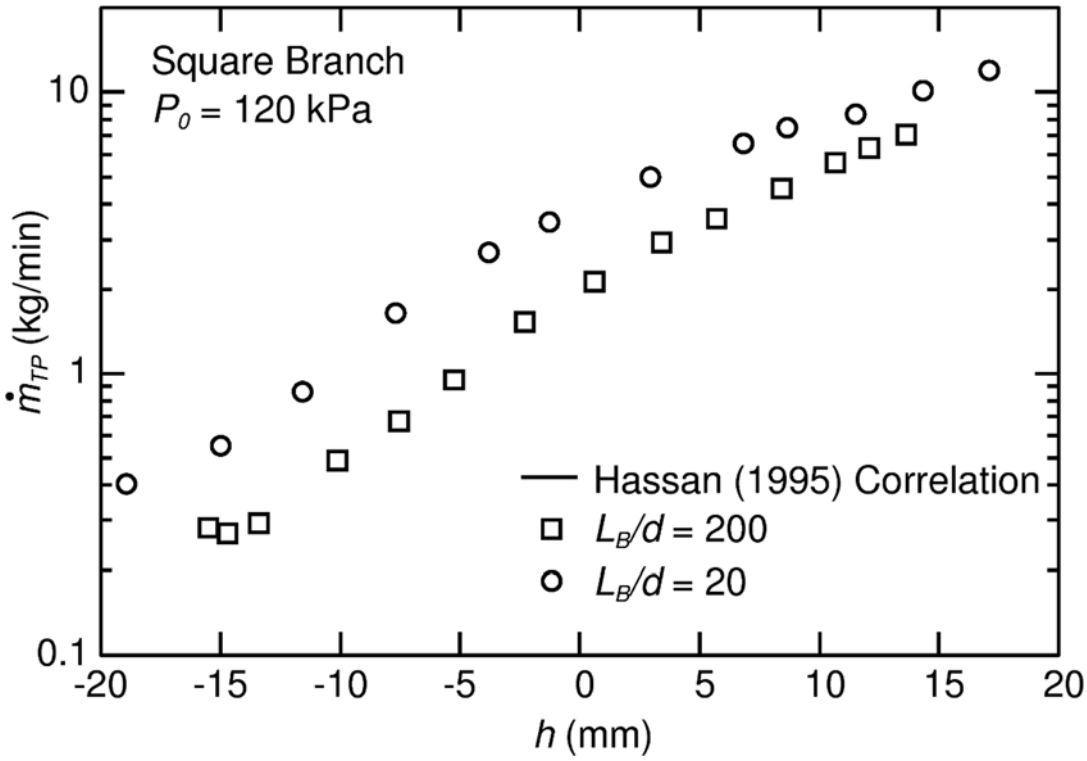

Figure 6.19. Effect of branch length on $\dot{m}_{TP}$ versus h for P_0 = 120 kPa

As was previously observed, the effects of P_0 and the branch cross section were absorbed when the two-phase flow results were plotted using the dimensionless parameters M (Equation (2.5)), x, and H (Equation (2.6)). The numerical results for Geometries G1 and G2 for P_0 = 120 kPa are now plotted using these same dimensionless parameters in Figures 6.20 and 6.21, along with Hassan's (1995) correlations. These figures show that the effect of the branch length is largely absorbed when the data are plotted as M versus H (Figure 6.20) and as x versus H (Figure 6.21). In addition, the results show reasonable agreement with the Hassan correlations.

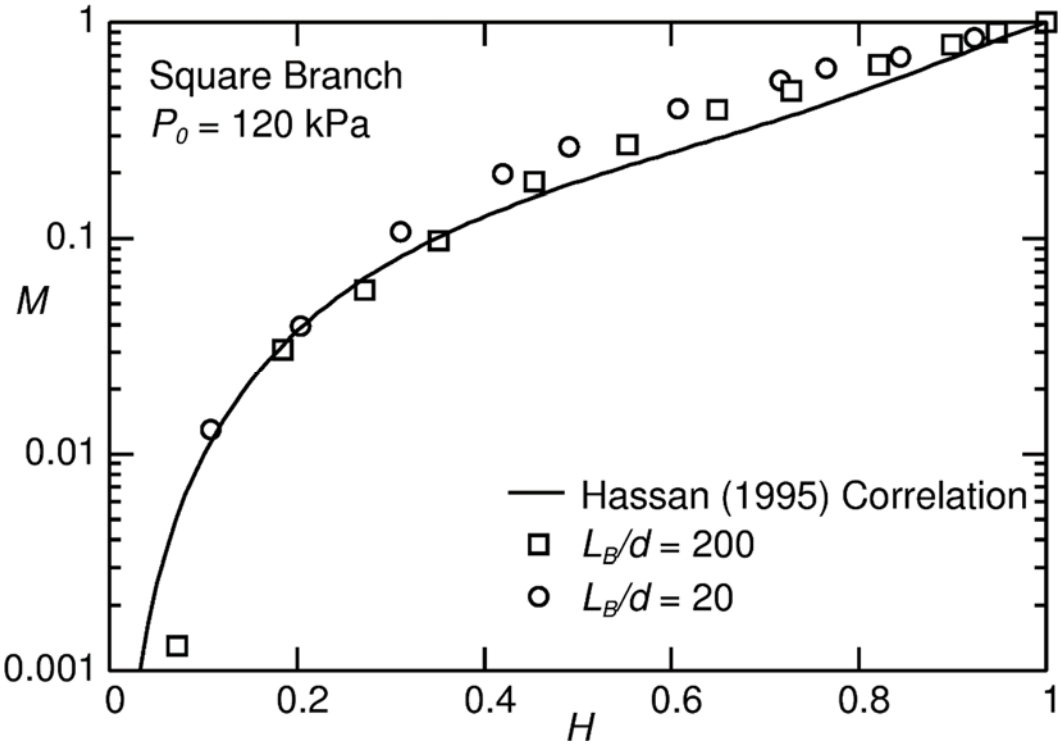

Figure 6.20 - Effect of branch length on M versus H for P_0 = 120 kPa

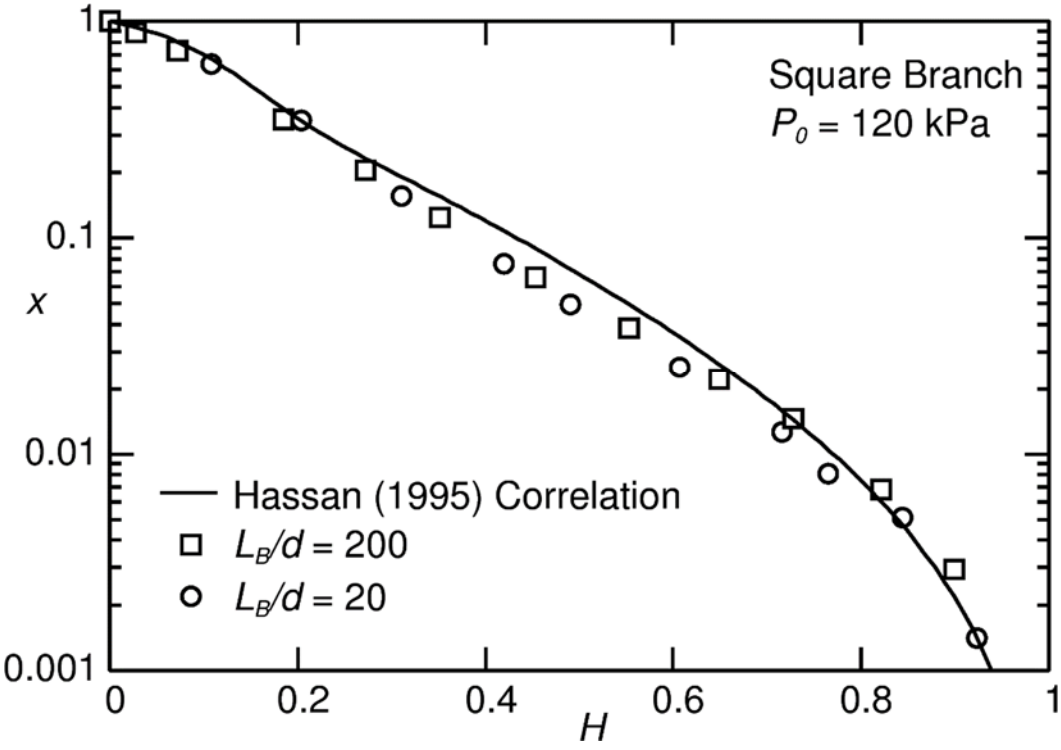

Figure 6.21 - Effect of branch length on x versus H for P_0 = 120 kPa

In summary, the length of the branch has a small effect on the onsets of liquid and gas entrainment critical heights, while the mass flow rate through the branches decreases with increasing branch length due to the increased resistance in the branch. The effect of branch length is largely absorbed when the results are plotted using the dimensionless parameters M, x and H and agree well with Hassan's correlation.

6.5 Results for Geometry with Dual Inclined Branches (G5)

For the geometry shown in Figures 5.3 and 5.4 (b) consisting of a large reservoir with two branches separated by a distance of L/d = 1.5 and an angle of θ = 30°, OLE, OGE and two-phase flow results were obtained for P_0 = 60 and 120 kPa and are presented in Sections 6.5.1 to 6.5.3. The numerical results in this section will be compared with experimental results from Chapter 4 to assess the numerical model.

6.5.1 OLE Results for Geometry G5

OLE results for Geometry G5 were obtained at both the upper and lower branches for $\mathrm{Fr}_{G,OLE,A} = \mathrm{Fr}_{G,OLE,B}$ = 12.63 and 21.87, corresponding to P_0 = 60 and 120 kPa, respectively. As was previously discussed in Section 5.1 for Geometry G5, the onset of liquid entrainment at the bottom branch was determined by monitoring the air volume fraction near the bottom of the Branch B inlet at an angle of 21° measured clockwise from the bottom of the *x*-*y* centreplane of Branch B, $\alpha_{GB,BBI}$. The instant at which $\alpha_{GB,BBI}$ dropped below 1 was taken as the OLE and the interface height at this time was determined at taken as $h_{OLE,B}$.

Figure 6.22 (a) to (d) shows the air volume fraction contours near the OLE at Branch B for $\mathrm{Fr}_{G,OLE,B}$ = 21.87, corresponding to P_0 = 120 kPa. The contours are plotted on a *y*-*z* plane located at *x* = 72 mm and the view shown in the figures is taken looking into the outlets of the branches. The red region represents nearly 100% air (0.0975 < α_G < 1) and the blue region represents nearly 100% water (0.0975 < α_L < 1). In Figure 6.22 (a) it can be seen that as the interface approaches the critical height for the OLE at Branch B, the interface starts to rise in the region underneath the branch. A slight increase in the interface height causes a fine stream of liquid to start rising towards the branch inlet (Figure 6.22 (b)); however, $\alpha_{GB,BBI}$ at this time is still 1. As the interface height

increases further (Figure 6.22 (c)), $\alpha_{GB,BBI}$ drops to 0.990 and the interface extends up and reaches the bottom of the branch inlet; this instant was declared as the OLE. A further increase in the interface height shows that the liquid stream underneath the branch thickens and $\alpha_{GB,BBI}$ drops to 0.977. The OLE at branch B for these conditions occurred very suddenly; the overall increase in the interface height was only 0.006 mm (corresponding to h/d of 0.001) from Figure 6.22 (a) to 6.22 (d). It is interesting to note that the shape of the interface shown in Figures 6.22 (c) and (d) is quite similar to what was observed experimentally for this same geometry in Figure 4.3 (a).

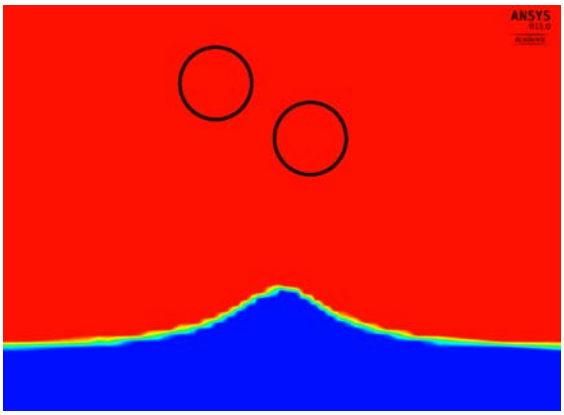

a) $\alpha_{GB,BBI} = 1$, $h_B = -18.379$ mm

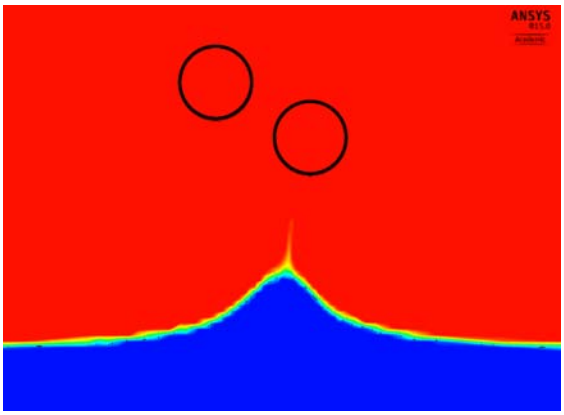

b) $\alpha_{GB,BBI} = 1$, $h_B = -18.378$ mm

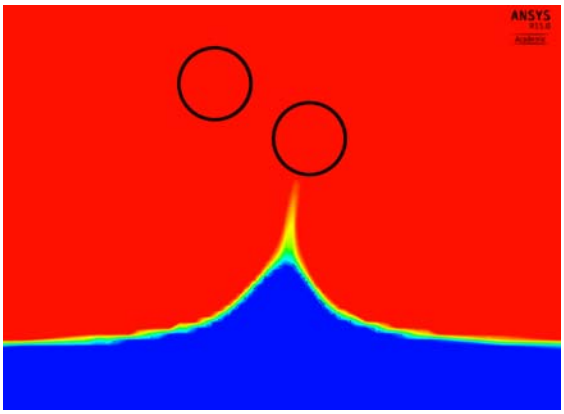

c) $\alpha_{GB,BBI} = 0.990$, $h_B = -18.374$ mm

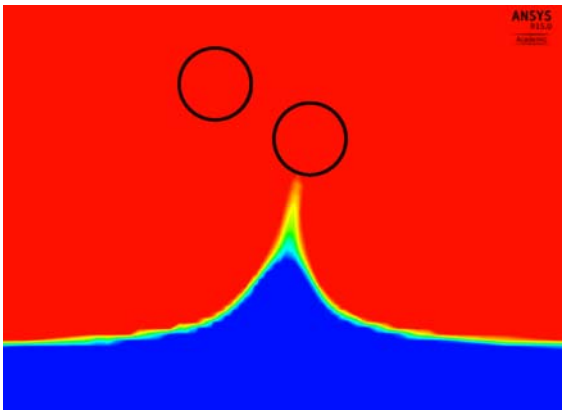

d) $\alpha_{GB,BBI} = 0.977$, $h_B = -18.373$ mm

Figure 6.22 - Air volume fraction contours for $Fr_{G,OLE,B} = 21.87$ near the OLE at Branch B for geometry with dual inclined branches (G5)

The numerical OLE results of $|h_{OLE,B}|/d$ versus $\mathrm{Fr}_{G,OLE,B}$ at Branch B for both values of $\mathrm{Fr}_{G,OLE,B}$ are plotted in Figure 6.23, along with the experimental correlation from the present work and Maier et al.'s (2001) theoretical model. The numerical model's predictions for $|h_{OLE,B}|/d$ are higher than the experimental results. The numerical point that fell within the range of the experimental correlation showed a 13.3% deviation from the experimental correlation. This deviation could be a result of the drag coefficient used in the numerical model. Better accuracy may be attained by adjusting the drag coefficient; however, it was decided to leave this parameter constant at 0.05 for all geometries and cases studied in this research.

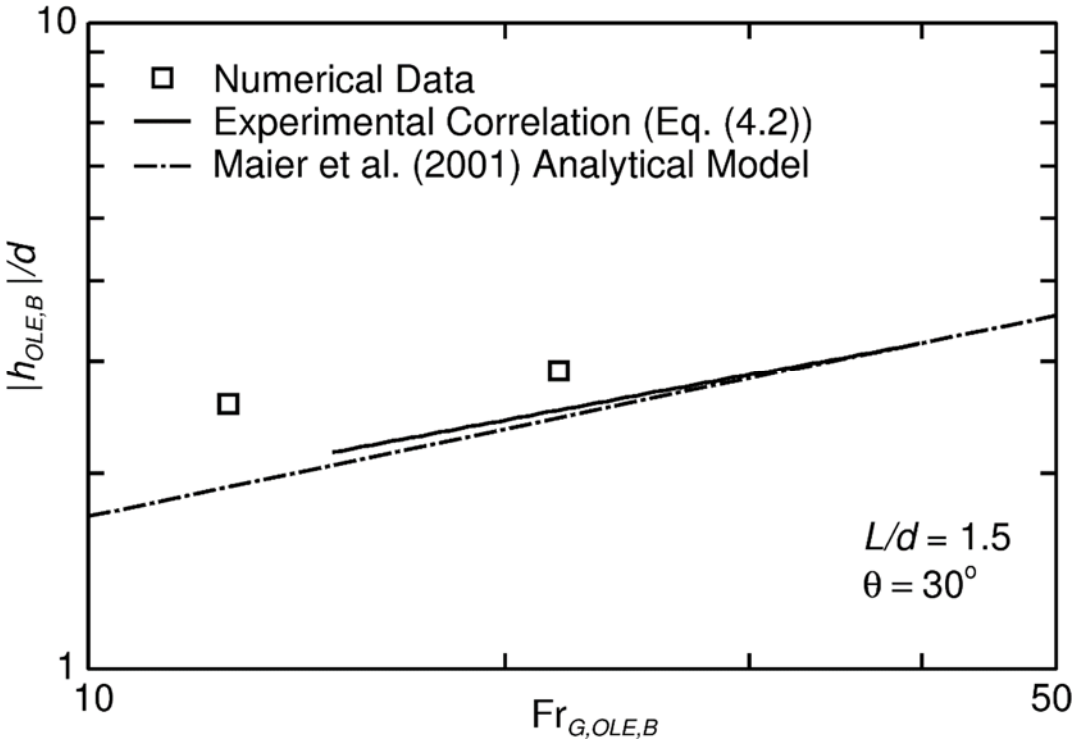

Figure 6.23 - Numerical data and experimental correlation for $|h_{OLE,B}|/d$ versus $\mathrm{Fr}_{G,OLE,B}$ for Geometry G5

Air volume fraction contours for the OLE at Branch A are plotted in Figures 6.24 (a) to (d) for $\mathrm{Fr}_{G,OLE,A} = 21.87$. The same plane was used for these contours as was used for Figure 6.22 and the view is again taken looking into the branch outlets. For the OLE at Branch A, the air

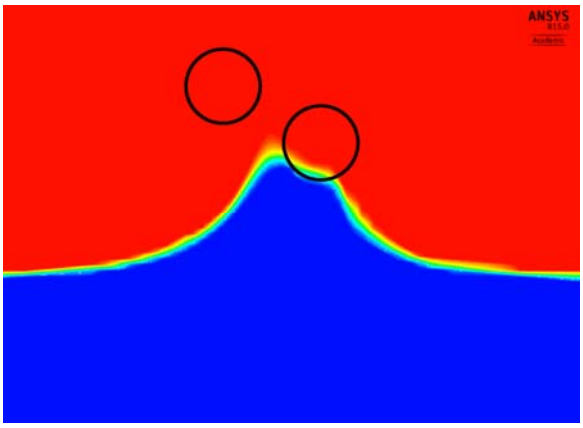

a) $\alpha_{GA,BBI} = 1,\ h_A = -16.631$ mm

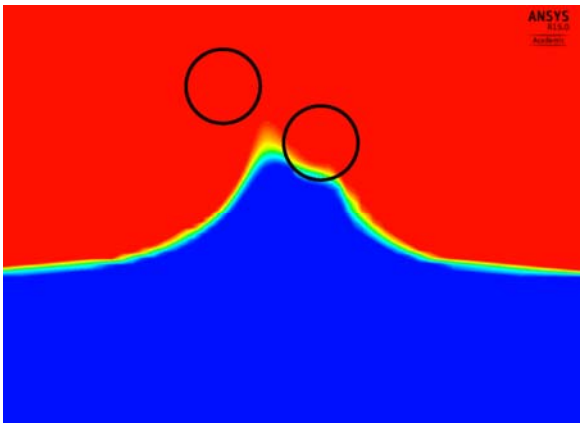

b) $\alpha_{GA,BBI} = 1,\ h_A = -16.273$ mm

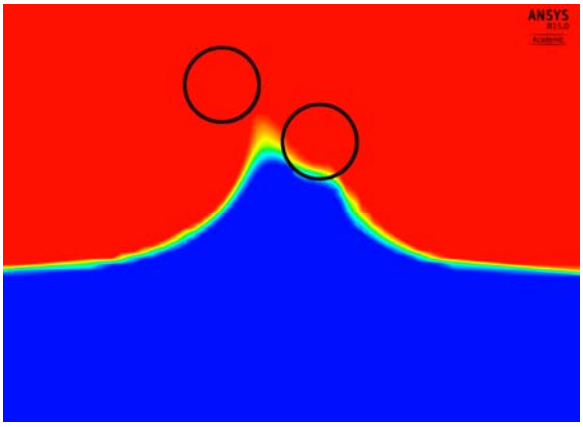

c) $\alpha_{GA,BBI} = 0.992,\ h_A = -16.087$ mm

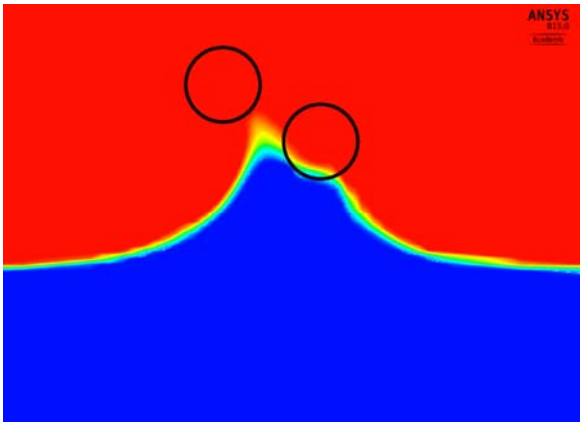

d) $\alpha_{GA,BBI} = 0.972,\ h_A = -15.866$ mm

Figure 6.24 - Air volume fraction contours for $\mathrm{Fr}_{G,OLE,A} = 21.87$ near the OLE at Branch A for geometry with dual inclined branches (G5)

volume fraction, $\alpha_{GA,BBI}$, was monitored at a point on the circumference of the Branch A inlet measured 40° counter clockwise from the bottom of the branch *x*-*y* centreplane, as shown in Figure 5.5. In Figure 6.24 (a), there is a large peak in the interface as liquid flows through the bottom branch and a second smaller peak is observed near the top left side of the main peak due to suction through the upper branch. As the interface rises towards the OLE height, Figure 6.24 (b) shows that the top left side of the peak rises slightly towards the top branch; $\alpha_{GA,BBI}$ at this instant is still 1. A further increase in the interface height causes the liquid to rise further and the tip of the peak

to just reach the location where $\alpha_{GA,BBI}$ is measured thus causing $\alpha_{GA,BBI}$ to drop to 0.992 (Figure 6.24 (c)); this instant was selected as the OLE and the interface height h_A = -16.087 mm was set to $h_{OLE,A}$. As the interface is raised beyond this level, $\alpha_{GA,BBI}$ drops further as more liquid enters the top branch. By comparing the air volume fraction contours in Figure 6.24 with the picture of the interface taken during the experiments just after the OLE at Branch A for the same geometry (Figure 4.4 (a)), it is observed that the shape of the interface, as predicted by the numerical model, resembles the shape of the interface in the experiments as liquid is entrained into the upper branch.

In Figure 6.25, numerical results of $|h_{OLE,A}|/d$ versus $\mathrm{Fr}_{G,OLE,A}$ are plotted for P_0 = 60 and 120 kPa. The experimental correlation from the present work is also included in this figure. The data point that fell within the range of the experimental correlation agreed very well with the correlation with a deviation of 2.56%.

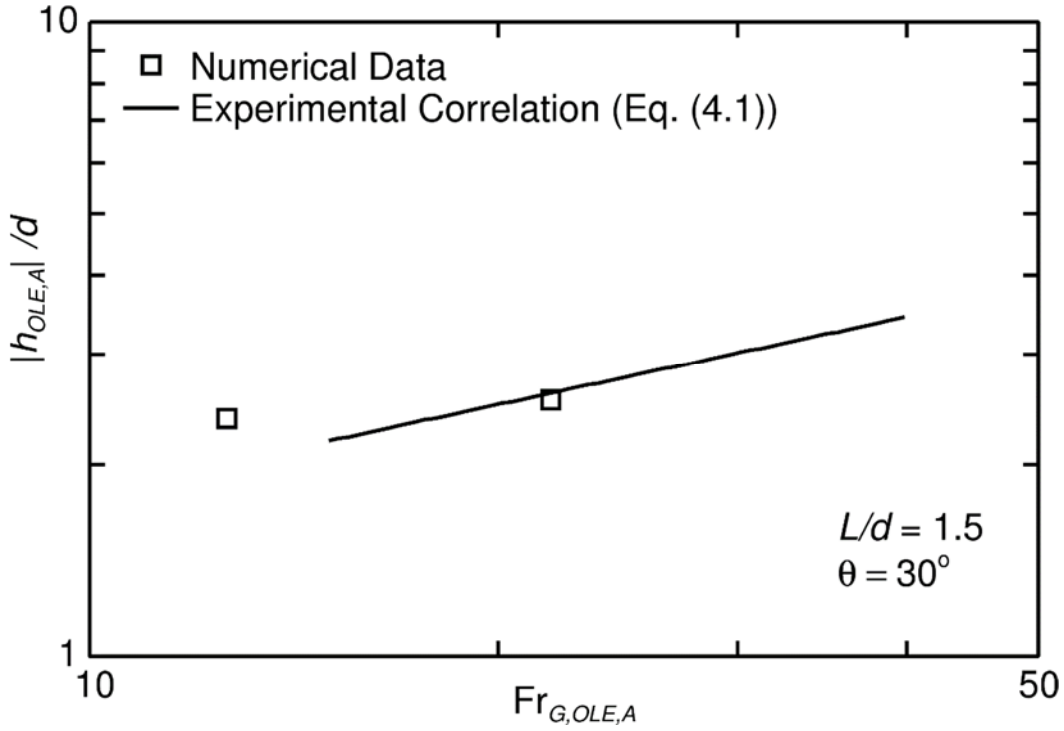

Figure 6.25 - Numerical data and experimental correlation for $|h_{OLE,A}|/d$ versus $\mathrm{Fr}_{G,OLE,A}$ for Geometry G5

6.5.2 OGE Results for Geometry G5

For the geometry with dual inclined branches (G5), results for the onset of gas entrainment at both the upper and lower branches were obtained for $\mathrm{Fr}_{L,OGE,A} = \mathrm{Fr}_{L,OGE,B} = 17.78$ and 25.85, corresponding to $P_0 = 60$ and 120 kPa, respectively. For this geometry, the OGE at Branch A was determined by monitoring $\dot{m}_{G,A}$ and the air volume fraction at the top of the Branch A inlet, $\alpha_{GA,BTI}$, and the OGE at Branch B was determined by monitoring $\dot{m}_{G,B}$ and $\alpha_{GB,BTI}$ at a point on the circumference of the Branch B inlet offset 19.5° (clockwise) from the top of the Branch B *x*-*y* centreplane, as was shown in Figure 5.6. The same criteria was used in selecting the timestep corresponding to the OGE at each branch for this geometry (G5) as was used for the single branch geometry (G3) described in Section 6.2.2.

Air volume fraction contours are plotted in Figure 6.26 (a) to (d) for $\mathrm{Fr}_{L,OGE,A} = 25.85$ at four timesteps near the OGE at Branch A. Two views are included in these figures: a front view looking into the branch outlets with the contour plotted on a *y*-*z* plane located at the branch inlet ($x = 72$ mm) , and a side view with the contour plotted on an *x*-*y* plane located at the centreplane of the upper branch ($z = 70.749$ mm). The side view is included here to show the formation of a gas cone at the OGE. In Figure 6.26 (a), with the interface located approximately 1 mm above $h_{OGE,A}$, there is a dip in the interface above the upper branch. As the interface is lowered close to the critical height, the interface dips further towards the top of the Branch A inlet and a gas cone begins to form underneath the dip (Figure 6.26 (b)); the air volume fraction at this time is just barely above 0 ($\alpha_{GA,BTI} = 0.006$). Figure 6.26 (c) shows that a slight drop further in the interface height causes the gas cone to extend towards the branch inlet and $\alpha_{GA,BTI} = 0.158$; this instant was taken as the OGE and $h_A = 15.258$ mm was set equal to $h_{OGE,A}$. The contours plotted in Figure 6.26 (d) show that as the interface is lowered further past the critical height, the air flows freely along the wall above the branch inlet. The numerical observations on the shape of the interface at the OGE at Branch A are again consistent with what was observed experimentally for this same geometry, as shown in Figure 4.15 (a).

Front Views | Side Views

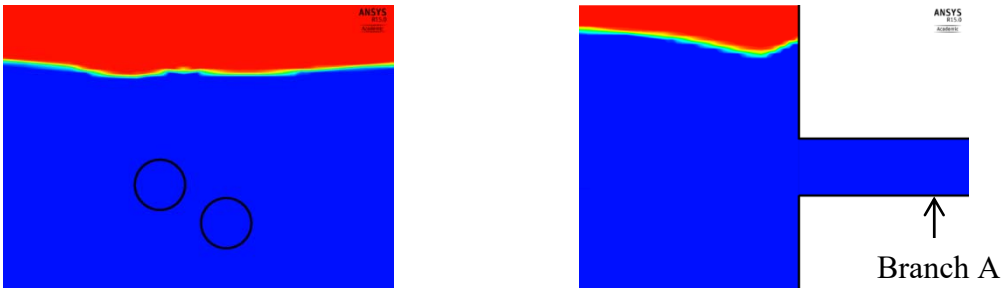

(a) $\alpha_{GA,BTI}$ = 0, h_A = 16.228 mm

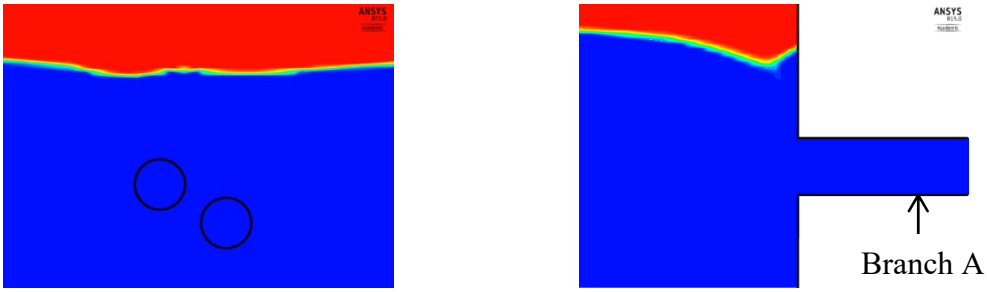

(b) $\alpha_{GA,BTI}$ = 0.006, h_A = 15.640 mm

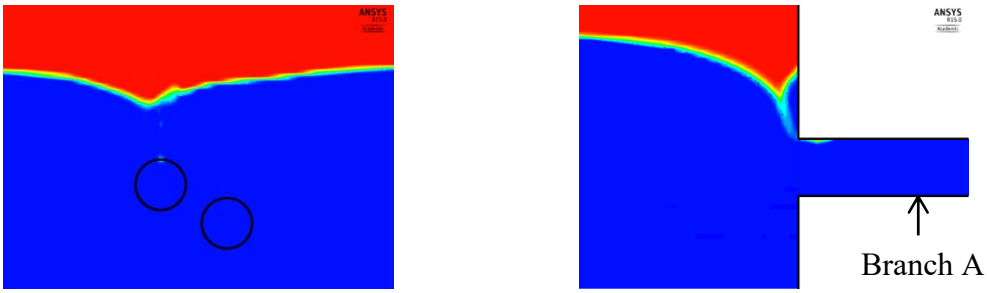

(c) $\alpha_{GA,BTI}$ = 0.158, h_A = 15.258 mm

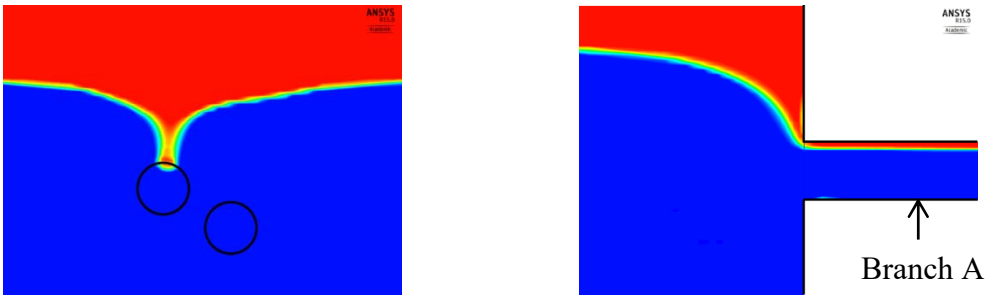

(d) $\alpha_{GA,BTI}$ = 0.880, h_A = 14.747 mm

Figure 6.26 - Air volume fraction contours for $Fr_{L,OGE,A}$ = 25.85 near the OGE at Branch A for geometry with dual inclined branches (G5)

The numerical results of $h_{OGE,A}/d$ versus $\mathrm{Fr}_{L,OGE,A}$ for Geometry G5 are plotted in Figure 6.27 along with the experimental correlation from the present work. Excellent agreement was found between the numerical data and the experimental correlation with an RMS deviation of 4.95 % .

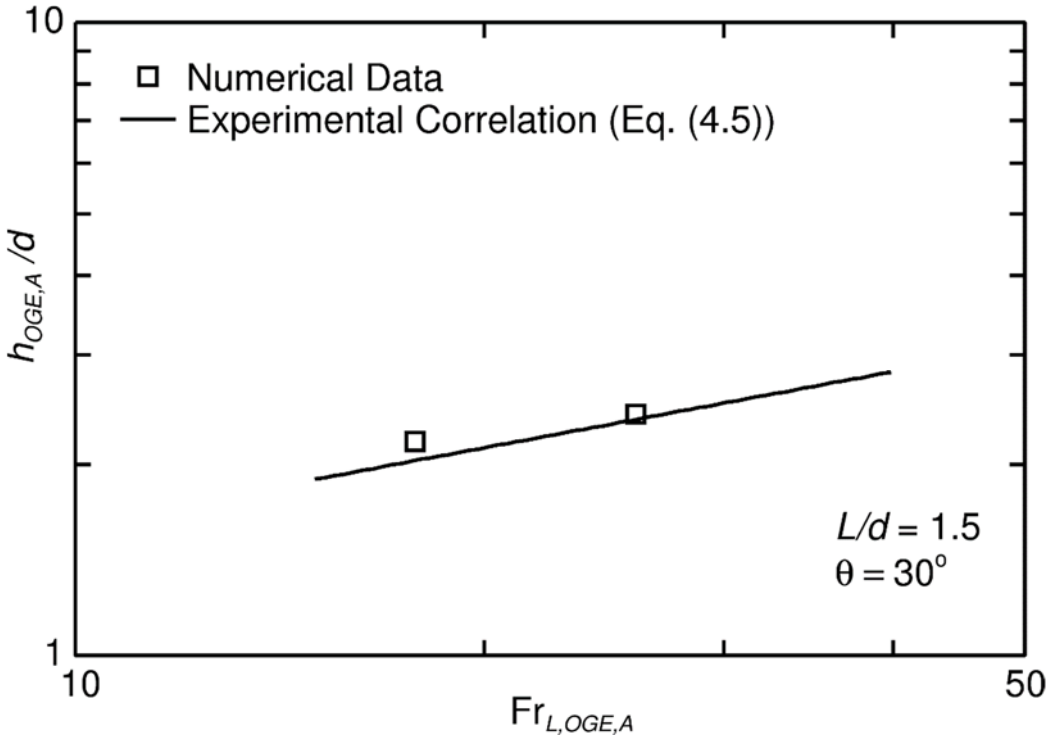

Figure 6.27 - Numerical data and experimental correlation for $h_{OGE,A}/d$ versus $\mathrm{Fr}_{L,OGE,A}$ for Geometry G5

Air volume fraction contours are plotted in Figure 6.28 (a) to (d) at timesteps near the OGE at Branch B for P_0 = 120 kPa. The front views in the figures are contours plotted on a *y*-*z* plane located at the branch inlet (*x* = 72 mm) and the side views show contours plotted on an *x*-*y* plane located at *z* = 63.56 mm; this plane was selected as it passed through the point where $\alpha_{GB,BTI}$ is monitored and where air first enters the branch. With the interface located slightly above $h_{OGE,B}$ (Figure 6.28 (a)), the front view shows how the interface drops above Branch A as both air and water flow through this branch; the shape of the interface in this view and at this timestep is fairly symmetrical around Branch A. The side view shown in Figure 6.28 (a) shows that the interface

Front Views | Side Views

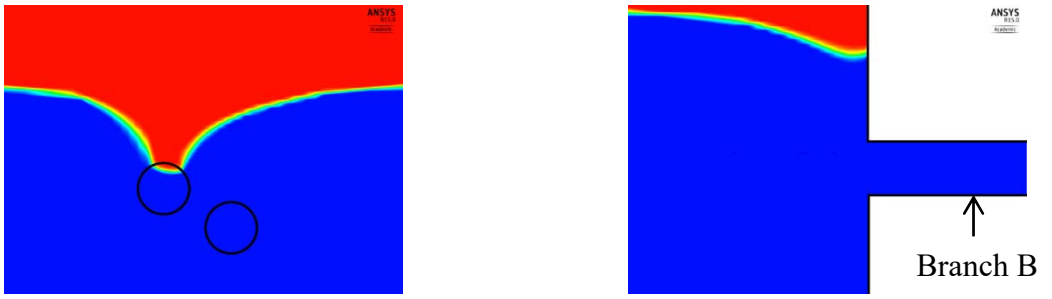

(a) $\alpha_{GB,BTI} = 0,\ h_B = 16.859$ mm

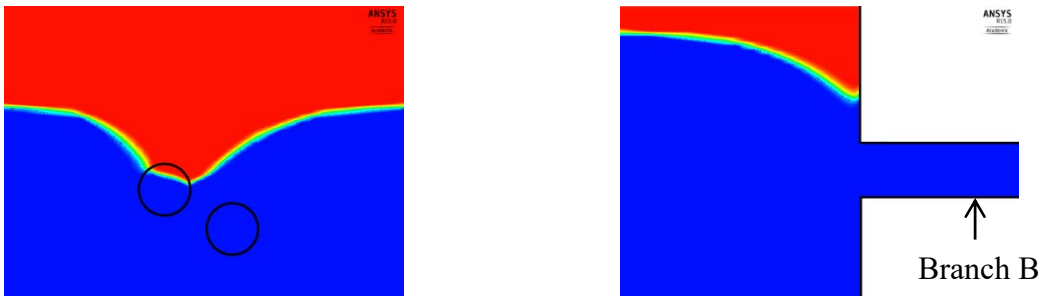

(b) $\alpha_{GB,BTI} = 0.008,\ h_B = 15.740$ mm

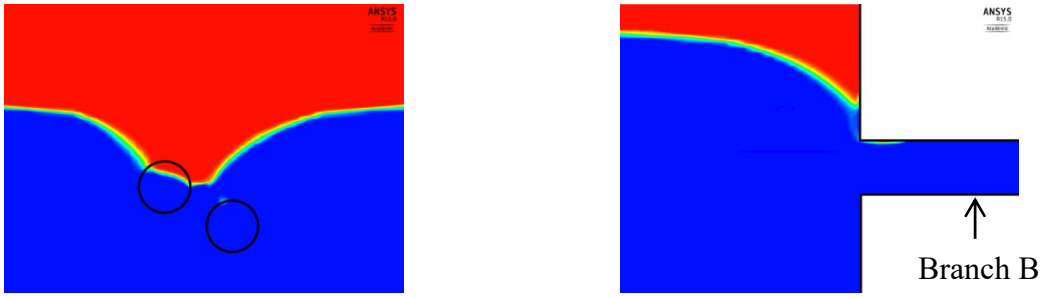

(c) $\alpha_{GB,BTI} = 0.191,\ h_B = 15.744$ mm

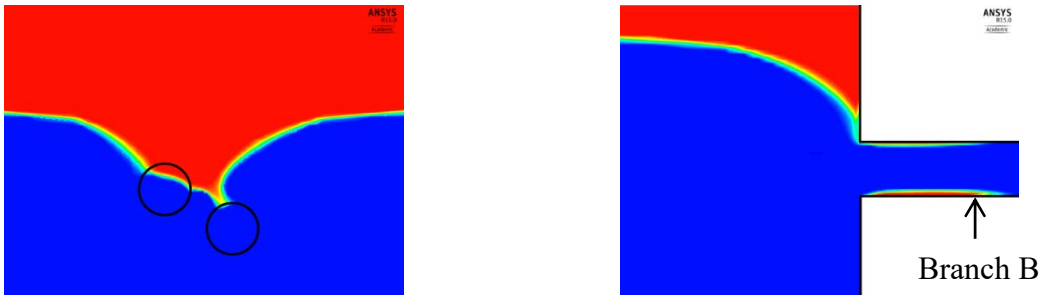

(d) $\alpha_{GB,BTI} = 0.532,\ h_B = 15.691$ mm

Figure 6.28 - Air volume fraction contours for $\mathrm{Fr}_{L,OGE,B} = 25.84$ near the OGE at Branch B for geometry with dual inclined branches (G5)

dips down near the wall above Branch B. As the interface drops close to the critical height (Figure 6.28 (b)), the shape of the interface shown in the front view is no longer symmetrical around Branch A as it is pulled towards Branch B and the side view shows that the interface is dipping closer to the Branch B inlet. With a slight drop further in the interface height, the side view in Figure 6.28 (c) shows that a gas cone has formed and extends from the dip in the interface down to the Branch B inlet; the OGE was declared at this time and h_B = 15.744 mm was set equal to $h_{OGE,B}$. Although the gas cone cannot be observed in the front view of Figure 6.28 (c) because the plane is located at the wall, traces of air can be seen at the location where $\alpha_{GB,BTI}$ is measured. Figure 6.28 (d) shows that as the interface is lowered even further, the gas cone thickens as more air enters the branch.

In Figure 6.29, the numerical results of $h_{OGE,B}/d$ versus $\mathrm{Fr}_{L,OGE,B}$ are plotted for P_0 = 60 and 120 kPa along with the experimental correlation. Excellent agreement is observed with an RMS deviation of 3.56%.

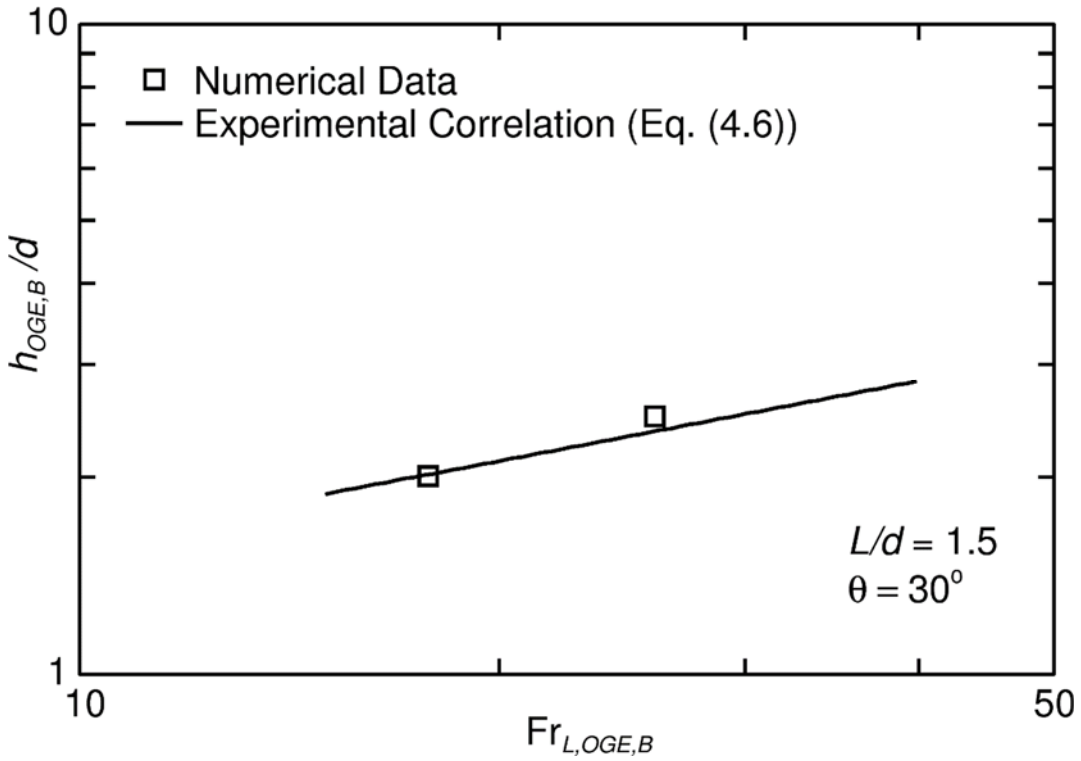

Figure 6.29 - Numerical data and experimental correlation for $h_{OGE,B}/d$ versus $\mathrm{Fr}_{L,OGE,B}$ for Geometry G5

6.5.3 Two-Phase Flow Results for Geometry G5

The numerical two-phase flow data for P_0 = 60 and 120 kPa are compared with the experimental data to assess the capabilities of ANSYS CFX in predicting two-phase flow from a large tank through dual branches with L/d = 1.5 and $\theta = 30°$ (Geometry G5). Numerical results of $\dot{m}_{TP}$ and x versus h at Branches A and B are plotted in Figures 6.30 to 6.35. In Figure 6.30, $\dot{m}_{TP}$ results for both Branches A and B are plotted together versus the interface height h_A for P_0 = 60 kPa (note that in the numerical model, $P_0 = \Delta P$ because the outlet pressure is zero). This plot is compared with a similar plot of the experimental results for ΔP = 40 kPa, shown in Figure 4.25. Although the magnitudes are different in these two figures due to the differences in ΔP and R, the trends are quite similar. In both, the numerical and experimental results, $\dot{m}_{TP,B} > \dot{m}_{TP,A}$, and the relative differences in the magnitudes of the $\dot{m}_{TP,A}$ and $\dot{m}_{TP,B}$ curves are similar. Another similarity between the numerical and experimental results shown in these figures is the relative magnitudes of the onset heights. Both numerically and experimentally, $h_{OGE,A} > h_{OGE,B}$ and $|h_{OLE,A}| < |h_{OLE,B}|$, and the relative differences between the OGE heights at Branches A and B and the relative differences between the OLE heights at Branches A and B are similar. The numerical results of x versus h_A for Branches A and B for Geometry G5 with P_0 = 60 kPa are plotted in Figure 6.31 and a qualitative comparison is made between these results and the experimental results for ΔP = 40 kPa shown in Figure 4.26. The trends in the numerical and experimental data shown in these figures are again the same with $x_A > x_B$.

In Figures 6.32 and 6.33, the numerical results of $\dot{m}_{TP,A}$ and x_A are plotted versus h_A for P_0 = 60 and 120 kPa to examine if the effect of ΔP is the same for the numerical results as it was for the experimental results. Similar plots of the experimental data for $\dot{m}_{TP,A}$ and x_A versus h_A for ΔP = 40 and 123 kPa were plotted in Figures 4.27 and 4.29. The numerical results in Figure 6.32 show that as P_0 increases, $\dot{m}_{TP,A}$ increases, as was observed by the experimental results in Figure 4.27; the increase is, however, smaller in the numerical results since there is less

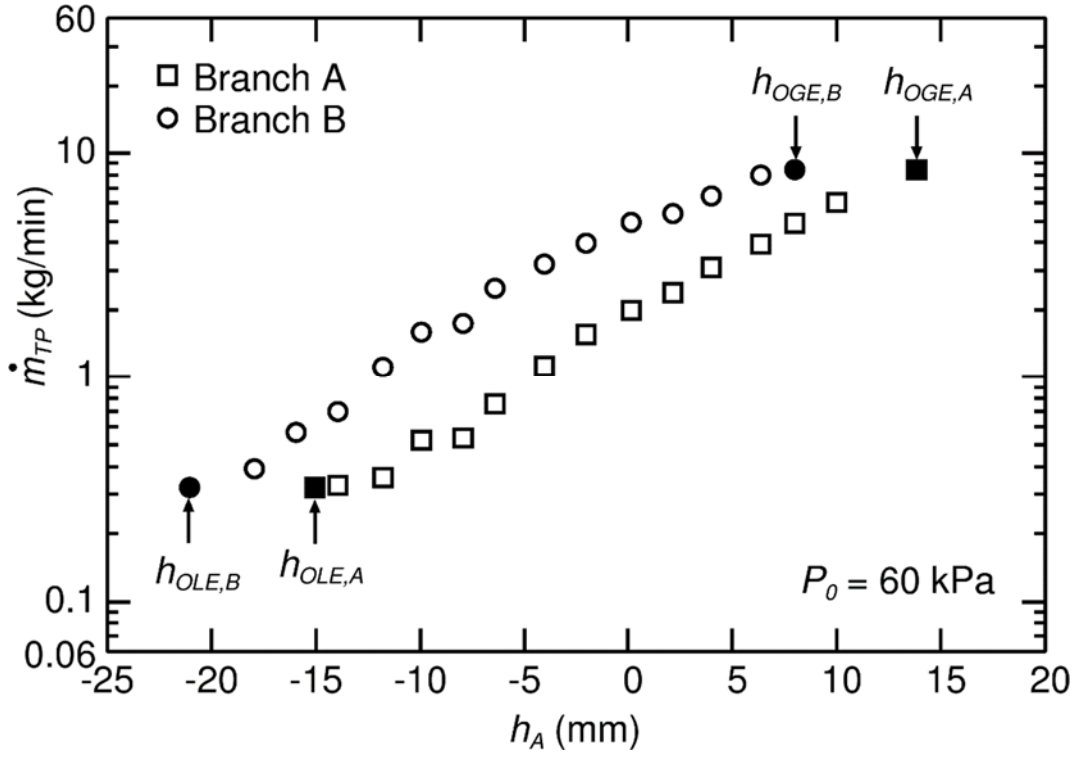

Figure 6.30 - $\dot{m}_{TP}$ versus h_A for Geometry G5 with P_0 = 60 kPa

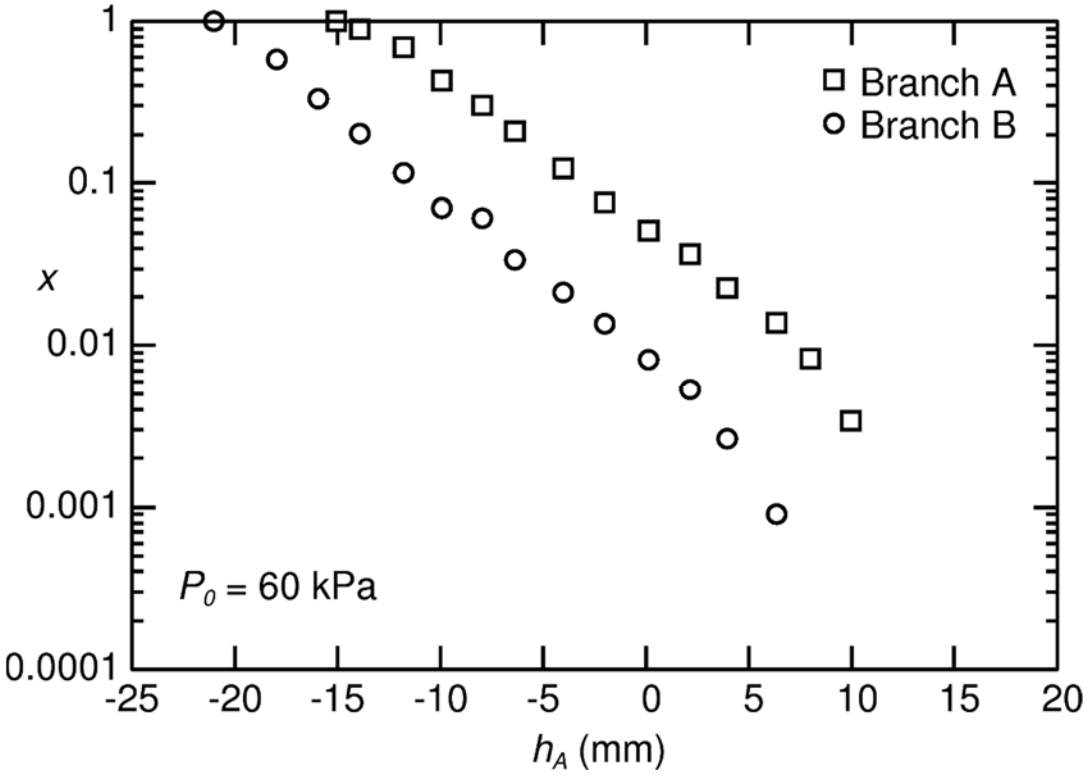

Figure 6.31 - x versus h_A for Geometry G5 with P_0 = 60 kPa

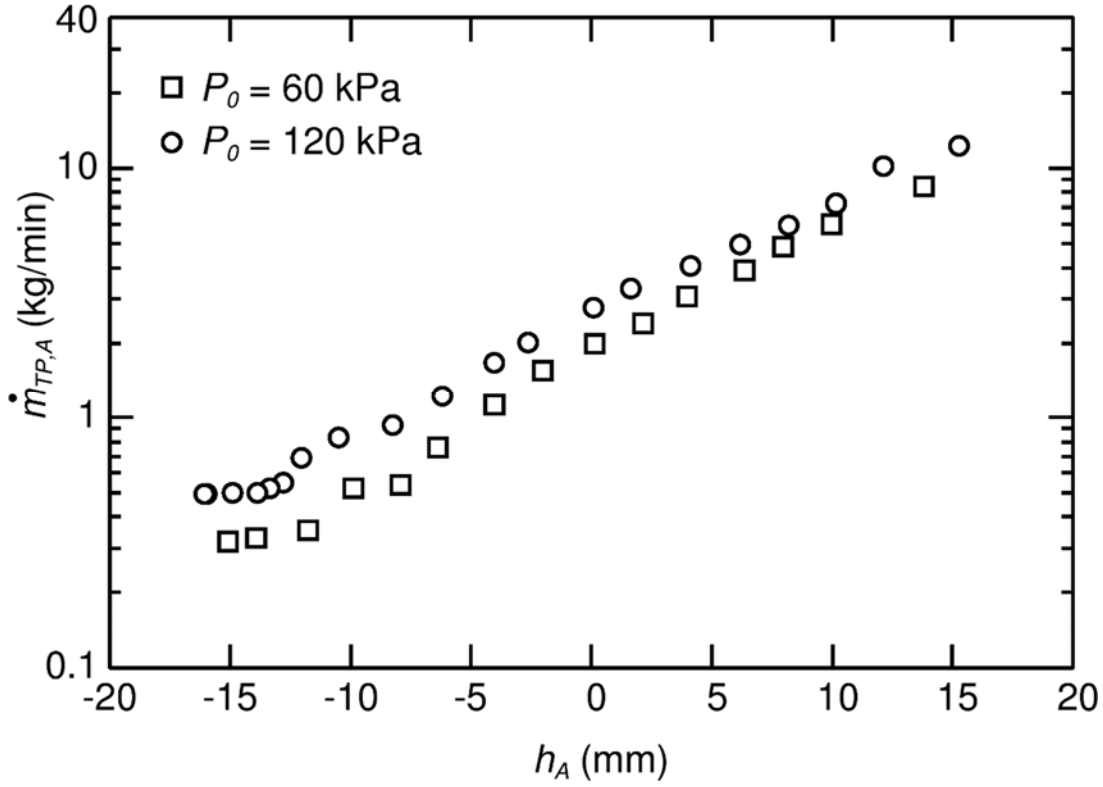

Figure 6.32 - $\dot{m}_{TP,A}$ versus h_A for Geometry G5

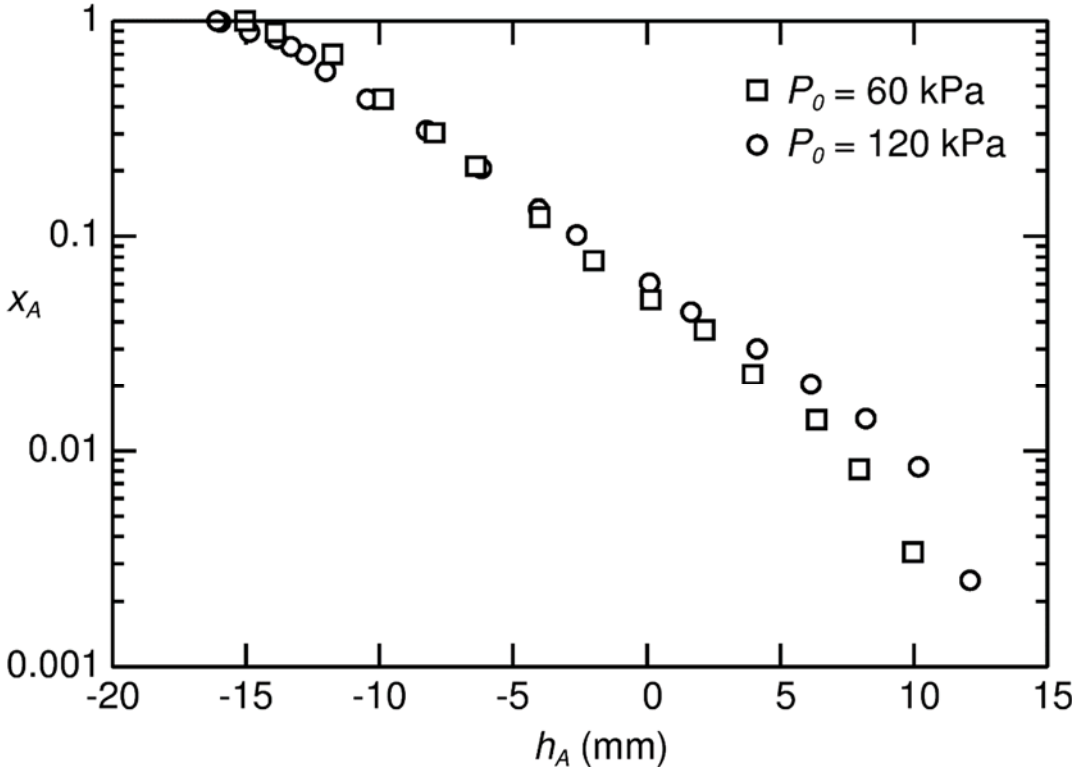

Figure 6.33 - x_A versus h_A for Geometry G5

difference between the two values of P_0 (or ΔP) compared numerically (60 and 120 kPa) as there is between the values of ΔP compared experimentally (40 and 123 kPa). The numerical results for x_A versus h_A (Figure 6.33) show the same trends as the experimental results in Figure 4.29; the curves for the two values of P_0 cross and x_A increases with decreasing P_0 at low h_A and decreases with decreasing P_0 at high h_A.

The numerical results for $\dot{m}_{TP,B}$ versus h_B and x_B versus h_B are plotted in Figures 6.34 and 6.35, respectively, for P_0 = 60 and 120 kPa. As P_0 increases, $\dot{m}_{TP,B}$ increases and x_B decreases at low h_B and increases at high h_B. These trends are consistent with those observed from the experimental results shown in Figures 4.28 and 4.30.

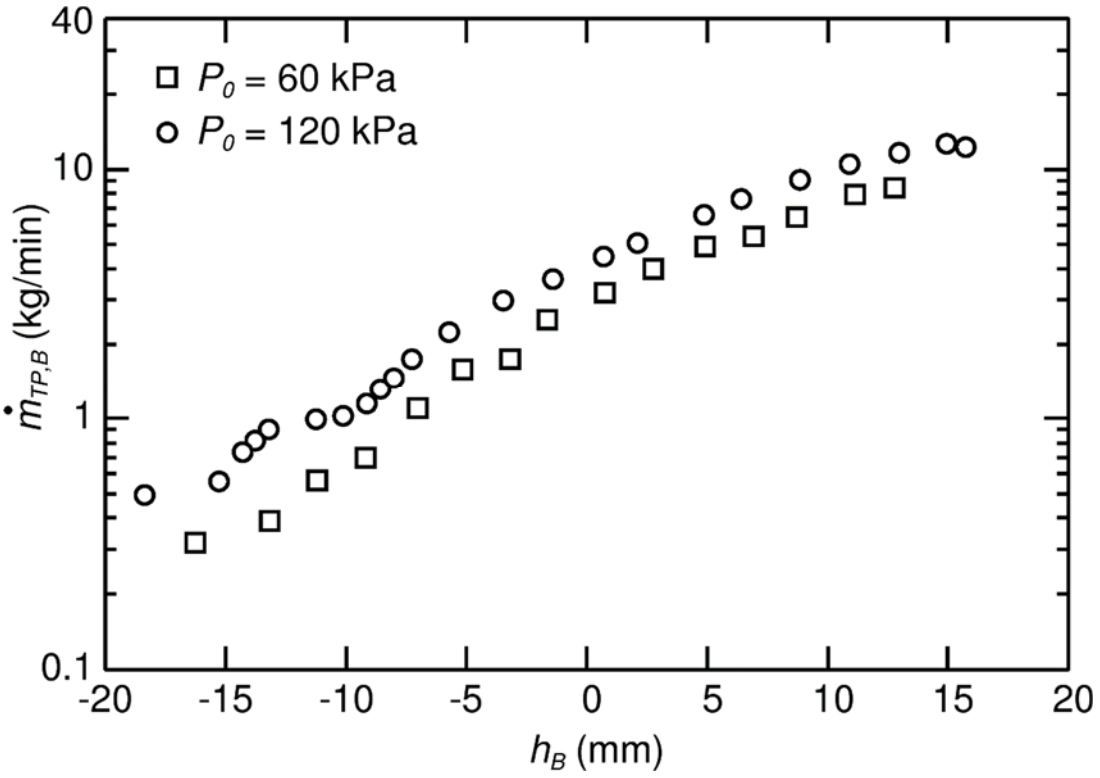

Figure 6.34 - $\dot{m}_{TP,B}$ versus h_B for Geometry G5

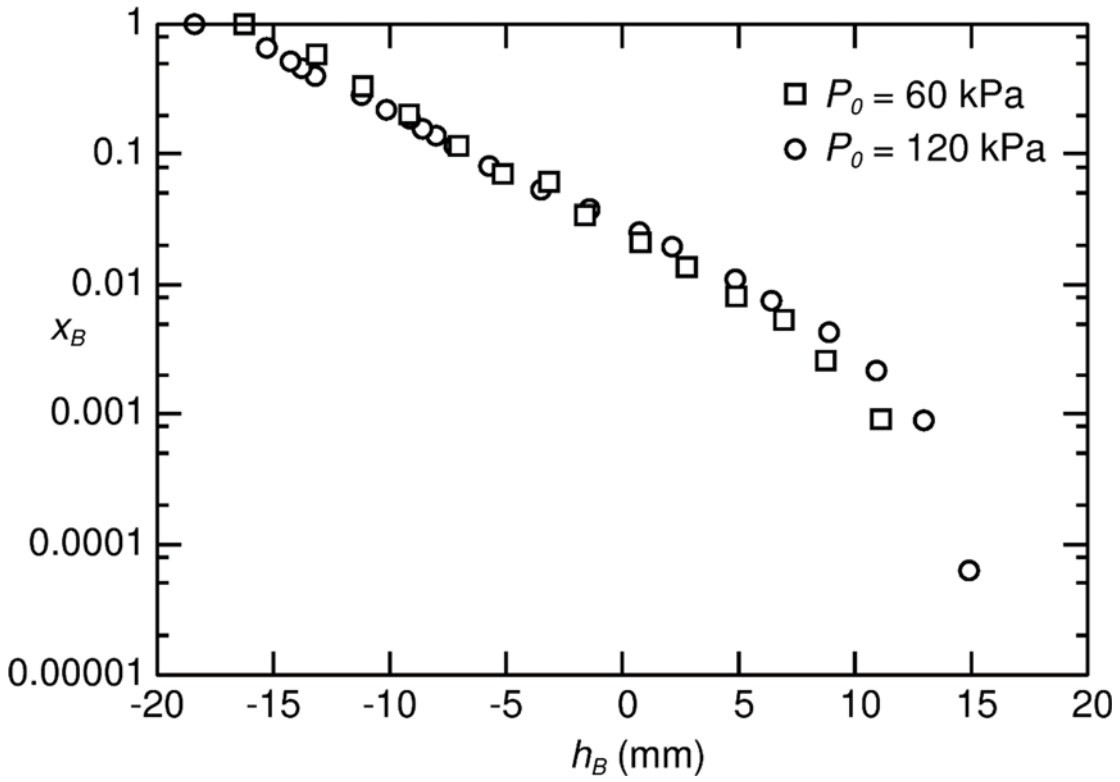

Figure 6.35 - x_B versus h_B for Geometry G5

From the numerical results in Figures 6.30 to 6.35, only qualitative comparisons could be made with the experimental results because the values of P_0, ΔP and R from the numerical model do not match those from the experiments. However, a quantitative comparison is possible by comparing the dimensionless results of M and x versus H at Branches A and B because the effects of P_0, ΔP and R are absorbed when the results are plotted in this way. In Figures 6.36 to 6.39, numerical results of M_A versus H_A, x_A versus H_A, M_B versus H_B, and x_B versus H_B are plotted for P_0 = 60 and 120 kPa along with the experimental correlations presented in Chapter 4. The results for Branch A show that there is some deviation between the numerical and experimental results for M_A (Figure 6.36) but excellent agreement in x_A (Figure 6.37). The numerical model is therefore over predicting the mass flow rates of both gas and liquid at Branch A while still predicting the correct quality, x_A. For Branch B, the numerical results of M_B versus H_B, and x_B versus H_B, in Figures 6.38 and 6.39, respectively, show even better agreement with the experimental correlations with only a slight deviation in x_B at high values of H_B. Figures

6.36 to 6.39 also show how the effect of P_0 is absorbed when the numerical results are plotted using the dimensionless variables, as was proved experimentally in Chapter 4.

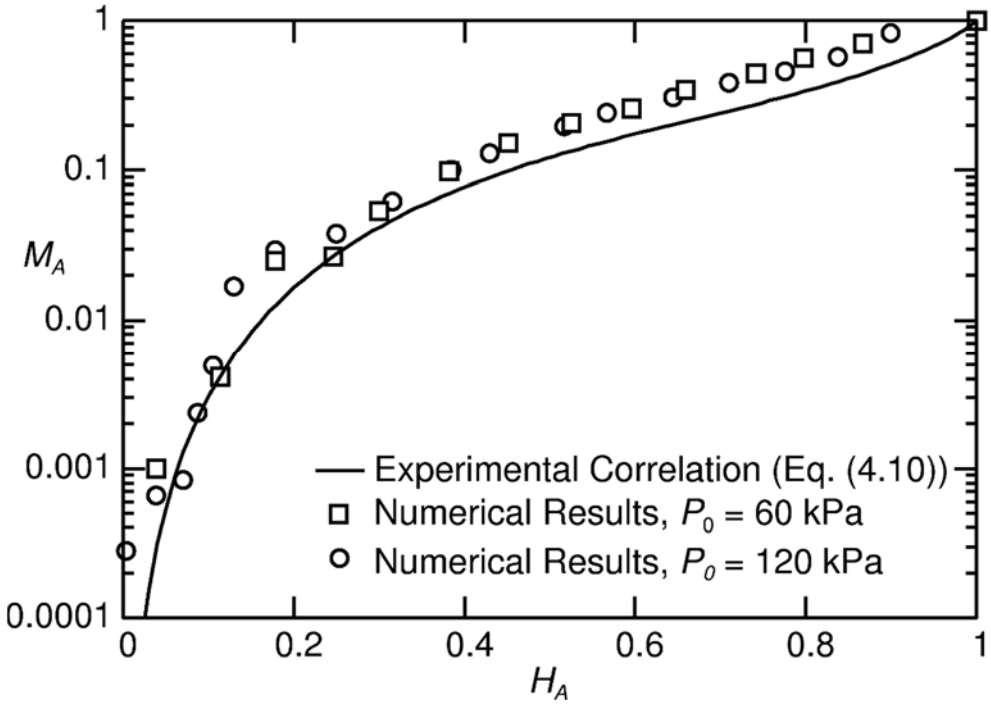

Figure 6.36 - M_A versus H_A for Geometry G5

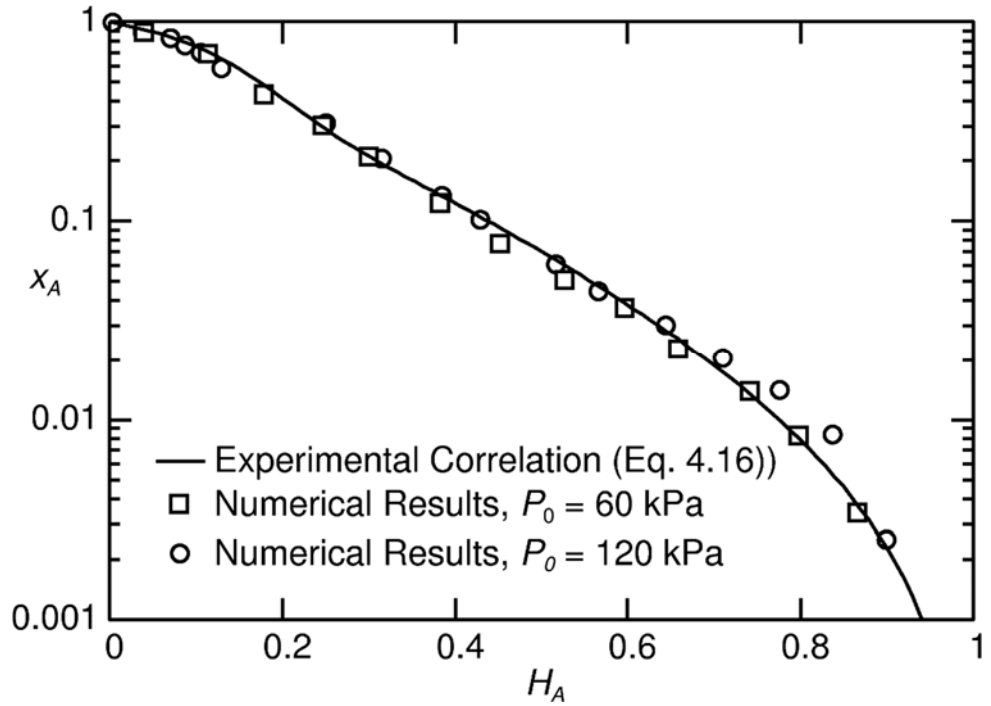

Figure 6.37 - x_A versus H_A for Geometry G5

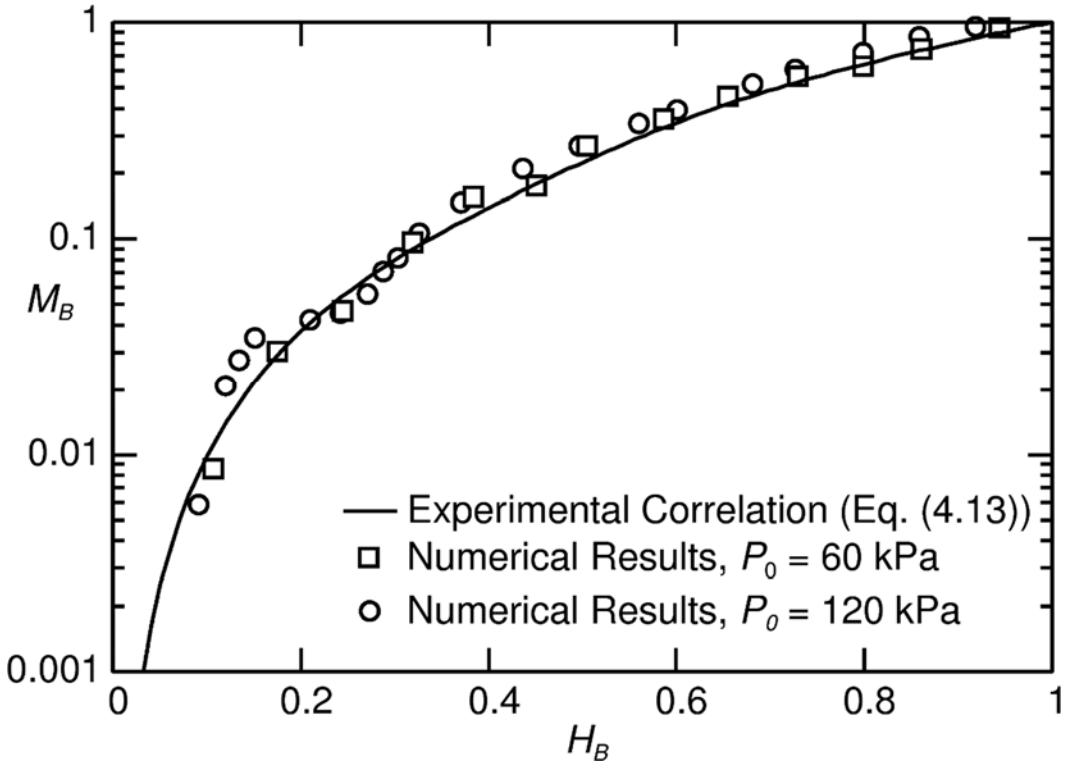

Figure 6.38 - M_B versus H_B for Geometry G5

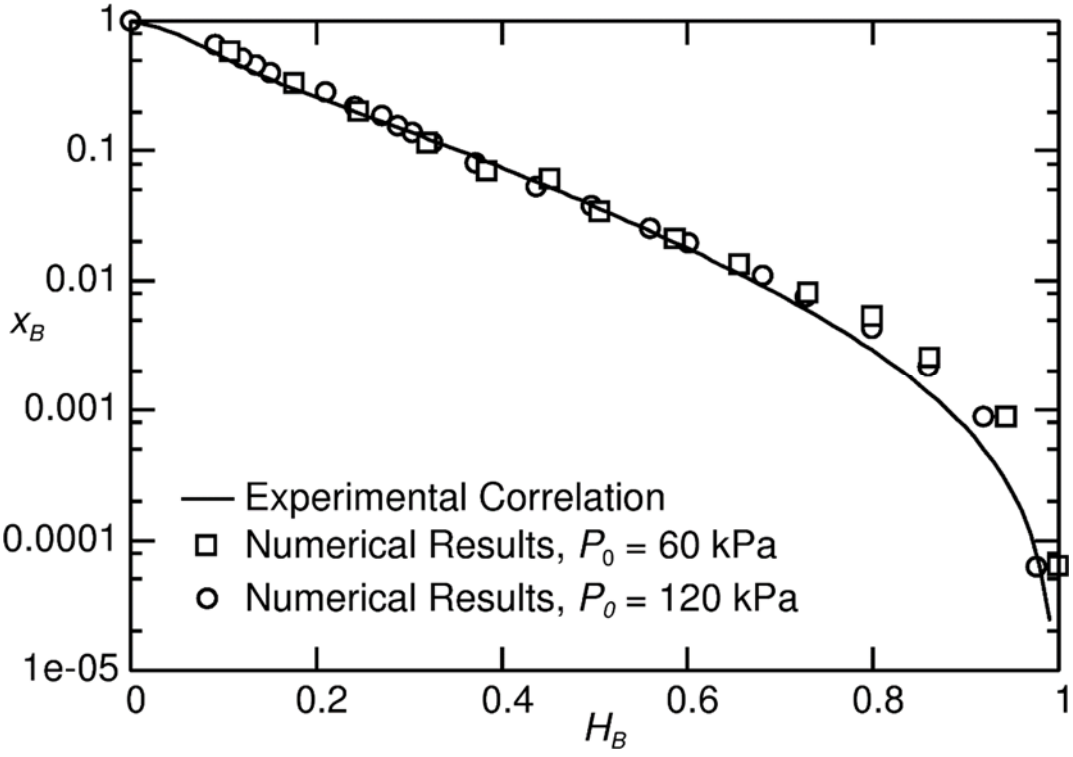

Figure 6.39 - x_B versus H_B for Geometry G5

6.5.4 Summary of Results for Geometry G5

For Geometry G5 with two-phase flow discharging through two branches separated by a distance of $L/d = 1.5$ and an angle of $\theta = 30°$, good agreement was found between the numerical results and the experimental correlations for the OLE, OGE and two-phase flow results. The percent deviation in the OLE results at Branches A and B were 2.56% and 13.30%, respectively, and the RMS deviation between the OGE results at Branches A and B were 4.95% and 3.56%, respectively. In addition, the shape of the interface at the onsets of liquid and gas entrainment as observed by the air volume fraction contours from the numerical results resembled the shape of the interface observed in the experimental investigation. For two-phase flow through the branches, the mass flow rates and qualities from the numerical model show the same trends as were observed experimentally and good quantitative agreement is observed when the results are plotted using the dimensionless variables M, x and H. ANSYS CFX is therefore capable of predicting the correct flow phenomena for two-phase flow through this geometry.

6.6 Results for Geometry with Two Branches Located One on Top of the Other (G4)

This section presents numerical results for the Geometry G4 shown in Figures 5.3 and 5.4 (a) with two branches located one on top of the other ($\theta = 90°$) with centrelines spaced a distance of $L/d = 1.5$ from one another. The numerical model for this geometry was successful at producing converged results for certain interface heights and unsuccessful for others. Figures 6.40 and 6.41 show the converged numerical results of $\dot{m}_{TP}$ versus h_A for Branches A and B that were obtained for $P_0 = 120$ and 400 kPa, respectively. For both values of P_0, converged results were obtained for $h_{OLE,B}$, $h_{OGE,A}$ and for interface heights that fell within the following two ranges: $h_{OLE,B} < h < h_{OLE,A}$ and $h_{OGE,B} < h < h_{OGE,A}$. In other words, the model converged as long as there was single phase flow through one of the two branches. In Figures 6.40 and 6.41, the two vertical dashed lines represent the values of $h_{OLE,A}$ and $h_{OGE,B}$ calculated using Hassan's (1995) correlations. Within the range of $h_{OLE,A} < h < h_{OGE,B}$, Hassan's correlations predict that there will be two-phase flow in both branches. The numerical model did not produce a converged solution for interface heights within this range.

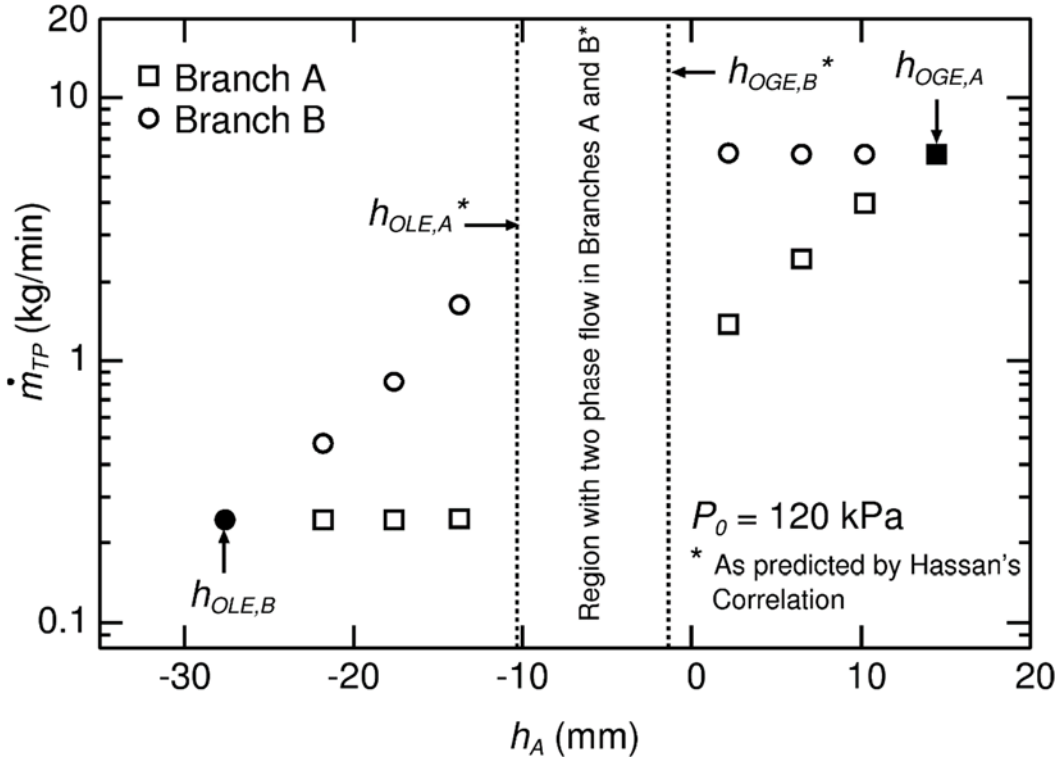

Figure 6.40 - $\dot{m}_{TP}$ versus h_A for Geometry G4 with P_0 = 120 kPa

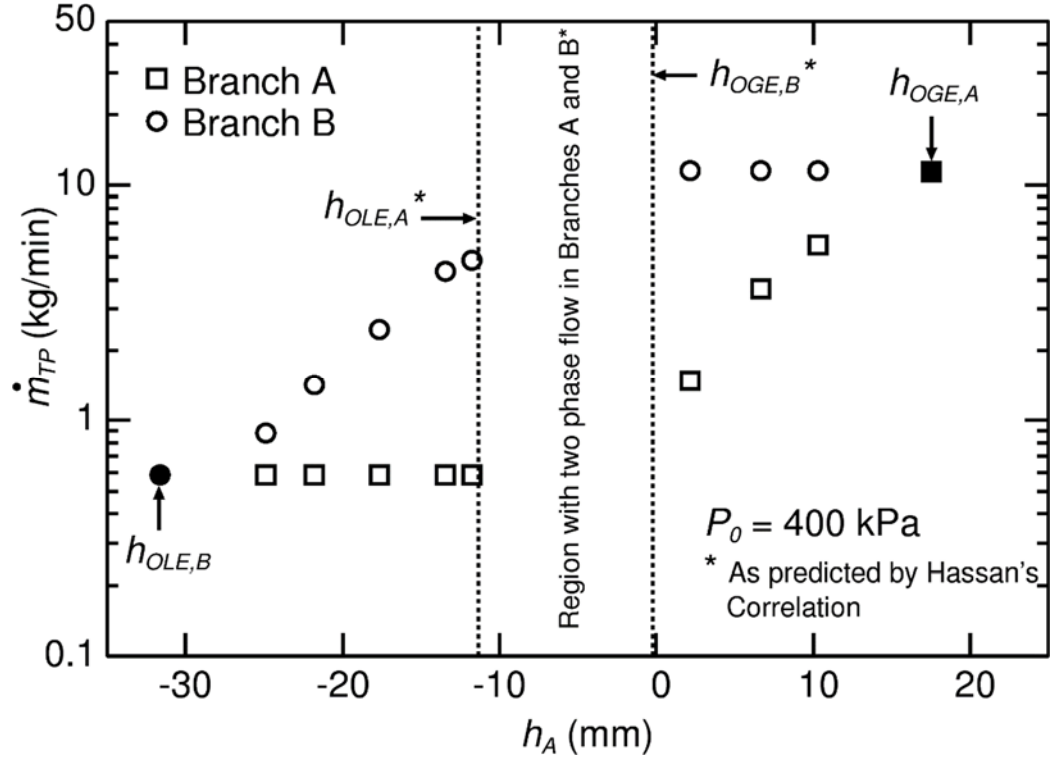

Figure 6.41 - $\dot{m}_{TP}$ versus h_A for Geometry G4 with P_0 = 400 kPa

Figure 6.42 is a sketch of the shape of the interface for an interface height within the range of $h_{OLE,A} < h < h_{OGE,B}$, which was observed experimentally in the present work and in Hassan's (1995) work. In the experiments, when the interface is located between the two branches as shown, liquid flows to the upper branch in two streams from each side while gas flows to the lower branch through the middle. All attempts made with the CFX code for this geometry failed to predict this complicated flow phenomena.

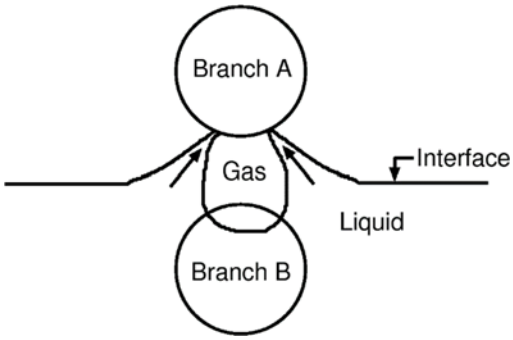

Figure 6.42 - Sketch of interface shape for $h_{OLE,A} < h < h_{OGE,B}$ as observed in experiments for Geometry G4

For P_0 = 120 kPa and an interface height of h_A = -5.7 mm, Figure 6.43 shows the air volume fraction contour looking into the branch outlets plotted on a *y*-*z* plane at the branch inlet. This result was not quite converged after over 80,000 iterations and the mass flow rate of the water through Branch A remained steady at 0. This shows that the numerical model was incapable of predicting the two-phase flow in both branches that was observed experimentally.

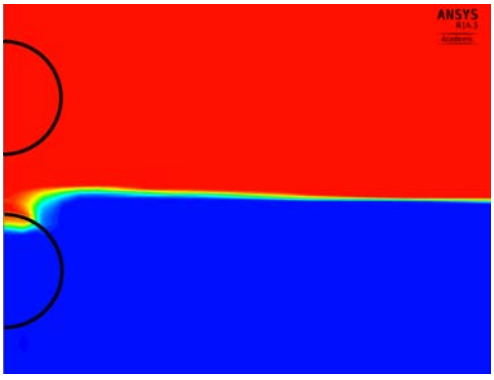

Figure 6.43 - Air volume fraction contours for Geometry G4 with P_0 = 120 kPa and h_A = -5.7 mm

Using the same inhomogeneous, free surface model, additional tests were done for these conditions in an attempt to obtain a converged solution with two-phase flow through both branches simultaneously. These tests involved the following:

- Reducing the size of the mesh in the region near the branch inlet.
- Changing the boundary conditions at the outlet of the branches such that the outlet pressure at the top branch dropped linearly from P_0 to 0 Pa over the first 2000 iterations, followed by a drop in the outlet pressure at the lower branch from P_0 to 0 Pa. This was done to help pull liquid through the upper branch before pulling gas through the lower branch.
- Increasing the drag coefficient from 0.05 to 5.
- Decreasing the drag coefficient from 0.05 to 0.005.

None of the above tests resulted in a converged solution nor were they able to predict two-phase flow through both branches simultaneously.

One last test was conducted using the mixture model instead of the free surface model to solve the same case described above (Geometry G4, P_0 = 120 kPa, h_A = -5.7 mm). With the mixture model, the interfacial area density, which is calculated using Equation (5.12) for the free surface model, is calculated as follows:

$$A_{LG} = \frac{\alpha_L \alpha_G}{d_{LG}} \tag{6.5}$$

Where d_{LG} is an interfacial length scale and was set to the default value of 1 mm. The mixture model was able to predict two-phase flow in each branch for this geometry, as shown in the air volume fraction contours plotted in Figure 6.44 (a) (on a y-z plane located at the branch inlet); however, the solution would not converge and water was appearing in the air region far above the interface near the symmetry plane (Figure 6.44 (b)). More research is required for this geometry to develop a model that is capable of predicting two-phase flow through both branches. It is possible that in order to correctly model this flow phenomenon, different equations are needed for the drag coefficient and/or the interfacial area density for different regions of the domain, similar to the Algebraic Interfacial Area Density (AIAD) model by Hohne et al. (2014).

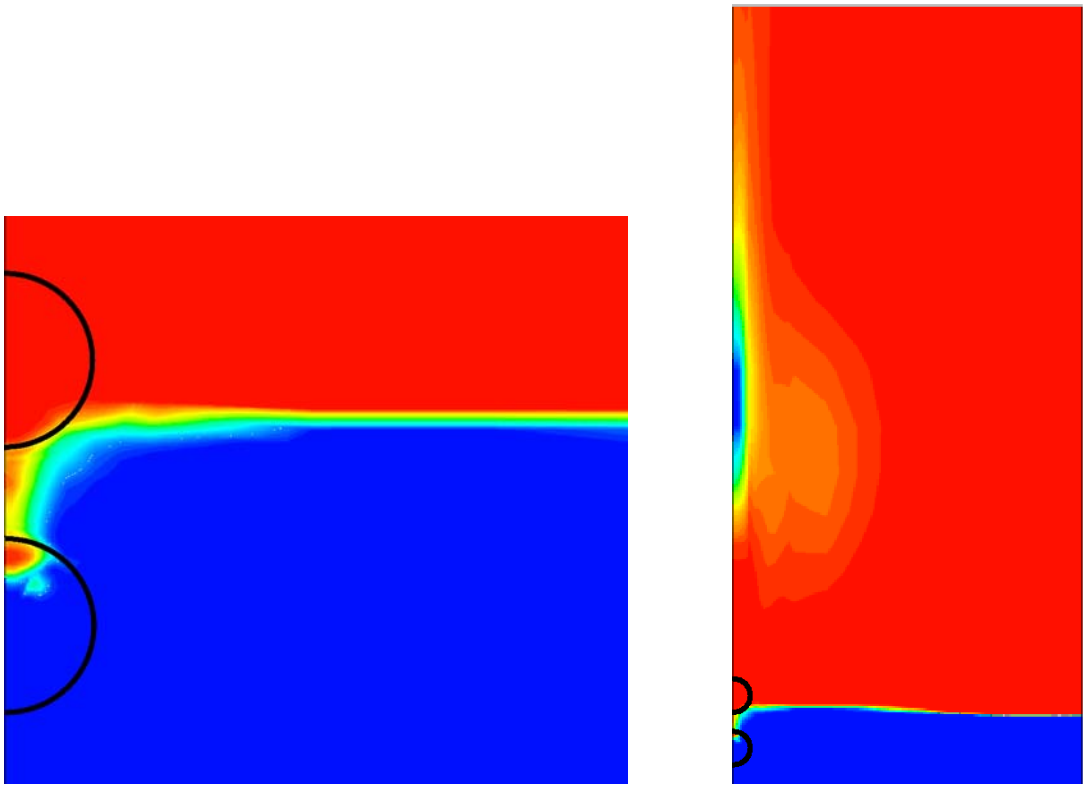

a) Close up view of branches b) View of air region above branches

Figure 6.44 - Air volume fraction contours for Geometry G4 for P_0 = 120 kPa and h_A = -5.7 mm using the mixture model

In summary, for the geometry with L/d = 1.5 and two branches located one on top of the other, converged results were obtained for interface heights between the following two ranges: $h_{OLE,B} \le h < h_{OLE,A}$ and $h_{OGE,B} < h \le h_{OGE,A}$, where single phase air or water flows through one of the two branches. When the interface is located between the two branches and two phases flow through both branches simultaneously, the flow phenomena is too complicated and the model does not converge.

Chapter 7
Conclusion

Two-phase discharging flow from a stratified region of liquid and gas through single or multiple horizontal branches was studied both experimentally and numerically. In the experimental investigation, data were collected for flow through two horizontal branches (d = 6.35 mm) with centrelines separated by a distance L and an angle θ. For 16 different combinations of P_0, ΔP, L/d and θ, measurements of the critical heights at the onsets of gas and liquid entrainment at each branch were taken and the mass flow rates of liquid and gas were measured in each branch for a range of interface heights h. For completeness, additional measurements of the critical heights at the onsets of gas and liquid entrainment were taken to cover a wide range of Froude numbers.

The present experimental results along with Hassan's (1995) correlations for the onset of liquid entrainment show that for the OLE at the lower branch (Branch B), as the angle decreases from θ = 90° (one on top of the other) to θ = 0° (side by side), there is very little variation in $\left|h_{OLE,B}\right|$. For the OLE at Branch A, as the angle increases from θ = 0° to θ = 90°, Branch B competes more with Branch A for liquid entrainment and $\left|h_{OLE,A}\right|$ decreases. Empirical correlations were developed from the present experimental data and Hassan's experimental data for $\left|h_{OLE,A}\right|/d$ and $\left|h_{OLE,B}\right|/d$ and show good agreement with RMS deviations of 4.19% and 2.51%, respectively, for L/d = 1.5 to 8, θ = 0 to 90° and $\mathrm{Fr}_{G,OLE,A} = \mathrm{Fr}_{G,OLE,B}$ = 15 to 40.

For the onset of gas entrainment, the present experimental results along with Hassan's (1995) correlations show that for the OGE at the upper branch (Branch A), as θ decreases from

90° to 0°, Branch B provides more assistance to Branch A with gas entrainment and $h_{OGE,A}$ increases. For the OGE at Branch B, as the angle increases from 0° to 90°, Branch A competes more with Branch B for gas entrainment and $h_{OGE,B}$ decreases. Empirical correlations were developed for $h_{OGE,A}/d$ and $h_{OGE,B}/d$ and show good agreement with RMS deviations of 4.48% and 5.75%, respectively, over the ranges from L/d = 1.5 to 8, θ = 0 to 90° and $\mathrm{Fr}_{G,OLE,A} = \mathrm{Fr}_{G,OLE,B}$ = 15 to 40.

For interface heights between $h_{OLE,B}$ and $h_{OGE,A}$ when two phases flow through the branches, the experimental results for θ = 30° and 60° show that $\dot{m}_{TP,A}$ and $\dot{m}_{TP,B}$ increase with increasing ΔP, and x_A and x_B increase with increasing ΔP at high values of h and decrease with increasing ΔP at low values of h. However, the effects of ΔP and P_0 are absorbed when the results are plotted as M versus H and the effect of ΔP is absorbed when the results are plotted as x versus H, similar to what Hassan (1995) found for single and dual branch geometries for θ = 0 and 90°.

By comparing the mass flow rate and quality results at Branch A with those for Branch B for the 16 cases tested in this study, it was concluded that the branches have less influence on one another and behave more as independent branches as ΔP and θ decrease and as L/d increases. In fact, for the case with the lowest ΔP and θ and the highest L/d (P_0 = 316 kPa, ΔP = 40 kPa, θ = 30° and L/d = 3), there was negligible difference between the results at Branches A and B and they are therefore behaving as completely independent branches.

The effect of θ was analyzed more closely by plotting results for $\dot{m}_{TP}$ and x at different values of θ together on one plot. In general, for Branch A and at low values of h, $\dot{m}_{TP}$ decreases and x increases with increasing θ due to $|h_{OLE,A}|$ decreasing with increasing θ. As the interface is raised past the OLE, the later occurrence of the OLE at higher values of θ results in less liquid flowing through the branch and a lower $\dot{m}_{TP}$ and higher x. At high values of h, the opposite trend occurs: $\dot{m}_{TP}$ increases and x decreases with increasing θ. This trend can be explained by the decreasing h_{OGE} with increasing θ, i.e., as the interface is lowered past the OGE, the later

occurrence of the OGE at higher values of θ results in less gas (or more liquid) flowing through the branch and thus a higher $\dot{m}_{TP}$ and lower x. The same trends were observed at Branch B at high values of h while at low values h, the data became indistinguishable because the variation of $\left|h_{OLE,B}\right|$ with θ was negligible.

From the present experimental data and Hassan's (1995) correlations, new correlations were developed for $M_A\left(H_A, L/d, \theta\right)$, $M_B\left(H_B, L/d, \theta\right)$, $x_A\left(H_A, L/d, \theta, \rho_L/\rho_G\right)$ and $x_B\left(H_B, L/d, \theta, \rho_L/\rho_G\right)$. The correlations are valid over the following ranges: P_0 = 316 to 517 kPa; ΔP = 40 to 235 kPa; θ = 0 to 90°; L/d = 1.5 to ∞ and show reasonable agreement with the experimental results with RMS deviations of 11.42% for M_A (for $0.1 \le M_A \le 1$), 8.06% for M_B (for $0.1 \le M_B \le 1$), 19.07% for x_A (for $0.01 \le x_A \le 1$), and 17.22% for x_B (for $0.01 \le x_B \le 1$).

For the numerical portion of this study, the inhomogeneous free surface model in ANSYS CFX was used to model discharge from a stratified two-phase region through the following branch geometries:

- single branch with square cross section and L_B/d = 20 (G1)
- single branch with square cross section and L_B/d = 200 (G2)
- single branch with circular cross section and L_B/d = 200 (G3)
- dual branches located one-on-top of the other with L_B/d = 200 (G4)
- dual branches located at an angle of 30° from one another with L_B/d = 200 (G5)

Results from the numerical model were obtained for the critical heights of the interface at the onsets of gas and liquid entrainment, as well as the mass flow rate and quality during two-phase discharge. For Geometries G1, G2, G3 and G5, good agreement was found between the numerical results and the present and previous experimental data and correlations. The numerical model also provides additional results that were not obtained experimentally including pressure contours and force balances at the onset of gas and liquid entrainments, respectively. These results provide insight into the flow characteristics just before the onsets. This success of CFX is valid for the conditions tested here and it remains to be seen if it extends to other conditions.

For Geometry G4 with the branches located one on top of the other, the numerical model was unable to predict results when the interface was located between $h_{OLE,A}$ and $h_{OGE,B}$ such that the two phases flow through both branches. Under these conditions, experimental investigations have observed a complicated flow phenomena with both branches pulling fluid from the same region; liquid flows to the upper branch in two streams around a spout of gas flowing downwards to the lower branch. Several modifications were made to the model in an attempt to obtain a converged solution including changing the drag coefficient, the initial boundary conditions and using the mixture model instead of the free surface model; however, CFX was still unable to predict results. It is possible that in order to correctly model this flow phenomenon, different equations are needed for the drag coefficient and/or the interfacial area density for different regions of the domain. This is beyond the scope of this project but would be useful to explore in the future.

References

Ahmad, T. and Hassan, I., 2006. Experimental investigation on the onset of gas entrainment from a stratified two-phase region through multiple branches mounted on a curved surface. *Journal of Fluids Engineering*, vol. 128, pp. 726-733.

Ahmed, M., Hassan, I. and Esmail, N., 2003. Modeling of the onset of gas entrainment through a finite-side branch. *Journal of Fluids Engineering*, vol. 125, pp. 902-909.

Ahmed, M., Hassan, I. and Esmail, N., 2004. Theoretical analysis of the onset of gas entrainment from a stratified region through a single side-oriented branch at moderate Froude numbers. *The Canadian Journal of Chemical Engineering*, vol. 82, pp. 1175-1182.

Ahmed, M., Hassan, I. and Esmail, N., 2004. The onset of gas pull-through during dual discharge from a stratified two-phase region: Theoretical analysis. *Physics of Fluids*, vol. 16, pp. 3385-3392.

Ahmed, M., 2006. Theoretical analysis of the onset of gas entrainment from a stratified two-phase region through two side-oriented branches mounted on a vertical wall. *Journal of Fluids Engineering*, vol. 128, pp. 131-141.

Ahmed, M., 2008. Influence of wall inclination angles on the onset of gas entrainment during single and dual discharges from a reservoir. *Journal of Fluids Engineering*, vol. 130, pp. 1-16.

Andaleeb, A.F., Hassan, I., Saleh, W. and Ahmad, T., 2006. Modeling of the onset of gas entrainment from a stratified two-phase region through branches on a curved surface. *Journal of Fluids Engineering*, vol. 128, pp. 717-725.

ANSYS® Academic Research, Release 15.0, 2013. *CFX-Solver Theory Manual, CFX-Solver Modeling Guide*, ANSYS, Inc., Canonsburg, PA.

Armstrong, K.F., Parrott, D., Sims, G.E., Soliman, H.M. and Krishnan, V.S., 1992. Theoretical and experimental study of the onset of liquid entrainment during dual discharge from large reservoirs. *International Journal of Multiphase Flow*, vol. 18, no. 2, pp 217-227.

Barth, T.J. and Jespersen, D.C., 1989. The design and application of upwind schemes on unstructured meshes. AIAA Paper 89-0366.

Bartley, J.T., Soliman, H.M. and Sims, G.E., 2004. Analytical prediction of single and dual two-phase discharges from stratified regions. *Proceedings of the Third International Symposium on Two-Phase Flow Modelling and Experimentation*, Pisa, Italy.

Bartley, J.T., Soliman, H.M. and Sims, G.E., 2008. Experimental investigation of the onsets of gas and liquid entrainment from a small branch mounted on an inclined wall. *International Journal of Multiphase Flow*, vol. 34, pp. 905-915.

Bartley, J.T., Soliman, H.M. and Sims, G.E., 2010. Experimental investigation of two-phase discharge from a stratified region through a small branch mounted on an inclined wall. *International Journal of Multiphase Flow*, vol. 36, pp. 588-597.

Bergman, T.L., Lavine, A.S., Incropera, F.P. and DeWitt, D.P., 2011. *Fundamentals of Heat and Mass Transfer*, 7th Ed., John Wiley and Sons.

Bowden, R.C. and Hassan, I.G., 2008. Incipience of liquid entrainment from a stratified gas-liquid region in multiple discharging branches. *Journal of Fluid Engineering*, vol. 130, pp. 1-10.

Craya, A., 1949. Theoretical research on the flow of non-homogeneous fluids. *Houille Blanche*, vol. 4, pp. 44-55.

Gardner, G.C., 1988. Co-current flow of air and water from a reservoir into a short horizontal pipe. *International Journal of Multiphase Flow*, vol. 14, pp. 375-388.

Hassan, I., 1995. Single, dual and triple discharge from a large, stratified, two-phase region through small branches. *Ph.D. Thesis*, University of Manitoba.

Hassan, I.G., Soliman, H.M., Sims, G.E. and Kowalski, J.E., 1996. Discharge from a smooth stratified two-phase region through two horizontal side branches located in the same vertical plane. *International Journal of Multiphase Flow*, vol. 22, no. 6, pp. 1123-1142.

Hassan, I.G., Soliman, H.M., Sims, G.E. and Kowalski, J.E., 1996. Experimental investigation of the two-phase discharge from a stratified region through two side branches oriented horizontally. *Experimental Thermal and Fluid Science*, vol. 13, pp. 117-128.

Hassan, I.G., Soliman, H.M., Sims, G.E. and Kowalski, J.E., 1997. Single and multiple discharge from a stratified two-phase region through small branches. *Nuclear Engineering and Design*, vol. 176, pp. 233-245.

Hassan, I.G., Soliman, H.M., Sims, G.E. and Kowalski, J.E., 1998. Two-phase flow from a stratified region through a small side branch. *Journal of Fluids Engineering*, vol. 120, pp. 605-612.

Hohne, T. and Mehlhoop, J.P., 2014. Validation of closure models for interfacial drag and turbulence in numerical simulations of horizontal stratified gas-liquid flows. *International Journal of Multiphase Flow*, vol. 62, pp. 1-16.

Kline, S.J. and McClintock, F.A., 1987. Describing the uncertainties in single-sample experiments. *AIChE Annual Meeting*, New York.

Kowalski, J.E. and Hanna, B.N., 1988. Refill study of a CANDU-type header/feeder system under near-zero header-to-header pressure drop. *Canadian Nuclear Society 9th Annual Conference Proceedings*, pp. 229-236.

Kowalski, J.E. and Hanna, B.B., 1989. Studies of two-phase flow distribution in a CANDU-type header/feeder system. *Proceedings of the 4th International Topical Meeting on Nuclear Reactor Thermal-Hydraulics*, vol. 1, pp. 28-33.

Kowalski, J.E. and Krishnan, V.S., 1987. Two-phase distribution in a large manifold. AIChE Annual Meeting, New York, NY.

Lee, J.Y., Hwang, S.H., Kim, M. and Park, G.C., 2007. Onset condition of gas and liquid entrainment at an inclined branch pipe on a horizontal header. *Nuclear Engineering and Design*, vol. 237, pp. 1046-1054.

Lubin, B.T. and Springer, G.S., 1967. The formation of a dip on the surface of a liquid draining from a tank. *Journal of Fluid Mechanics*, vol. 29, pp. 385-390.

Maier, M., 1998. Onsets of liquid and gas entrainment during discharge from a stratified air-water region through two horizontal side branches with centerlines falling in an inclined plane. *M.Sc. Thesis*, University of Manitoba.

Maier, M.R., Soliman, H.M., Sims, G.E. and Armstrong, K.F., 2001. Onsets of entrainment during dual discharge from a stratified two-phase region through horizontal branches with centrelines falling in an inclined plane: Part 1 – Analysis of liquid entrainment. *International Journal of Multiphase Flow*, vol. 27, pp. 1011-1028.

Maier, M.R., Soliman, H.M. and Sims, G.E., 2001. Onsets of entrainment during dual discharge from a stratified two-phase region through horizontal branches with centrelines falling in an inclined plane: Part 2 – Experiments on gas and liquid entrainment. *International Journal of Multiphase Flow*, vol. 27, pp. 1029-1049.

Micaelli, J.C. and Memponteil, A., 1989. Two-phase flow behavior in a tee-junction – the CATHARE model. *Proceedings of the 4th International Topical Meeting on Nuclear Reactor Thermal-Hydraulics*, Karlsruhe, F.R.G., vol. 2, pp. 1024-1030.

Parrott, S.D., Soliman, H.M., Sims, G.E. and Krishnan, V.S., 1991. Experiments on the onset of gas pull-through during dual discharge from a reservoir. *International Journal of Multiphase Flow*, vol. 17, no. 1, pp. 119-129.

Parrott, S., 1993. Experiments on the onsets of gas pull-through and liquid entrainment during dual discharge form a large reservoir. *M.Sc. Thesis*, University of Manitoba.

Saleh, W., Bowden, R.C., Hassan, I.G. and Kadem, L., 2009. A hybrid model to predict the onset of gas entrainment with surface tension effects. *Journal of Fluids Engineering*, vol. 131, pp. 1-10.

Saleh, W., Bowden, R.C., Hassan, I.G. and Kadem, L., 2011. Theoretical analysis of the onset of gas entrainment from a stratified region through multiple branches. *International Journal of Multiphase Flow*, vol. 37, pp. 1348-1357.

Schrock, V.E., Revankar, S.T., Mannheimer, R., Wang, C.H. and Jia, D., 1986. Steam-water critical flow through small pipes from stratified upstream regions. *Proceedings of the 8th Int. Heat Transfer Conf.*, San Francisco, California, vol. 5, pp. 2307-2311.

Shaban, H. and Tavoularis, S., 2012. Simulations of air-water flow in header/feeder systems using the volume of fluid method. *1000 Islands Fluid Mechanics Meeting*.

Shaban, H. and Tavoularis, S., 2015. Distribution of downward air-water flow in vertical tubes connected to a horizontal cylindrical header. *Nuclear Engineering and Design*, vol. 291, pp. 90-100.

Smoglie, C. and Reimann, J., 1986. Two-phase flow through small branches in a horizontal pipe with stratified flow. *International Journal of Multiphase Flow*, vol. 12, no. 4, pp. 609-625.

Soliman, H.M. and Sims, G.E., 1991. Theoretical analysis of the onset of liquid entrainment for slots of finite width. *International Journal of Heat and Fluid Flow*, vol. 12, no. 4, pp. 360-364.

Soliman, H.M. and Sims, G.E., 1992. Theoretical analysis of the onset of liquid entrainment for orifices of finite diameter. *International Journal of Multiphase Flow*, vol. 18, no. 2, pp. 229-235.

Teclemeriam, Z., Soliman, H.M., Sims, G.E. and Kowalski, J.E., 2003. Experimental investigation of the two-phase flow distribution in the outlets of a horizontal multi-branch header. *Nuclear Engineering and Design*, vol. 222, pp. 29-39.

Yonomoto, T. and Tasaka, K., 1988. New theoretical model for two-phase flow discharged from stratified two-phase region through small break. *Journal of Nuclear Science and Technology*, vol. 25, no. 5, pp. 441-455.

Zuber, N., 1980. Problems in modeling of small break LOCA. *Nuclear Regulatory Commission Report NUREG-0724*.

Zwart, P.J., Scheuerer, M. and Bogner, M., 2003. Free surface flow modelling of an impinging jet. *ASTAR Int. Workshop on Advanced Numerical Methods for Multidimensional Simulation of Two-Phase Flows*, GRS, Garching, Germany, pp. 1-12.

Appendix A

Instrument Calibration

A.1 Thermocouple Calibration

The four Type T thermocouples, TC1 – TC4, used in the experiments were calibrated at three different temperatures: freezing point, ambient room temperature and boiling point. For freezing conditions, an ice bath mixture of water and crushed ice was used and for boiling point, water was heated in a glass flask using a hot plate. The thermocouples were connected to a type T thermocouple reader and temperatures in °C were read directly from this reader and compared with the readings from mercury thermometers. Table A.1 shows the results from these calibrations. During the experiments, linear interpolation was done using the tabulated data to convert the thermocouple reader temperatures into actual temperatures.

Table A.1 - Thermocouple calibration data

Conditions	TC1 (°C)	TC2 (°C)	TC3 (°C)	TC4 (°C)	Thermometer (°C)
Ice Point	0.8	0.7	0.7	0.7	0.2
Room Temperature	22.6	22.5	22.6	22.6	22.9
Boiling	100	99.9	100.2	100.2	100.3

A.2 Pressure Gauge Calibration

Four pressure gauges, PG1 – PG4, were calibrated for measuring air pressures in the test section (PG1), the two separators (PG2 and PG3) and the outlet header (PG4). Pressure gauges, PG1-PG3, are Bourdon-tube type pressure gauges and were calibrated over a range of 0 to 100 psi and PG4 is a digital gauge and was calibrated over a range of 0 to 60 psi. An Ashcroft dead-weight testing device was used for these calibrations. The results are tabulated in Table A.2. Linear interpolation was done to correct the pressure readings throughout the experiments. The corrected values were then converted from units of psi to kPa.

Table A.2 - Calibrated data for pressure gauges PG1 – PG4

Calibration Load (psi)	PG1 Gauge Pressure Reading (psi)	PG2 Gauge Pressure Reading (psi)	PG3 Gauge Pressure Reading (psi)	PG4 Gauge Pressure Reading (psi)
0	0.0	0.0	0.0	0.00
5	5.0	7.5	6.5	4.97
10	10.0	12.5	11.5	9.96
15	15.5	17.5	16.5	15.00
20	20.5	22.5	21.5	19.94
25	25.5	27.5	27.0	24.93
30	30.5	32.5	32.0	29.94
35	35.5	37.5	37.5	34.94
40	40.5	42.5	42.0	39.88
45	45.5	46.5	47.0	44.90
50	50.5	51.5	52.0	49.96
55	54.5	56.5	57.5	54.85
60	60.0	61.5	62.0	59.81
65	64.5	66.0	67.0	-
70	69.5	71.0	72.0	-
75	74.0	76.0	77.0	-
80	79.5	81.0	82.0	-
85	84.0	86.0	87.0	-
90	89.5	90.5	92.0	-
95	94.5	96.0	97.0	-
100	99.0	100.5	101.5	-

A.3 Water Rotameter Calibration

All eight water rotameters, Wa1 – Wa4 and Wb1 – Wb4, were calibrated using a weigh and time method. For each rotameter, the water that passed through was collected for a period of time ranging from 2 minutes for the largest scales on the largest rotameters to 20 minutes for the smallest scales on the smallest rotameters. The collected water was then weighed and the actual flow rate was calculated for each scale decade by dividing the mass by the time. Tables A.3 to A.6 show the results of these calibrations for all eight water rotameters. Throughout the experiments, the values in these tables were interpolated to obtain the actual mass flow rate in kg/s.

Table A.3 - Calibration data for water rotameters Wa1 and Wb1

Scale (%)	Wa1			Wb1		
	Weight (kg)	Time (s)	$\dot{m}_{L,A}$ (kg/s)	Weight (kg)	Time (s)	$\dot{m}_{L,A}$ (kg/s)
10	26.0362	300.65	0.0866	27.2155	300.01	0.0907
20	36.5595	240.11	0.1523	38.0110	239.85	0.1585
30	51.9817	240.08	0.2165	52.8889	240.15	0.2202
40	54.5218	190.25	0.2866	51.6188	180.00	0.2868
50	55.9733	160.53	0.3487	52.8889	150.10	0.3524
60	58.3320	139.98	0.4167	59.0577	141.35	0.4178
70	56.5176	120.16	0.4704	58.2413	120.29	0.4842
80	62.1422	115.66	0.5373	53.8868	97.90	0.5504
90	60.4185	100.03	0.6040	56.3362	90.40	0.6232
100	60.6907	89.90	0.6751	58.6041	85.05	0.6891

Table A.4 - Calibration data for water rotameters Wa2 and Wb2

Scale (%)	Wa2			Wb2		
	Weight (kg)	Time (s)	$\dot{m}_{L,A}$ (kg/s)	Weight (kg)	Time (s)	$\dot{m}_{L,A}$ (kg/s)
10	3.0300	300.28	0.0101	2.9170	332.91	0.0088
20	4.5985	300.13	0.0153	4.2775	300.76	0.0142
30	6.2730	300.38	0.0209	6.0490	300.65	0.0201
40	8.1410	300.28	0.0271	7.9165	301.65	0.0262
50	10.0065	300.01	0.0334	9.7790	300.25	0.0326
60	11.9805	300.29	0.0399	11.6675	300.18	0.0389
70	13.9745	300.16	0.0466	14.7800	322.75	0.0458
80	15.9460	300.13	0.0531	12.6180	240.41	0.0525
90	18.3685	305.85	0.0601	17.8810	300.21	0.0596
100	16.0645	240.33	0.0668	15.9125	240.15	0.0663

Table A.5 - Calibration data for water rotameters Wa3 and Wb3

Scale (%)	Wa3			Wb3		
	Weight (kg)	Time (s)	$\dot{m}_{L,A}$ (kg/s)	Weight (kg)	Time (s)	$\dot{m}_{L,A}$ (kg/s)
10	0.2625	1200.11	2.19E-04	0.2180	1218.31	1.79E-04
20	0.4475	600.08	7.46E-04	0.4400	601.05	7.32E-04
30	0.8360	600.36	1.39E-03	0.6205	450.95	1.38E-03
40	1.2355	600.28	2.06E-03	1.1565	579.48	2.00E-03
50	1.4945	540.08	2.77E-03	1.2385	450.16	2.75E-03
60	1.0450	300.18	3.48E-03	1.4290	409.68	3.49E-03
70	1.2505	300.16	4.17E-03	1.2740	300.75	4.24E-03
80	1.5100	315.16	4.79E-03	1.4705	298.88	4.92E-03
90	1.6850	300.15	5.61E-03	1.6840	299.91	5.62E-03
100	1.8825	303.40	6.20E-03	1.8890	301.28	6.27E-03
110	2.0850	300.15	6.95E-03	2.3780	340.33	6.99E-03
120	2.3170	300.26	7.72E-03	2.3225	300.23	7.74E-03
130	2.4920	300.21	8.30E-03	2.6800	316.23	8.47E-03
140	2.9950	332.09	9.02E-03	2.8135	305.58	9.21E-03
150	2.8550	301.08	9.48E-03	2.9690	300.15	9.89E-03

Table A.6 - Calibration data for water rotameters Wa4 and Wb4

Scale (%)	Wa4			Wb4		
	Weight (kg)	Time (s)	$\dot{m}_{L,A}$ (kg/s)	Weight (kg)	Time (s)	$\dot{m}_{L,A}$ (kg/s)
10	0.0595	1293.61	4.5995E-05	0.0445	600.39	7.4118E-05
20	0.1395	1010.00	1.3812E-04	0.0915	600.37	1.5241E-04
30	0.1650	600.08	2.7496E-04	0.1445	605.50	2.3865E-04
40	0.2325	600.20	3.8737E-04	0.2540	600.38	4.2307E-04
50	0.3040	620.02	4.9031E-04	0.3230	600.25	5.3811E-04
60	0.3555	600.15	5.9235E-04	0.4055	634.73	6.3885E-04
70	0.4120	600.06	6.8660E-04	0.4335	600.48	7.2192E-04
80	0.4940	620.28	7.9641E-04	0.4970	600.75	8.2730E-04
90	0.5340	600.05	8.8993E-04	0.5580	600.22	9.2966E-04
100	0.5905	603.40	9.7862E-04	0.6085	599.99	1.0142E-03
110	0.6485	600.06	1.0807E-03	0.6520	602.28	1.0826E-03
120	0.7125	599.87	1.1878E-03	0.6910	569.80	1.2127E-03
130	0.7855	599.98	1.3092E-03	0.7875	600.25	1.3120E-03
140	0.8500	610.08	1.3933E-03	0.8755	600.49	1.4580E-03
150	0.8955	600.39	1.4915E-03	0.9725	600.43	1.6197E-03

A.4 Air Rotameter Calibration

The eight air rotameters, Aa1 – Aa4 and Ab1 – Ab4, were calibrated by measuring the volume of air flow through each rotameter (at each decade) over a certain amount of time. For most flow rates, either a 10 [dm^3] or a 1000 [dm^3] Elster-Handel wet-type gas meter was connected to the outlet header to measure the volume of air flow. The actual mass flow rate was then calculated using the following equation:

$$\dot{m}_G = Q_G \rho_{G,calib} \tag{A.1}$$

where $\rho_{G,calib}$ is calculated using the ideal gas law:

$$\rho_{G,calib} = \frac{P_{calib}}{R_G T_{G,0,calib}} \tag{A.2}$$

In Equation (A.2), P_{calib} is the pressure in the outlet air header measured by the pressure gauge PG4 during calibrations and $T_{G,0,calib}$ is the temperature of air in the test section (TC1) during calibrations.

For some of the largest flow rates, venturi tubes were used (0.375 inch throat or 0.625 inch throat) and the static pressure at the inlet to the throat and the pressure difference between the upstream and the throat were recorded. An expression was then used to calculate the actual mass flow rate using these pressure measurements along with the geometry of the venturi, a discharge coefficient, and a compressibility factor.

Regardless of which instrument was used in the calibrations, the standard mass flow rate was calculated as follows:

$$\dot{m}_{G,STD} = \dot{m}_G \sqrt{\rho_{STD} / \rho_{G,calib}} \tag{A.3}$$

where the standard density was taken as 1.19978 kg/m^3. The results from the calibrations of the air rotameters are shown in Tables A.7 to A.10 below. Throughout the experiments, the standard mass flow rates were interpolated using these tables and then converted to actual mass flow rates as discussed in Section 3.4.

Table A.7 - Calibration data for air rotameters Aa1 and Ab1

Aa1		Ab1	
Scale (%)	**$\dot{m}_{G,STD}$ (kg/s)**	**Scale (%)**	**$\dot{m}_{G,STD}$ (kg/s)**
10	2.3487E-03	10	2.6848E-03
20	4.9467E-03	20	5.2905E-03
30	7.4523E-03	30	7.6412E-03
40	1.0034E-02	40	1.0392E-02
50	1.2746E-02	50	1.3146E-02
60	1.5241E-02	60	1.5856E-02
70	1.8369E-02	70	1.8698E-02
80	2.0965E-02	78	2.0743E-02

Table A.8 - Calibration data for air rotameters Aa2 and Ab2

Scale (%)	**Aa2**	**Ab2**
	$\dot{m}_{G,STD}$ (kg/s)	**$\dot{m}_{G,STD}$ (kg/s)**
10	3.7117E-04	3.7077E-04
20	6.7134E-04	6.8611E-04
30	9.8152E-04	9.9060E-04
40	1.2972E-03	1.3217E-03
50	1.6130E-03	1.6411E-03
60	1.9257E-03	1.9531E-03
70	2.2770E-03	2.2934E-03
80	2.5926E-03	2.6446E-03
90	2.9594E-03	3.0319E-03
100	3.2623E-03	3.3469E-03

Table A.9 - Calibration data for air rotameters Aa3 and Ab3

Scale (%)	Aa3	Ab3
	$\dot{m}_{G,STD}$ (kg/s)	$\dot{m}_{G,STD}$ (kg/s)
10	2.1039E-05	1.9493E-05
20	4.5346E-05	4.4080E-05
30	6.7465E-05	6.6717E-05
40	9.2528E-05	9.1654E-05
50	1.1283E-04	1.1118E-04
60	1.3373E-04	1.3476E-04
70	1.5694E-04	1.5558E-04
80	1.7703E-04	1.7803E-04
90	2.0260E-04	1.9986E-04
100	2.2166E-04	2.2506E-04
110	2.4021E-04	2.4263E-04
120	2.6279E-04	2.6383E-04
130	2.8372E-04	2.8440E-04
140	3.0451E-04	3.0724E-04
150	3.2902E-04	3.2571E-04

Table A.10 - Calibration data for air rotameters Aa4 and Ab4

Scale (%)	Aa4	Ab4
	$\dot{m}_{G,STD}$ (kg/s)	$\dot{m}_{G,STD}$ (kg/s)
10	3.7219E-06	3.7018E-06
20	8.0185E-06	7.6931E-06
30	1.1996E-05	1.1498E-05
40	1.6342E-05	1.5031E-05
50	1.8199E-05	1.8284E-05
60	2.1810E-05	2.1422E-05
70	2.5470E-05	2.5314E-05
80	2.8841E-05	2.8232E-05
90	3.1715E-05	3.1251E-05
100	3.3480E-05	3.4912E-05
110	3.6196E-05	3.6185E-05
120	3.8816E-05	3.8888E-05
130	4.1546E-05	4.1279E-05
140	4.4038E-05	4.4008E-05
150	4.6551E-05	4.6155E-05

A.5 Pressure Transducer Calibration

The pressure transducers were calibrated by connecting the high side to a hand pump and a manometer as shown in Figure A.1 and leaving the low side open to atmosphere.

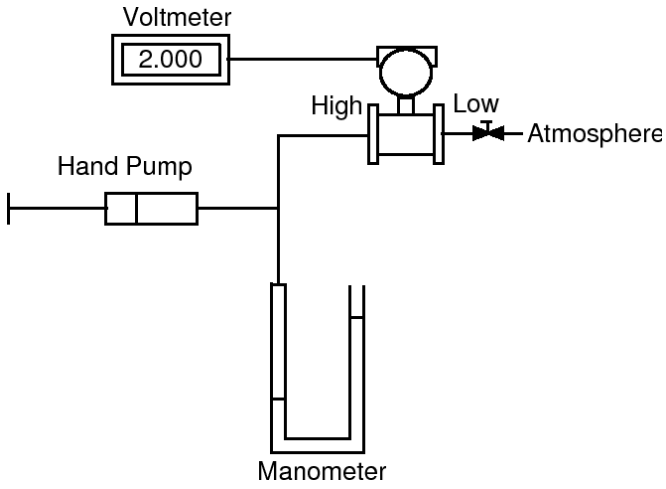

Figure A.1 - Diagram for calibration of pressure transducers

For the pressure transducer on the test section, the desired range of static head was from zero to 165 mm H_2O, as shown in Figure 3.5. Since the pressure transducer is located $L_{zero} = 217$ mm below the desired zero elevation, the zero on the transducer was adjusted to give a reading of 2.0 Volts when applying a pressure of 217 mm H_2O. The span on the pressure transducer was also adjusted such that the maximum desired pressure reading of 165 mm H_2O corresponded to a signal reading of 10.0 Volts. A total of 15 measurements were taken between these two limits and a second order polynomial was fit to the data, as shown in Figure A.2. The following polynomial fit the data well with an RMS deviation of 0.8%. Throughout the experiments, this voltage reading was converted to an interface height measurement using the method described in Section 3.2.5.

$$P(\mathrm{mmH_2O}) = -41.323 + 20.619E_L - 0.0171E_L^2 \qquad \text{(A.4)}$$

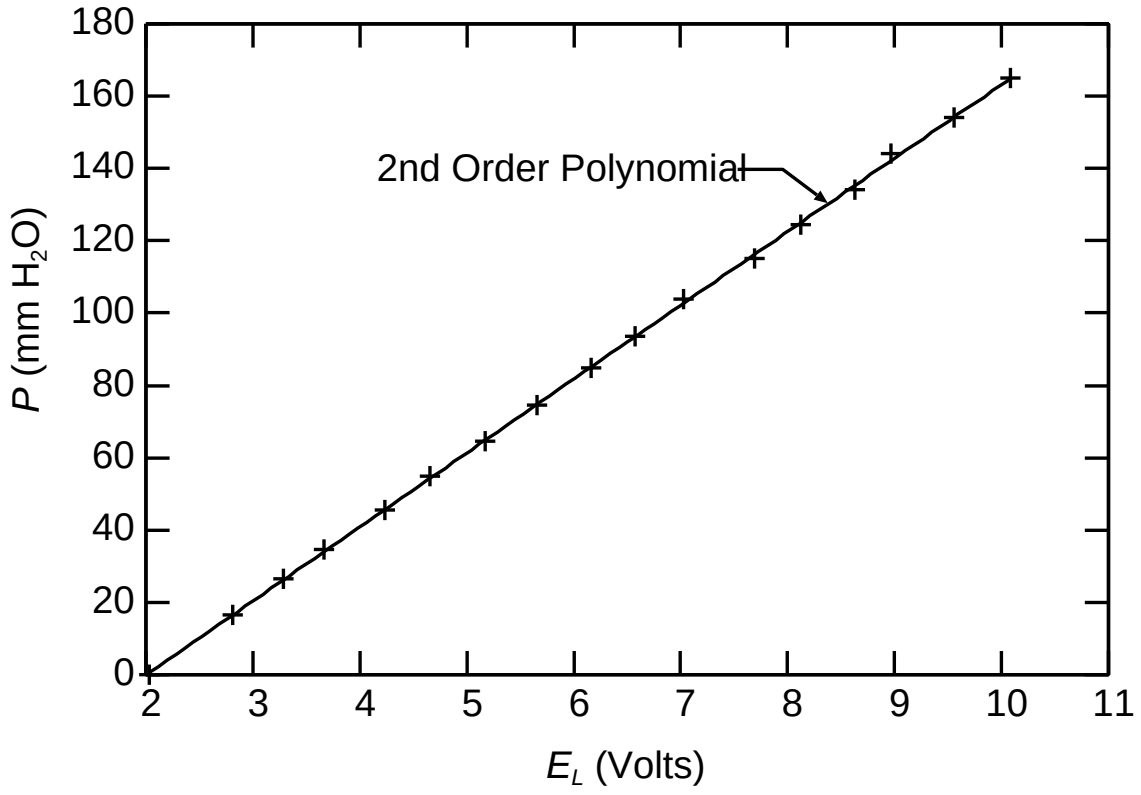

Figure A.2 - Calibration results for test section pressure transducer

The pressure transducer on the separators was calibrated such that the low limit (2.0 Volts) corresponded to -38 cm H_2O and the high limit (10.0 Volts) corresponded to 38 cm H_2O. Throughout the experiments, the reading on the pressure transducer was maintained at 6.0 Volts to ensure the pressure difference across the separators was zero.

Appendix B

Estimates of Experimental Uncertainty

B.1 General Uncertainty Equation

The method of estimating experimental uncertainty, presented by Kline and McClintock (1987) will be followed in this study. In this method, the uncertainty, ω_R , for a result, R, that depends on variables, v_1, v_2, … v_n, with uncertainties, ω_1 , ω_2, .. ω_n, respectively is calculated using the following:

$$\omega_R = \left[\left(\frac{\partial R}{\partial v_1} \omega_1 \right)^2 + \left(\frac{\partial R}{\partial v_2} \omega_2 \right)^2 + \ldots + \left(\frac{\partial R}{\partial v_n} \omega_n \right)^2 \right]^{0.5} \tag{B.1}$$

B.2 Uncertainty in Mass Flow Rates

The uncertainties in the mass flow rates, $\dot{m}_L$ and $\dot{m}_G$, were taken to be the root sum square of the uncertainties in the rotameter readings and the uncertainties in the calibrations. For both liquid and gas, the uncertainties in the rotameter readings and the calibrations were estimated to be ± 0.5% and ± 0.4%, respectively, of the rotameter full scale reading. The uncertainties in kg/s for all eight rotameters are shown in the following table:

Table B.1 – Uncertainty in $\dot{m}_L$

Rotameter	$\omega_{\dot{m}_L}$ (kg/s)
Wa1	4.323E-03
Wa2	4.280E-04
Wa3	6.072E-05
Wa4	9.550E-06
Wb1	4.412E-03
Wb2	4.243E-04
Wb3	6.334E-05
Wb4	1.037E-05

Table B.2 – Uncertainty in $\dot{m}_G$

Rotameter	$\omega_{\dot{m}_G}$ (kg/s)
Aa1	1.491E-04
Aa2	2.105E-05
Aa3	2.113E-06
Aa4	2.992E-07
Ab1	1.474E-04
Ab2	2.159E-05
Ab3	2.089E-06
Ab4	2.955E-07

The uncertainty in the two-phase mass flow rate, $\omega_{\dot{m}_{TP}}$, can then be calculated with the following equation. The results for $\omega_{\dot{m}_{TP}}$ are shown for all the experimental runs in Tables B.7 to B.38.

$$\omega_{\dot{m}_{TP}} = \left[\omega_{\dot{m}_L}{}^2 + \omega_{\dot{m}_G}{}^2 \right]^{0.5} \tag{B.2}$$

B.3 Uncertainty in Froude Numbers

The liquid Froude number is a function of $\dot{m}_{L,OGE}$, A, d, g, ρ_L and ρ_G. The uncertainty in the gravitational acceleration was assumed negligible. The uncertainty in the branch diameter was estimated to be $\omega_d = \pm 0.1$ mm and the uncertainty in A was calculated using Equation (B.1) as:

$$\omega_A = \frac{\pi d \omega_d}{2} = \pm 0.9975 \text{ mm}^2 \tag{B.3}$$

The water density used in calculating the liquid Froude number was taken from steam tables using the measured temperature of the water. The uncertainty in the steam table is ± 0.2 kg/m^3. The uncertainty in the gas density at the throat was mainly due to the assumption of isentropic expansion with n = 1.4, as discussed in Section 3.4. Parrott (1993) reasoned that the uncertainty in air density could be calculated as the difference between the throat density using n = 1.2 (assuming a polytropic, adiabatic expansion) and the value of 1.4 that was used in this analysis. Using Equation (B.1), the uncertainty in $\text{Fr}_{L,OGE}$ can be calculated as:

$$\omega_{\text{Fr}_{L,OGE}} = \left[\begin{array}{l} \left(\dfrac{\omega_{\dot{m}_{L,OGE}}}{A\sqrt{gd\rho_L(\rho_L-\rho_G)}} \right)^2 + \left(\dfrac{-\dot{m}_{L,OGE}\omega_A}{A^2\sqrt{gd\rho_L(\rho_L-\rho_G)}} \right)^2 + \left(\dfrac{-\dot{m}_{L,OGE}\omega_d}{2A\sqrt{gd^3\rho_L(\rho_L-\rho_G)}} \right)^2 \\ + \left(\dfrac{-\dot{m}_{L,OGE}(2\rho_L-\rho_G)\omega_{\rho_L}}{2A\sqrt{gd\left(\rho_L^2-\rho_L\rho_G\right)^3}} \right)^2 + \left(\dfrac{\dot{m}_{L,OGE}\rho_L\omega_{\rho_G}}{2A\sqrt{gd\left(\rho_L^2-\rho_L\rho_G\right)^3}} \right)^2 \end{array} \right]^{0.5} \tag{B.4}$$

The gas Froude number is a function of $\dot{m}_{L,OGE}$, A, d, g, ρ_L and ρ_G and can be calculated as:

$$\omega_{\text{Fr}_{G,OLE}} = \left[\begin{array}{l} \left(\dfrac{\omega_{\dot{m}_G}}{A\sqrt{gd\rho_G(\rho_L-\rho_G)}} \right)^2 + \left(\dfrac{-\dot{m}_G\omega_A}{A^2\sqrt{gd\rho_G(\rho_L-\rho_G)}} \right)^2 + \left(\dfrac{-\dot{m}_G\omega_d}{2A\sqrt{gd^3\rho_G(\rho_L-\rho_G)}} \right)^2 \\ + \left(\dfrac{-\dot{m}_G\rho_G\omega_{\rho_L}}{2A\sqrt{gd\left(\rho_L\rho_G-\rho_G^2\right)^3}} \right)^2 + \left(\dfrac{-\dot{m}_G(\rho_L-2\rho_G)\omega_{\rho_G}}{2A\sqrt{gd\left(\rho_L\rho_G-\rho_G^2\right)^3}} \right)^2 \end{array} \right]^{0.5} \tag{B.5}$$

Using the above equations, the uncertainties were calculated for $\mathrm{Fr}_{L,OGE}$ and $\mathrm{Fr}_{G,OLE}$ in Branches A and B and the results are shown in Tables B.3 to B.6 for branch spacings of $L/d = 1.5$ and 3 and angles of $\theta = 30$ and 60°.

Table B.3 - Uncertainty in Froude numbers for $L/d = 1.5$ and $\theta = 30°$

$\mathbf{Fr}_{G,OLE,A}$	$\omega_{\mathrm{Fr}_{G,OLE,A}}$ %	$\mathbf{Fr}_{G,OLE,B}$	$\omega_{\mathrm{Fr}_{G,OLE,B}}$ %	$\mathbf{Fr}_{L,OGE,A}$	$\omega_{\mathrm{Fr}_{L,OGE,A}}$ %	$\mathbf{Fr}_{L,OGE,B}$	$\omega_{\mathrm{Fr}_{L,OGE,B}}$ %
15.68	3.38%	15.74	3.91%	15.89	4.74%	15.92	4.79%
18.36	3.53%	18.58	3.93%	19.14	4.33%	19.27	4.36%
22.96	3.95%	22.63	4.14%	23.43	4.00%	23.48	4.03%
25.32	4.34%	25.20	4.50%	27.54	3.81%	27.62	3.83%
31.28	4.25%	31.35	4.34%	35.78	3.59%	35.63	3.61%
35.80	4.99%	36.06	5.08%	43.56	3.48%	43.98	3.49%
40.15	5.50%	40.47	5.60%	46.97	3.45%	49.83	3.44%

Table B.4 - Uncertainty in Froude numbers for $L/d = 3$ and $\theta = 30°$

$\mathbf{Fr}_{G,OLE,A}$	$\omega_{\mathrm{Fr}_{G,OLE,A}}$ %	$\mathbf{Fr}_{G,OLE,B}$	$\omega_{\mathrm{Fr}_{G,OLE,B}}$ %	$\mathbf{Fr}_{L,OGE,A}$	$\omega_{\mathrm{Fr}_{L,OGE,A}}$ %	$\mathbf{Fr}_{L,OGE,B}$	$\omega_{\mathrm{Fr}_{L,OGE,B}}$ %
14.53	3.34%	14.80	3.95%	15.58	4.79%	16.03	4.77%
17.79	3.48%	18.39	3.90%	18.72	4.37%	18.84	4.40%
21.29	3.75%	21.41	4.03%	23.43	4.00%	23.47	4.03%
24.23	4.16%	24.63	4.40%	27.34	3.82%	27.82	3.82%
31.28	4.25%	30.43	4.21%	35.57	3.59%	35.64	3.61%
33.89	4.65%	35.56	4.97%	42.77	3.49%	43.99	3.49%
38.04	5.06%	39.67	5.39%	49.77	3.43%	50.65	3.43%

Table B.5 - Uncertainty in Froude numbers for $L/d = 1.5$ and $\theta = 60°$

$\mathbf{Fr}_{G,OLE,A}$	$\omega_{\mathrm{Fr}_{G,OLE,A}}$ %	$\mathbf{Fr}_{G,OLE,B}$	$\omega_{\mathrm{Fr}_{G,OLE,B}}$ %	$\mathbf{Fr}_{L,OGE,A}$	$\omega_{\mathrm{Fr}_{L,OGE,A}}$ %	$\mathbf{Fr}_{L,OGE,B}$	$\omega_{\mathrm{Fr}_{L,OGE,B}}$ %
15.32	3.37%	15.16	3.93%	17.41	4.52%	17.34	4.58%
19.30	3.57%	19.26	3.92%	20.46	4.21%	22.61	4.08%
23.11	3.96%	22.38	4.11%	25.87	3.88%	25.62	3.91%
25.61	4.41%	26.32	3.79%	30.62	3.71%	30.10	3.74%
31.70	4.31%	31.57	4.36%	36.21	3.58%	36.03	3.60%
36.48	5.15%	36.44	5.19%	44.36	3.47%	44.19	3.49%
40.58	5.58%	40.35	5.56%	46.95	3.45%	49.41	3.44%

Table B.6 - Uncertainty in Froude numbers for $L/d = 3$ and $\theta = 60°$

$\mathbf{Fr}_{G,OLE,A}$	$\omega_{\mathbf{Fr}_{G,OLE,A}}$ %	$\mathbf{Fr}_{G,OLE,B}$	$\omega_{\mathbf{Fr}_{G,OLE,B}}$ %	$\mathbf{Fr}_{L,OGE,A}$	$\omega_{\mathbf{Fr}_{L,OGE,A}}$ %	$\mathbf{Fr}_{L,OGE,B}$	$\omega_{\mathbf{Fr}_{L,OGE,B}}$ %
14.05	3.33%	14.51	3.96%	15.59	4.79%	15.61	4.84%
17.87	3.48%	18.69	3.90%	19.75	4.27%	20.53	4.24%
21.29	3.75%	21.78	4.06%	24.64	3.94%	25.03	3.94%
24.20	4.17%	25.23	4.51%	29.90	3.73%	30.24	3.74%
30.00	4.08%	31.46	4.35%	34.66	3.61%	35.35	3.61%
34.58	4.80%	36.30	5.15%	42.77	3.49%	43.71	3.49%
38.15	5.10%	39.95	5.46%	45.23	3.47%	49.20	3.44%

B.4 Uncertainty in Interface Heights

The equation used to calculate the interface height (Equation (3.2)) shows that h depends on γ_1, γ_2, γ_3, E_L, $E_{L,CL,atm}$, L_{zero} and χ. The uncertainties in γ_1, γ_2 and γ_3 were estimated based on the average difference between the values predicted by the second order polynomial (Equation (3.1)) and the measured values over the range from 4 to 9 Volts (this was the voltage range for which interface height measurements were taken during the experiments). The uncertainties in the coefficients were taken as $\omega_{\gamma_1} = \pm$ 0.015 [mmH2O/Volt], $\omega_{\gamma_2} = \pm$ 4e-5 [Volt^{-1}] and $\omega_{\gamma_3} = \pm$ 0.0015 [Volt]. Differences of this amount in the coefficients of Equation (3.1) resulted in approximately the average difference between the predicted and measured values of the pressure in mmH2O.

The uncertainty in the voltmeter reading, E_L, was taken as ± 0.001 [Volt] since the resolution of the voltmeter was 0.001 [Volt] and the uncertainty in $E_{L,CL,atm}$ was estimated to be ± 0.005 [Volt]. The height, L_{zero}, was measured with a ruler and the uncertainty was estimated as ± 1 mm. Finally, the uncertainty in the value for χ depends on the uncertainties in the liquid and gas densities in the test section, ρ_L and $\rho_{G,0}$ and was calculated using the following expression:

$$\omega_\chi = \left(\left(\frac{(\rho_{G,atm} - \rho_{G,0})}{(\rho_L - \rho_{G,0})^2} \omega_{\rho_L} \right)^2 + \left(\frac{(\rho_L - \rho_{G,atm})}{(\rho_L - \rho_{G,0})^2} \omega_{\rho_{G,0}} \right)^2 \right)^{0.5} \tag{B.6}$$

The gas density in the test section was calculated using the ideal gas law and neglecting the uncertainty in the gas constant, R, the uncertainty in the gas density is:

$$\omega_{\rho_{G,0}} = \left(\left(\frac{\omega_{P_0}}{RT_0} \right)^2 + \left(\frac{-P_0 \omega_{T_0}}{RT_0^{\,2}} \right)^2 \right)^{0.5} \tag{B.7}$$

where the uncertainty in the pressure and temperature readings were ± 3.5 kPa and ± 0.2°C, respectively. With the uncertainties for all the dependent variables knows, the uncertainty in the interface height was calculated using the following equation:

$$\omega_h = \left[\begin{array}{l} \left(\left[\left(E_L - \gamma_2 E_L^2 - \gamma_3 \right)\chi - \left(E_{CL,atm} - \gamma_2 E_{CL,atm}^2 - \gamma_3 \right) \right] \omega_{\gamma_1} \right)^2 + \left(\left[-\gamma_1 E_L^2 \chi + \gamma_1 E_{CL,atm}^2 \right] \omega_{\gamma_2} \right)^2 + \\ \left(\left[-\gamma_1 \chi + \gamma_1 \right] \omega_{\gamma_3} \right)^2 + \left(\left[\gamma_1 \chi - 2\gamma_2 \gamma_1 \chi E_L \right] \omega_{E_L} \right)^2 + \left(\left[\gamma_1 \left(E_L - \gamma_2 E_L^2 - \gamma_3 \right) + L_{zero} \right] \omega_\chi \right)^2 + \\ \left(\left[-\gamma_1 + 2\gamma_1 \gamma_2 E_{CL,atm} \right] \omega_{E_{CL,atm}} \right)^2 + \left(\left[\chi - 1 \right] \omega_{L,zero} \right)^2 \end{array} \right]^{0.5} \tag{B.8}$$

Finally, the uncertainty for h/d was calculated as follows:

$$\omega_{h/d} = \left[\left(\frac{\omega_h}{d} \right)^2 + \left(\frac{-h\omega_d}{d^2} \right)^2 \right]^{0.5} \tag{B.9}$$

The uncertainties in h and h/d for both branch A and B and for all the experimental runs are shown in Tables B.7 to B.38.

B.5 Uncertainty in Dimensionless Mass Flow Rates and Interface Heights

The dimensionless interface height, H, defined by Equation (2.6) depends on h, h_{OLE} and h_{OGE} and the dimensionless mass flow rate, M, defined by Equation (2.5), depends on $\dot{m}_{TP}$, $\dot{m}_{L,OGE}$ and $\dot{m}_{G,OGE}$. The uncertainties in H and M, ω_{H} and ω_{M}, respectively, were calculated as follows:

$$\omega_{\mathrm{H}} = \left[\left(\frac{\omega_h}{h_{OGE} - h_{OLE}} \right)^2 + \left(\frac{h - h_{OGE}}{\left(h_{OGE} - h_{OLE} \right)^2} \omega_{h_{OLE}} \right)^2 + \left(\frac{h_{OLE} - h}{\left(h_{OGE} - h_{OLE} \right)^2} \omega_{h_{OGE}} \right)^2 \right]^{0.5}$$

$$\omega_{\mathrm{M}} = \left[\left(\frac{\omega_{\dot{m}_{TP}}}{\dot{m}_{L,OGE} - \dot{m}_{G,OLE}} \right)^2 + \left(\frac{\dot{m}_{TP} - \dot{m}_{L,OGE}}{\left(\dot{m}_{L,OGE} - \dot{m}_{G,OLE}\right)^2} \omega_{\dot{m}_{G,OLE}} \right)^2 + \left(\frac{\dot{m}_{G,OLE} - \dot{m}_{TP}}{\left(\dot{m}_{L,OGE} - \dot{m}_{G,OLE}\right)^2} \omega_{\dot{m}_{L,OGE}} \right)^2 \right]^{0.5}$$

The uncertainties in M and H for Branches A and B are shown in Tables B.7 to B.38.

Table B.7 - Uncertainties in Branch A mass flow rates, interface heights and qualities for Case 1 - $P_0 = 316$ kPa, $\Delta P = 40$ kPa, $L/d = 1.5$ and $\theta = 30°$

Case #	$\omega_{\dot{m}_{TP,A}}$ (%)	ω_{M_A} (%)	ω_{h_A} (mm)	$\omega_{h_A/d}$	ω_{H_A} (%)	ω_{x_A} (%)
1- 1	3.45%	5.19%	0.2121	0.0444	1.39%	-
1- 2	4.59%	6.20%	0.2123	0.0426	1.41%	4.93%
1- 3	5.11%	6.70%	0.2124	0.0413	1.43%	5.21%
1- 4	7.08%	8.87%	0.2126	0.0398	1.47%	7.10%
1- 5	8.57%	10.71%	0.2128	0.0386	1.50%	9.22%
1- 6	0.92%	3.84%	0.2130	0.0369	1.57%	2.82%
1- 7	1.05%	3.90%	0.2132	0.0358	1.63%	2.36%
1- 8	1.18%	3.98%	0.2134	0.0350	1.70%	2.12%
1- 9	1.29%	4.05%	0.2136	0.0345	1.77%	2.17%
1- 10	1.41%	4.16%	0.2139	0.0340	1.88%	2.00%
1- 11	1.59%	4.33%	0.2141	0.0338	2.02%	2.03%
1- 12	1.73%	4.49%	0.2143	0.0338	2.16%	2.09%
1- 13	1.94%	4.77%	0.2146	0.0341	2.40%	2.18%
1- 14	2.10%	5.05%	0.2148	0.0344	2.55%	2.29%
1- 15	2.43%	5.75%	0.2151	0.0351	2.90%	2.56%
1- 16	2.66%	6.35%	0.2153	0.0360	3.30%	2.75%
1- 17	2.95%	7.35%	0.2156	0.0370	3.76%	3.02%
1- 18	3.27%	8.80%	0.2158	0.0381	4.36%	3.32%
1- 19	0.60%	6.16%	0.2161	0.0397	5.43%	0.81%
1- 20	0.68%	8.65%	0.2164	0.0412	6.76%	0.84%
1- 21	0.76%	16.51%	0.2166	0.0429	9.12%	0.88%

Table B.8 - Uncertainties in Branch B mass flow rates, interface heights and qualities for Case 1 - $P_0 = 316\,\text{kPa}$, $\Delta P = 40\,\text{kPa}$, $L/d = 1.5$ and $\theta = 30°$

Case #	$\omega_{\dot{m}_{TP,B}}$ (%)	ω_{M_B} (%)	ω_{h_B} (mm)	$\omega_{h_B/d}$	ω_{H_B} (%)	ω_{x_B} (%)
1- 6	4.03%	5.10%	0.2122	0.0431	1.48%	7.17%
1- 7	4.68%	5.03%	0.2124	0.0413	1.51%	5.02%
1- 8	5.54%	4.98%	0.2126	0.0398	1.55%	5.63%
1- 9	6.46%	4.98%	0.2128	0.0388	1.58%	6.54%
1- 10	0.70%	2.17%	0.2130	0.0373	1.64%	0.91%
1- 11	0.77%	2.09%	0.2132	0.0361	1.71%	0.88%
1- 12	0.83%	2.04%	0.2134	0.0353	1.78%	3.76%
1- 13	0.92%	1.96%	0.2137	0.0345	1.89%	3.07%
1- 14	0.98%	1.93%	0.2138	0.0341	1.96%	2.63%
1- 15	1.08%	1.89%	0.2141	0.0338	2.12%	2.20%
1- 16	1.19%	1.85%	0.2143	0.0338	2.30%	2.07%
1- 17	1.28%	1.85%	0.2145	0.0339	2.49%	1.94%
1- 18	1.42%	1.81%	0.2147	0.0343	2.73%	1.90%
1- 19	1.68%	1.73%	0.2150	0.0350	3.11%	2.04%
1- 20	1.95%	1.69%	0.2153	0.0358	3.51%	2.19%
1- 21	2.26%	1.71%	0.2155	0.0368	4.11%	2.44%
1- 22	2.65%	1.77%	0.2158	0.0379	4.83%	2.78%
1- 23	3.11%	2.01%	0.2161	0.0395	6.11%	3.20%
1- 24	0.56%	1.14%	0.2163	0.0408	7.66%	0.81%

Table B.9 - Uncertainties in Branch A mass flow rates, interface heights and qualities for Case 2 - $P_0 = 316$ kPa, $\Delta P = 123$ kPa, $L/d = 1.5$ and $\theta = 30°$

Case #	$\omega_{\dot{m}_{TP,A}}$ (%)	ω_{M_A} (%)	ω_{h_A} (mm)	$\omega_{h_A/d}$	ω_{H_A} (%)	ω_{x_A} (%)
2- 1	1.83%	2.73%	0.2115	0.0516	1.08%	-
2- 2	2.51%	3.31%	0.2116	0.0491	1.10%	2.75%
2- 3	2.99%	3.79%	0.2118	0.0469	1.12%	3.04%
2- 4	3.44%	4.26%	0.2120	0.0456	1.13%	4.90%
2- 5	4.59%	5.60%	0.2122	0.0427	1.17%	5.03%
2- 6	5.05%	6.17%	0.2125	0.0408	1.20%	5.33%
2- 7	5.52%	6.79%	0.2127	0.0390	1.24%	5.73%
2- 8	6.47%	8.10%	0.2130	0.0370	1.31%	6.57%
2- 9	0.67%	2.11%	0.2132	0.0358	1.36%	1.21%
2- 10	0.73%	2.15%	0.2135	0.0348	1.44%	1.14%
2- 11	0.81%	2.21%	0.2138	0.0341	1.54%	1.11%
2- 12	0.92%	2.32%	0.2141	0.0338	1.65%	1.13%
2- 13	1.02%	2.43%	0.2143	0.0338	1.77%	1.19%
2- 14	1.20%	2.69%	0.2147	0.0342	1.95%	1.31%
2- 15	1.49%	3.20%	0.2151	0.0352	2.22%	3.80%
2- 16	1.73%	3.82%	0.2153	0.0361	2.46%	3.58%
2- 17	1.98%	4.73%	0.2157	0.0377	2.87%	3.44%
2- 18	2.21%	5.84%	0.2160	0.0391	3.25%	3.39%
2- 19	2.52%	8.01%	0.2163	0.0411	3.93%	3.45%
2- 20	1.16%	10.70%	0.2169	0.0447	5.78%	2.28%
2- 21	1.18%	12.13%	0.2171	0.0457	6.54%	2.24%

Table B.10 - Uncertainties in Branch B mass flow rates, interface heights and qualities for Case 2 - $P_0 = 316$ kPa, $\Delta P = 123$ kPa, $L/d = 1.5$ and $\theta = 30°$

Case #	$\omega_{\dot{m}_{TP,B}}$ (%)	ω_{M_B} (%)	ω_{h_B} (mm)	$\omega_{h_B/d}$	ω_{H_B} (%)	ω_{x_B} (%)
2- 5	2.00%	2.63%	0.2115	0.0508	1.16%	2.30%
2- 6	2.31%	2.57%	0.2117	0.0484	1.17%	3.20%
2- 7	2.63%	2.56%	0.2119	0.0461	1.20%	2.87%
2- 8	3.11%	2.58%	0.2122	0.0432	1.23%	6.45%
2- 9	3.39%	2.65%	0.2124	0.0413	1.26%	5.22%
2- 10	3.83%	2.73%	0.2127	0.0393	1.31%	4.97%
2- 11	4.27%	2.85%	0.2129	0.0376	1.36%	4.93%
2- 12	4.86%	2.97%	0.2132	0.0362	1.42%	5.24%
2- 13	5.32%	3.12%	0.2134	0.0352	1.49%	5.57%
2- 14	6.19%	3.32%	0.2137	0.0343	1.59%	6.33%
2- 15	0.66%	0.89%	0.2141	0.0338	1.73%	1.28%
2- 16	0.74%	0.86%	0.2143	0.0338	1.86%	1.18%
2- 17	0.82%	0.86%	0.2147	0.0341	2.06%	1.15%
2- 18	0.90%	0.85%	0.2149	0.0347	2.24%	1.15%
2- 19	1.04%	0.84%	0.2153	0.0357	2.55%	1.22%
2- 20	1.47%	0.87%	0.2158	0.0381	3.24%	3.80%
2- 21	1.54%	0.90%	0.2160	0.0388	3.49%	3.70%
2- 22	2.01%	0.96%	0.2164	0.0408	4.27%	3.53%
2- 23	2.44%	1.15%	0.2167	0.0431	5.53%	3.57%
2- 24	2.95%	1.39%	0.2170	0.0449	7.01%	3.73%
2- 25	1.17%	0.90%	0.2173	0.0472	10.07%	2.31%

Table B.11 - Uncertainties in Branch A mass flow rates, interface heights and qualities for Case 3 - P_0 = 517 kPa, ΔP = 97 kPa, L/d = 1.5 and θ = 30°

Case #	$\omega_{\dot{m}_{TP,A}}$ (%)	ω_{M_A} (%)	ω_{h_A} (mm)	$\omega_{h_A/d}$	ω_{H_A} (%)	ω_{x_A} (%)
3- 1	2.00%	3.04%	0.2117	0.0501	1.10%	-
3- 2	2.47%	3.46%	0.2119	0.0482	1.11%	2.72%
3- 3	3.03%	4.02%	0.2121	0.0457	1.14%	3.06%
3- 4	4.02%	5.17%	0.2123	0.0431	1.17%	4.37%
3- 5	4.60%	5.92%	0.2126	0.0412	1.20%	4.79%
3- 6	5.26%	6.83%	0.2128	0.0390	1.24%	5.36%
3- 7	5.70%	7.47%	0.2130	0.0376	1.28%	5.77%
3- 8	0.63%	2.31%	0.2133	0.0360	1.35%	0.99%
3- 9	0.69%	2.35%	0.2136	0.0350	1.42%	0.96%
3- 10	0.78%	2.43%	0.2140	0.0341	1.52%	0.96%
3- 11	0.84%	2.48%	0.2142	0.0338	1.60%	0.98%
3- 12	0.92%	2.59%	0.2145	0.0338	1.72%	1.03%
3- 13	1.09%	2.85%	0.2148	0.0342	1.91%	1.16%
3- 14	1.27%	3.26%	0.2152	0.0351	2.15%	1.32%
3- 15	1.47%	3.95%	0.2156	0.0364	2.45%	1.51%
3- 16	1.72%	4.84%	0.2158	0.0375	2.72%	2.76%
3- 17	1.97%	6.63%	0.2162	0.0395	3.27%	2.76%
3- 18	2.20%	9.48%	0.2165	0.0412	3.80%	2.82%

Table B.12 - Uncertainties in Branch B mass flow rates and interface heights, and qualities for Case 3 - $P_0 = 517$ kPa, $\Delta P = 97$ kPa, $L/d = 1.5$ and $\theta = 30°$

Case #	$\omega_{\dot{m}_{TP,B}}$ (%)	ω_{M_B} (%)	ω_{h_B} (mm)	$\omega_{h_B/d}$	ω_{H_B} (%)	ω_{x_B} (%)
3- 5	2.16%	3.05%	0.2118	0.0489	1.18%	2.29%
3- 6	2.58%	2.97%	0.2121	0.0461	1.21%	2.70%
3- 7	2.79%	3.01%	0.2123	0.0441	1.23%	2.84%
3- 8	3.23%	3.04%	0.2125	0.0416	1.27%	4.53%
3- 9	3.61%	3.11%	0.2128	0.0397	1.31%	4.32%
3- 10	4.18%	3.23%	0.2131	0.0376	1.38%	4.51%
3- 11	4.46%	3.35%	0.2133	0.0365	1.42%	4.69%
3- 12	4.83%	3.52%	0.2135	0.0354	1.50%	4.99%
3- 13	5.73%	3.75%	0.2139	0.0343	1.61%	5.82%
3- 14	0.63%	1.08%	0.2142	0.0338	1.74%	1.03%
3- 15	0.69%	1.09%	0.2146	0.0338	1.91%	0.98%
3- 16	0.74%	1.07%	0.2148	0.0341	2.06%	0.97%
3- 17	0.84%	1.05%	0.2152	0.0349	2.34%	1.00%
3- 18	0.96%	1.01%	0.2154	0.0358	2.59%	1.03%
3- 19	1.15%	1.00%	0.2158	0.0374	3.09%	1.22%
3- 20	1.31%	1.01%	0.2161	0.0388	3.54%	1.36%
3- 21	1.58%	1.06%	0.2165	0.0407	4.30%	1.62%
3- 22	1.98%	1.30%	0.2168	0.0429	5.51%	2.82%
3- 23	2.34%	1.65%	0.2172	0.0452	7.46%	2.94%
3- 24	0.94%	1.11%	0.2176	0.0476	11.19%	1.76%

Table B.13 - Uncertainties in Branch A mass flow rates, interface heights and qualities for Case 4 - P_0 = 517 kPa, ΔP = 235 kPa, L/d = 1.5 and θ = 30°

Case #	$\omega_{\dot{m}_{TP,A}}$ (%)	ω_{M_A} (%)	ω_{h_A} (mm)	$\omega_{h_A/d}$	ω_{H_A} (%)	ω_{x_A} (%)
4- 1	1.26%	1.90%	0.2112	0.0566	0.93%	-
4- 2	1.58%	2.18%	0.2113	0.0551	0.93%	1.73%
4- 3	1.90%	2.49%	0.2115	0.0522	0.95%	3.41%
4- 4	2.54%	3.21%	0.2118	0.0484	0.97%	2.89%
4- 5	3.06%	3.85%	0.2121	0.0459	1.00%	3.22%
4- 6	3.35%	4.23%	0.2123	0.0436	1.02%	3.46%
4- 7	3.79%	4.85%	0.2126	0.0411	1.06%	3.86%
4- 8	4.22%	5.49%	0.2130	0.0382	1.12%	4.26%
4- 9	4.72%	6.29%	0.2133	0.0365	1.17%	4.74%
4- 10	5.15%	7.04%	0.2136	0.0351	1.24%	5.17%
4- 11	5.76%	8.16%	0.2139	0.0342	1.32%	6.31%
4- 12	6.45%	9.56%	0.2143	0.0338	1.42%	6.86%
4- 13	0.77%	1.83%	0.2147	0.0340	1.56%	2.17%
4- 14	0.84%	1.98%	0.2150	0.0345	1.70%	2.04%
4- 15	0.99%	2.37%	0.2154	0.0358	1.92%	1.94%
4- 16	1.12%	2.82%	0.2158	0.0373	2.15%	1.92%
4- 17	1.30%	3.76%	0.2162	0.0394	2.52%	1.89%
4- 18	1.50%	5.52%	0.2166	0.0415	2.92%	1.98%
4- 19	1.73%	9.96%	0.2171	0.0447	3.69%	2.08%

Table B.14 - Uncertainties in Branch B mass flow rates, interface heights and qualities for Case 4 - P_0 = 517 kPa, ΔP = 235 kPa, L/d = 1.5 and θ = 30°

Case #	$\omega_{\dot{m}_{TP,B}}$ (%)	ω_{M_B} (%)	ω_{h_B} (mm)	$\omega_{h_B/d}$	ω_{H_B} (%)	ω_{x_B} (%)
4- 5	1.43%	2.05%	0.2114	0.0546	0.98%	2.35%
4- 6	2.14%	2.74%	0.2116	0.0518	0.99%	2.29%
4- 7	1.89%	2.48%	0.2118	0.0488	1.01%	4.72%
4- 8	2.17%	2.78%	0.2122	0.0450	1.05%	3.12%
4- 9	2.47%	3.12%	0.2125	0.0424	1.08%	2.96%
4- 10	2.76%	3.46%	0.2128	0.0399	1.13%	3.06%
4- 11	3.11%	3.91%	0.2130	0.0379	1.18%	3.28%
4- 12	3.47%	4.40%	0.2134	0.0362	1.24%	3.59%
4- 13	3.90%	5.00%	0.2137	0.0347	1.33%	3.97%
4- 14	4.30%	5.61%	0.2140	0.0341	1.41%	4.35%
4- 15	4.76%	6.35%	0.2144	0.0338	1.54%	4.79%
4- 16	5.39%	7.44%	0.2148	0.0340	1.67%	5.41%
4- 17	6.07%	8.72%	0.2152	0.0348	1.87%	6.58%
4- 18	0.67%	1.71%	0.2155	0.0360	2.08%	2.39%
4- 19	0.81%	1.94%	0.2160	0.0380	2.45%	2.13%
4- 20	0.95%	2.26%	0.2164	0.0400	2.85%	2.03%
4- 21	1.19%	3.21%	0.2169	0.0430	3.59%	1.95%
4- 22	1.34%	4.18%	0.2172	0.0451	4.29%	2.01%
4- 23	1.74%	10.95%	0.2176	0.0480	5.65%	2.17%

Table B.15 - Uncertainties in Branch A mass flow rates, interface heights and qualities for Case 5 - $P_0 = 316$ kPa, $\Delta P = 40$ kPa, $L/d = 3$ and $\theta = 30°$

Case #	$\omega_{\dot{m}_{TP,A}}$ (%)	ω_{M_A} (%)	ω_{h_A} (mm)	$\omega_{h_A/d}$	ω_{H_A} (%)	ω_{x_A} (%)
5- 1	3.52%	5.28%	0.2125	0.0424	1.59%	-
5- 2	4.68%	6.28%	0.2128	0.0404	1.63%	4.97%
5- 3	5.53%	7.12%	0.2129	0.0391	1.67%	5.61%
5- 4	0.68%	3.81%	0.2132	0.0374	1.74%	0.87%
5- 5	0.85%	3.87%	0.2135	0.0359	1.83%	0.95%
5- 6	0.99%	3.92%	0.2137	0.0351	1.92%	2.89%
5- 7	1.12%	3.99%	0.2139	0.0344	2.04%	2.23%
5- 8	1.33%	4.12%	0.2143	0.0339	2.25%	2.01%
5- 9	1.49%	4.26%	0.2145	0.0338	2.48%	2.01%
5- 10	1.66%	4.42%	0.2148	0.0339	2.72%	2.01%
5- 11	1.93%	4.74%	0.2150	0.0344	3.08%	2.18%
5- 12	2.47%	5.71%	0.2154	0.0354	3.77%	2.61%
5- 13	2.84%	6.65%	0.2157	0.0366	4.61%	2.93%
5- 14	3.46%	9.03%	0.2159	0.0376	5.56%	3.52%
5- 15	0.61%	5.79%	0.2162	0.0391	7.38%	0.83%
5- 16	0.78%	12.86%	0.2165	0.0410	11.06%	0.91%

Table B.16 - Uncertainties in Branch B Mass flow rates, interface heights and qualities for Case 5 - $P_0 = 316$ kPa, $\Delta P = 40$ kPa, $L/d = 3$ and $\theta = 30°$

Case #	$\omega_{\dot{m}_{TP,B}}$ (%)	ω_{M_B} (%)	ω_{h_B} (mm)	$\omega_{h_B/d}$	ω_{H_B} (%)	ω_{x_B} (%)
5- 9	4.48%	6.08%	0.2128	0.0404	1.56%	5.30%
5- 10	5.11%	6.68%	0.2130	0.0390	1.59%	5.24%
5- 11	6.31%	7.93%	0.2133	0.0376	1.64%	6.35%
5- 12	0.78%	3.81%	0.2136	0.0360	1.74%	0.89%
5- 13	0.88%	3.85%	0.2138	0.0350	1.83%	3.22%
5- 14	1.04%	3.92%	0.2140	0.0344	1.93%	2.76%
5- 15	1.17%	3.99%	0.2143	0.0339	2.08%	2.30%
5- 16	1.38%	4.14%	0.2146	0.0338	2.28%	2.08%
5- 17	1.56%	4.30%	0.2149	0.0340	2.59%	2.00%
5- 18	1.88%	4.67%	0.2151	0.0345	2.89%	2.17%
5- 19	2.12%	5.04%	0.2154	0.0352	3.33%	2.32%
5- 20	2.79%	6.58%	0.2157	0.0363	4.02%	2.90%
5- 21	3.31%	8.54%	0.2160	0.0376	4.95%	3.38%
5- 22	0.59%	5.20%	0.2163	0.0392	6.44%	0.85%
5- 23	0.76%	9.70%	0.2167	0.0413	9.78%	0.91%

Table B.17 - Uncertainties in Branch A Mass flow rates, interface heights and qualities for Case 6 - $P_0 = 316$ kPa, $\Delta P = 123$ kPa, $L/d = 3$ and $\theta = 30°$

Case #	$\omega_{\dot{m}_{TP,A}}$ (%)	ω_{M_A} (%)	ω_{h_A} (mm)	$\omega_{h_A/d}$	ω_{H_A} (%)	ω_{x_A} (%)
6- 1	1.93%	2.88%	0.2119	0.0493	1.20%	-
6- 2	2.26%	3.15%	0.2121	0.0465	1.23%	3.50%
6- 3	2.90%	3.74%	0.2124	0.0438	1.26%	2.99%
6- 4	3.51%	4.37%	0.2126	0.0417	1.30%	5.15%
6- 5	4.10%	5.03%	0.2129	0.0394	1.35%	4.83%
6- 6	4.88%	5.96%	0.2131	0.0377	1.41%	5.20%
6- 7	6.28%	7.80%	0.2135	0.0358	1.51%	6.40%
6- 8	0.67%	2.21%	0.2137	0.0349	1.58%	1.25%
6- 9	0.74%	2.25%	0.2140	0.0342	1.70%	1.18%
6- 10	0.86%	2.34%	0.2144	0.0338	1.87%	1.15%
6- 11	0.99%	2.47%	0.2147	0.0339	2.07%	1.20%
6- 12	1.16%	2.69%	0.2150	0.0343	2.30%	1.30%
6- 13	1.48%	3.19%	0.2154	0.0354	2.71%	4.05%
6- 14	1.85%	4.14%	0.2158	0.0369	3.24%	3.65%
6- 15	2.10%	5.09%	0.2161	0.0384	3.85%	3.54%
6- 16	2.55%	7.70%	0.2164	0.0403	4.82%	3.57%
6- 17	1.09%	6.68%	0.2168	0.0425	6.39%	2.45%
6- 18	1.31%	23.30%	0.2172	0.0453	10.08%	2.21%

Table B.18 - Uncertainties in Branch B mass flow rates, interface heights and qualities for Case 6 - $P_0 = 316$ kPa, $\Delta P = 123$ kPa, $L/d = 3$ and $\theta = 30°$

Case #	$\omega_{\dot{m}_{TP,B}}$ (%)	ω_{M_B} (%)	ω_{h_B} (mm)	$\omega_{h_B/d}$	ω_{H_B} (%)	ω_{x_B} (%)
6- 8	2.33%	3.18%	0.2122	0.0465	1.22%	3.37%
6- 9	2.68%	3.50%	0.2124	0.0441	1.24%	2.83%
6- 10	3.22%	4.04%	0.2127	0.0415	1.29%	5.76%
6- 11	3.75%	4.61%	0.2130	0.0394	1.33%	5.10%
6- 12	4.29%	5.22%	0.2132	0.0378	1.38%	4.93%
6- 13	4.99%	6.07%	0.2136	0.0360	1.47%	5.31%
6- 14	6.14%	7.58%	0.2139	0.0347	1.58%	6.28%
6- 15	0.64%	2.14%	0.2142	0.0341	1.69%	1.32%
6- 16	0.74%	2.21%	0.2145	0.0338	1.83%	1.39%
6- 17	0.83%	2.27%	0.2148	0.0339	2.02%	1.16%
6- 18	0.99%	2.44%	0.2152	0.0345	2.31%	1.18%
6- 19	1.13%	2.62%	0.2155	0.0354	2.60%	1.28%
6- 20	1.52%	3.28%	0.2158	0.0369	3.10%	3.81%
6- 21	1.83%	4.12%	0.2162	0.0384	3.68%	3.61%
6- 22	2.28%	6.12%	0.2165	0.0402	4.50%	3.54%
6- 23	3.00%	13.94%	0.2170	0.0432	6.64%	3.73%
6- 24	1.22%	14.06%	0.2173	0.0452	9.07%	2.30%

Table B.19 - Uncertainties in Branch A mass flow rates, interface heights and qualities for Case 7 - $P_0 = 517$ kPa, $\Delta P = 97$ kPa, $L/d = 3$ and $\theta = 30°$

Case #	$\omega_{\dot{m}_{TP,A}}$ (%)	ω_{M_A} (%)	ω_{h_A} (mm)	$\omega_{h_A/d}$	ω_{H_A} (%)	ω_{x_A} (%)
7- 1	2.01%	3.06%	0.2122	0.0470	1.27%	-
7- 2	2.57%	3.56%	0.2124	0.0449	1.29%	2.81%
7- 3	2.96%	3.95%	0.2126	0.0428	1.32%	3.01%
7- 4	3.60%	4.65%	0.2129	0.0407	1.35%	4.50%
7- 5	4.28%	5.49%	0.2132	0.0385	1.41%	4.63%
7- 6	5.15%	6.65%	0.2135	0.0367	1.48%	5.28%
7- 7	6.06%	8.01%	0.2137	0.0356	1.55%	6.15%
7- 8	0.66%	2.34%	0.2141	0.0345	1.67%	1.01%
7- 9	0.73%	2.40%	0.2144	0.0340	1.80%	0.98%
7- 10	0.84%	2.50%	0.2147	0.0338	1.98%	1.00%
7- 11	0.95%	2.64%	0.2150	0.0340	2.18%	1.07%
7- 12	1.14%	2.95%	0.2153	0.0348	2.48%	1.21%
7- 13	1.31%	3.37%	0.2157	0.0359	2.90%	1.37%
7- 14	1.71%	4.71%	0.2161	0.0375	3.52%	2.85%
7- 15	1.90%	5.94%	0.2164	0.0390	4.19%	2.83%
7- 16	2.31%	11.14%	0.2168	0.0413	5.62%	2.91%
7- 17	2.64%	24.37%	0.2171	0.0433	7.41%	3.08%

Table B.20 - Uncertainties in Branch B mass flow rates, interface heights and qualities for Case 7 - $P_0 = 517$ kPa, $\Delta P = 97$ kPa, $L/d = 3$ and $\theta = 30°$

Case #	$\omega_{\dot{m}_{TP,B}}$ (%)	ω_{M_B} (%)	ω_{h_B} (mm)	$\omega_{h_B/d}$	ω_{H_B} (%)	ω_{x_B} (%)
7- 8	2.45%	3.45%	0.2125	0.0452	1.26%	2.98%
7- 9	2.79%	3.79%	0.2127	0.0428	1.30%	2.88%
7- 10	3.26%	4.28%	0.2130	0.0405	1.34%	4.73%
7- 11	3.72%	4.81%	0.2132	0.0387	1.38%	4.53%
7- 12	4.25%	5.46%	0.2135	0.0369	1.45%	4.54%
7- 13	4.83%	6.24%	0.2138	0.0355	1.54%	5.00%
7- 14	5.90%	7.79%	0.2142	0.0345	1.65%	5.98%
7- 15	6.56%	8.84%	0.2144	0.0340	1.76%	6.61%
7- 16	0.73%	2.41%	0.2148	0.0338	1.96%	0.98%
7- 17	0.79%	2.47%	0.2151	0.0341	2.14%	0.99%
7- 18	0.94%	2.64%	0.2154	0.0349	2.49%	1.06%
7- 19	1.08%	2.87%	0.2157	0.0358	2.79%	1.17%
7- 20	1.36%	3.62%	0.2161	0.0375	3.44%	1.42%
7- 21	1.70%	4.95%	0.2164	0.0389	4.00%	2.92%
7- 22	2.14%	9.28%	0.2168	0.0411	5.26%	2.94%
7- 23	2.43%	17.48%	0.2171	0.0430	6.82%	3.00%

Table B.21 - Uncertainties in Branch A mass flow rates, interface heights and qualities for Case 8 - P_0 = 517 kPa, ΔP = 235 kPa, L/d = 3 and θ = 30°

Case #	$\omega_{\dot{m}_{TP,A}}$ (%)	ω_{M_A} (%)	ω_{h_A} (mm)	$\omega_{h_A/d}$	ω_{H_A} (%)	ω_{x_A} (%)
8- 1	1.29%	1.93%	0.2117	0.0533	1.03%	-
8- 2	1.48%	2.10%	0.2118	0.0513	1.04%	2.24%
8- 3	1.81%	2.40%	0.2121	0.0484	1.06%	1.89%
8- 4	2.25%	2.87%	0.2124	0.0451	1.10%	2.99%
8- 5	2.71%	3.39%	0.2127	0.0423	1.14%	3.01%
8- 6	3.41%	4.29%	0.2130	0.0398	1.18%	3.53%
8- 7	3.95%	5.04%	0.2133	0.0377	1.24%	4.01%
8- 8	4.42%	5.75%	0.2137	0.0358	1.32%	4.46%
8- 9	4.81%	6.36%	0.2140	0.0347	1.40%	4.83%
8- 10	5.73%	7.94%	0.2144	0.0339	1.53%	6.40%
8- 11	6.11%	8.68%	0.2147	0.0338	1.66%	6.61%
8- 12	0.76%	1.81%	0.2151	0.0342	1.86%	2.30%
8- 13	0.86%	1.99%	0.2155	0.0352	2.09%	2.13%
8- 14	1.05%	2.47%	0.2159	0.0368	2.45%	2.00%
8- 15	1.22%	3.10%	0.2163	0.0387	2.90%	1.96%
8- 16	1.47%	4.73%	0.2167	0.0411	3.57%	1.99%
8- 17	1.73%	8.17%	0.2172	0.0439	4.60%	2.10%
8- 18	1.98%	17.99%	0.2176	0.0467	6.25%	2.24%

Table B.22 - Uncertainties in Branch B mass flow rates, interface heights and qualities for Case 8 - P_0 = 517 kPa, ΔP = 235 kPa, L/d = 3 and θ = 30°

Case #	$\omega_{\dot{m}_{TP,B}}$ (%)	ω_{M_B} (%)	ω_{h_B} (mm)	$\omega_{h_B/d}$	ω_{H_B} (%)	ω_{x_B} (%)
8- 7	1.40%	2.03%	0.2118	0.0521	1.05%	2.71%
8- 8	1.75%	2.34%	0.2121	0.0485	1.08%	1.84%
8- 9	1.98%	2.58%	0.2124	0.0458	1.11%	3.70%
8- 10	2.33%	2.95%	0.2127	0.0427	1.15%	2.98%
8- 11	2.59%	3.26%	0.2130	0.0404	1.19%	2.96%
8- 12	3.04%	3.81%	0.2133	0.0381	1.25%	3.21%
8- 13	3.45%	4.35%	0.2136	0.0363	1.32%	3.55%
8- 14	3.94%	5.05%	0.2140	0.0348	1.42%	4.00%
8- 15	4.40%	5.74%	0.2144	0.0341	1.53%	4.43%
8- 16	5.19%	7.05%	0.2147	0.0338	1.68%	5.21%
8- 17	5.89%	8.34%	0.2151	0.0342	1.88%	6.51%
8- 18	0.69%	1.73%	0.2155	0.0351	2.12%	2.40%
8- 19	0.77%	1.85%	0.2159	0.0363	2.40%	2.20%
8- 20	0.96%	2.27%	0.2163	0.0383	2.88%	2.02%
8- 21	1.16%	3.01%	0.2168	0.0409	3.64%	1.96%
8- 22	1.45%	5.04%	0.2172	0.0434	4.62%	2.02%
8- 23	1.82%	13.86%	0.2176	0.0462	6.23%	2.18%

Table B.23 - Uncertainties in Branch A mass flow rates, interface heights and qualities for Case 9 - P_0 = 316 kPa, ΔP = 40 kPa, L/d = 1.5 and θ = 60°

Case #	$\omega_{\dot{m}_{TP,A}}$ (%)	ω_{M_A} (%)	ω_{h_A} (mm)	$\omega_{h_A/d}$	ω_{H_A} (%)	ω_{x_A} (%)
9- 1	3.20%	4.79%	0.2122	0.0431	1.45%	-
9- 2	3.77%	5.26%	0.2125	0.0410	1.48%	7.34%
9- 3	4.89%	6.31%	0.2127	0.0393	1.52%	5.02%
9- 4	5.85%	7.32%	0.2129	0.0378	1.57%	5.89%
9- 5	0.74%	3.49%	0.2131	0.0364	1.63%	3.31%
9- 6	0.87%	3.54%	0.2134	0.0354	1.70%	2.56%
9- 7	1.13%	3.68%	0.2136	0.0346	1.79%	2.13%
9- 8	1.38%	3.87%	0.2139	0.0340	1.92%	1.97%
9- 9	1.87%	4.44%	0.2142	0.0337	2.08%	2.14%
9- 10	2.07%	4.76%	0.2145	0.0338	2.29%	2.26%
9- 11	2.35%	5.34%	0.2147	0.0342	2.51%	2.49%
9- 12	2.62%	6.02%	0.2150	0.0348	2.82%	2.72%
9- 13	2.99%	7.27%	0.2153	0.0359	3.31%	3.06%
9- 14	3.66%	10.79%	0.2156	0.0371	3.91%	3.70%
9- 15	0.63%	6.54%	0.2159	0.0387	4.83%	0.82%
9- 16	0.74%	11.95%	0.2162	0.0404	6.22%	0.87%

Table B.24 - Uncertainties in Branch B mass flow rates, interface heights and qualities for Case 9 - $P_0 = 316$ kPa, $\Delta P = 40$ kPa, $L/d = 1.5$ and $\theta = 60°$

Case #	$\omega_{\dot{m}_{TP,B}}$ (%)	ω_{M_B} (%)	ω_{h_B} (mm)	$\omega_{h_B/d}$	ω_{H_B} (%)	ω_{x_B} (%)
9- 9	3.64%	5.21%	0.2127	0.0398	1.61%	3.93%
9- 10	4.19%	5.69%	0.2129	0.0381	1.65%	5.49%
9- 11	4.92%	6.38%	0.2131	0.0369	1.70%	5.10%
9- 12	5.54%	7.02%	0.2134	0.0357	1.76%	5.62%
9- 13	0.64%	3.56%	0.2136	0.0347	1.86%	0.89%
9- 14	0.75%	3.59%	0.2139	0.0341	1.97%	0.87%
9- 15	0.84%	3.63%	0.2142	0.0338	2.12%	3.48%
9- 16	0.99%	3.69%	0.2144	0.0338	2.31%	2.74%
9- 17	1.10%	3.76%	0.2147	0.0341	2.53%	2.41%
9- 18	1.30%	3.89%	0.2150	0.0348	2.89%	2.03%
9- 19	1.53%	4.09%	0.2153	0.0357	3.31%	2.06%
9- 20	2.00%	4.71%	0.2156	0.0370	4.02%	2.27%
9- 21	2.37%	5.43%	0.2159	0.0381	4.67%	2.56%
9- 22	3.10%	7.72%	0.2162	0.0397	5.97%	3.19%
9- 23	3.95%	13.23%	0.2165	0.0416	8.16%	4.01%

Table B.25 - Uncertainties in Branch A mass flow rates, interface heights and qualities for Case 10 - $P_0 = 316$ kPa, $\Delta P = 123$ kPa, $L/d = 1.5$ and $\theta = 60°$

Case #	$\omega_{\dot{m}_{TP,A}}$ (%)	ω_{M_A} (%)	ω_{h_A} (mm)	$\omega_{h_A/d}$	ω_{H_A} (%)	ω_{x_A} (%)
10- 1	1.79%	2.67%	0.2117	0.0494	1.17%	-
10- 2	2.10%	2.93%	0.2119	0.0462	1.20%	3.19%
10- 3	2.78%	3.55%	0.2121	0.0440	1.23%	8.46%
10- 4	3.29%	4.08%	0.2124	0.0417	1.26%	4.91%
10- 5	4.44%	5.40%	0.2127	0.0394	1.31%	4.87%
10- 6	5.38%	6.60%	0.2129	0.0376	1.37%	5.58%
10- 7	0.70%	2.09%	0.2133	0.0359	1.45%	1.12%
10- 8	0.86%	2.23%	0.2136	0.0347	1.56%	1.10%
10- 9	0.99%	2.36%	0.2138	0.0341	1.66%	1.16%
10- 10	1.11%	2.53%	0.2141	0.0338	1.80%	1.25%
10- 11	1.40%	3.00%	0.2145	0.0339	2.01%	3.77%
10- 12	1.55%	3.34%	0.2148	0.0343	2.20%	3.60%
10- 13	1.88%	4.36%	0.2152	0.0354	2.55%	3.39%
10- 14	2.16%	5.62%	0.2155	0.0368	2.98%	3.40%
10- 15	2.57%	8.66%	0.2159	0.0387	3.66%	3.44%
10- 16	1.07%	7.56%	0.2163	0.0409	4.67%	2.34%
10- 17	1.23%	20.36%	0.2167	0.0433	6.22%	2.19%

Table B.26 - Uncertainties in Branch B mass flow rates, interface heights and qualities for Case 10 - P_0 = 316 kPa, ΔP = 123 kPa, L/d = 1.5 and θ = 60°

Case #	$\omega_{\dot{m}_{TP,B}}$ (%)	ω_{M_B} (%)	ω_{h_B} (mm)	$\omega_{h_B/d}$	ω_{H_B} (%)	ω_{x_B} (%)
10- 8	1.90%	2.81%	0.2122	0.0441	1.23%	2.81%
10- 9	2.19%	3.04%	0.2124	0.0421	1.26%	3.38%
10- 10	2.51%	3.33%	0.2127	0.0400	1.29%	2.83%
10- 11	2.98%	3.79%	0.2130	0.0378	1.35%	3.03%
10- 12	3.26%	4.08%	0.2132	0.0365	1.39%	5.72%
10- 13	3.89%	4.77%	0.2135	0.0351	1.47%	4.90%
10- 14	4.34%	5.29%	0.2138	0.0342	1.57%	4.96%
10- 15	5.33%	6.53%	0.2142	0.0338	1.70%	5.63%
10- 16	6.15%	7.64%	0.2145	0.0339	1.87%	6.33%
10- 17	0.67%	2.14%	0.2149	0.0344	2.08%	1.36%
10- 18	0.76%	2.20%	0.2152	0.0354	2.37%	1.23%
10- 19	0.89%	2.32%	0.2155	0.0366	2.69%	1.19%
10- 20	1.01%	2.45%	0.2159	0.0382	3.16%	1.22%
10- 21	1.32%	2.94%	0.2163	0.0403	3.90%	1.43%
10- 22	1.76%	3.97%	0.2166	0.0424	4.90%	3.70%
10- 23	2.57%	8.73%	0.2170	0.0450	6.73%	3.63%
10- 24	1.15%	11.18%	0.2175	0.0480	11.04%	2.38%

Table B.27 - Uncertainties in Branch A mass flow rates, interface heights and qualities for Case 11 - $P_0 = 517$ kPa, $\Delta P = 97$ kPa, $L/d = 1.5$ and $\theta = 60°$

Case #	$\omega_{\dot{m}_{TP,A}}$ (%)	ω_{M_A} (%)	ω_{h_A} (mm)	$\omega_{h_A/d}$	ω_{H_A} (%)	ω_{x_A} (%)
11- 1	1.96%	3.00%	0.2119	0.0477	1.18%	-
11- 2	2.26%	3.26%	0.2122	0.0451	1.21%	2.61%
11- 3	2.99%	3.98%	0.2124	0.0425	1.24%	4.85%
11- 4	3.41%	4.45%	0.2126	0.0405	1.27%	4.15%
11- 5	4.41%	5.70%	0.2129	0.0387	1.32%	4.64%
11- 6	5.41%	7.11%	0.2132	0.0367	1.39%	5.51%
11- 7	0.71%	2.35%	0.2136	0.0351	1.48%	0.94%
11- 8	0.88%	2.53%	0.2139	0.0343	1.57%	1.01%
11- 9	0.98%	2.67%	0.2141	0.0339	1.66%	1.08%
11- 10	1.12%	2.94%	0.2145	0.0338	1.84%	1.19%
11- 11	1.34%	3.43%	0.2148	0.0341	2.00%	2.90%
11- 12	1.54%	4.20%	0.2151	0.0348	2.22%	2.88%
11- 13	1.78%	5.56%	0.2155	0.0359	2.54%	2.75%
11- 14	2.02%	8.06%	0.2159	0.0376	3.00%	2.78%
11- 15	2.30%	14.04%	0.2162	0.0393	3.55%	2.86%
11- 16	0.93%	22.75%	0.2167	0.0419	4.68%	1.76%
11- 17	1.03%	-37.20%	0.2171	0.0444	6.31%	1.67%
11- 18	1.05%	-24.22%	0.2174	0.0467	8.77%	1.61%

Table B.28 - Uncertainties in Branch B mass flow rates, interface heights and qualities for Case 11 - P_0 = 517 kPa, ΔP = 97 kPa, L/d = 1.5 and θ = 60°

Case #	$\omega_{\dot{m}_{TP,B}}$ (%)	ω_{M_B} (%)	ω_{h_B} (mm)	$\omega_{h_B/d}$	ω_{H_B} (%)	ω_{x_B} (%)
11- 8	2.06%	3.12%	0.2125	0.0428	1.27%	2.41%
11- 9	2.30%	3.33%	0.2126	0.0412	1.29%	2.95%
11- 10	2.70%	3.71%	0.2130	0.0387	1.34%	2.81%
11- 11	3.05%	4.07%	0.2132	0.0372	1.38%	3.08%
11- 12	3.38%	4.43%	0.2135	0.0359	1.43%	4.50%
11- 13	3.91%	5.05%	0.2138	0.0347	1.50%	4.38%
11- 14	4.35%	5.61%	0.2141	0.0340	1.61%	4.64%
11- 15	5.08%	6.60%	0.2144	0.0338	1.72%	5.23%
11- 16	6.00%	7.96%	0.2148	0.0341	1.92%	6.08%
11- 17	0.66%	2.38%	0.2152	0.0348	2.14%	1.04%
11- 18	0.74%	2.43%	0.2155	0.0358	2.39%	1.00%
11- 19	0.85%	2.55%	0.2158	0.0372	2.73%	1.02%
11- 20	1.02%	2.80%	0.2162	0.0392	3.31%	1.13%
11- 21	1.32%	3.52%	0.2166	0.0413	4.07%	1.38%
11- 22	1.73%	5.16%	0.2170	0.0434	5.11%	2.86%
11- 23	2.50%	23.58%	0.2174	0.0464	7.50%	3.06%

Table B.29 - Uncertainties in Branch A mass flow rates, interface heights and qualities for Case 12 - P_0 = 517 kPa, ΔP = 235 kPa, L/d = 1.5 and θ = 60°

Case #	$\omega_{\dot{m}_{TP,A}}$ (%)	ω_{M_A} (%)	ω_{h_A} (mm)	$\omega_{h_A/d}$	ω_{H_A} (%)	ω_{x_A} (%)
12- 1	1.24%	1.87%	0.2114	0.0545	1.02%	-
12- 2	1.42%	2.02%	0.2116	0.0511	1.04%	1.75%
12- 3	1.87%	2.45%	0.2119	0.0476	1.07%	3.42%
12- 4	2.29%	2.90%	0.2122	0.0449	1.10%	2.78%
12- 5	2.99%	3.76%	0.2125	0.0420	1.14%	3.14%
12- 6	3.68%	4.71%	0.2128	0.0397	1.19%	3.74%
12- 7	4.80%	6.46%	0.2131	0.0373	1.25%	5.76%
12- 8	5.77%	8.24%	0.2134	0.0358	1.32%	6.34%
12- 9	0.67%	1.68%	0.2138	0.0345	1.43%	2.31%
12- 10	0.74%	1.79%	0.2141	0.0339	1.54%	2.17%
12- 11	0.87%	2.04%	0.2145	0.0338	1.70%	1.97%
12- 12	0.99%	2.37%	0.2149	0.0342	1.89%	1.91%
12- 13	1.15%	3.00%	0.2153	0.0353	2.17%	1.87%
12- 14	1.33%	4.04%	0.2157	0.0369	2.53%	1.90%
12- 15	1.55%	6.49%	0.2161	0.0390	3.04%	1.97%
12- 16	1.73%	10.68%	0.2166	0.0416	3.84%	2.05%
12- 17	0.70%	17.30%	0.2170	0.0440	4.85%	1.22%

Table B.30 - Uncertainties in Branch B mass flow rates, interface heights and qualities for Case 12 - $P_0 = 517$ kPa, $\Delta P = 235$ kPa, $L/d = 1.5$ and $\theta = 60°$

Case #	$\omega_{\dot{m}_{TP,B}}$ (%)	ω_{M_B} (%)	ω_{h_B} (mm)	$\omega_{h_B/d}$	ω_{H_B} (%)	ω_{x_B} (%)
12- 8	1.32%	1.95%	0.2121	0.0467	1.07%	9.76%
12- 9	1.55%	2.15%	0.2124	0.0435	1.10%	1.82%
12- 10	1.75%	2.35%	0.2127	0.0411	1.13%	1.84%
12- 11	2.01%	2.61%	0.2130	0.0387	1.17%	3.53%
12- 12	2.30%	2.92%	0.2133	0.0368	1.22%	3.06%
12- 13	2.58%	3.26%	0.2136	0.0352	1.29%	2.97%
12- 14	2.95%	3.71%	0.2140	0.0342	1.38%	3.17%
12- 15	3.45%	4.38%	0.2144	0.0338	1.50%	3.57%
12- 16	3.85%	4.93%	0.2148	0.0340	1.65%	3.92%
12- 17	4.37%	5.73%	0.2151	0.0347	1.82%	4.41%
12- 18	5.14%	7.01%	0.2155	0.0359	2.06%	5.16%
12- 19	6.20%	9.02%	0.2160	0.0377	2.39%	6.76%
12- 20	0.68%	1.72%	0.2164	0.0398	2.81%	2.46%
12- 21	0.85%	2.02%	0.2168	0.0422	3.41%	2.16%
12- 22	1.12%	2.90%	0.2173	0.0453	4.50%	2.03%
12- 23	1.61%	7.84%	0.2177	0.0484	6.17%	2.12%

Table B.31 - Uncertainties in Branch A mass flow rates, interface heights and qualities for Case 13 - $P_0 = 316$ kPa, $\Delta P = 40$ kPa, $L/d = 3$ and $\theta = 60°$

Case #	$\omega_{\dot{m}_{TP,A}}$ (%)	ω_{M_A} (%)	ω_{h_A} (mm)	$\omega_{h_A/d}$	ω_{H_A} (%)	ω_{x_A} (%)
13- 1	3.52%	5.27%	0.2126	0.0413	1.60%	-
13- 2	4.43%	6.04%	0.2128	0.0392	1.65%	5.03%
13- 3	5.24%	6.82%	0.2131	0.0376	1.70%	5.34%
13- 4	0.69%	3.81%	0.2133	0.0361	1.78%	6.45%
13- 5	0.87%	3.87%	0.2137	0.0347	1.92%	3.48%
13- 6	1.06%	3.95%	0.2140	0.0340	2.07%	2.45%
13- 7	1.21%	4.04%	0.2144	0.0338	2.31%	2.03%
13- 8	1.47%	4.23%	0.2146	0.0339	2.58%	1.96%
13- 9	1.83%	4.58%	0.2149	0.0345	2.94%	2.12%
13- 10	2.35%	5.39%	0.2153	0.0356	3.59%	2.51%
13- 11	2.87%	6.63%	0.2157	0.0371	4.59%	2.97%
13- 12	0.60%	5.46%	0.2160	0.0386	5.86%	0.84%
13- 13	0.74%	8.85%	0.2164	0.0408	8.80%	0.90%

Table B.32 - Uncertainties in Branch B mass flow rates, interface heights and qualities for Case 13 - $P_0 = 316$ kPa, $\Delta P = 40$ kPa, $L/d = 3$ and $\theta = 60°$

Case #	$\omega_{\dot{m}_{TP,B}}$ (%)	ω_{M_B} (%)	ω_{h_B} (mm)	$\omega_{h_B/d}$	ω_{H_B} (%)	ω_{x_B} (%)
13- 12	3.74%	5.50%	0.2129	0.0400	1.59%	4.62%
13- 13	4.73%	6.37%	0.2132	0.0379	1.64%	5.61%
13- 14	6.16%	7.81%	0.2134	0.0364	1.70%	6.23%
13- 15	0.70%	3.89%	0.2137	0.0352	1.79%	0.92%
13- 16	0.90%	3.96%	0.2141	0.0342	1.93%	3.56%
13- 17	1.06%	4.03%	0.2144	0.0338	2.09%	2.77%
13- 18	1.27%	4.15%	0.2147	0.0338	2.30%	2.21%
13- 19	1.51%	4.34%	0.2150	0.0344	2.67%	2.08%
13- 20	1.88%	4.74%	0.2153	0.0351	3.05%	2.19%
13- 21	2.33%	5.48%	0.2157	0.0364	3.73%	2.53%
13- 22	3.16%	7.83%	0.2161	0.0382	4.85%	3.25%
13- 23	0.59%	5.19%	0.2165	0.0404	6.88%	0.88%
13- 24	0.81%	12.48%	0.2169	0.0428	11.11%	0.96%

Table B.33 - Uncertainties in Branch A mass flow rates, interface heights and qualities for Case 14 - $P_0 = 316$ kPa, $\Delta P = 123$ kPa, $L/d = 3$ and $\theta = 60°$

Case #	$\omega_{\dot{m}_{TP,A}}$ (%)	ω_{M_A} (%)	ω_{h_A} (mm)	$\omega_{h_A/d}$	ω_{H_A} (%)	ω_{x_A} (%)
14- 1	1.84%	2.73%	0.2120	0.0471	1.25%	-
14- 2	2.34%	3.16%	0.2122	0.0442	1.28%	3.11%
14- 3	2.96%	3.75%	0.2125	0.0414	1.32%	3.04%
14- 4	3.81%	4.65%	0.2129	0.0389	1.38%	4.90%
14- 5	4.55%	5.52%	0.2132	0.0369	1.45%	5.07%
14- 6	5.93%	7.29%	0.2136	0.0351	1.56%	6.10%
14- 7	0.65%	2.10%	0.2139	0.0343	1.68%	1.31%
14- 8	0.81%	2.21%	0.2143	0.0338	1.86%	1.15%
14- 9	0.93%	2.32%	0.2146	0.0339	2.04%	1.15%
14- 10	1.30%	2.84%	0.2150	0.0346	2.37%	1.41%
14- 11	1.76%	3.81%	0.2154	0.0358	2.80%	3.70%
14- 12	2.19%	5.43%	0.2158	0.0377	3.48%	3.52%
14- 13	2.56%	7.78%	0.2163	0.0399	4.47%	3.53%
14- 14	1.11%	7.28%	0.2166	0.0421	5.90%	2.35%
14- 15	1.31%	23.68%	0.2171	0.0453	9.67%	2.20%

Table B.34 - Uncertainties in Branch B mass flow rates, interface heights and qualities for Case 14 - $P_0 = 316$ kPa, $\Delta P = 123$ kPa, $L/d = 3$ and $\theta = 60°$

Case #	$\omega_{\dot{m}_{TP,B}}$ (%)	ω_{M_B} (%)	ω_{h_B} (mm)	$\omega_{h_B/d}$	ω_{H_B} (%)	ω_{x_B} (%)
14- 12	2.06%	2.93%	0.2124	0.0440	1.29%	6.22%
14- 13	2.65%	3.46%	0.2127	0.0410	1.33%	2.85%
14- 14	3.07%	3.88%	0.2130	0.0387	1.38%	3.12%
14- 15	3.70%	4.55%	0.2133	0.0369	1.44%	5.11%
14- 16	4.41%	5.37%	0.2137	0.0352	1.55%	5.03%
14- 17	5.40%	6.61%	0.2140	0.0343	1.66%	5.69%
14- 18	6.45%	8.04%	0.2144	0.0338	1.81%	6.60%
14- 19	0.75%	2.18%	0.2148	0.0340	2.04%	1.23%
14- 20	0.87%	2.29%	0.2152	0.0347	2.36%	1.17%
14- 21	1.09%	2.55%	0.2156	0.0359	2.73%	1.26%
14- 22	1.40%	3.02%	0.2160	0.0376	3.33%	3.96%
14- 23	1.91%	4.47%	0.2164	0.0399	4.29%	3.57%
14- 24	2.44%	7.41%	0.2168	0.0424	5.84%	3.55%
14- 25	1.13%	9.50%	0.2173	0.0455	9.33%	2.36%

Table B.35 - Uncertainties in Branch A mass flow rates, interface heights and qualities for Case 15 - $P_0 = 517$ kPa, $\Delta P = 97$ kPa, $L/d = 3$ and $\theta = 60°$

Case #	$\omega_{\dot{m}_{TP,A}}$ (%)	ω_{M_A} (%)	ω_{h_A} (mm)	$\omega_{h_A/d}$	ω_{H_A} (%)	ω_{x_A} (%)
15- 1	2.03%	3.09%	0.2122	0.0459	1.27%	-
15- 2	2.52%	3.52%	0.2125	0.0432	1.30%	2.71%
15- 3	3.10%	4.10%	0.2128	0.0405	1.35%	3.13%
15- 4	3.93%	5.06%	0.2131	0.0381	1.41%	4.37%
15- 5	4.68%	6.00%	0.2135	0.0361	1.49%	4.90%
15- 6	5.87%	7.71%	0.2138	0.0348	1.59%	5.95%
15- 7	0.66%	2.36%	0.2142	0.0340	1.72%	1.00%
15- 8	0.75%	2.42%	0.2145	0.0338	1.88%	0.97%
15- 9	0.98%	2.69%	0.2149	0.0341	2.15%	1.09%
15- 10	1.31%	3.36%	0.2153	0.0350	2.47%	1.36%
15- 11	1.68%	4.58%	0.2157	0.0363	2.90%	2.89%
15- 12	1.98%	6.50%	0.2161	0.0383	3.61%	2.79%
15- 13	2.27%	10.05%	0.2165	0.0404	4.54%	2.89%
15- 14	0.98%	17.07%	0.2169	0.0430	6.31%	1.79%

Table B.36 - Uncertainties in Branch B mass flow rates, interface heights and qualities for Case 15 - $P_0 = 517$ kPa, $\Delta P = 97$ kPa, $L/d = 3$ and $\theta = 60°$

Case #	$\omega_{\dot{m}_{TP,B}}$ (%)	ω_{M_B} (%)	ω_{h_B} (mm)	$\omega_{h_B/d}$	ω_{H_B} (%)	ω_{x_B} (%)
15- 11	2.20%	3.23%	0.2126	0.0431	1.29%	4.08%
15- 12	2.74%	3.74%	0.2130	0.0403	1.33%	2.85%
15- 13	3.11%	4.12%	0.2132	0.0383	1.38%	3.13%
15- 14	3.77%	4.87%	0.2136	0.0364	1.45%	4.46%
15- 15	4.43%	5.69%	0.2140	0.0349	1.54%	4.75%
15- 16	5.36%	6.96%	0.2143	0.0341	1.67%	5.48%
15- 17	6.39%	8.53%	0.2147	0.0338	1.82%	6.46%
15- 18	0.73%	2.42%	0.2150	0.0341	2.03%	1.02%
15- 19	0.88%	2.57%	0.2154	0.0350	2.35%	1.05%
15- 20	1.11%	2.94%	0.2159	0.0367	2.84%	1.19%
15- 21	1.43%	3.67%	0.2163	0.0384	3.42%	2.90%
15- 22	1.88%	6.07%	0.2167	0.0410	4.53%	2.82%
15- 23	2.28%	11.55%	0.2171	0.0431	5.85%	2.98%

Table B.37 - Uncertainties in Branch A mass flow rates, interface heights and qualities for Case 16 - $P_0 = 517$ kPa, $\Delta P = 235$ kPa, $L/d = 3$ and $\theta = 60°$

Case #	$\omega_{\dot{m}_{TP,A}}$ (%)	ω_{M_A} (%)	ω_{h_A} (mm)	$\omega_{h_A/d}$	ω_{H_A} (%)	ω_{x_A} (%)
16- 1	1.29%	1.94%	0.2117	0.0519	1.06%	-
16- 2	1.52%	2.13%	0.2120	0.0483	1.08%	1.82%
16- 3	1.94%	2.54%	0.2123	0.0444	1.12%	3.69%
16- 4	2.46%	3.10%	0.2127	0.0415	1.16%	2.96%
16- 5	3.01%	3.78%	0.2130	0.0387	1.22%	3.21%
16- 6	3.74%	4.76%	0.2134	0.0366	1.29%	3.82%
16- 7	4.40%	5.73%	0.2138	0.0350	1.38%	4.43%
16- 8	5.36%	7.33%	0.2142	0.0340	1.50%	6.15%
16- 9	0.68%	1.71%	0.2146	0.0338	1.66%	2.45%
16- 10	0.90%	2.10%	0.2150	0.0343	1.87%	2.07%
16- 11	1.05%	2.51%	0.2155	0.0355	2.18%	1.98%
16- 12	1.28%	3.50%	0.2159	0.0374	2.59%	1.94%
16- 13	1.49%	5.07%	0.2164	0.0399	3.21%	1.97%
16- 14	1.78%	9.76%	0.2169	0.0428	4.17%	2.10%
16- 15	0.73%	16.76%	0.2174	0.0461	5.88%	1.25%

Table B.38 - Uncertainties in Branch B mass flow rates and interface heights for Case 16 - $P_0 = 517$ kPa, $\Delta P = 235$ kPa, $L/d = 3$ and $\theta = 60°$

Case #	$\omega_{\dot{m}_{TP,B}}$ (%)	ω_{M_B} (%)	ω_{h_B} (mm)	$\omega_{h_B/d}$	ω_{H_B} (%)	ω_{x_B} (%)
16- 10	1.35%	1.99%	0.2121	0.0483	1.08%	4.82%
16- 11	1.62%	2.23%	0.2125	0.0446	1.11%	1.83%
16- 12	1.96%	2.56%	0.2128	0.0415	1.15%	3.95%
16- 13	2.26%	2.89%	0.2132	0.0387	1.20%	3.04%
16- 14	2.69%	3.39%	0.2136	0.0365	1.27%	3.03%
16- 15	3.11%	3.92%	0.2140	0.0349	1.35%	3.29%
16- 16	3.73%	4.77%	0.2143	0.0340	1.46%	3.82%
16- 17	4.31%	5.63%	0.2147	0.0338	1.61%	4.36%
16- 18	5.27%	7.24%	0.2152	0.0344	1.81%	5.29%
16- 19	0.65%	1.68%	0.2156	0.0356	2.09%	2.69%
16- 20	0.82%	1.96%	0.2161	0.0377	2.49%	2.19%
16- 21	1.00%	2.42%	0.2166	0.0401	3.05%	2.01%
16- 22	1.35%	4.24%	0.2171	0.0434	4.04%	1.98%
16- 23	1.69%	9.66%	0.2176	0.0466	5.53%	2.11%

Appendix C

Experimental Data

C.1 Experimental Data for $\theta = 0°$ and $L/d = 1.5$

Table C.1 – Experimental OLE and OGE data for $\theta = 0°$ *and* $L/d = 1.5$

$\mathrm{Fr}_{G,OLE,A}$	$\lvert h_{OLE,A}\rvert / d$	$\mathrm{Fr}_{G,OLE,B}$	$\lvert h_{OLE,B}\rvert / d$	$\mathrm{Fr}_{L,OGE,A}$	$h_{OGE,A}/d$	$\mathrm{Fr}_{L,OGE,B}$	$h_{OGE,B}/d$
15.45	2.317	15.30	2.317	16.18	2.048	16.63	2.048
36.05	3.240	35.97	3.240	43.49	3.280	43.93	3.280

Table C.2 – Experimental two-phase flow data for

$P_0 = 316$ kPa, $\Delta P = 40$ kPa, $\theta = 0°$ and $L/d = 1.5$

h_A (mm)	$\dot{m}_{L,A}$ (kg/s)	$\dot{m}_{G,A}$ (kg/s)	h_B (mm)	$\dot{m}_{L,B}$ (kg/s)	$\dot{m}_{G,B}$ (kg/s)
13.005	1.275E-01	0.000E+00	13.005	1.310E-01	0.000E+00
10.697	1.005E-01	9.315E-05	10.697	1.004E-01	7.873E-05
9.567	8.655E-02	1.818E-04	9.567	8.542E-02	1.792E-04
8.284	6.924E-02	2.809E-04	8.284	6.948E-02	2.763E-04
7.142	5.950E-02	3.771E-04	7.142	5.809E-02	3.858E-04
5.858	4.977E-02	5.203E-04	5.858	5.012E-02	5.170E-04
4.635	4.775E-02	7.360E-04	4.635	4.852E-02	7.422E-04
3.493	4.155E-02	8.496E-04	3.493	4.129E-02	8.613E-04
2.207	3.726E-02	1.047E-03	2.207	3.711E-02	1.082E-03
0.819	3.224E-02	1.324E-03	0.819	3.260E-02	1.343E-03
-0.356	2.913E-02	1.482E-03	-0.356	2.938E-02	1.523E-03
-1.762	2.509E-02	1.798E-03	-1.762	2.510E-02	1.824E-03
-2.842	2.140E-02	1.939E-03	-2.842	2.129E-02	1.947E-03
-4.003	1.849E-02	2.241E-03	-4.003	1.804E-02	2.270E-03
-5.207	1.491E-02	2.462E-03	-5.207	1.422E-02	2.480E-03
-6.594	1.218E-02	2.765E-03	-6.594	1.151E-02	2.795E-03
-8.044	9.087E-03	3.141E-03	-8.044	8.755E-03	3.120E-03
-9.066	7.271E-03	3.466E-03	-9.066	7.242E-03	3.547E-03
-10.300	6.445E-03	4.194E-03	-10.300	6.360E-03	4.276E-03
-11.444	4.167E-03	4.887E-03	-11.444	4.240E-03	4.972E-03
-12.342	2.593E-03	5.447E-03	-12.342	2.562E-03	5.477E-03
-13.710	9.397E-04	6.031E-03	-13.710	9.248E-04	6.096E-03
-14.715	0.000E+00	7.378E-03	-14.715	0.000E+00	7.306E-03

Table C.3 - Experimental two-phase flow data for

P_0 = 517 kPa, ΔP = 235 kPa, $\theta = 0°$ and $L/d = 1.5$

h_A (mm)	$\dot{m}_{L,A}$ (kg/s)	$\dot{m}_{G,A}$ (kg/s)	h_B (mm)	$\dot{m}_{L,B}$ (kg/s)	$\dot{m}_{G,B}$ (kg/s)
20.841	3.423E-01	0.000E+00	20.841	3.457E-01	0.000E+00
18.935	3.143E-01	1.171E-04	18.935	3.131E-01	1.013E-04
17.036	2.635E-01	3.271E-04	17.036	2.571E-01	2.907E-04
14.891	2.216E-01	7.073E-04	14.891	2.192E-01	7.061E-04
13.093	1.863E-01	1.170E-03	13.093	1.899E-01	1.139E-03
11.180	1.674E-01	1.495E-03	11.180	1.683E-01	1.498E-03
9.242	1.398E-01	1.969E-03	9.242	1.421E-01	1.979E-03
7.611	1.259E-01	2.374E-03	7.611	1.285E-01	2.370E-03
5.776	1.079E-01	2.948E-03	5.776	1.098E-01	2.946E-03
3.508	9.641E-02	3.709E-03	3.508	9.623E-02	3.724E-03
1.626	8.656E-02	4.402E-03	1.626	8.658E-02	4.419E-03
-0.419	7.574E-02	5.311E-03	-0.419	7.633E-02	5.258E-03
-2.180	6.276E-02	6.071E-03	-2.180	6.379E-02	6.031E-03
-4.291	5.666E-02	7.399E-03	-4.291	5.485E-02	7.220E-03
-5.846	4.889E-02	7.992E-03	-5.846	4.809E-02	7.782E-03
-8.016	3.759E-02	9.025E-03	-8.016	3.680E-02	8.689E-03
-9.920	2.961E-02	9.817E-03	-9.920	2.859E-02	9.425E-03
-11.959	2.133E-02	1.112E-02	-11.959	1.924E-02	1.100E-02
-13.602	1.571E-02	1.235E-02	-13.602	1.332E-02	1.224E-02
-13.703	1.599E-02	1.248E-02	-13.703	1.387E-02	1.238E-02
-15.590	1.061E-02	1.397E-02	-15.590	9.272E-03	1.430E-02
-15.766	1.022E-02	1.398E-02	-15.766	8.863E-03	1.398E-02
-17.682	4.961E-03	1.581E-02	-17.682	4.309E-03	1.648E-02
-20.581	0.000E+00	2.147E-02	-20.581	0.000E+00	2.141E-02

C.2 Experimental Data for $\theta = 90°$ and $L/d = 1.5$

Table C.4 – Experimental OLE and OGE data for $\theta = 90°$ and $L/d = 1.5$

$\mathrm{Fr}_{G,OLE,A}$	$\lvert h_{OLE,A} \rvert / d$	$\mathrm{Fr}_{G,OLE,B}$	$\lvert h_{OLE,B} \rvert / d$	$\mathrm{Fr}_{L,OGE,A}$	$h_{OGE,A}/d$	$\mathrm{Fr}_{L,OGE,B}$	$h_{OGE,B}/d$
15.30	1.556	15.15	2.141	15.99	1.604	16.96	0.999
36.89	1.748	37.40	3.062	21.56	1.903	21.66	1.099
				30.80	2.254	30.02	1.235
				44.32	2.701	44.52	1.306

Table C.5 - Experimental two-phase flow data for

P_0 = 517 kPa, ΔP = 235 kPa, $\theta = 90°$ and $L/d = 1.5$

h_A (mm)	$\dot{m}_{L,A}$ (kg/s)	$\dot{m}_{G,A}$ (kg/s)	h_B (mm)	$\dot{m}_{L,B}$ (kg/s)	$\dot{m}_{G,B}$ (kg/s)
17.152	3.483E-01	0.000E+00	26.510	3.499E-01	0.000E+00
12.783	2.051E-01	1.016E-03	22.308	3.490E-01	0.000E+00
11.004	1.666E-01	1.604E-03	20.529	3.490E-01	0.000E+00
9.368	1.325E-01	2.376E-03	18.893	3.490E-01	0.000E+00
7.670	1.079E-01	3.149E-03	17.195	3.490E-01	0.000E+00
5.623	8.222E-02	4.754E-03	15.148	3.490E-01	0.000E+00
3.801	6.059E-02	6.291E-03	13.326	3.490E-01	0.000E+00
1.917	4.321E-02	8.642E-03	11.442	3.490E-01	0.000E+00
-0.110	2.399E-02	1.095E-02	9.415	3.490E-01	0.000E+00
-3.185	9.120E-03	1.453E-02	6.340	2.934E-01	1.182E-04
-5.357	6.224E-03	1.590E-02	4.168	2.538E-01	3.347E-04
-7.079	3.270E-03	1.751E-02	2.446	2.176E-01	7.274E-04
-9.347	9.722E-04	1.987E-02	0.178	1.829E-01	1.269E-03
-8.908	5.514E-04	2.001E-02	0.617	2.006E-01	9.175E-04
-11.819	0.000E+00	2.144E-02	-2.294	1.446E-01	2.004E-03
-14.279	0.000E+00	2.264E-02	-4.754	1.047E-01	3.053E-03
-16.041	0.000E+00	2.260E-02	-6.516	8.315E-02	4.280E-03
-18.688	0.000E+00	2.262E-02	-9.163	5.126E-02	6.762E-03
-20.431	0.000E+00	2.254E-02	-10.906	4.164E-02	8.143E-03
-22.113	0.000E+00	2.238E-02	-12.588	2.666E-02	9.639E-03
-23.345	0.000E+00	2.227E-02	-13.820	2.013E-02	1.043E-02
-25.374	0.000E+00	2.209E-02	-15.849	8.419E-03	1.327E-02
-25.371	0.000E+00	2.212E-02	-15.846	8.861E-03	1.328E-02
-26.909	0.000E+00	2.202E-02	-17.384	4.514E-03	1.600E-02
-28.967	0.000E+00	2.189E-02	-19.442	0.000E+00	2.219E-02

C.3 Experimental Data for $\theta = 90°$ and $L/d = 3$

Table C.6 – Experimental OLE and OGE data for $\theta = 90°$ and $L/d = 3$

$\mathrm{Fr}_{L,OGE,A}$	$h_{OGE,A}/d$	$\mathrm{Fr}_{L,OGE,B}$	$h_{OGE,B}/d$
15.26	1.474	16.53	1.240
20.68	1.760	21.56	1.334
29.24	2.059	29.49	1.520
41.93	2.427	43.02	1.667

C.4 Experimental Data for $\theta = 30°$ and $L/d = 1.5$

Table C.7 – Experimental OLE and OGE data for $\theta = 30°$ and $L/d = 1.5$

$\mathrm{Fr}_{G,OLE,A}$	$\lvert h_{OLE,A}\rvert/d$	$\mathrm{Fr}_{G,OLE,B}$	$\lvert h_{OLE,B}\rvert/d$	$\mathrm{Fr}_{L,OGE,A}$	$h_{OGE,A}/d$	$\mathrm{Fr}_{L,OGE,B}$	$h_{OGE,B}/d$
15.68	2.232	15.74	2.106	15.87	1.855	15.98	1.849
18.36	2.383	18.58	2.234	19.11	1.996	19.33	1.973
22.96	2.596	22.63	2.454	23.40	2.220	23.53	2.164
25.32	2.734	25.20	2.605	27.49	2.371	27.66	2.330
31.28	3.036	31.35	2.860	35.72	2.678	35.63	2.627
35.80	3.204	36.06	3.070	43.52	2.909	43.95	2.862
40.15	3.326	40.47	3.209	46.93	3.029	49.78	2.985

Table C.8 – Experimental two-phase flow data for Case 1

with P_0 = 316 kPa, ΔP = 40 kPa, θ = 30° and L/d = 1.5

Case #	h_A **(mm)**	$\dot{m}_{L,A}$ **(kg/s)**	$\dot{m}_{G,A}$ **(kg/s)**	h_B **(mm)**	$\dot{m}_{L,B}$ **(kg/s)**	$\dot{m}_{G,B}$ **(kg/s)**
1- 1	11.777	1.252E-01	0.000E+00	16.521	1.254E-01	0.000E+00
1- 2	10.646	9.399E-02	1.176E-04	15.390	1.254E-01	0.000E+00
1- 3	9.789	8.443E-02	2.047E-04	14.533	1.254E-01	0.000E+00
1- 4	8.686	6.062E-02	4.075E-04	13.431	1.254E-01	0.000E+00
1- 5	7.710	4.979E-02	6.199E-04	12.454	1.263E-01	0.000E+00
1- 6	6.243	4.589E-02	7.889E-04	10.987	1.094E-01	3.525E-05
1- 7	5.047	3.990E-02	9.956E-04	9.791	9.410E-02	1.154E-04
1- 8	3.968	3.515E-02	1.196E-03	8.712	7.938E-02	2.098E-04
1- 9	3.105	3.211E-02	1.203E-03	7.849	6.804E-02	2.165E-04
1- 10	1.833	2.883E-02	1.481E-03	6.577	6.023E-02	3.623E-04
1- 11	0.632	2.524E-02	1.675E-03	5.376	5.496E-02	4.744E-04
1- 12	-0.348	2.291E-02	1.794E-03	4.397	5.081E-02	5.879E-04
1- 13	-1.716	2.005E-02	2.093E-03	3.028	4.545E-02	7.373E-04
1- 14	-2.450	1.810E-02	2.308E-03	2.295	4.268E-02	8.834E-04
1- 15	-3.777	1.493E-02	2.684E-03	0.968	3.824E-02	1.127E-03
1- 16	-4.920	1.323E-02	2.907E-03	-0.175	3.446E-02	1.270E-03
1- 17	-5.962	1.127E-02	3.264E-03	-1.218	3.162E-02	1.480E-03
1- 18	-6.984	9.460E-03	3.637E-03	-2.239	2.814E-02	1.707E-03
1- 19	-8.268	6.798E-03	3.868E-03	-3.523	2.349E-02	1.864E-03
1- 20	-9.330	5.203E-03	4.295E-03	-4.585	1.968E-02	2.161E-03
1- 21	-10.494	3.755E-03	4.701E-03	-5.749	1.643E-02	2.353E-03
1- 22	-11.535	1.858E-03	5.378E-03	-6.790	1.340E-02	2.605E-03
1- 23	-12.801	1.134E-03	5.837E-03	-8.057	1.067E-02	2.969E-03
1- 24	-13.789	0.000E+00	6.822E-03	-9.045	8.364E-03	3.655E-03
1- 25	-16.112	0.000E+00	7.111E-03	-11.368	3.304E-03	4.580E-03
1- 26	-18.119	0.000E+00	7.455E-03	-13.374	0.000E+00	7.482E-03

Table C.9 – Experimental two-phase flow data for Case 2

with P_0 = 316 kPa, ΔP = 123 kPa, θ = 30° and L/d = 1.5

Case #	h_A **(mm)**	$\dot{m}_{L,A}$ **(kg/s)**	$\dot{m}_{G,A}$ **(kg/s)**	h_B **(mm)**	$\dot{m}_{L,B}$ **(kg/s)**	$\dot{m}_{G,B}$ **(kg/s)**
2- 1	15.870	2.358E-01	0.000E+00	20.615	2.369E-01	0.000E+00
2- 2	14.548	1.723E-01	1.859E-04	19.293	2.369E-01	0.000E+00
2- 3	13.264	1.441E-01	4.043E-04	18.008	2.369E-01	0.000E+00
2- 4	12.508	1.252E-01	6.034E-04	17.252	2.369E-01	0.000E+00
2- 5	10.709	9.317E-02	1.019E-03	15.453	2.202E-01	2.620E-05
2- 6	9.410	8.443E-02	1.230E-03	14.154	1.909E-01	9.430E-05
2- 7	8.065	7.686E-02	1.394E-03	12.810	1.677E-01	1.799E-04
2- 8	6.313	6.495E-02	1.849E-03	11.058	1.415E-01	3.819E-04
2- 9	5.049	6.209E-02	2.077E-03	9.793	1.297E-01	5.443E-04
2- 10	3.544	5.642E-02	2.385E-03	8.288	1.144E-01	6.835E-04
2- 11	2.098	5.017E-02	2.751E-03	6.842	1.026E-01	8.703E-04
2- 12	0.756	4.356E-02	3.152E-03	5.501	8.958E-02	1.110E-03
2- 13	-0.526	3.859E-02	3.447E-03	4.219	8.164E-02	1.301E-03
2- 14	-2.034	3.195E-02	3.887E-03	2.711	6.962E-02	1.648E-03
2- 15	-3.808	2.618E-02	4.270E-03	0.937	6.191E-02	1.984E-03
2- 16	-5.012	2.151E-02	4.757E-03	-0.267	5.532E-02	2.334E-03
2- 17	-6.625	1.755E-02	5.301E-03	-1.881	4.914E-02	2.667E-03
2- 18	-7.756	1.467E-02	5.810E-03	-3.012	4.424E-02	3.025E-03
2- 19	-9.263	1.166E-02	6.321E-03	-4.518	3.761E-02	3.368E-03
2- 20	-11.648	6.353E-03	7.581E-03	-6.904	2.640E-02	4.207E-03
2- 21	-12.258	5.850E-03	7.834E-03	-7.513	2.471E-02	4.380E-03
2- 22	-13.766	3.338E-03	9.069E-03	-9.022	1.724E-02	5.079E-03
2- 23	-15.340	0.000E+00	9.807E-03	-10.596	1.272E-02	5.652E-03
2- 24	-16.505	0.000E+00	1.092E-02	-11.761	8.762E-03	6.473E-03
2- 25	-17.875	0.000E+00	1.153E-02	-13.130	6.270E-03	7.400E-03
2- 26	-21.289	0.000E+00	1.186E-02	-16.544	0.000E+00	1.180E-02

Table C.10 – Experimental two-phase flow data for Case 3

with P_0 = 517 kPa, ΔP = 97 kPa, θ = 30° and L/d = 1.5

Case #	h_A (mm)	$\dot{m}_{L,A}$ (kg/s)	$\dot{m}_{G,A}$ (kg/s)	h_B (mm)	$\dot{m}_{L,B}$ (kg/s)	$\dot{m}_{G,B}$ (kg/s)
3- 1	15.059	2.165E-01	0.000E+00	19.803	2.171E-01	0.000E+00
3- 2	14.014	1.748E-01	1.848E-04	18.759	2.141E-01	0.000E+00
3- 3	12.565	1.424E-01	4.617E-04	17.309	2.141E-01	0.000E+00
3- 4	10.993	1.063E-01	1.230E-03	15.737	2.141E-01	0.000E+00
3- 5	9.664	9.235E-02	1.570E-03	14.408	2.040E-01	3.996E-05
3- 6	8.068	8.010E-02	2.048E-03	12.813	1.708E-01	2.585E-04
3- 7	6.827	7.361E-02	2.283E-03	11.572	1.576E-01	4.072E-04
3- 8	5.238	6.549E-02	2.745E-03	9.982	1.359E-01	6.792E-04
3- 9	3.852	5.936E-02	3.144E-03	8.597	1.212E-01	9.135E-04
3- 10	2.115	5.099E-02	3.756E-03	6.859	1.043E-01	1.266E-03
3- 11	1.052	4.721E-02	4.100E-03	5.796	9.749E-02	1.490E-03
3- 12	-0.304	4.189E-02	4.569E-03	4.440	8.958E-02	1.730E-03
3- 13	-2.028	3.434E-02	5.091E-03	2.717	7.484E-02	2.136E-03
3- 14	-3.682	2.805E-02	5.758E-03	1.063	6.459E-02	2.668E-03
3- 15	-5.277	2.275E-02	6.334E-03	-0.533	5.885E-02	3.108E-03
3- 16	-6.385	1.949E-02	6.909E-03	-1.641	5.372E-02	3.450E-03
3- 17	-8.111	1.532E-02	7.722E-03	-3.366	4.646E-02	4.012E-03
3- 18	-9.313	1.218E-02	8.440E-03	-4.568	3.887E-02	5.529E-03
3- 19	-11.071	9.082E-03	9.494E-03	-6.327	3.194E-02	5.126E-03
3- 20	-12.239	6.057E-03	1.042E-02	-7.494	2.688E-02	5.605E-03
3- 21	-13.690	4.166E-03	1.113E-02	-8.946	2.073E-02	6.157E-03
3- 22	-15.209	1.925E-03	1.272E-02	-10.465	1.540E-02	7.325E-03
3- 23	-16.661	0.000E+00	1.390E-02	-11.917	1.095E-02	8.286E-03
3- 24	-18.093	0.000E+00	1.546E-02	-13.348	7.212E-03	9.895E-03
3- 25	-19.404	0.000E+00	1.601E-02	-14.659	3.488E-03	1.115E-02
3- 26	-21.189	0.000E+00	1.547E-02	-16.445	0.000E+00	1.548E-02

Table C.11 – Experimental two-phase flow data for Case 4

with P_0 = 517 kPa, ΔP = 235 kPa, θ = 30° and L/d = 1.5

Case #	h_A **(mm)**	$\dot{m}_{L,A}$ **(kg/s)**	$\dot{m}_{G,A}$ **(kg/s)**	h_B **(mm)**	$\dot{m}_{L,B}$ **(kg/s)**	$\dot{m}_{G,B}$ **(kg/s)**
4- 1	18.475	3.425E-01	0.000E+00	23.219	3.458E-01	0.000E+00
4- 2	17.718	2.726E-01	3.001E-04	22.463	3.392E-01	0.000E+00
4- 3	16.183	2.270E-01	7.416E-04	20.927	3.392E-01	0.000E+00
4- 4	14.164	1.683E-01	1.546E-03	18.908	3.392E-01	0.000E+00
4- 5	12.715	1.391E-01	2.095E-03	17.459	3.081E-01	1.124E-04
4- 6	9.591	1.112E-01	2.879E-03	14.335	2.335E-01	4.986E-04
4- 7	7.401	9.891E-02	3.608E-03	12.146	2.025E-01	9.609E-04
4- 8	5.768	8.742E-02	4.243E-03	10.512	1.770E-01	1.325E-03
4- 9	4.029	7.902E-02	4.863E-03	8.773	1.585E-01	1.631E-03
4- 10	2.372	6.928E-02	5.792E-03	7.117	1.398E-01	2.075E-03
4- 11	0.736	6.062E-02	6.418E-03	5.480	1.246E-01	2.429E-03
4- 12	-1.263	5.182E-02	7.360E-03	3.481	1.102E-01	2.969E-03
4- 13	-2.732	4.589E-02	8.025E-03	2.012	9.919E-02	3.423E-03
4- 14	-4.653	3.663E-02	8.966E-03	0.092	8.845E-02	4.190E-03
4- 15	-6.187	3.086E-02	9.594E-03	-1.443	7.711E-02	4.728E-03
4- 16	-8.030	2.400E-02	1.086E-02	-3.286	6.690E-02	5.816E-03
4- 17	-9.566	1.866E-02	1.155E-02	-4.822	6.023E-02	6.417E-03
4- 18	-11.614	1.310E-02	1.304E-02	-6.870	4.780E-02	7.488E-03
4- 19	-13.193	1.035E-02	1.400E-02	-8.449	3.921E-02	8.226E-03
4- 20	-15.283	5.614E-03	1.606E-02	-10.539	2.814E-02	9.522E-03
4- 21	-16.614	2.413E-03	1.772E-02	-11.869	2.349E-02	9.911E-03
4- 22	-18.310	1.069E-03	1.927E-02	-13.565	1.437E-02	1.144E-02
4- 23	-20.231	0.000E+00	2.141E-02	-15.487	8.841E-03	1.359E-02
4- 24	-21.953	0.000E+00	2.188E-02	-17.208	2.600E-03	1.729E-02
4- 25	-24.238	0.000E+00	2.131E-02	-19.493	0.000E+00	2.147E-02

C.5 Experimental Data for θ = 30° and L/d = 3

Table C.12 – Experimental OLE and OGE data for $\theta = 30°$ and $L/d = 3$

$\mathrm{Fr}_{G,OLE,A}$	$\lvert h_{OLE,A} \rvert / d$	$\mathrm{Fr}_{G,OLE,B}$	$\lvert h_{OLE,B} \rvert / d$	$\mathrm{Fr}_{L,OGE,A}$	$h_{OGE,A}/d$	$\mathrm{Fr}_{L,OGE,B}$	$h_{OGE,B}/d$
14.53	1.921	14.80	2.020	15.56	1.658	16.09	1.665
17.79	2.131	18.39	2.204	18.69	1.783	18.90	1.765
21.29	2.256	21.41	2.339	23.39	1.978	23.53	1.995
24.23	2.418	24.63	2.465	27.29	2.094	27.86	2.131
31.28	2.643	30.43	2.646	35.50	2.401	35.63	2.409
33.89	2.857	35.56	2.809	42.73	2.644	43.95	2.635
38.04	3.007	39.67	2.927	49.72	2.897	49.72	2.844

Table C.13 – Experimental two-phase flow data for Case 5 with

P_0 = 316 kPa, ΔP = 40 kPa, $\theta = 30°$ and $L/d = 3$

Case #	h_A (mm)	$\dot{m}_{L,A}$ (kg/s)	$\dot{m}_{G,A}$ (kg/s)	h_B (mm)	$\dot{m}_{L,B}$ (kg/s)	$\dot{m}_{G,B}$ (kg/s)
5- 1	10.526	1.227E-01	0.000E+00	19.775	1.263E-01	0.000E+00
5- 2	9.097	9.235E-02	1.245E-04	18.346	1.263E-01	0.000E+00
5- 3	8.095	7.794E-02	2.205E-04	17.344	1.263E-01	0.000E+00
5- 4	6.603	6.277E-02	3.822E-04	15.851	1.263E-01	0.000E+00
5- 5	5.113	4.984E-02	5.002E-04	14.362	1.263E-01	0.000E+00
5- 6	3.986	4.256E-02	7.740E-04	13.235	1.263E-01	0.000E+00
5- 7	2.764	3.728E-02	1.093E-03	12.013	1.263E-01	0.000E+00
5- 8	1.120	3.086E-02	1.390E-03	10.369	1.195E-01	1.169E-05
5- 9	-0.133	2.711E-02	1.569E-03	9.116	9.834E-02	7.412E-05
5- 10	-1.198	2.400E-02	1.847E-03	8.051	8.618E-02	1.767E-04
5- 11	-2.444	2.019E-02	2.068E-03	6.805	6.962E-02	2.839E-04
5- 12	-4.099	1.480E-02	2.529E-03	5.150	5.425E-02	4.875E-04
5- 13	-5.449	1.218E-02	2.914E-03	3.800	4.747E-02	6.966E-04
5- 14	-6.491	9.208E-03	3.194E-03	2.757	3.991E-02	8.462E-04
5- 15	-7.781	6.724E-03	3.758E-03	1.468	3.525E-02	1.089E-03
5- 16	-9.152	3.755E-03	4.464E-03	0.096	2.933E-02	1.394E-03
5- 17	-10.693	1.101E-03	5.451E-03	-1.444	2.556E-02	1.728E-03
5- 18	-11.817	4.822E-04	6.258E-03	-2.568	2.058E-02	1.997E-03
5- 19	-13.065	0.000E+00	7.053E-03	-3.816	1.776E-02	2.285E-03
5- 20	-14.457	0.000E+00	7.078E-03	-5.208	1.258E-02	2.668E-03
5- 21	-15.748	0.000E+00	7.093E-03	-6.500	9.854E-03	2.997E-03
5- 22	-17.080	0.000E+00	7.008E-03	-7.831	7.810E-03	3.531E-03
5- 23	-18.658	0.000E+00	7.057E-03	-9.410	4.578E-03	4.245E-03
5- 24	-19.827	0.000E+00	7.120E-03	-10.579	2.449E-03	5.139E-03
5- 25	-21.119	0.000E+00	7.174E-03	-11.870	9.297E-04	5.987E-03
5- 26	-22.075	0.000E+00	6.913E-03	-12.827	0.000E+00	7.040E-03

Table C.14 – Experimental two-phase flow data for Case 6

with P_0 = 316 kPa, ΔP = 123 kPa, θ = 30° and L/d = 3

Case #	h_A **(mm)**	$\dot{m}_{L,A}$ **(kg/s)**	$\dot{m}_{G,A}$ **(kg/s)**	h_B **(mm)**	$\dot{m}_{L,B}$ **(kg/s)**	$\dot{m}_{G,B}$ **(kg/s)**
6- 1	14.611	2.235E-01	0.000E+00	23.860	2.335E-01	0.000E+00
6- 2	13.057	1.908E-01	7.930E-05	22.306	2.335E-01	0.000E+00
6- 3	11.417	1.490E-01	2.799E-04	20.666	2.335E-01	0.000E+00
6- 4	9.991	1.227E-01	5.575E-04	19.240	2.335E-01	0.000E+00
6- 5	8.377	1.047E-01	8.234E-04	17.625	2.335E-01	0.000E+00
6- 6	6.946	8.742E-02	1.165E-03	16.194	2.335E-01	0.000E+00
6- 7	4.961	6.711E-02	1.709E-03	14.210	2.335E-01	0.000E+00
6- 8	3.774	6.192E-02	1.994E-03	13.023	1.894E-01	8.582E-05
6- 9	2.322	5.521E-02	2.314E-03	11.571	1.647E-01	2.240E-04
6- 10	0.617	4.721E-02	2.766E-03	9.866	1.365E-01	4.522E-04
6- 11	-0.936	4.023E-02	3.131E-03	8.313	1.170E-01	6.248E-04
6- 12	-2.284	3.335E-02	3.540E-03	6.964	1.021E-01	8.884E-04
6- 13	-4.125	2.664E-02	3.958E-03	5.124	8.731E-02	1.186E-03
6- 14	-5.823	1.977E-02	4.741E-03	3.426	7.030E-02	1.595E-03
6- 15	-7.178	1.630E-02	5.245E-03	2.070	6.442E-02	1.863E-03
6- 16	-8.670	1.179E-02	5.979E-03	0.578	5.558E-02	1.841E-03
6- 17	-10.183	8.009E-03	6.778E-03	-0.934	4.881E-02	2.661E-03
6- 18	-11.963	3.961E-03	8.344E-03	-2.714	3.973E-02	3.300E-03
6- 19	-13.293	1.925E-03	9.528E-03	-4.045	3.383E-02	3.659E-03
6- 20	-15.014	0.000E+00	1.123E-02	-5.766	2.533E-02	4.222E-03
6- 21	-16.408	0.000E+00	1.127E-02	-7.159	1.982E-02	4.734E-03
6- 22	-17.807	0.000E+00	1.139E-02	-8.558	1.422E-02	5.457E-03
6- 23	-19.917	0.000E+00	1.128E-02	-10.668	8.324E-03	6.644E-03
6- 24	-21.165	0.000E+00	1.133E-02	-11.916	5.546E-03	7.561E-03
6- 25	-22.887	0.000E+00	1.140E-02	-13.638	2.373E-03	9.119E-03
6- 26	-24.904	0.000E+00	1.136E-02	-15.655	0.000E+00	1.155E-02

Table C.15 – Experimental two-phase flow data for Case 7

with P_0 = 517 kPa, ΔP = 97 kPa, θ = 30° and L/d = 3

Case #	h_A **(mm)**	$\dot{m}_{L,A}$ **(kg/s)**	$\dot{m}_{G,A}$ **(kg/s)**	h_B **(mm)**	$\dot{m}_{L,B}$ **(kg/s)**	$\dot{m}_{G,B}$ **(kg/s)**
7- 1	13.300	2.149E-01	0.000E+00	22.549	2.187E-01	0.000E+00
7- 2	12.091	1.683E-01	1.832E-04	21.339	2.171E-01	0.000E+00
7- 3	10.718	1.457E-01	3.902E-04	19.966	2.171E-01	0.000E+00
7- 4	9.324	1.194E-01	7.797E-04	18.573	2.171E-01	0.000E+00
7- 5	7.582	9.973E-02	1.200E-03	16.830	2.171E-01	0.000E+00
7- 6	5.921	8.227E-02	1.746E-03	15.170	2.171E-01	0.000E+00
7- 7	4.670	6.928E-02	2.015E-03	13.918	2.171E-01	0.000E+00
7- 8	2.991	6.175E-02	2.778E-03	12.240	1.801E-01	1.224E-04
7- 9	1.478	5.521E-02	3.225E-03	10.727	1.576E-01	3.017E-04
7- 10	-0.082	4.721E-02	3.857E-03	9.167	1.348E-01	6.304E-04
7- 11	-1.457	4.056E-02	4.323E-03	7.792	1.178E-01	8.334E-04
7- 12	-3.079	3.273E-02	4.938E-03	6.170	1.026E-01	1.336E-03
7- 13	-4.681	2.711E-02	5.537E-03	4.568	8.958E-02	1.675E-03
7- 14	-6.385	2.005E-02	6.523E-03	2.863	7.257E-02	2.237E-03
7- 15	-7.658	1.671E-02	7.107E-03	1.591	6.463E-02	2.622E-03
7- 16	-9.403	1.114E-02	8.457E-03	-0.155	5.532E-02	3.272E-03
7- 17	-10.696	7.820E-03	9.379E-03	-1.448	4.981E-02	3.651E-03
7- 18	-12.547	3.755E-03	1.118E-02	-3.299	4.095E-02	4.339E-03
7- 19	-13.758	1.925E-03	1.226E-02	-4.510	3.477E-02	4.743E-03
7- 20	-15.626	0.000E+00	1.530E-02	-6.378	2.563E-02	5.560E-03
7- 21	-16.777	0.000E+00	1.530E-02	-7.529	2.012E-02	6.230E-03
7- 22	-18.483	0.000E+00	1.537E-02	-9.235	1.368E-02	7.324E-03
7- 23	-19.777	0.000E+00	1.525E-02	-10.529	1.013E-02	8.370E-03
7- 24	-21.668	0.000E+00	1.539E-02	-12.420	5.337E-03	1.030E-02
7- 25	-24.635	0.000E+00	1.524E-02	-15.387	0.000E+00	1.577E-02

Table C.16 – Experimental two-phase flow data for Case 3

with P_0 = 517 kPa, ΔP = 235 kPa, θ = 30° and L/d = 3

Case #	h_A **(mm)**	$\dot{m}_{L,A}$ **(kg/s)**	$\dot{m}_{G,A}$ **(kg/s)**	h_B **(mm)**	$\dot{m}_{L,B}$ **(kg/s)**	$\dot{m}_{G,B}$ **(kg/s)**
8- 1	16.789	3.363E-01	0.000E+00	26.037	3.458E-01	0.000E+00
8- 2	15.739	2.912E-01	1.259E-04	24.988	3.376E-01	0.000E+00
8- 3	14.101	2.384E-01	4.002E-04	23.350	3.376E-01	0.000E+00
8- 4	12.177	1.908E-01	1.068E-03	21.426	3.376E-01	0.000E+00
8- 5	10.393	1.579E-01	1.618E-03	19.642	3.376E-01	0.000E+00
8- 6	8.611	1.244E-01	2.354E-03	17.859	3.376E-01	0.000E+00
8- 7	6.911	1.063E-01	3.029E-03	16.159	3.146E-01	8.988E-05
8- 8	4.923	9.399E-02	3.720E-03	14.171	2.518E-01	3.664E-04
8- 9	3.344	8.552E-02	4.352E-03	12.592	2.219E-01	6.899E-04
8- 10	1.436	7.036E-02	5.193E-03	10.684	1.886E-01	1.160E-03
8- 11	-0.151	6.481E-02	5.938E-03	9.097	1.688E-01	1.506E-03
8- 12	-2.037	5.313E-02	6.876E-03	7.212	1.432E-01	2.061E-03
8- 13	-3.719	4.522E-02	7.648E-03	5.530	1.254E-01	2.502E-03
8- 14	-5.687	3.450E-02	8.742E-03	3.561	1.088E-01	3.166E-03
8- 15	-7.411	2.758E-02	9.702E-03	1.838	9.664E-02	3.721E-03
8- 16	-9.237	1.963E-02	1.112E-02	0.012	8.051E-02	4.549E-03
8- 17	-11.068	1.362E-02	1.254E-02	-1.819	6.962E-02	5.314E-03
8- 18	-12.792	8.577E-03	1.432E-02	-3.543	5.850E-02	6.405E-03
8- 19	-14.373	4.666E-03	1.565E-02	-5.125	5.148E-02	7.160E-03
8- 20	-16.301	1.231E-03	1.838E-02	-7.052	3.871E-02	8.280E-03
8- 21	-18.351	0.000E+00	2.073E-02	-9.102	2.941E-02	9.315E-03
8- 22	-20.034	0.000E+00	2.079E-02	-10.786	2.043E-02	1.053E-02
8- 23	-21.719	0.000E+00	2.067E-02	-12.471	1.245E-02	1.222E-02
8- 24	-23.526	0.000E+00	2.056E-02	-14.277	6.772E-03	1.479E-02
8- 25	-25.622	0.000E+00	2.054E-02	-16.373	2.034E-03	1.795E-02
8- 26	-27.092	0.000E+00	2.024E-02	-17.843	0.000E+00	2.124E-02

C.6 Experimental Data for $\theta = 60°$ and $L/d = 1.5$

Table C.17 – Experimental OLE and OGE data for $\theta = 60°$ and $L/d = 1.5$

$\mathrm{Fr}_{G,OLE,A}$	$\lvert h_{OLE,A} \rvert / d$	$\mathrm{Fr}_{G,OLE,B}$	$\lvert h_{OLE,B} \rvert / d$	$\mathrm{Fr}_{L,OGE,A}$	$h_{OGE,A}/d$	$\mathrm{Fr}_{L,OGE,B}$	$h_{OGE,B}/d$
15.32	2.198	15.62	2.145	17.39	1.724	17.40	1.472
19.30	2.407	19.26	2.296	20.44	1.892	21.76	1.643
23.11	2.458	22.38	2.496	25.83	2.095	25.83	1.807
25.61	2.524	26.32	2.693	30.57	2.312	30.58	1.940
31.70	2.741	31.57	2.892	36.15	2.477	36.15	2.053
36.48	2.823	36.44	3.015	44.32	2.743	44.32	2.194
40.58	2.967	40.35	3.226	46.91	2.813	49.37	2.345

Table C.18 – Experimental two-phase flow data for Case 9

with P_0 = 316 kPa, ΔP = 40 kPa, θ = 60° and L/d = 1.5

Case #	h_A **(mm)**	$\dot{m}_{L,A}$ **(kg/s)**	$\dot{m}_{G,A}$ **(kg/s)**	h_B **(mm)**	$\dot{m}_{L,B}$ **(kg/s)**	$\dot{m}_{G,B}$ **(kg/s)**
9- 1	10.956	1.350E-01	0.000E+00	19.166	1.339E-01	0.000E+00
9- 2	9.578	1.145E-01	3.358E-05	17.788	1.339E-01	0.000E+00
9- 3	8.292	8.824E-02	1.843E-04	16.502	1.339E-01	0.000E+00
9- 4	7.007	7.361E-02	3.091E-04	15.217	1.339E-01	0.000E+00
9- 5	5.683	5.729E-02	6.530E-04	13.893	1.339E-01	0.000E+00
9- 6	4.517	4.853E-02	8.757E-04	12.727	1.339E-01	0.000E+00
9- 7	3.189	3.663E-02	1.170E-03	11.399	1.339E-01	0.000E+00
9- 8	1.801	2.961E-02	1.499E-03	10.011	1.339E-01	0.000E+00
9- 9	0.432	2.088E-02	2.030E-03	8.642	1.212E-01	1.996E-05
9- 10	-0.906	1.838E-02	2.327E-03	7.304	1.051E-01	5.905E-05
9- 11	-2.053	1.560E-02	2.599E-03	6.157	8.958E-02	1.549E-04
9- 12	-3.321	1.349E-02	2.852E-03	4.889	7.938E-02	2.250E-04
9- 13	-4.771	1.114E-02	3.185E-03	3.439	6.593E-02	3.356E-04
9- 14	-6.058	8.072E-03	3.646E-03	2.152	5.602E-02	4.767E-04
9- 15	-7.427	6.146E-03	4.010E-03	0.783	4.981E-02	6.399E-04
9- 16	-8.755	4.098E-03	4.613E-03	-0.544	4.198E-02	8.468E-04
9- 17	-9.940	2.981E-03	5.040E-03	-1.730	3.745E-02	1.009E-03
9- 18	-11.405	1.392E-03	5.861E-03	-3.195	3.130E-02	1.383E-03
9- 19	-12.653	8.104E-04	6.322E-03	-4.443	2.624E-02	1.566E-03
9- 20	-14.147	0.000E+00	7.121E-03	-5.937	1.924E-02	1.998E-03
9- 21	-15.128	0.000E+00	7.231E-03	-6.918	1.570E-02	2.236E-03
9- 22	-16.457	0.000E+00	7.277E-03	-8.247	1.095E-02	2.778E-03
9- 23	-17.787	0.000E+00	7.251E-03	-9.577	7.448E-03	3.298E-03
9- 24	-19.750	0.000E+00	7.370E-03	-11.540	2.972E-03	4.494E-03
9- 25	-21.833	0.000E+00	7.307E-03	-13.622	0.000E+00	7.232E-03

Table C.19 – Experimental two-phase flow data for Case 10

with P_0 = 316 kPa, ΔP = 123 kPa, θ = 60° and L/d = 1.5

Case #	h_A (mm)	$\dot{m}_{L,A}$ (kg/s)	$\dot{m}_{G,A}$ (kg/s)	h_B (mm)	$\dot{m}_{L,B}$ (kg/s)	$\dot{m}_{G,B}$ (kg/s)
10- 1	14.679	2.410E-01	0.000E+00	22.889	2.369E-01	0.000E+00
10- 2	12.887	2.053E-01	8.823E-05	21.097	2.369E-01	0.000E+00
10- 3	11.518	1.555E-01	2.633E-04	19.728	2.369E-01	0.000E+00
10- 4	10.050	1.309E-01	5.777E-04	18.260	2.369E-01	0.000E+00
10- 5	8.339	9.640E-02	1.044E-03	16.549	2.369E-01	0.000E+00
10- 6	6.829	7.900E-02	1.405E-03	15.039	2.369E-01	0.000E+00
10- 7	5.072	5.867E-02	2.405E-03	13.282	2.369E-01	0.000E+00
10- 8	3.419	4.656E-02	3.059E-03	11.629	2.319E-01	1.453E-05
10- 9	2.071	4.006E-02	3.438E-03	10.281	2.017E-01	8.103E-05
10- 10	0.580	3.483E-02	3.699E-03	8.790	1.755E-01	1.607E-04
10- 11	-1.169	2.805E-02	4.265E-03	7.041	1.475E-01	3.843E-04
10- 12	-2.396	2.462E-02	4.585E-03	5.814	1.348E-01	4.591E-04
10- 13	-4.155	1.880E-02	5.287E-03	4.055	1.127E-01	7.229E-04
10- 14	-5.708	1.532E-02	5.675E-03	2.502	1.009E-01	8.956E-04
10- 15	-7.445	1.114E-02	6.512E-03	0.765	8.164E-02	1.184E-03
10- 16	-9.141	7.834E-03	7.161E-03	-0.931	7.030E-02	1.449E-03
10- 17	-10.716	4.873E-03	8.224E-03	-2.506	6.157E-02	1.833E-03
10- 18	-12.349	3.124E-03	9.067E-03	-4.139	5.372E-02	2.222E-03
10- 19	-13.716	1.659E-03	9.903E-03	-5.506	4.510E-02	2.740E-03
10- 20	-15.230	8.104E-04	1.096E-02	-7.020	3.887E-02	3.167E-03
10- 21	-16.886	0.000E+00	1.221E-02	-8.676	2.846E-02	3.840E-03
10- 22	-18.360	0.000E+00	1.234E-02	-10.150	2.104E-02	4.519E-03
10- 23	-19.996	0.000E+00	1.235E-02	-11.786	1.177E-02	5.735E-03
10- 24	-21.796	0.000E+00	1.220E-02	-13.586	6.844E-03	7.084E-03
10- 25	-23.268	0.000E+00	1.226E-02	-15.058	2.600E-03	8.727E-03
10- 26	-24.902	0.000E+00	1.202E-02	-16.692	0.000E+00	1.196E-02

Table C.20 – Experimental two-phase flow data for Case 11

with P_0 = 517 kPa, ΔP = 97 kPa, $\theta = 60°$ and $L/d = 1.5$

Case #	h_A (mm)	$\dot{m}_{L,A}$ (kg/s)	$\dot{m}_{G,A}$ (kg/s)	h_B (mm)	$\dot{m}_{L,B}$ (kg/s)	$\dot{m}_{G,B}$ (kg/s)
11- 1	13.735	2.200E-01	0.000E+00	21.945	2.171E-01	0.000E+00
11- 2	12.186	1.908E-01	1.637E-04	20.396	2.171E-01	0.000E+00
11- 3	10.567	1.441E-01	5.520E-04	18.777	2.171E-01	0.000E+00
11- 4	9.215	1.260E-01	8.890E-04	17.425	2.171E-01	0.000E+00
11- 5	7.769	9.645E-02	1.486E-03	15.979	2.171E-01	0.000E+00
11- 6	5.946	7.794E-02	2.025E-03	14.156	2.171E-01	0.000E+00
11- 7	3.981	5.659E-02	3.459E-03	12.191	2.171E-01	0.000E+00
11- 8	2.550	4.423E-02	4.313E-03	10.760	2.141E-01	2.360E-05
11- 9	1.444	3.908E-02	4.684E-03	9.654	1.917E-01	1.128E-04
11- 10	-0.461	3.304E-02	5.197E-03	7.749	1.631E-01	2.718E-04
11- 11	-1.789	2.805E-02	5.788E-03	6.421	1.441E-01	5.155E-04
11- 12	-3.181	2.322E-02	6.139E-03	5.029	1.297E-01	7.284E-04
11- 13	-4.759	1.838E-02	7.118E-03	3.451	1.119E-01	1.085E-03
11- 14	-6.437	1.454E-02	7.848E-03	1.773	1.000E-01	1.336E-03
11- 15	-7.891	1.088E-02	8.819E-03	0.319	8.505E-02	1.735E-03
11- 16	-9.815	7.255E-03	9.975E-03	-1.605	7.144E-02	2.136E-03
11- 17	-11.454	4.354E-03	1.132E-02	-3.244	6.124E-02	2.712E-03
11- 18	-12.826	3.124E-03	1.223E-02	-4.616	5.443E-02	3.171E-03
11- 19	-14.262	1.526E-03	1.354E-02	-6.051	4.613E-02	3.821E-03
11- 20	-16.025	6.403E-04	1.513E-02	-7.815	3.698E-02	4.493E-03
11- 21	-17.583	0.000E+00	1.651E-02	-9.373	2.672E-02	5.401E-03
11- 22	-19.018	0.000E+00	1.651E-02	-10.808	1.953E-02	6.472E-03
11- 23	-20.863	0.000E+00	1.643E-02	-12.653	9.581E-03	8.352E-03
11- 24	-23.262	0.000E+00	1.640E-02	-15.052	3.712E-03	1.097E-02
11- 25	-25.308	0.000E+00	1.626E-02	-17.098	0.000E+00	1.592E-02

Table C.21 – Experimental two-phase flow data for Case 12

with P_0 = 517 kPa, ΔP = 235 kPa, θ = 60° and L/d = 1.5

Case #	h_A (mm)	$\dot{m}_{L,A}$ (kg/s)	$\dot{m}_{G,A}$ (kg/s)	h_B (mm)	$\dot{m}_{L,B}$ (kg/s)	$\dot{m}_{G,B}$ (kg/s)
12- 1	17.419	3.487E-01	0.000E+00	25.629	3.474E-01	0.000E+00
12- 2	15.631	3.037E-01	2.073E-04	23.841	3.474E-01	0.000E+00
12- 3	13.687	2.305E-01	7.351E-04	21.897	3.474E-01	0.000E+00
12- 4	12.064	1.876E-01	1.330E-03	20.274	3.474E-01	0.000E+00
12- 5	10.262	1.424E-01	2.198E-03	18.472	3.474E-01	0.000E+00
12- 6	8.563	1.145E-01	3.009E-03	16.773	3.474E-01	0.000E+00
12- 7	6.598	8.552E-02	4.682E-03	14.808	3.474E-01	0.000E+00
12- 8	4.981	6.928E-02	5.672E-03	13.191	3.351E-01	2.160E-05
12- 9	3.016	6.057E-02	6.747E-03	11.226	2.851E-01	2.198E-04
12- 10	1.411	5.365E-02	7.309E-03	9.621	2.518E-01	3.694E-04
12- 11	-0.415	4.389E-02	8.403E-03	7.795	2.187E-01	7.434E-04
12- 12	-2.099	3.679E-02	9.109E-03	6.111	1.909E-01	1.072E-03
12- 13	-4.004	2.930E-02	1.008E-02	4.206	1.693E-01	1.477E-03
12- 14	-5.785	2.322E-02	1.099E-02	2.425	1.475E-01	1.859E-03
12- 15	-7.649	1.699E-02	1.226E-02	0.561	1.254E-01	2.365E-03
12- 16	-9.582	1.284E-02	1.342E-02	-1.372	1.119E-01	2.856E-03
12- 17	-11.163	8.126E-03	1.490E-02	-2.953	9.749E-02	3.543E-03
12- 18	-12.968	5.203E-03	1.626E-02	-4.758	8.164E-02	4.254E-03
12- 19	-14.813	2.732E-03	1.773E-02	-6.603	6.577E-02	5.469E-03
12- 20	-16.472	1.263E-03	1.932E-02	-8.262	5.973E-02	6.241E-03
12- 21	-18.195	0.000E+00	2.185E-02	-9.985	4.545E-02	7.419E-03
12- 22	-20.204	0.000E+00	2.234E-02	-11.994	3.130E-02	8.728E-03
12- 23	-21.982	0.000E+00	2.248E-02	-13.772	1.717E-02	1.067E-02
12- 24	-23.786	0.000E+00	2.231E-02	-15.576	9.718E-03	1.286E-02
12- 25	-27.356	0.000E+00	2.176E-02	-19.146	0.000E+00	2.173E-02

C.7 Experimental Data for $\theta = 60°$ and $L/d = 3$

Table C.22 – Experimental OLE and OGE data for $\theta = 60°$ and $L/d = 3$

$\mathrm{Fr}_{G,OLE,A}$	$\lvert h_{OLE,A} \rvert / d$	$\mathrm{Fr}_{G,OLE,B}$	$\lvert h_{OLE,B} \rvert / d$	$\mathrm{Fr}_{L,OGE,A}$	$h_{OGE,A}/d$	$\mathrm{Fr}_{L,OGE,B}$	$h_{OGE,B}/d$
14.04	2.014	14.51	2.110	15.57	1.534	15.66	1.427
17.88	2.126	18.69	2.262	19.72	1.715	20.59	1.662
21.29	2.274	21.79	2.365	24.61	1.924	25.08	1.817
24.20	2.440	25.23	2.478	29.68	2.113	30.27	1.961
29.99	2.682	31.47	2.704	34.59	2.217	35.35	2.121
34.58	2.850	36.30	2.941	42.72	2.523	43.68	2.294
38.15	2.938	39.95	3.025	45.19	2.586	49.17	2.458

Table C.23 – Experimental two-phase flow data for Case 13

with P_0 = 316 kPa, ΔP = 40 kPa, $\theta = 60°$ and $L/d = 3$

Case #	h_A (mm)	$\dot{m}_{L,A}$ (kg/s)	$\dot{m}_{G,A}$ (kg/s)	h_B (mm)	$\dot{m}_{L,B}$ (kg/s)	$\dot{m}_{G,B}$ (kg/s)
13- 1	9.743	1.227E-01	0.000E+00	25.883	1.229E-01	0.000E+00
13- 2	8.166	9.760E-02	8.840E-05	24.305	1.229E-01	0.000E+00
13- 3	6.838	8.227E-02	2.050E-04	22.977	1.229E-01	0.000E+00
13- 4	5.324	6.175E-02	3.281E-04	21.463	1.229E-01	0.000E+00
13- 5	3.447	4.853E-02	6.245E-04	19.586	1.229E-01	0.000E+00
13- 6	1.914	3.957E-02	9.526E-04	18.053	1.229E-01	0.000E+00
13- 7	0.196	3.401E-02	1.293E-03	16.336	1.229E-01	0.000E+00
13- 8	-1.193	2.742E-02	1.629E-03	14.946	1.229E-01	0.000E+00
13- 9	-2.605	2.151E-02	1.968E-03	13.535	1.229E-01	0.000E+00
13- 10	-4.319	1.588E-02	2.365E-03	11.821	1.229E-01	0.000E+00
13- 11	-6.018	1.205E-02	2.861E-03	10.122	1.229E-01	0.000E+00
13- 12	-7.347	7.024E-03	3.631E-03	8.792	1.178E-01	1.095E-05
13- 13	-9.025	4.604E-03	4.097E-03	7.114	9.326E-02	6.931E-05
13- 14	-10.457	2.271E-03	5.012E-03	5.682	7.144E-02	2.157E-04
13- 15	-12.033	8.104E-04	5.881E-03	4.107	5.990E-02	3.552E-04
13- 16	-13.751	0.000E+00	7.047E-03	2.388	4.646E-02	6.274E-04
13- 17	-15.266	0.000E+00	6.964E-03	0.873	3.921E-02	8.437E-04
13- 18	-16.658	0.000E+00	6.919E-03	-0.519	3.225E-02	1.193E-03
13- 19	-18.480	0.000E+00	6.993E-03	-2.341	2.656E-02	1.519E-03
13- 20	-19.791	0.000E+00	6.871E-03	-3.652	2.073E-02	1.903E-03
13- 21	-21.430	0.000E+00	6.854E-03	-5.291	1.599E-02	2.228E-03
13- 22	-23.130	0.000E+00	6.980E-03	-6.991	1.067E-02	2.785E-03
13- 23	-24.851	0.000E+00	6.871E-03	-8.711	8.031E-03	3.330E-03
13- 24	-26.509	0.000E+00	6.781E-03	-10.370	4.049E-03	4.226E-03
13- 25	-27.780	0.000E+00	6.629E-03	-11.640	2.373E-03	4.971E-03
13- 26	-29.538	0.000E+00	6.707E-03	-13.399	0.000E+00	6.926E-03

Table C.24 – Experimental two-phase flow data for Case 14

with P_0 = 316 kPa, ΔP = 123 kPa, $\theta = 60°$ and $L/d = 3$

Case #	h_A (mm)	$\dot{m}_{L,A}$ (kg/s)	$\dot{m}_{G,A}$ (kg/s)	h_B (mm)	$\dot{m}_{L,B}$ (kg/s)	$\dot{m}_{G,B}$ (kg/s)
14- 1	13.415	2.353E-01	0.000E+00	29.554	2.380E-01	0.000E+00
14- 2	11.678	1.844E-01	1.032E-04	27.817	2.380E-01	0.000E+00
14- 3	9.817	1.457E-01	2.993E-04	25.957	2.380E-01	0.000E+00
14- 4	7.939	1.129E-01	6.826E-04	24.078	2.380E-01	0.000E+00
14- 5	6.202	9.399E-02	9.459E-04	22.341	2.380E-01	0.000E+00
14- 6	4.118	7.144E-02	1.469E-03	20.257	2.380E-01	0.000E+00
14- 7	2.524	6.362E-02	1.863E-03	18.663	2.380E-01	0.000E+00
14- 8	0.561	5.050E-02	2.560E-03	16.701	2.380E-01	0.000E+00
14- 9	-0.890	4.323E-02	3.054E-03	15.249	2.380E-01	0.000E+00
14- 10	-2.830	2.898E-02	3.933E-03	13.309	2.380E-01	0.000E+00
14- 11	-4.631	2.119E-02	4.578E-03	11.508	2.141E-01	3.562E-05
14- 12	-6.574	1.532E-02	5.401E-03	9.565	1.662E-01	2.021E-04
14- 13	-8.374	1.153E-02	6.142E-03	7.765	1.432E-01	3.802E-04
14- 14	-9.949	7.255E-03	7.205E-03	6.190	1.187E-01	6.118E-04
14- 15	-11.974	3.824E-03	8.459E-03	4.165	9.919E-02	8.950E-04
14- 16	-13.610	1.328E-03	9.957E-03	2.529	8.051E-02	1.200E-03
14- 17	-15.411	0.000E+00	1.137E-02	0.728	6.690E-02	1.544E-03
14- 18	-17.315	0.000E+00	1.170E-02	-1.176	5.479E-02	2.212E-03
14- 19	-19.199	0.000E+00	1.173E-02	-3.059	4.579E-02	2.775E-03
14- 20	-20.837	0.000E+00	1.166E-02	-4.697	3.540E-02	3.429E-03
14- 21	-22.634	0.000E+00	1.173E-02	-6.494	2.814E-02	3.978E-03
14- 22	-24.518	0.000E+00	1.164E-02	-8.379	1.865E-02	4.882E-03
14- 23	-26.301	0.000E+00	1.164E-02	-10.162	1.272E-02	5.708E-03
14- 24	-28.247	0.000E+00	1.162E-02	-12.108	7.062E-03	7.106E-03
14- 25	-30.071	0.000E+00	1.143E-02	-13.932	3.525E-03	8.358E-03
14- 26	-31.877	0.000E+00	1.135E-02	-15.738	0.000E+00	1.184E-02

Table C.25 – Experimental two-phase flow data for Case 15

with P_0 = 517 kPa, ΔP = 97 kPa, $\theta = 60°$ and $L/d = 3$

Case #	h_A (mm)	$\dot{m}_{L,A}$ (kg/s)	$\dot{m}_{G,A}$ (kg/s)	h_B (mm)	$\dot{m}_{L,B}$ (kg/s)	$\dot{m}_{G,B}$ (kg/s)
15- 1	12.663	2.133E-01	0.000E+00	28.802	2.171E-01	0.000E+00
15- 2	11.004	1.715E-01	2.098E-04	27.143	2.171E-01	0.000E+00
15- 3	9.180	1.391E-01	4.685E-04	25.319	2.171E-01	0.000E+00
15- 4	7.253	1.088E-01	1.109E-03	23.392	2.171E-01	0.000E+00
15- 5	5.329	9.103E-02	1.430E-03	21.468	2.171E-01	0.000E+00
15- 6	3.587	7.144E-02	2.162E-03	19.726	2.171E-01	0.000E+00
15- 7	1.803	6.209E-02	2.780E-03	17.942	2.171E-01	0.000E+00
15- 8	0.247	5.382E-02	3.389E-03	16.386	2.171E-01	0.000E+00
15- 9	-1.824	3.924E-02	4.441E-03	14.315	2.171E-01	0.000E+00
15- 10	-3.568	2.727E-02	5.504E-03	12.572	2.171E-01	0.000E+00
15- 11	-5.207	2.061E-02	6.345E-03	10.932	2.009E-01	6.069E-05
15- 12	-7.105	1.532E-02	7.597E-03	9.034	1.608E-01	2.618E-04
15- 13	-8.707	1.166E-02	8.343E-03	7.432	1.415E-01	5.034E-04
15- 14	-10.512	6.501E-03	9.944E-03	5.627	1.161E-01	9.082E-04
15- 15	-12.420	3.481E-03	1.144E-02	3.720	9.834E-02	1.268E-03
15- 16	-14.225	9.398E-04	1.371E-02	1.914	8.051E-02	1.864E-03
15- 17	-15.907	0.000E+00	1.567E-02	0.232	6.690E-02	2.194E-03
15- 18	-17.733	0.000E+00	1.610E-02	-1.593	5.496E-02	3.048E-03
15- 19	-19.621	0.000E+00	1.570E-02	-3.482	4.476E-02	3.772E-03
15- 20	-21.674	0.000E+00	1.600E-02	-5.534	3.320E-02	4.983E-03
15- 21	-23.317	0.000E+00	1.578E-02	-7.178	2.563E-02	5.834E-03
15- 22	-25.304	0.000E+00	1.579E-02	-9.165	1.688E-02	7.000E-03
15- 23	-26.744	0.000E+00	1.561E-02	-10.604	1.204E-02	7.681E-03
15- 24	-28.941	0.000E+00	1.580E-02	-12.802	5.844E-03	1.010E-02
15- 25	-32.311	0.000E+00	1.515E-02	-16.172	0.000E+00	1.556E-02

Table C.26 – Experimental two-phase flow data for Case 16

with P_0 = 517 kPa, ΔP = 235 kPa, $\theta = 60°$ and $L/d = 3$

Case #	h_A (mm)	$\dot{m}_{L,A}$ (kg/s)	$\dot{m}_{G,A}$ (kg/s)	h_B (mm)	$\dot{m}_{L,B}$ (kg/s)	$\dot{m}_{G,B}$ (kg/s)
16- 1	16.023	3.363E-01	0.000E+00	32.162	3.437E-01	0.000E+00
16- 2	14.093	2.848E-01	2.084E-04	30.233	3.437E-01	0.000E+00
16- 3	11.797	2.218E-01	6.707E-04	27.937	3.437E-01	0.000E+00
16- 4	9.873	1.748E-01	1.280E-03	26.013	3.437E-01	0.000E+00
16- 5	7.767	1.416E-01	1.902E-03	23.907	3.437E-01	0.000E+00
16- 6	5.882	1.129E-01	2.700E-03	22.021	3.437E-01	0.000E+00
16- 7	3.853	9.481E-02	3.552E-03	19.992	3.437E-01	0.000E+00
16- 8	1.865	7.577E-02	4.948E-03	18.004	3.437E-01	0.000E+00
16- 9	-0.103	6.040E-02	6.339E-03	16.037	3.437E-01	0.000E+00
16- 10	-2.090	4.223E-02	7.997E-03	14.049	3.261E-01	4.513E-05
16- 11	-4.259	3.417E-02	8.919E-03	11.880	2.718E-01	2.470E-04
16- 12	-6.250	2.509E-02	1.027E-02	9.889	2.247E-01	6.286E-04
16- 13	-8.342	1.880E-02	1.156E-02	7.797	1.940E-01	1.064E-03
16- 14	-10.372	1.218E-02	1.335E-02	5.767	1.626E-01	1.538E-03
16- 15	-12.443	7.101E-03	1.481E-02	3.696	1.398E-01	2.036E-03
16- 16	-14.412	3.124E-03	1.683E-02	1.728	1.156E-01	2.683E-03
16- 17	-16.360	1.069E-03	1.889E-02	-0.221	9.919E-02	3.254E-03
16- 18	-18.433	0.000E+00	2.115E-02	-2.294	7.938E-02	4.334E-03
16- 19	-20.506	0.000E+00	2.123E-02	-4.367	6.392E-02	5.653E-03
16- 20	-22.641	0.000E+00	2.114E-02	-6.502	4.780E-02	7.236E-03
16- 21	-24.653	0.000E+00	2.110E-02	-8.514	3.666E-02	8.459E-03
16- 22	-26.913	0.000E+00	2.115E-02	-10.773	2.318E-02	1.017E-02
16- 23	-28.863	0.000E+00	2.104E-02	-12.723	1.481E-02	1.175E-02
16- 24	-30.691	0.000E+00	2.088E-02	-14.552	7.884E-03	1.422E-02
16- 25	-32.540	0.000E+00	2.081E-02	-16.401	3.563E-03	1.657E-02
16- 26	-34.819	0.000E+00	2.060E-02	-18.680	0.000E+00	2.163E-02

Appendix D

Numerical Data

D.1 Numerical Data for Geometry G1

Table D.1 – Numerical OLE data for Geometry G1

$\mathbf{Fr}_{G,OLE}$	h_{OLE} (mm)
3.92	-8.28
7.74	-10.74
23.56	-16.68
32.83	-18.90

Table D.2 - Numerical OGE data for Geometry G1

$\mathbf{Fr}_{L,OGE}$	h_{OGE} (mm)
14.00	10.85
24.30	13.10
31.50	14.55
45.80	17.10

Table D.3 - Numerical two-phase flow data for Geometry G1, $P_0 = 35$ kPa

h (mm)	$\dot{m}_L$ (kg/s)	$\dot{m}_G$ (kg/s)	$\dot{m}_{TP}$ (kg/s)
13.10	1.058E-01	0.000E+00	1.058E-01
10.82	8.667E-02	1.572E-04	8.683E-02
5.65	6.053E-02	6.300E-04	6.116E-02
3.15	4.971E-02	9.162E-04	5.062E-02
0.50	3.770E-02	1.202E-03	3.890E-02
-2.95	2.443E-02	1.640E-03	2.607E-02
-6.40	1.444E-02	2.044E-03	1.649E-02
-8.30	1.102E-02	2.310E-03	1.333E-02
-9.10	8.546E-03	2.343E-03	1.089E-02
-9.90	6.746E-03	2.368E-03	9.114E-03
-10.05	5.957E-03	2.411E-03	8.368E-03
-12.60	2.842E-03	2.845E-03	5.687E-03
-14.25	1.537E-03	3.090E-03	4.626E-03
-15.90	2.044E-04	3.429E-03	3.634E-03
-17.78	0.000E+00	3.595E-03	3.595E-03

Table D.4 - Numerical two-phase flow data for Geometry G1, P_0 = 120 kPa

h (mm)	$\dot{m}_L$ (kg/s)	$\dot{m}_G$ (kg/s)	$\dot{m}_{TP}$ (kg/s)
17.10	1.991E-01	0.000E+00	1.991E-01
14.35	1.682E-01	2.386E-04	1.684E-01
11.50	1.382E-01	7.120E-04	1.390E-01
8.65	1.239E-01	1.015E-03	1.249E-01
6.85	1.085E-01	1.394E-03	1.099E-01
2.95	8.096E-02	2.104E-03	8.306E-02
-1.25	5.491E-02	2.860E-03	5.777E-02
-3.80	4.148E-02	3.419E-03	4.490E-02
-7.70	2.309E-02	4.272E-03	2.736E-02
-11.55	9.306E-03	4.987E-03	1.429E-02
-15.00	3.346E-03	5.854E-03	9.200E-03
-18.90	0.000E+00	6.702E-03	6.702E-03

D.2 Numerical Data for Geometry G2

Table D.5 – Numerical OLE data for Geometry G2

$\mathrm{Fr}_{G,OLE}$	h_{OLE} (mm)
0.13	-3.00
0.22	-3.00
0.60	-4.00
7.86	-10.20
13.44	-12.36
22.82	-15.48
36.85	-18.42

Table D.6 - Numerical OGE data for Geometry G2

$\mathrm{Fr}_{L,OGE}$	h_{OGE} (mm)
7.78	8.50
13.88	10.70
27.09	13.65
51.88	18.05

Table D.7 - Numerical two-phase flow data for Geometry G2, P_0 = 35 kPa

h (mm)	$\dot{m}_L$ (kg/s)	$\dot{m}_G$ (kg/s)	$\dot{m}_{TP}$ (kg/s)
10.70	6.040E-02	0.000E+00	6.040E-02
8.50	5.048E-02	1.269E-04	5.061E-02
6.40	4.224E-02	2.224E-04	4.246E-02
4.50	3.298E-02	3.526E-04	3.333E-02
2.05	2.546E-02	4.744E-04	2.593E-02
0.00	1.557E-02	5.205E-04	1.609E-02
-2.05	1.241E-02	7.415E-04	1.316E-02
-3.70	8.373E-03	8.218E-04	9.195E-03
-6.20	4.622E-03	9.614E-04	5.583E-03
-8.25	2.720E-03	1.293E-03	4.014E-03
-10.05	1.401E-03	1.534E-03	2.935E-03
-12.36	0.000E+00	2.251E-03	2.251E-03

Table D.8 - Numerical two-phase flow data for Geometry G2, P_0 = 120 kPa

h (mm)	$\dot{m}_L$ (kg/s)	$\dot{m}_G$ (kg/s)	$\dot{m}_{TP}$ (kg/s)
13.65	1.178E-01	0.000E+00	1.178E-01
12.10	1.058E-01	5.009E-05	1.058E-01
10.70	9.385E-02	2.768E-04	9.413E-02
8.45	7.577E-02	5.248E-04	7.629E-02
5.70	5.826E-02	8.686E-04	5.913E-02
3.40	4.788E-02	1.080E-03	4.896E-02
0.60	3.413E-02	1.375E-03	3.551E-02
-2.30	2.373E-02	1.672E-03	2.540E-02
-5.25	1.378E-02	1.964E-03	1.574E-02
-7.55	8.942E-03	2.335E-03	1.128E-02
-10.10	5.294E-03	2.883E-03	8.177E-03
-13.40	1.319E-03	3.548E-03	4.867E-03
-14.70	5.189E-04	3.961E-03	4.480E-03
-15.48	0.000E+00	4.719E-03	4.719E-03

D.3 Numerical Data for Geometry G3

Table D.9 – Numerical OLE data for Geometry G3

$\mathbf{Fr}_{G,OLE}$	h_{OLE} (mm)
0.23	-3.18
0.61	-3.78
2.06	-5.88
4.32	-7.85
7.71	-9.00
13.19	-11.64
22.55	-14.19
36.46	-16.98

Table D.10 - Numerical OGE data for Geometry G3

$\mathbf{Fr}_{L,OGE}$	h_{OGE} (mm)
7.62	7.86
13.58	9.54
26.51	11.88
51.13	16.44

Table D.11 - Numerical two-phase flow data for Geometry G3, P_0 = 35 kPa

h (mm)	$\dot{m}_L$ (kg/s)	$\dot{m}_G$ (kg/s)	$\dot{m}_{TP}$ (kg/s)
9.54	4.641E-02	0.000E+00	4.641E-02
7.30	3.774E-02	1.001E-04	3.784E-02
5.55	2.979E-02	1.830E-04	2.997E-02
3.50	2.300E-02	2.647E-04	2.326E-02
2.05	1.745E-02	3.583E-04	1.781E-02
-0.10	1.283E-02	4.631E-04	1.330E-02
-1.60	1.034E-02	6.007E-04	1.094E-02
-2.70	7.351E-03	6.928E-04	8.044E-03
-5.30	4.772E-03	8.004E-04	5.573E-03
-7.50	1.776E-03	9.299E-04	2.706E-03
-9.15	1.212E-03	1.226E-03	2.438E-03
-11.64	0.000E+00	1.734E-03	1.734E-03

Table D.12 - Numerical two-phase flow data for Geometry G3, P_0 = 120 kPa

h (mm)	$\dot{m}_L$ (kg/s)	$\dot{m}_G$ (kg/s)	$\dot{m}_{TP}$ (kg/s)
11.90	9.052E-02	0.000E+00	9.052E-02
9.25	7.333E-02	3.269E-04	7.366E-02
6.70	5.445E-02	4.637E-04	5.491E-02
4.65	4.360E-02	6.278E-04	4.423E-02
2.75	3.340E-02	8.521E-04	3.425E-02
-0.10	2.435E-02	1.131E-03	2.548E-02
-2.30	1.745E-02	1.397E-03	1.885E-02
-4.55	1.199E-02	1.690E-03	1.368E-02
-6.80	7.461E-03	1.898E-03	9.359E-03
-9.20	3.332E-03	2.163E-03	5.495E-03
-12.10	1.567E-03	2.951E-03	4.518E-03
-13.30	5.490E-04	3.088E-03	3.637E-03
-14.19	0.000E+00	3.653E-03	3.653E-03

D.4 Numerical Data for Geometry G4

Table D.13 - Numerical two-phase flow data for Geometry G4, P_0 = 120 kPa

h_A (mm)	$\dot{m}_{L,A}$ (kg/s)	$\dot{m}_{G,A}$ (kg/s)	$\dot{m}_{TP,A}$ (kg/s)	h_B (mm)	$\dot{m}_{L,B}$ (kg/s)	$\dot{m}_{G,B}$ (kg/s)	$\dot{m}_{TP,B}$ (kg/s)
*14.43	1.014E-01	0.00E+00	1.014E-01	23.96	1.017E-01	0.00E+00	1.017E-01
10.20	6.547E-02	4.190E-04	6.589E-02	19.73	1.017E-01	0.00E+00	1.017E-01
6.50	3.965E-02	8.304E-04	4.048E-02	16.03	1.017E-01	0.00E+00	1.017E-01
2.15	2.150E-02	1.375E-03	2.287E-02	11.68	1.023E-01	0.00E+00	1.023E-01
-13.75	0.00E+00	4.108E-03	4.108E-03	-4.22	2.592E-02	1.282E-03	2.720E-02
-17.60	0.00E+00	4.097E-03	4.097E-03	-8.08	1.191E-02	1.916E-03	1.383E-02
-21.80	0.00E+00	4.097E-03	4.097E-03	-12.28	4.938E-03	3.075E-03	8.013E-03
-27.60	0.00E+00	4.095E-03	4.095E-03	**-18.08	0.00E+00	4.095E-03	4.095E-03

* $h_{OGE,A}$, ** $h_{OLE,B}$

Table D.14 - Numerical two-phase flow data for Geometry G4, P_0 = 400 kPa

h_A (mm)	$\dot{m}_{L,A}$ (kg/s)	$\dot{m}_{G,A}$ (kg/s)	$\dot{m}_{TP,A}$ (kg/s)	h_B (mm)	$\dot{m}_{L,B}$ (kg/s)	$\dot{m}_{G,B}$ (kg/s)	$\dot{m}_{TP,B}$ (kg/s)
*17.57	1.897E-01	0.00E+00	1.897E-01	27.10	1.897E-01	0.00E+00	1.897E-01
10.30	9.206E-02	1.658E-03	9.372E-02	19.83	1.918E-01	0.00E+00	1.918E-01
6.65	5.785E-02	2.735E-03	6.059E-02	16.18	1.918E-01	0.00E+00	1.918E-01
2.15	1.969E-02	4.983E-03	2.467E-02	11.68	1.924E-01	0.00E+00	1.924E-01
-11.75	0.00E+00	9.760E-03	9.760E-03	-2.22	7.794E-02	2.307E-03	8.025E-02
-13.45	0.00E+00	9.770E-03	9.770E-03	-3.93	6.976E-02	2.610E-03	7.237E-02
-17.65	0.00E+00	9.758E-03	9.758E-03	-8.13	3.565E-02	5.078E-03	4.073E-02
-21.80	0.00E+00	9.757E-03	9.757E-03	-12.28	1.675E-02	6.884E-03	2.363E-02
-24.85	0.00E+00	9.757E-03	9.757E-03	-15.33	7.950E-03	6.720E-03	1.467E-02
-31.59	0.00E+00	9.753E-03	9.753E-03	**-22.07	0.00E+00	9.751E-03	9.751E-03

* $h_{OGE,A}$, ** $h_{OLE,B}$

D.5 Numerical Data for Geometry G5

Table D.15 - Numerical two-phase flow data for Geometry G5, P_0 = 60 kPa

h_A (mm)	$\dot{m}_{L,A}$ (kg/s)	$\dot{m}_{G,A}$ (kg/s)	$\dot{m}_{TP,A}$ (kg/s)	h_B (mm)	$\dot{m}_{L,B}$ (kg/s)	$\dot{m}_{G,B}$ (kg/s)	$\dot{m}_{TP,B}$ (kg/s)
*13.83	1.400E-01	0.00E+00	1.400E-01	18.59	1.401E-01	0.00E+00	1.401E-01
9.96	9.969E-02	3.435E-04	1.000E-01	14.73	1.399E-01	0.00E+00	1.399E-01
7.96	8.046E-02	6.726E-04	8.113E-02	12.73	1.462E-01	9.446E-06	1.462E-01
6.36	6.424E-02	9.070E-04	6.515E-02	11.13	1.325E-01	1.192E-04	1.326E-01
3.96	5.035E-02	1.174E-03	5.152E-02	8.73	1.066E-01	2.753E-04	1.069E-01
2.16	3.834E-02	1.463E-03	3.980E-02	6.93	8.915E-02	4.804E-04	8.963E-02
0.13	3.147E-02	1.688E-03	3.316E-02	4.90	8.084E-02	6.710E-04	8.151E-02
-2.01	2.393E-02	1.998E-03	2.593E-02	2.76	6.538E-02	8.952E-04	6.628E-02
-4.01	1.644E-02	2.311E-03	1.875E-02	0.76	5.229E-02	1.136E-03	5.342E-02
-6.39	9.954E-03	2.641E-03	1.259E-02	-1.63	4.015E-02	1.420E-03	4.157E-02
-7.94	6.221E-03	2.702E-03	8.924E-03	-3.18	2.732E-02	1.774E-03	2.909E-02
-9.91	4.967E-03	3.757E-03	8.724E-03	-5.14	2.466E-02	1.862E-03	2.652E-02
-11.78	1.808E-03	4.096E-03	5.905E-03	-7.02	1.627E-02	2.153E-03	1.843E-02
-13.93	5.935E-04	4.889E-03	5.483E-03	-9.17	9.258E-03	2.361E-03	1.162E-02
-15.94	1.884E-08	5.351E-03	5.351E-03	-11.18	6.270E-03	3.140E-03	9.410E-03
-17.94	0.00E+00	5.350E-03	5.350E-03	-13.18	2.719E-03	3.788E-03	6.507E-03
-20.89	0.00E+00	5.347E-03	5.347E-03	**-16.27	0.00E+00	5.346E-03	5.346E-03

* $h_{OGE,A}$, ** $h_{OLE,B}$, $h_{OLE,A}$ = -15.06 mm, $h_{OGE,B}$ = 12.77 mm

Table D.16 - Numerical two-phase flow data for Geometry G5, P_0 = 120 kPa

h_A (mm)	$\dot{m}_{L,A}$ (kg/s)	$\dot{m}_{G,A}$ (kg/s)	$\dot{m}_{TP,A}$ (kg/s)	h_B (mm)	$\dot{m}_{L,B}$ (kg/s)	$\dot{m}_{G,B}$ (kg/s)	$\dot{m}_{TP,B}$ (kg/s)
*15.26	2.035E-01	0.00E+00	2.035E-01	19.88	2.036E-01	0.00E+00	2.036E-01
12.11	1.694E-01	4.255E-04	1.698E-01	16.88	2.038E-01	0.00E+00	2.038E-01
10.16	1.194E-01	1.020E-03	1.204E-01	14.93	2.103E-01	1.325E-05	2.103E-01
8.21	9.682E-02	1.381E-03	9.820E-02	12.98	1.945E-01	1.748E-04	1.947E-01
6.16	8.120E-02	1.686E-03	8.289E-02	10.93	1.741E-01	3.831E-04	1.745E-01
4.11	6.615E-02	2.053E-03	6.820E-02	8.88	1.497E-01	6.473E-04	1.504E-01
1.66	5.257E-02	2.461E-03	5.503E-02	6.43	1.250E-01	9.487E-04	1.260E-01
0.11	4.351E-02	2.810E-03	4.631E-02	4.88	1.077E-01	1.210E-03	1.090E-01
-2.64	2.996E-02	3.404E-03	3.336E-02	2.13	8.295E-02	1.667E-03	8.462E-02
-4.04	2.396E-02	3.723E-03	2.769E-02	0.73	7.250E-02	1.904E-03	7.440E-02
-6.19	1.615E-02	4.192E-03	2.034E-02	-1.43	5.831E-02	2.288E-03	6.060E-02
-8.24	1.077E-02	4.823E-03	1.559E-02	-3.47	4.694E-02	2.664E-03	4.960E-02
-10.48	7.880E-03	6.025E-03	1.390E-02	-5.72	3.401E-02	3.016E-03	3.703E-02
-12.02	4.796E-03	6.673E-03	1.147E-02	-7.26	2.570E-02	3.338E-03	2.904E-02
-12.79	2.777E-03	6.391E-03	9.168E-03	-8.02	2.090E-02	3.386E-03	2.429E-02
-13.34	2.100E-03	6.570E-03	8.670E-03	-8.58	1.853E-02	3.459E-03	2.199E-02
-13.89	1.449E-03	6.922E-03	8.372E-03	-9.13	1.558E-02	3.579E-03	1.916E-02
-13.94	1.575E-03	6.773E-03	8.348E-03	-9.18	1.588E-02	3.490E-03	1.937E-02
-14.89	9.155E-04	7.423E-03	8.338E-03	-10.13	1.331E-02	3.780E-03	1.709E-02
-15.99	8.613E-05	8.179E-03	8.265E-03	-11.23	1.183E-02	4.672E-03	1.650E-02
-15.94	2.430E-04	8.049E-03	8.292E-03	-11.18	1.183E-02	4.416E-03	1.625E-02
-17.99	0.00E+00	8.213E-03	8.213E-03	-13.23	9.026E-03	6.036E-03	1.506E-02
-18.54	0.00E+00	8.213E-03	8.213E-03	-13.78	7.361E-03	6.218E-03	1.358E-02
-19.04	0.00E+00	8.213E-03	8.213E-03	-14.28	5.924E-03	6.358E-03	1.228E-02
-20.04	0.00E+00	8.215E-03	8.215E-03	-15.28	3.163E-03	6.198E-03	9.361E-03
-23.14	0.00E+00	8.210E-03	8.210E-03	**-18.37	0.00E+00	8.210E-03	8.210E-03

* $h_{OGE,A}$, ** $h_{OLE,B}$, $h_{OLE,A}$ = -18.37 mm, $h_{OGE,B}$ = 15.74 mm